UNIVERSITY OF CALIFORNIA SAN DIEGO

The synthesis and processing of epitaxially strained rare earth iron garnet films

A Dissertation submitted in partial satisfaction of the requirements
for the degree Doctor of Philosophy

in

Materials Science and Engineering

by

Chad Ronald Warren

Committee in charge:

Professor Javier Garay, Chair
Professor Prabhakar Bandaru
Professor Eric Fullerton
Professor Yasuhiro Kodera
Professor Vitali Nesterenko
Professor Jeffrey Rinehart

2023

The Dissertation of Chad Ronald Warren is approved, and it is acceptable in quality and form for publication on microfilm and electronically.

University of California San Diego

2023

DEDICATION

I am deeply humbled and grateful for the opportunity granted to me of pursuing a PhD. The hard work, love and support of my parents paved the way for this to ever be possible, and then at a critical point in my life, Professor Lutz saw something more in me and planted a seed. For some reason or another, certain individuals and society at large then decided it was worthwhile to invest in me. While it required some serious work and at times felt nebulous and never ending, I can't imagine taking a different path in life. I am fortunate to have had such a kind and patient advisor, who both guided me according to my abilities, and allowed me to make mistakes and grow. I'm thankful to both Pathi and Yasu for teaching me how to do research and for always pushing me to do it better. I even met some lasting friends along the way too. Kyle and Darren, you are two of the kindest, hardest working people I've ever known, and you made this process so much more enjoyable. Lastly, the support of my friends and family kept me sane and reminded me of what I had to look forward to after graduation. I think that should just about cover everyone.

TABLE OF CONTENTS

LIST OF FIGURES

LIST OF TABLES

ACKNOWLEDGEMENTS

I'd like to personally acknowledge Kyle Chan for teaching me how to handle various chemicals and lab equipment, amongst other lab work related things. I'd also like to acknowledge Pathi Sellappan for mentoring me during my earlier work and for teaching me how to synthesize ceramics with the polymeric-steric entrapment technique. I'd additionally like to acknowledge Yasu Kodera for teaching me how to synthesize nitrate salts, how to synthesize ceramics using the sol-gel route, and for helping me understand reciprocal space mapping and how to perform XRD measurements of single crystals. Other people I'd like to acknowledge are Victor Ortiz, Mohammed Aldosary, Alex Dupuy and Professor Jing Shi for their varied assistance and useful conversations.

Chapter 3 contains unpublished material. The dissertation author was the primary researcher and author of this chapter. Pathikumar Sellappan provided the data used to make **Fig. 3.23**.

Chapter 4 contains unpublished material. The dissertation author was the primary researcher and author of this chapter.

Chapter 5 contains data and figures as they were published in V. H. Ortiz, B. Askook, J. Li, M. Aldosary, M. Biggerstaff, W. Yuan, C. Warren, Y. Kodera, J. E. Garay, I. Barsukov, and J. Shi. First- and second-order magnetic anisotropy and damping of europium iron garnet under high strain. Phys. Rev. Mater., 5 (2021) 124414. The dissertation author was a co-author and co-researcher on this paper.

Chapter 6, in part, is a reprint of the material as it appears in C. R. Warren, V. Ortiz, L. Scipioni, J. Greer, J. Shi, Y. Kodera, and J. E. Garay. Robust perpendicular magnetic anisotropy

in off-axis sputtered europium iron garnet (EuIG) thin films. J. Magn. Magn. Mater., 560 (2022) 169513. The dissertation author was the primary researcher and author of this material.

VITA

2013 Bachelor of Science in Physics, University of California Davis

2015 Master of Science in Materials Science and Engineering, University of California Riverside

2023 Doctor of Philosophy in Materials Science and Engineering, University of California San Diego

ABSTRACT OF THE DISSERTATION

The synthesis and processing of epitaxially strained rare earth iron garnet films

by

Chad Ronald Warren

Doctor of Philosophy in Materials Science and Engineering

University of California San Diego, 2023

Professor Javier Garay, Chair

The rare earth iron garnets (REIG) are a technologically important class of materials owing to their ferrimagnetism, low spin damping, large band gaps, high Curie points and chemical stability. Epitaxial REIG films are also capable of producing perpendicular magnetic anisotropy (PMA) which results from the interfacial strain due to lattice mismatch between film and substrate, and causes the easy axis of magnetization to point out-of-plane of the film. This

unique set of properties makes REIGs attractive for spintronics device research in addition to fundamental spin transport studies. One obstacle that researchers face is that high-quality targets are not commercially available for many REIG compositions. Our work demonstrates a method of producing dense, fine structured REIG targets via wet chemical synthesis routes and subsequent consolidation of REIG powders using the current-activated, pressure-assisted densification technique. So far, PMA has been successfully tuned in REIG films by means of controlling the substrate material, substrate orientation, film thickness, and to a lesser extent by chemical substitution. Our method can easily produce chemically substituted REIG targets because we synthesize our own powders, which we demonstrated by the synthesis of a full compositional range of $Y_{3(1-X)}Tm_{3X}Fe_5O_{12}$ solid solution powders. The lattice parameter and magnetic saturation of the $Y_{3(1-X)}Tm_{3X}Fe_5O_{12}$ powders varied with composition, enabling further control over growth induced PMA. Most REIG films with PMA grown for research are produced using pulsed laser deposition (PLD), however, our work demonstrates that off-axis RF sputtering can also produce films with PMA. Sputtering is important for the large-scale manufacture of these films because it is more widely used in industry and has the added benefit of producing larger area films than PLD. Specifically, we grew epitaxial europium iron garnet (EuIG) films with robust PMA at a maximum thickness of 102 nm, the thickest EuIG films with PMA to date. Through the use of asymmetric reciprocal space mapping, we additionally showed that the lattice parameter and elastic properties of EuIG films grown by sputtering or PLD can deviate substantially from the literature values, which is likely explained through a combination of stoichiometric deviation and atomic point defects.

CHAPTER 1

Magnetic Properties of Rare Earth Iron Garnet Films

1.1. Magnetic Anisotropy

1.1.1. Introduction to Magnetic Anisotropy

In all magnetic materials, both the magnetization direction and the degree of demagnetization depend on the type and prevalence of magnetic anisotropy. There are several sources of anisotropy, such as crystalline, shape, stress, induced and exchange.[2] Of these, only the crystalline anisotropy, or rather, the magnetocrystalline anisotropy, is an intrinsic property of a material. All other sources of magnetic anisotropy are the result of extrinsic factors. Every magnetic material will at the very least possess both crystalline and shape anisotropy. Thin films can also possess stress induced anisotropy that results from interfacial strain caused by a mismatch of film and substrate lattice parameters. For most rare earth iron garnet films, the anisotropy can be fully described by the crystalline, shape and stress anisotropy terms.

The crystalline anisotropy is what determines the amount of energy required to cause the magnetization vector in a single crystal to rotate from the easy axis of magnetization to the hard one. These directions are intimately related to the structure and composition of a given material and they tend to lie either along the crystal's principal axes or the unit cell diagonals. The crystal anisotropy energy E_C per unit volume for cubic systems can be expressed as a series expansion in terms of the cosines of the angles a, b, and c made between the magnetization direction with respect to the principal axes. Let α_1, α_2, and α_3 be the cosines of these angles, and then to third order the expression for the crystalline anisotropy of a cubic system is

$$E_C = K_0 + K_1(\alpha_1^2\alpha_2^2 + \alpha_2^2\alpha_3^2 + \alpha_3^2\alpha_1^2) + K_2(\alpha_1^2\alpha_2^2\alpha_3^2) \quad (1.1)$$

where K_0, K_1, and K_2 are temperature dependent constants for a given material expressed in terms of erg/cm^3 or J/m^3.[2] In general, any higher order terms are small enough to be neglected. Note that the term K_0 contains all isotropic energy contributions, whereas K_1 and K_2 are the anisotropy constants. The above expression can also be expressed as a uniaxial anisotropy energy term $E_{Uni.}$ as follows:

$$E_{Uni.} = -K_1\cos^2\theta - K_2\cos^4\theta, \tag{1.2}$$

where θ is the angle made between the magnetization and the easy crystallographic direction. For cubic materials, the crystallographic easy direction lies in the <100> family of directions for $K_1 > 0$, and in the <111> family of directions for $K_1 < 0$.[39]

One of the most important sources of anisotropy in thin films is due to the long-range dipolar interaction, most commonly called shape anisotropy.[3] The field lines radiating out from atomic dipoles near the edges of a material extend beyond the body of the material, effectively sensing its boundaries. Because dipoles also interact with other nearby dipoles, the combined effect is that the shape of the material produces an anisotropy term of its own that influences the easy direction of magnetization. Oftentimes shape anisotropy is described using an anisotropic field called the demagnetizing field $\mathbf{H_d}$ as follows:

$$\mathbf{H_d} = -N\mathbf{M}, \tag{1.3}$$

where **M** is the magnetization vector and N is the shape-dependent demagnetizing tensor.[3] For thin films, all tensor elements belonging to N are zero except for the direction normal to the plane of the film, which is N = 1 in the SI convention or $N = 4\pi$ in the cgs convention. The total shape anisotropy energy per unit volume E_S of a film is calculated by assuming a uniform magnetization and then integrating the magnetostatic energy of the demagnetization field over its entire volume, resulting in the following expression:

$$E_S = \frac{1}{2}\mu_0 {M_S}^2 \cos^2\theta, \quad (1.4)$$

where M_S is the saturation magnetization of the film and θ is the angle made between the magnetization direction and the film normal.[3] This expression is written in the SI convention but can equivalently be expressed as $2\pi {M_S}^2 \cos^2\theta$ in the cgs convention, which gives a shape anisotropy term of $K_S = 2\pi {M_S}^2$.

In what is essentially the inverse of the magnetostriction effect, the magnetocrystalline anisotropy of a material changes in response to lattice strain. Stress induced strain can therefore alter the magnetization direction of a film. Common sources of strain in films include the thermal strain that results from differences in thermal expansion coefficients between adjacent layers, strain that emerges as a byproduct of the specific deposition conditions, and strain that is produced by mismatching lattice parameters of adjacent layers.[3] The most technologically significant technique for engineering magnetoelastic anisotropy in rare earth iron garnet films is the careful selection of a substrate with a lattice parameter that optimizes the strain conditions. The orientation of the substrate also plays a critical role in determining the magnetoelastic anisotropy since magnetoelastic constants are dependent on the film's orientation. The magnetoelastic energy per unit volume E_λ in an elastically isotropic and uniformly strained epitaxial film with isotropic magnetostriction is expressed as

$$E_\lambda = -\frac{3}{2}\lambda\sigma_{//}\cos^2\theta, \quad (1.5)$$

where λ is the magnetostriction constant, $\sigma_{//}$ is the in-plane stress, and θ is the angle created between the magnetization and the direction of uniform stress.[3] The magnetoelastic anisotropy term is therefore given by $K_\lambda = -\frac{3}{2}\lambda\sigma_{//}$.[9,10] The in-plane stress $\sigma_{//}$ is proportional to the in-plane strain $\varepsilon_{//}$ through a linear combination of the elastic stiffness constants, of which the exact relationship depends on the orientation of the film.

1.1.2. Stress Induced Perpendicular Magnetic Anisotropy

To first order, the effective anisotropy K_{eff} of an epitaxially strained rare earth iron garnet film is the sum of the crystalline, shape and magnetoelastic terms according to

$$K_{eff} = K_S + K_\lambda + K_1. \text{ [9,10]} \quad (1.6)$$

The anisotropy field H_a can then be calculated from K_{eff} from the following expression:

$$H_a = \frac{2K_{eff}}{M_S}. \text{ [9,10]} \quad (1.7)$$

When the net anisotropy field H_a is less than 0, the film has perpendicular magnetic anisotropy, meaning that its magnetization points out of plane. The exact expression for K_{eff} will take on slightly different forms depending on the growth direction and the crystallographic easy axis. Note that for all stoichiometric rare earth iron garnets except $Pr_3Fe_5O_{12}$, $K_1 < 0$ and the crystallographic easy axes are the <111> family of directions. The exact solutions of eq. (1.7) have been worked out for cubic films grown along the (100), (110) and (111) orientations.[4] For most rare earth iron garnet films, the value of K_1 is low and the dominant anisotropy terms come from its shape and stress. Therefore, perpendicular magnetic anisotropy in these materials is mostly a competition between the shape and magnetoelastic terms.

It is easier to attain perpendicular magnetic anisotropy in certain rare earth iron garnets than others. The reason for this is that perpendicular magnetic anisotropy depends on the crystalline anisotropy, magnetostriction constants and M_S of the material. Each material therefore requires a different amount of in-plane strain for a given orientation of film. Some materials require such high strains that it causes nonuniform strain relaxation to take place within short thicknesses of films, such that the average strain in the film is too low to produce enough magnetoelastic anisotropy to overcome the shape anisotropy. For this exact reason, producing

perpendicular anisotropy in YIG films is very difficult. A summary of the K_1, λ, and $4\pi M_S$ values for most rare earth iron garnets is provided in **Table 1.1**.

Table 1.1: Magnetostriction and cubic anisotropy coefficients for various rare earth iron garnets.

Compound	**K_1 (erg/cm^2)** [5]	**λ_{100} (x10^{-6})** [6]	**λ_{111} (x10^{-6})** [6]	**$4\pi M_S$ (G)** [40]
$Y_3Fe_5O_{12}$	-6,000	-1.30	-2.25	1800
$La_3Fe_5O_{12}$	~-6,000	--	--	--
$Pr_3Fe_5O_{12}$	+4,200	--	--	2065
$Nd_3Fe_5O_{12}$	-15,000	--	--	2080
$Sm_3Fe_5O_{12}$	-13,000	21.0	-8.45	1680
$Eu_3Fe_5O_{12}$	-31,000	21.0	1.85	1170
$Gd_3Fe_5O_{12}$	-6,000	0	-3.00	57
$Tb_3Fe_5O_{12}$	-8,200	-3.25	12.0	200
$Dy_3Fe_5O_{12}$	<-5,000	-12.4	-5.80	380
$Ho_3Fe_5O_{12}$	<-5,000	-3.90	-3.30	880
$Er_3Fe_5O_{12}$	-6,900	2.05	-4.80	1240
$Tm_3Fe_5O_{12}$	-7,000	1.45	-5.10	1400
$Yb_3Fe_5O_{12}$	-3,400	1.50	-4.45	1560
$Lu_3Fe_5O_{12}$	-5,200	--	--	1820

1.1.3. Review of Perpendicular Magnetic Anisotropy in Rare Earth Iron Garnets

The rare earth iron garnet (REIG) films were extensively studied for bubble domain memory applications in the 1970's owing to their ability to produce perpendicular magnetic anisotropy (PMA) in response to interfacial strain. The rare earth iron garnets proved more capable at producing perpendicular anisotropy than most materials because of their wide range of magnetostriction coefficients [6] and because their strain relaxes over relatively large distances, typically on the order of 10's of nanometers. This body of work showed that their perpendicular magnetic anisotropy could be tuned via controlling the amount of strain in the film. In recent

years, the rare earth iron garnets have received renewed scientific attention from the spintronics community in part because of their ability to produce perpendicular anisotropy, which is a requisite for many spintronics devices and low dissipation spin current conduction pathways.[41-44]

Many different rare earth iron garnets have been able to produce perpendicular magnetic anisotropy as a result of lattice mismatch strain. Their perpendicular anisotropy has been successfully tuned via growing films on different single crystal substrates, using different substrate orientations, varying film thickness, and sometimes through stoichiometric modification. To date, the rare earth iron garnets that have produced perpendicular magnetic anisotropy include yttrium iron garnet (YIG), samarium iron garnet (SmIG), europium iron garnet (EuIG), terbium iron garnet (TbIG), dysprosium iron garnet (DyIG), thulium iron garnet (TmIG), highly substituted manganese:YIG (Mn:YIG), highly substituted bismuth:YIG (Bi:YIG), and highly substituted cerium:YIG (Ce:YIG). It is worth mentioning that one theoretical study also suggests the possibility of PMA in holmium iron garnet (HoIG) when epitaxially grown on (111) oriented gadolinium gallium garnet (GGG), terbium gallium garnet (TbGG) or yttrium aluminum garnet (YAG) substrates, although this has yet to be experimentally verified.[9]

A thicker film with robust perpendicular magnetic anisotropy is often more valuable for spintronics applications than a thinner one owing to its larger magnetic moment which enables greater interaction with adjacent layers. There is typically a limit to how thick a film can be grown with stress induced perpendicular magnetic anisotropy. This is because the stress energy in a film scales with the strained volume, and at a certain strained thickness, it becomes energetically more favorable to produce dislocations within the material. The lattice size of the

film approaches the unstrained lattice parameter as more dislocations are formed, i.e., the strain relaxes. While higher average strains lead to larger anisotropy fields, greater strains more easily cause dislocation formation, and can sometimes lead to nonuniformly relaxing strain. Therefore, to maximize the thickness of a film with PMA, the film needs enough strain for the perpendicular anisotropy to overcome the shape anisotropy, but not too high of strain as to cause it to relax over small distances.

Due to its remarkably low spin damping, YIG would be the ideal candidate for spintronics studies, however, until recently, PMA was not possible in YIG due to a combination of relatively small magnetostriction constants and the fact that interfacial strain relaxes over shorter distances in YIG than most other REIG's. The earliest study to show PMA in YIG was in a pulsed laser deposition (PLD) grown bilayer structure that involved first depositing a 2.5 nm buffer layer of samarium gallium garnet (SmGG) on (111) oriented substituted gadolinium gallium garnet (SGGG) followed by the growth of a YIG layer on top. These bilayer structures showed clear PMA for thicknesses of YIG up to 20 nm, after which, PMA was lost.[10] Since then, two more studies have been published showing PMA in YIG, both of which used off-axis RF sputtering and a variety of substrates. The first of these studies found PMA in YIG grown on (111) oriented gadolinium yttrium scandium gallium garnet (GYSGG) substrates for thicknesses up to 15 nm, and also in YIG grown on (111) oriented gadolinium scandium gallium garnet (GSGG) for thicknesses up to 10 nm.[11] The last and most recent study to show PMA in YIG showed PMA in thickness up to 20 nm when grown on either (111) oriented yttrium scandium gallium garnet (YSGG) or SGGG, up to 40 nm on (111) oriented GYSGG, and up to 10 nm on (111) oriented GSGG.[12] Despite the recent progress in YIG films, PMA in YIG is not as robust as in other REIG systems, making it less suitable for certain applications.

Beginning from left to right across the lanthanide series of the periodic table, the next REIG to exhibit PMA is SmIG. In the one study that could be found showing PMA in SmIG, PMA was observed for thicknesses up to 30 nm when grown on (100) oriented gadolinium gallium garnet (GGG) using PLD.[13] Continuing across the lanthanide series, the next REIG to exhibit PMA is EuIG. PMA has been observed in PLD grown EuIG on (111) oriented GGG for thickness up to 56 nm by two separate studies, the more recent of which being for a europium-rich EuIG.[14, 16] Another study shows weak PMA in PLD grown polycrystalline EuIG on z-quartz for thicknesses up to 49 nm, suggesting a way of incorporating EuIG films with PMA into traditional silicon-based electronics.[15] It should be noted that the previously mentioned study is the only one covered in this section that did not have complete epitaxy in its films. Our own work produced PMA in off-axis sputtered epitaxial EuIG on (100) oriented GGG at a maximum thickness of 102 nm.[37] This is the thickest EuIG film reported with PMA to date.

The next REIG with PMA is TbIG. In two of the previously mentioned studies of EuIG on GGG, PMA was also observed in PLD grown TbIG on (100) oriented GGG for thickness up to 100 nm, and for terbium-rich TbIG grown on (111) GGG using PLD for thicknesses up to 90 nm.[14,16] An earlier study showed robust PMA in 250 nm thick TbIG grown on (110) GGG.[38] This is by far the thickest TbIG shown with PMA, and remarkably, it exhibits a high degree of mosaicity just like our 102 nm thick off-axis sputtered EuIG films.[37] After TbIG comes DyIG, which is also the most recently discovered REIG with PMA. In the single study showing PMA in DyIG, PMA was found in PLD grown DyIG films up to 35 nm thick when grown on either (111) oriented SGGG or (111) oriented GSGG.[25] That same study also showed robust PMA in DyIG films deposited on silicon for thicknesses up to 39 nm, making DyIG the simplest known REIG to incorporate into traditional electronics. The last of the un-

doped REIG's to exhibit PMA is TmIG. The earliest known study to show PMA in REIG's was also performed on TmIG. That study claimed PMA in PLD grown TmIG on (111) oriented GGG for thicknesses up to 350 nm, thus making TmIG the thicket REIG film with PMA to date. It should be noted that this study provides no evidence regarding the robustness of PMA in terms of the hysteretic squareness of the 350 nm film, although they do show reciprocal space maps confirming highly uniform strain in the film.[18] Other studies have shown PMA in PLD grown TmIG on (111) oriented SGGG and also on (111) oriented GGG, although these studies were for films in the 10 nm range.[17,19] An off-axis sputtered TmIG film on (111) oriented GGG showed PMA for a thickness of 9 nm.[35] More recently, one study even shows PMA in off-axis RF sputtered TmIG grown on (111) oriented GGG for thicknesses up to 30 nm.[20]

All of the stoichiometrically modified REIG studies showing PMA involved heavily substituted YIG. There are two primary methods of increasing PMA in YIG via atomic substitution: (1) increase the magnetoelastic coefficient by substituting Fe^{3+} cations with other magnetic atoms, and (2) adjust the in-plane strain by tuning the lattice parameter via substituting Y^{3+} cations with different sized atoms. The elastic stiffness coefficients and magnetic saturation are also subject to changing as a result of modifying the stoichiometry. Both of these terms also affect the magnitude of the stress-induced PMA, however, their roles were not as well explored. Mn:YIG is the only such material in which PMA was discovered by increasing the magnetoelastic coefficients. Using combinatorial PLD, they showed clear PMA in films with thicknesses up to 56 nm on (111) GGG for the composition $Y_3Mn_{5-X}Fe_XO_{12}$ where X = 1.12.[21] In Bi:YIG, PMA was achieved via substituting Y^{3+} with larger Bi^{3+} cations, thus increasing its lattice parameter. In the earliest Bi:YIG study, the presence of PMA was shown in PLD grown Bi:YIG on (111) oriented YAG, although robust, squared magnetic hysteresis loops were not

observed.[23] The second study showed robust PMA in PLD grown Bi:YIG on (111) oriented SGGG for thicknesses up to 30 nm for the composition $Bi_xY_{3-x}Fe_5O_{12}$ where X=1.[22] The final study to show PMA in REIG's was in Ce:YIG with the composition $Ce_{0.59}Y_{2.86}Fe_{4.55}O_{12}$ grown with PLD on (111) GGG, however, this material isn't very useful for most spintronics applications because PMA was only observed at temperatures below -100°C.[24] A summary of all of the discussed rare earth iron garnet films showing clear room temperature PMA is provided in **Table 1.2**.

Table 1.2: A summary of the rare earth iron garnet films found in literature showing clear room temperature PMA.

Material	Substrate	Maximum thickness	Deposition method	First author	Reference number
YIG	2.5 nm SmGG on (111) GGG	20 nm	PLD	J. Fu	[10]
YIG	(111) GYSGG	15 nm	RF sputtering	G. Li	[11]
YIG	(111) GSGG	10 nm	RF sputtering	G. Li	[11]
YIG	(111) YSGG	20 nm	RF sputtering	C. Y. Guo	[12]
YIG	(111) SGGG	20 nm	RF sputtering	C. Y. Guo	[12]
YIG	(111) GYSGG	40 nm	RF sputtering	C. Y. Guo	[12]
YIG	(111) GSGG	10 nm	RF sputtering	C. Y. Guo	[12]
SmIG	(100) GGG	30 nm	PLD	H. Yamahara	[13]
EuIG	(100) GGG	56 nm	PLD	V. H. Ortiz	[14]
EuIG	(100) GGG	102 nm	RF sputtering	C. R. Warren	[37]
Eu-rich EuIG	(100) GGG	56 nm	PLD	E. R. Rosenberg	[16]
Polycrystalline EuIG	z-quartz	49 nm	PLD	J. J. Bauer	[15]
TbIG	(100) GGG	100 nm	PLD	V. H. Ortiz	[14]
TbIG	(110) GGG	250 nm	PLD	N. Kumar	[38]
Tb-rich TbIG	(111) GGG	90 nm	PLD	E. R. Rosenberg	[16]
DyIG	(111) SGGG	35 nm	PLD	J. J. Bauer	[25]
DyIG	(111) GsGG	35 nm	PLD	J. J. Bauer	[25]
DyIG	silicon	39 nm	PLD	J. J. Bauer	[25]
TmIG	(111) GGG	350 nm	PLD	M. Kubota	[18]
TmIG	(111) SGGG	10 nm	PLD	C. Tang	[17]
TmIG	(111) GGG	8 nm	PLD	C. O. Avci	[19]
TmIG	(111) GGG	9 nm	RF sputtering	C. N. Wu	[35]
TmIG	(111) GGG	30 nm	RF sputtered	C. N. Wu	[20]
Mn:YIG	(111) GGG	56 nm	PLD	C. T. Wang	[21]
Bi:YIG	(111) SGGG	30 nm	PLD	L. Souhmah	[22]

1.2. Magnetic Damping

1.2.1. Introduction to Magnetic Damping

Magnetic damping, or spin damping, is a form of resistance experienced by unpaired electrons bound within a ferro- or ferrimagnetic medium. As the orientation of an electron's spin orbital momentum changes, it experiences a damping like torque. This torque is analogous to mechanical damping and involves the transfer of energy from the spin angular momentum to microscopic thermal motion in the material.[7] The unitless term used to describe this damping torque is called the Gilbert damping constant α. Gilbert damping is phenomenological in nature, arising from interactions of an electron's magnetization field with spin waves, eddy currents, lattice vibrations and itinerant electrons.[7]

Historically, the Gilbert damping term emerged as a correction to the classical magnetodynamic equation originally published by Landau and Lifshitz in 1935. The revised form, called the Landau-Lifshitz-Gilbert (LLG) equation, was derived in 1955 when Gilbert included the damping like term α. The LLG equation is expressed as follows:

$$\frac{\partial \mathbf{M}}{\partial t} = \gamma(1+\alpha^2)\mathbf{M}\times\mathbf{H} - \frac{\alpha}{M_S}\mathbf{M}\times\frac{\partial \mathbf{M}}{\partial t}, \tag{1.8}$$

where **M** is the magnetization vector, M_S is the magnetic saturation, γ is the gyromagnetic ratio and **H** is the external magnetic field.[7] The damping term combines several different mechanisms, such as magnon-phonon scattering, magnon-magnon scattering, eddy currents and interactions with itinerant electrons. While the damping can be numerically determined in accordance with the LLG equation, it depends as much on the intrinsic material itself as it does on external factors such as its physical dimensions and proximity to external magnetic fields. Furthermore, many materials contain defects, grain boundaries and other microstructural variations which can inherently alter the type and abundance of damping mechanisms. Since

damping depends on so many physical attributes, it is often simpler and more practical to indirectly measure a given materials damping using a technique like FMR.

Spin damping determines the rate at which spin angular moments reorient and can reach equilibrium.[8] Spin waves, or magnons, can travel over longer distances and with lower losses in materials with low damping. Spintronics devices can therefore benefit from higher efficiency when using low damping materials. The rare earth iron garnets have damping that is typically 1-2 orders of magnitude lower than most metals. In particular, YIG and LuIG exhibit some of the lowest known spin damping for any material, with α values as low as $\sim 10^{-5}$. In addition to their ability to produce perpendicular magnetic anisotropy, low spin damping makes the rare earth iron garnets a very attractive material for spintronics based research.

1.2.2. Review of Spin Damping in Rare Earth Iron Garnets

Considering that the central focus of this work is on rare earth iron garnets with perpendicular magnetic anisotropy, this review only includes results from those REIG's which have successfully shown PMA. Furthermore, because bulk and single crystal spin damping values often differ from their thin film counterparts, only thin film studies will be discussed here. As findings are presented throughout this section, it's important to keep in mind that many factors effect spin damping. Defects, impurities, grain boundaries, and rough surfaces and interfaces all tend to increase spin damping.[28] Additionally, damping is often higher in films with PMA than those with an in-plane easy axis of magnetization. In general, as a film becomes thicker and its strain relaxes, its damping approaches the intrinsic single crystal value of the material, which provides a minimum bound on spin damping. However, PMA also disappears when the strain sufficiently relaxes, therefore special attention should be given to the lowest damping films for thicknesses at which PMA is possible.

As the quintessential low damping material, it's unsurprising that there are many reports on damping in YIG films. Several studies of PLD grown nanometric YIG on GGG report spin damping constants in the range of 2-5 x 10^{-4}.[28-31] The lowest value found was 1.0 x 10^{-4} for 30 nm thick YIG grown on (110) oriented GGG using PLD which the authors attributed to both thermally annealing the substrates prior to deposition and using a very slow deposition rate of 0.09 nm/min.[27] Sputtered YIG films tend to have slightly larger damping values than those grown by PLD since PLD offers more control over the deposition and growth.[32,33] However, the quality of sputtered films is beginning to approach that of their PLD grown counterparts, with one report showing a Gilbert damping of 6.13 x 10^{-4} in a 16 nm thick off-axis sputtered YIG film on (111) oriented GGG.[33] The damping of this last film is especially impressive when considering its small thickness.

Going from left to right across the lanthanide series of the periodic table, the next REIG to consider is EuIG. In the first report of spin damping in EuIG films, the authors measured a Gilbert damping of 2.57 x 10^{-2} and 2.42 x 10^{-2} in Eu-rich EuIG with PMA grown using PLD on (111) GGG for thicknesses of 26 and 56 nm, respectively.[16] In a later study of EuIG grown using PLD on a variety of (111) oriented substrates showing no PMA, the damping was insensitive to the varying amounts of in-plane strain and had an average value of 2.17 x 10^{-2} for films with thicknesses near 50 nm.[45] The damping of our own off-axis sputtered EuIG films with PMA grown by off-axis sputtering on (100) GGG were substantially higher with values of 0.27 and 0.24 for 74 nm and 102 nm thick films, respectively. We believe that the damping of our films is so much higher because they were likely oxygen deficient and contained atomic point defects.

Continuing across the lanthanides, the next material is DyIG, for which there is only one report. In that study, damping in a 116 nm thick DyIG film deposited on (111) oriented GGG using PLD was measured as 0.23.[34] The next and last of the un-doped REIG's to consider is TmIG. In a study of PLD grown 5.6 nm thick TmIG/Pt heterostructures on (100) GGG, the spin damping was found to be on the order of 10^{-3} with no additional information given.[34] In a separate study on off-axis sputtered TmIG on (111) GGG, a 9 nm thick film had its Gilbert damping reported as 1.33 $x10^{-2}$.[35] Both of these films are very thin yet PMA was seen in TmIG at a large thickness of 350 nm [18], which suggest that lower damping may be possible in thicker films.

Moving on to the stoichiometrically modified REIG's, the next material to consider is Bi:YIG. In a 30 nm thick PLD grown Bi:YIG on (111) oriented SGGG with the composition $Bi_xY_{3-x}Fe_5O_{12}$ where X=1, a spin damping constant of 3.10 x 10^{-4} was measured.[22] This places Bi:YIG on par with the damping of high quality YIG films, and remarkably, this Bi:YIG sample had PMA whereas the previously discussed YIG films did not. The next and final material to discuss is Ce:YIG. For a PLD grown Ce:YIG film on (111) GGG with a thickness of 52 nm and a composition of $Ce_{0.5}Y_{2.5}Fe_5O_{12}$, the Gilbert damping was measured as 6.9 $x10^{-4}$, possibly indicating a higher intrinsic damping than what's found in pristine YIG.[36] Unfortunately, no spin relaxation studies reporting Gilbert damping could be found for SmIG, TbIG or Mn:YIG films. A summary of the damping for all of the films discussed here is provided in **Table 1.3**.

1.3. Effects of Nonstoichiometry and Defects in Rare Earth Iron Garnet Films

There is a wide range in the reported properties of rare earth iron garnet films. For example, EuIG films produced by different groups have reported $4\pi M_S$ values ranging from 879 to 1565 G.[14-16,45,46] In comparison, the literature value for the $4\pi M_S$ of bulk EuIG is 1193

Table 1.3: A summary of the room temperature spin damping constants reported for various rare earth iron garnet films. This table only considers compositions for which perpendicular magnetic anisotropy has been previously observed in.

Material	Substrate	Deposition method	t (nm)	α	First author	Reference
YIG	(110) GGG	PLD	30	1.0×10^{-4}	C. Tang	[27]
YIG	(111) GGG	PLD	11	3.2×10^{-4}	Y. Sun	[28]
YIG	(111) GGG	PLD	19	2.3×10^{-4}	Y. Sun	[28]
YIG	(100) GGG	PLD	79	2.2×10^{-4}	M. C. Onbasli	[29]
YIG	(100) GGG	PLD	70	5.0×10^{-4}	A. Krysztofik	[30]
YIG	(111) GGG	PLD	20	2.3×10^{-4}	O. d'Allivy Kelly	[31]
YIG	(111) GGG	RF sputtering	10	1.0×10^{-3}	T. Liu	[32]
YIG	(111) GGG	RF sputtering	14	1.2×10^{-3}	T. Liu	[32]
YIG	(111) GGG	RF sputtering	26	9.9×10^{-4}	T. Liu	[32]
YIG	(111) GGG	RF sputtering	16	6.1×10^{-4}	J. T. Brangham	[33]
Eu-rich EuIG	(111) GGG	PLD	26	2.6×10^{-2}	E. R. Rosenberg	[16]
Eu-rich EuIG	(111) GGG	PLD	56	2.4×10^{-2}	E. R. Rosenberg	[16]
EuIG	(111) GSGG	PLD	25	1.6×10^{-2}	V. H. Ortiz	[45]
EuIG	(111) GSGG	PLD	50	2.5×10^{-2}	V. H. Ortiz	[45]
EuIG	(111) NGG	PLD	50	2.4×10^{-2}	V. H. Ortiz	[45]
EuIG	(111) SGGG	PLD	50	2.1×10^{-2}	V. H. Ortiz	[45]
EuIG	(111) YSGG	PLD	50	2.5×10^{-2}	V. H. Ortiz	[45]
EuIG	(111) GGG	PLD	50	2.2×10^{-2}	V. H. Ortiz	[45]
EuIG	(111) TGG	PLD	50	2.3×10^{-2}	V. H. Ortiz	[45]
EuIG	(111) YAG	PLD	20	1.9×10^{-2}	V. H. Ortiz	[45]
EuIG	(100) GGG	RF sputtering	74	2.7×10^{-1}	C. R. Warren	This work - Ch. 6
EuIG	(100) GGG	RF sputtering	102	2.4×10^{-1}	C. R. Warren	This work - Ch. 6
DyIG	(111) GGG	PLD	116	2.3×10^{-1}	J. J. Bauer	[25]
TmIG	(100) GGG	PLD	5.6	$\sim 10^{-3}$	A. Quindeau	[34]
TmIG	(111) GGG	RF sputtering	9	1.3×10^{-2}	C. N. Wu	[35]
Bi:YIG	(111) SGGG	PLD	30	3.1×10^{-4}	L. Soumah	[22]
Ce:YIG	(111) GGG	PLD	52	6.9×10^{-4}	F. Mohmed	[36]

G.[47] This shows that the magnetic saturation of EuIG films can vary by as much as 30% from the bulk value. For strained films, some of this variation can be explained by expansion or contraction of the unit cell volume. However, deviation from stoichiometry can also result in changes to the $4\pi M_S$. In the 30 nm thick off-axis sputtered EuIG films by Guo et al., this was demonstrated when the measured $4\pi M_S$ decreased from 1564 G to 904 G as the Eu/Fe cation

ratio decreased from 0.586 to 0.498.[46] A similar phenomenon was reported in off-axis sputtered TmIG films by Wu et al.[20,35]

As the cation ratio changes, constitutional defects such as antisite defects or atomic vacancies are likely to develop. These defects can affect the overall $4\pi M_S$ in a few distinct ways. First, the overall unit cell volume is likely to change as a result of nonstoichiometry and defects, which directly affects the $4\pi M_S$. Second, the presence of antisite defects between the iron and rare earth ions can dramatically change the $4\pi M_S$ since the garnet structure has two nonequivalent magnetic sublattices belonging to Fe and a separate magnetic sublattice belonging to Eu, and each ion has a different contribution to the overall magnetic moment.[1] Third, oxygen vacancies can donate electrons to neighboring cations, reducing them from a +3 to a +2 oxidation state.[48,49] Different oxidation states have different effective radii and magnetic contributions, both of which impact the overall $4\pi M_S$. All three of these effects could also potentially impact the oxygen mediated superexchange, which effects the magnetic ordering and thus the $4\pi M_S$.

In both of the previously mentioned examples of off-axis sputtered EuIG and TmIG, the $4\pi M_S$, coercivity, lattice parameter and perpendicular field all changed with the rare earth:iron (RE:Fe) cation ratio.[20,35,46] For each study, only one target was used to fabricate the films with varying compositions. The compositional changes occurred as a result of the deposition conditions. Specifically, both cases demonstrated that the RE:Fe ratio increased as the longitudinal target to substrate distance increased. They argued that the less massive Fe ions are more easily scattered away from the central sputtering axis than the heavier RE ions. While these findings create interesting possibilities of tuning the stoichiometry and properties of a rare earth

iron garnet film via off-axis sputtering, it also complicates comparing films produced from different groups and using different methods.

Growing films using PLD likely doesn't change the cation ratio of the resulting film as much as off-axis sputtering can, however, that only means that PLD films are likely better at retaining the cation ratio of the target. If a PLD target is nonstoichiometric to begin with, that suggests that the resulting films will also be nonstoichiometric. Furthermore, not many types of rare earth iron garnet targets are commercially available for sputtering or PLD. Consequently, most researchers fabricate their own rare earth iron garnet targets by a solid-state reaction of rare earth and iron oxides. The phase compositions of the resulting targets are typically characterized by XRD analysis. Oftentimes these home-made targets contain secondary phases of the intermediary perovskite phase and constituent oxides, but the relative amount of each phase is difficult to determine from XRD alone since many of the peaks overlap with one other. XRD of powder or bulk specimens is also insensitive to small volume fractions of secondary phases. Therefore, unless elemental analysis is performed on the target, the exact RE:Fe ratio of a target is usually unknown.

In addition to the magnetic properties, defects and nonstoichiometry can also affect the elastic behavior and structure of films. A common approach of determining the strain of rare earth iron garnet films involves measuring the out-of-plane interplanar d-spacings using 2θ-θ XRD measurements. The out-of-plane strain is then calculated by assuming that the unstrained film has the same lattice parameter as the reference value, and the in-plane strain is inferred from elastic equations by assuming that the elastic stiffness constants of the film match the literature values.[50] However, there are few reference values available in literature for many of the rare earth iron garnets, and these assumptions are not always valid. For example, in the PLD grown

EuIG films by Ortiz et al., the in-plane strain calculated from 2θ-θ XRD measurements and the elastic stiffness constants from literature was shown to systematically underestimate the true in-plane strain as determined by asymmetric reciprocal space mapping by ~42%.[45] Unlike 2θ-θ scans, asymmetric reciprocal space maps directly measure both the in-plane and out-of-plane interplanar spacings. Despite the large difference in elastic behavior, the theoretical magnetoelastic response of these films calculated from literature values was only ~11% less than was measured from FMR analysis.

Since the initial RE:Fe ratio of the target might deviate from a pristine garnet, and the deposition and growth process might additionally alter the RE:Fe ratio or introduce point defects, the unstrained lattice parameter of the film material inherently depends on the manner it was fabricated. The off-axis sputtered EuIG and TmIG films demonstrated that the lattice parameter is in fact dependent on the RE:Fe ratio.[20,35,46] Similarly, our own oxygen deficient off-axis sputtered EuIG films were shown to have an intrinsic lattice parameter that was ~0.5% larger than the reference value by using asymmetric reciprocal space mapping.[37] One problem that arises is that it is practically very difficult to determine the intrinsic lattice parameter of a film. A possible solution is to grow a thick enough film as to be considered a single crystal and then directly measure its lattice parameter, however, this is both time and resource expensive. Alternatively, if one knew the intrinsic elastic stiffness constants of the materials in the film, then one could calculate the unstrained lattice parameter from the in-plane and out-of-plane d-spacings. The elastic stiffness constants of the deposited film, however, are suspect to the same sort of scrutiny and doubt as the lattice parameter. In the instance where there is a sample set of uniformly relaxing films with different average strain values, it should be possible to determine the elastic behavior of the as-grown films from the slope produced by plotting the out-of-plane

lattice parameter versus the in-plane lattice parameter. As previously mentioned, asymmetric reciprocal space maps directly measure both the in-plane and out-of-plane structures. With the elastic response of the film known, it would then be possible to extrapolate the unstrained lattice parameter of the films.

For properties like spin damping which are greatly affected by the surface quality, crystallinity and defect concentration, it isn't a surprise that the damping can vary amongst samples made of the same material. However, this makes it more difficult to understand whether slight differences in damping are caused by deviations in stoichiometry, defects, or something else. It would seem that the field of epitaxially strained rare earth iron garnets has reached a point where more widespread structural characterization is needed in order to better correlate magnetic properties to crystal structure. In recent years, more researchers are using XPS to determine the atomic composition of their films. This in itself provides much more information about the material in a film, however, it doesn't reveal the exact type and prevalence of defects. Techniques like Mössbauer spectroscopy would complement XPS data in a way that could help reveal the types of defects in a material. Lastly, our own work has shown that 2θ-θ measurements are not sufficient for characterizing the in-plane strain of films, and that reciprocal space mapping is necessary to accurately measure the strain of epitaxial films. The systematic analysis of rare earth iron garnet films using these three techniques in addition to the more typical FMR and AFM could aid in engineering low damping films with PMA and help better explain why materials like YIG have such lower damping than magnetically similar materials such as EuIG. A better understanding of the role of defects in rare earth iron garnets could possibly enable tuning their properties in a similar way to doping of semiconductors.

REFERENCES

[1] S. Geller, and M. A. Gilleo. The Crystal Structure and Ferrimagnetism of Yttrium-Iron Garnet, $Y_3Fe_2(FeO_4)_3$. J. Phys. Chem. Solids, 3 (1957) 30-36.

[2] B. D. Cullity, and C. D. Graham. Introduction to Magnetic Materials, Second Edition. (Wiley, Hoboken, 2009).

[3] M. T. Johnson, P. J. H. Bloemen, F. J. A. den Broeder, and J. J. de Vries. Magnetic anisotropy in metallic multilayers. Rep. Prog. Phys., 59 (1996) 1409-1458.

[4] D. M. Heinz, P. J. Besser, J. M. Owens, J. E. Mee, and G. R. Pulliam. Mobile Cylindrical Magnetic Domains in Epitaxial Garnet Films. J. Appl. Phys., 42 (1971) 4.

[5] P. Hansen. Magnetic Anisotropy and Magnetostriction in Garnets. Physics of Magnetic Garnets, ed. A. Paoletti (North-Holland, Amsterdam, 1978) 56-133.

[6] S. Iida. Magnetostriction Constants of Rare Earth Iron Garnets. J. Phys. Soc. Japan, 22 (1967) 5.

[7] T. L. Gilbert. A Phenomenological Theory of Damping in Ferromagnetic Materials. IEEE Trans. Magn., 40 (2004) 6.

[8] M. C. Hickey, and J. S. Moodera. Origin of Intrinsic Gilbert Damping. Phys. Rev. Lett., 102 (2009) 137601.

[9] S. M. Zanjani, and M. C. Onbasli. Thin film rare earth iron garnets with perpendicular magnetic anisotropy for spintronics applications. AIP Adv., 9 (2019) 035024.

[10] J. Fu, M. Hua, X. Wen, M. Xue, S. Ding, M. Wang, P. Yu, S. Liu, J. Han, C. Wang, H. Du, Y. Yang, and J. Yang. Epitaxial growth of $Y_3Fe_5O_{12}$ thin films with perpendicular magnetic anisotropy. Appl. Phys. Lett., 110 (2017) 202403.

[11] G. Li, H. Bai, J. Su, Z. Z. Zhu, Y. Zhang, and J. W. Cai. Tunable perpendicular magnetic anisotropy in epitaxial $Y_3Fe_5O_{12}$ films. APL Mater., 7 (2019) 041104.

[12] C. Y. Guo, C. H. Wan, M. K. Zhao, H. Wu, C. Fang, Z. R. Yan, J. F. Feng, H. F. Liu, and X. F. Han. Spin-orbit torque switching in perpendicular $Y_3Fe_5O_{12}$/Pt bilayer. Appl. Phys. Lett., 114 (2019) 192409.

[13] H. Yamahara, M. Mikami, M. Seki, and H. Tabata. Epitaxial strain-induced magnetic anisotropy in $Sm_3Fe_5O_{12}$ thin films grown by pulsed laser deposition. J. Magn. Magn. Mater., 323 (2011) 3143-3146.

[14] V. H. Ortiz, M. Aldosary, J. Li, Y. Xu, M. I. Lohmann, P. Sellappan, Y. Kodera, J. E. Garay, and J. Shi. Systematic control of strain-induced perpendicular magnetic anisotropy in epitaxial europium and terbium iron garnet thin films. APL Mater., 6 (2018) 121113.

[15] J. J. Bauer, E. R. Rosenberg, and C. A. Ross. Perpendicular magnetic anisotropy and spin mixing conductance in polycrystalline europium iron garnet thin films. Appl. Phys. Lett., 114 (2019) 052403.

[16] E. R. Rosenberg, L. Beran, C. O. Avci, C. Zeledon, B. Song, C. Gonzales-Fuentes, J. Mendil, P. Gambardella, M. Veis, C. Garcia, G. S. D. Beach, and C. A. Ross. Magnetism and spin transport in rare-earth-rich epitaxial terbium and europium iron garnet films. Phys. Rev. Mater., 2 (2018) 094405.

[17] C. Tang, P. Sellappan, Y. Liu, Y. Xu, J. E. Garay, and J. Shi. Anomalous Hall hysteresis in $Tm_3Fe_5O_{12}$/Pt with strain-induced perpendicular magnetic anisotropy. Phys. Rev. B, 94 (2016) 140403(R).

[18] M. Kubota, A. Tsukazaki, F. Kagawa, K. Shibuya, Y. Tokunaga, M. Kawasaki, and Y. Tokura. Stress-Induced Perpendicular Magnetization in Epitaxial Iron Garnet Thin Films. Appl. Phys. Express, 5 (2012) 103002.

[19] C. O. Avci, A. Quindeau, M. Mann, C. Pai, C. A. Ross, and G. S. D. Beach. Spin transport in as-grown and annealed thulium iron garnet/platinum bilayers with perpendicular magnetic anisotropy. Phys. Rev. B, 95 (2017) 115428.

[20] C. N. Wu, C. C. Tseng, K. Y. Lin, C. K. Cheng, S. L. Yeh, Y. T. Fanchiang, M. Hong, and J. Kwo. High-quality single-crystal thulium iron garnet films with perpendicular magnetic anisotropy by off-axis sputtering. AIP Adv., 8 (2018) 055904.

[21] C. T. Wang, X. F. Liang, Y. Zhang, X. Liang, Y. P. Zhu, J. Qin, Y. Gao, B. Peng, N. X. Sun, and L. Bi. Controlling the magnetic anisotropy in epitaxial $Y_3Fe_5O_{12}$ films by manganese doping. Phys. Rev. B, 96 (2017) 224403.

[22] L. Souhmah, N. Beaulieu, L. Qassym, C. Carretero, E. Jacquet, R. Lebourgeios, J. B. Youssef, P. Bortolotti, V. Cros, and A. Anane. Ultra-low damping insulating magnetic thin films get perpendicular. Nat. Commun., 9:3355 (2018).

[23] P. Sellappan, C. Tang, J. Shi, and J. E. Garay. An integrated approach to doped thin films with strain-tunable magnetic anisotropy: powder synthesis, target preparation and pulsed laser deposition of Bi:YIG, Mater. Res. Lett., 5:1 (2017) 41-47.

[24] E. Lage, L. Beran, A. U. Quindeau, L. Ohnoutek, M. Kucera, R. Antos, S. R. Sani, G. F. Dionne, M. Veis, and C. A. Ross. Temperature-dependent Faraday rotation and magnetization reorientation in cerium-substituted yttrium iron garnet thin films. APL Mater., 5 (2017) 036104.

[25] J. J. Bauer, E. R. Rosenberg, S. Kundu, K. A. Mkhoyan, P. Quarterman, A. J. Grutter, B. J. Kirby, J. A. Borchers, and C. A. Ross. Dysprosium iron garnet thin films with perpendicular magnetic anisotropy on silicon. Adv. Electron. Mater., 1900820 (2019).

[26] M. Sparks, Ferromagnetic-Relaxation Theory (McGraw-Hill, New York, 1964).

[27] C. Tang, M. Aldosary, Z. Jiang, H. Chang, B. Madon, K. Chan, M. Wu, J. E. Garay, and J. Shi. Exquisite growth control and magnetic properties of yttrium iron garnet thin films. Appl. Phys. Lett., 108 (2016) 102403.

[28] Y. Sun, Y. Song, H. Chang, M. Kabatek, M. Jantz, W. Schneider, M. Wu, H. Schultheiss, and A. Hoffmann. Growth and ferromagnetic resonance properties of nanometer-thick yttrium iron garnet films. Appl. Phys. Lett., 101 (2012) 152405.

[29] M. C. Onbasli, A. Kehlberger, D. H. Kin, G. Jakob, M. Klaui, A. V. Chumak, B. Hillebrands, and C. A. Ross. Pulsed laser deposition of epitaxial yttrium iron garnet films with low Gilbert damping and bulk-like magnetization. APL Mater., 2 (2014) 106012.

[30] A. Krysztofik, L. E. Coy, P. Kuswik, K. Zaleski, H. Glowinski, and J. Dubowik. Ultra-low damping in lift-off structured yttrium iron garnet thin films. Appl. Phys. Lett., 111 (2017) 192404.

[31] O. d'Allivy Kelly, A. Anane, R. Bernard, B. Youssef, C. Hahn, A. H. Molpeceres, C. Carretero, E. Jacquet, C. Deranlot, P. Bortolotti, R. Lebourgeois, J. Mage, G. Loubens, O. Klein, V. Cros, and A. Fert. Inverse spin Hall effect in nanometer-thick yttrium iron garnet/Pt system. Appl. Phys. Lett., 103 (2013) 082408.

[32] T. Liu, H. Chang, V. Vlaminck, Y. Sun, M. Kabatek, A. Hoffman, L. Deng, and M. Wu. Ferromagnetic resonance of sputtered yttrium iron garnet nanometer films. J. Appl. Phys., 115 (2014) 17A501.

[33] J. T. Brangham, K. Meng, A. S. Yang, J. C. Gallagher, B. D. Esser, S. P. White, S. Yu, D. W. McComb, P. C. Hammel, and F. Yang. Thickness dependence of spin Hall angle of Au grown on Y3Fe5O12 epitaxial films. Phys. Rev. B, 94 (2016) 054418.

[34] A. Quindeau, C. O. Avci, E. Liu, C. Sun, M. Mann, A. S. Tang, M. C. Onbasli, D. Bono, P. M. Voyles, Y. Xu, J. Robinson, G. S. D. Beach, and C. A. Ross. Tm3Fe5O12/Pt Heterostructures with Perpendicular Magnetic Anisotropy for Spintronics Applications. Adv. Electron. Mater., 3 (2017) 1600376.

[35] C. N. Wu, C. C. Tseng, Y. T. Fanchiang, C. K. Cheng, K. Y. Lin, S. L. Yeh, S. R. Yang, C. T. Wu, T. Liu, M. Wu, M. Hong, and J. Kwo. High-quality thulium iron garnet films with perpendicular magnetic anisotropy by off-axis sputtering – correlation between magnetic properties and film strain. Sci. Rep., 8:11087 (2018).

[36] F. Mohmed, and Y. Lin. Investigation of spin Seebeck effect and magnetic damping in nanometer thick Ce0.5Y2.5Fe5O12 films. Appl. Surf. Sci., 480 (2019) 1025-1034.

[37] C. R. Warren, V. Ortiz, L. Scipioni, J. Greer, J. Shi, Y. Kodera, and J. E Garay. Robust perpendicular magnetic anisotropy in off-axis sputtered europium iron garnet (EuIG) thin films. J. Magn. Magn. Mater., 560 (2022) 169513.

[38] N. Kumar, N. G. Kim, Y. A. Park, N. Hur, J. H. Jung, K. J. Han, and K. J. Yee. Epitaxial growth of terbium iron garnet thin films with out-of-plane axis of magnetization. Thin Solid Films, 516 (2008) 7753-7757.

[39] S. Blundell. Magnetism in Condensed Matter, First edition. (Oxford University Press, 2001).

[40] V. J. Fratello, I. Mnushkina, S. J. Licht, and R. R. Abbott. Growth and Characterization of Magnetooptic Garnet Films with Planar Uniaxial Anisotropy. Mater. Res. Soc. Symp. Proc., 834 (2005) J6.2.1-J6.2.12.

[41] B. L. Giles, Z. H. Yang, J. S. Jamison, and R. S. Myers. Long-range pure magnon spin diffusion observed in a nonlocal spin-Seebeck geometry. Phys. Rev. B, 92 (2015) 224415.

[42] L. J. Cornelissen, J. Liu, R. A. Duine, J. B. Youssef, and B. J. van Wees. Long-distance transport of magnon spin information in a magnetic insulator at room temperature. Nat. Phys., 11 (2015) 1022–1026.

[43] C.-X. Liu, X.-L. Qi, X.I. Dai, Z. Fang, and S.-C. Zhang. Quantum Anomalous Hall Effect in $Hg_{1-Y}Mn_YTe$ Quantum Wells. Phys. Rev. Lett., 101 (2008) 146802.

[44] Z. Qiao, W. Ren, H. Chen, L. Bellaiche, Z. Zhang, A. H. MacDonald, and Q. Niu. Quantum Anomalous Hall Effect in Graphene Proximity Coupled to an Antiferromagnetic Insulator. Phys. Rev. Lett., 112 (2014) 116404.

[45] V. H. Ortiz, B. Askook, J. Li, M. Aldosary, M. Biggerstaff, W. Yuan, C. Warren, Y. Kodera, J. E. Garay, I. Barsukov, and J. Shi. First- and second-order magnetic anisotropy and damping of europium iron garnet under high strain. Phys. Rev. Mater., 5 (2021) 124414.

[46] M. X. Guo, C. K. Cheng, Y. C. Liu, C. N. Wu, W. N. Chen, T. Y. Chen, C. T. Wu, C. H. Hsu, S. Q. Zhou, C. F. Chang, L. H. Tjeng, S. F. Lee, C. F. Pai, M. Hong, and J. Kwo. Single-crystal epitaxial europium iron garnet films with strain-induced perpendicular magnetic anisotropy: Structural, strain, magnetic, and spin transport properties. Phys. Rev. Mater., 6 (2022) 054412.

[47] G. Winkler. *Magnetic Garnets* (Vieweg, Braunschweig, 1981).

[48] S. Tan, W. Zhang, L. Yang, J. Chen, and Z. Wang. Intrinsic defects in yttrium iron garnet: A first-principles study. J. Appl. Phys., 128 (2020) 183904.

[49] E. Enriquez, A. Chen, Z. Harrell, P. Dowden, N. Koskelo, J. Roback, M. Janoschek, C. Chen., and Q. Jia. Oxygen Vacancy-Tuned Physical Properties in Perovskite Thin Films with Multiple B-site Valence States. Sci. Rep., 7 (2017) 46184.

[50] E. Annastassakis. Strained supperlattices and heterostructures: elastic considerations. J. Appl. Phys., 68 (1990) 4561.

CHAPTER 2

Experimental Methods

2.1. Synthesis of Rare Earth Iron Garnet Nanopowders

2.1.1. A Review of Garnet Nanopowder Synthesis Routes

There are several commonly used methods for the synthesis of ceramic nanopowders, including but not limited to the co-precipitation, sol-gel, spark discharge, spray pyrolysis, solid-state reaction, reverse micellar, high-energy ball-milling and polymeric precursor processes.[1] Depending on the composition of the synthesized material, certain methods might provide advantages in terms of the morphology, particle size dispersion, grain size dispersion, yield or phase purity of the resulting powder. In the case of synthetic garnets with the characteristic stoichiometry $A_3B_5O_{12}$, where A and B represent different cation species and O is elemental oxygen, chemical routes such as the sol-gel [2,3,4,10], co-precipitation [11-13] and polymeric precursor [5,6] methods have been successfully used for the synthesis of high purity garnet nanopowders covering a wide compositional range. More traditional ceramic processing techniques such as solid-state reaction and high-energy ball milling have also been successful at producing sub-micron garnet powders but have proven difficult for attaining phase pure powders with an average crystallite size below ~100 nm.[4,7,15]

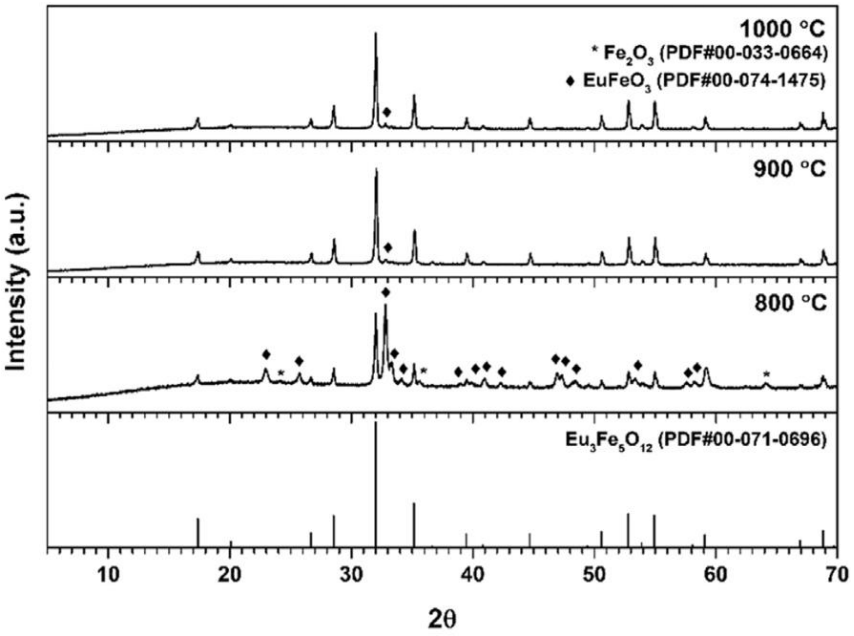

Fig. 2.1: XRD patternts of $Eu_3Fe_5O_{12}$ powders synthesized by Opuchovik et al. through a sol-gel route and then heat treated in air at different temperatures for 10 h.[2] The bottom-most line pattern is a reference EuIG XRD pattern.

A common link between the established garnet nanopowder synthesis techniques mentioned above is that the final step in which the garnet phase is formed is always a high temperature heat treatment in air at a temperature between 700-1200°C. One of the main reasons that such high temperatures are required is that several oxide phases, namely A_2O_3, B_2O_3, and the orthoferrite perovskite ABO_3, form prior to the garnet phase as the powder precursor undergoes heat treatment. The appearance of these intermediary phases is well demonstrated in **Fig. 2.1** by the XRD patterns of a sol-gel $Eu_3Fe_5O_{12}$ precursor that underwent heat treatments at different temperatures. This phase evolution occurs because the cubic garnet structure is both very large and complex, with some 8 formula units (160 atoms) per unit cell and lattice parameters in the range of 11-13 Å in length. In contrast, the oxide phases have much simpler symmetries and shorter-range repetition than the garnet. Since the cations must diffuse over longer distances to fully form the garnet structure, the aforementioned oxide phases will commonly be the first

phases to develop from a precursor material with lower levels of long-range order. For a visual comparison, the structures and lattice parameters of the $Y_3Fe_5O_{12}$ and $YFeO_3$ unit cells are shown in **Fig. 2.2 and 2.3**, respectively.

Of particular importance out of the different intermediary oxide phases is the ABO_3 perovskite phase. For most scientifically or commercially relevant families of garnets, e.g., iron garnets ($A_3Fe_5O_{12}$), aluminum garnets ($A_3Al_5O_{12}$), or gallium garnets ($A_3Ga_5O_{12}$), the perovskite

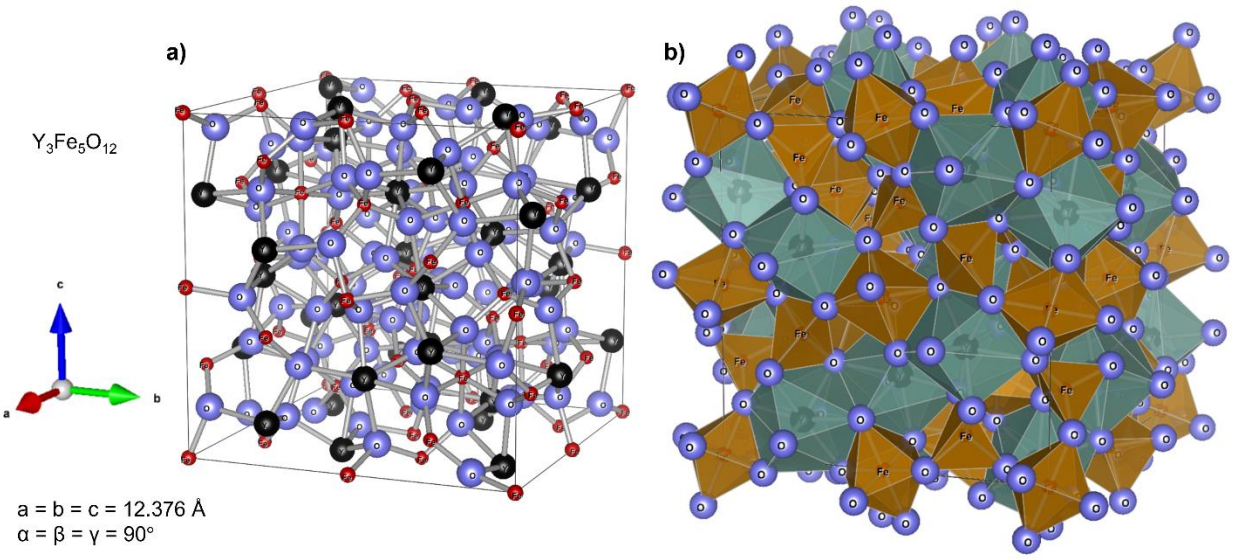

Fig. 2.2: a) Ball-and-stick, and b) polyhedron space-filling structural models of the yttrium iron garnet ($Y_3Fe_5O_{12}$) unit cell created using VESTA.[16]

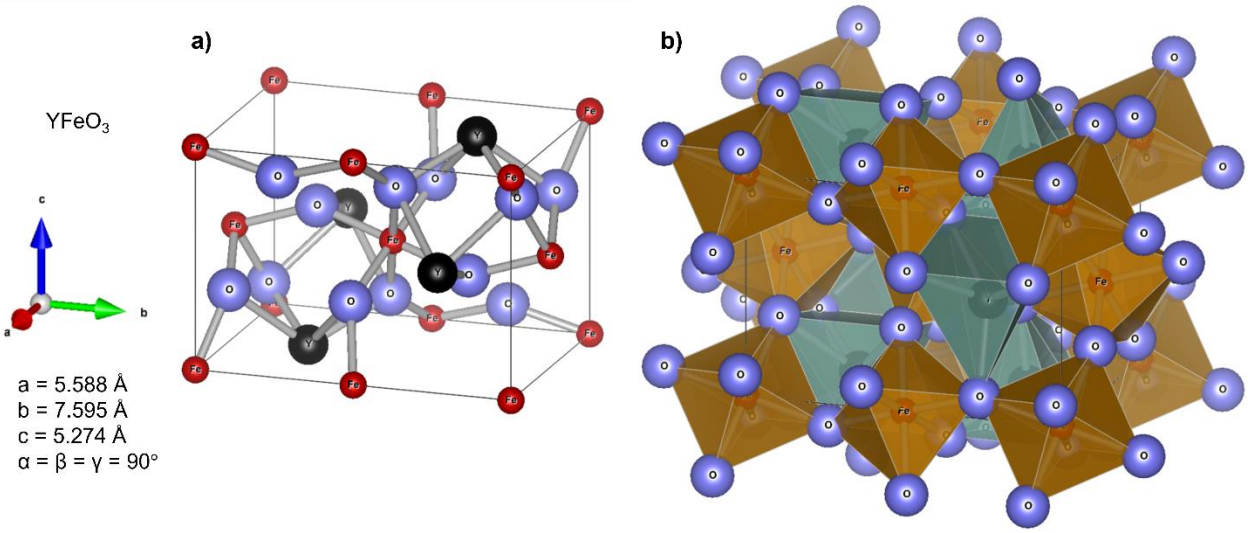

Fig. 2.3: a) Ball-and-stick, and b) polyhedron space-filling structural models of the yttrium iron perovskite ($YFeO_3$) unit cell created using VESTA.[16]

phase is one of the most thermally stable phases within a given A-B-O ternary system. Given that it's A:B cation ratio is relatively similar to garnet, the perovskite phase is normally present as an intermediary phase during the synthesis of garnets. In addition, perovskite is often one of the last remaining intermediary phases before the garnet is fully formed and it tends to be more tolerant of defects than garnet. Under certain conditions, it is even possible to form a disordered perovskite phase with an overall 3 A:5 B cation ratio like that of a garnet.[14] One other thing worth noting is that because garnets are line compounds, the presence of a secondary oxide phase in a fully reacted garnet powder is an indication that the overall stoichiometry of the as-synthesized powder differs from the 3 A:5 B cation ratio of pristine garnet. An example phase diagram of the Fe_2O_3 – Y_2O_3 binary system is shown in **Fig. 2.4** for reference.

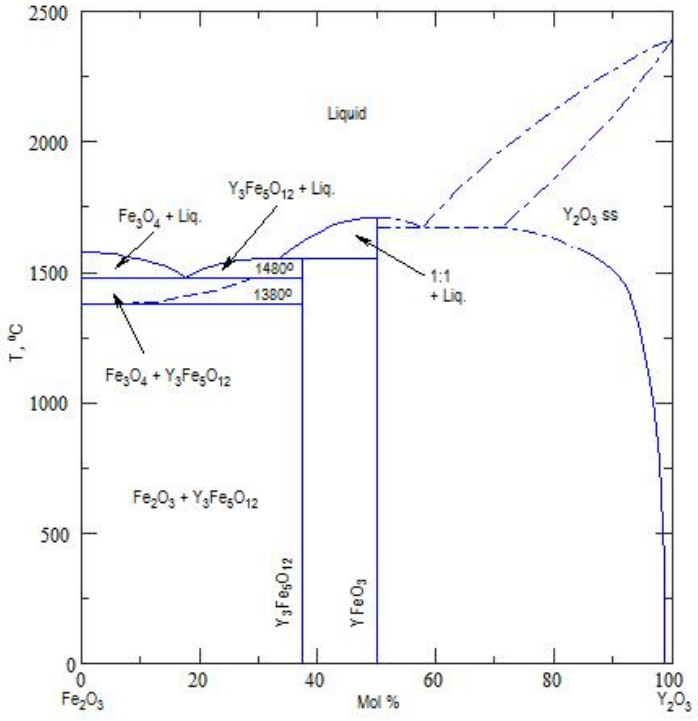

Fig. 2.4: A phase diagram of the Fe_2O_3 – Y_2O_3 binary system at atmospheric conditions.[17]

The high temperatures required during heat treatment also means that the cations will have increased diffusion rates during this step. This condition favors grain growth, particle coarsening, and sintering, which collectively act to increase the average crystallite size and broaden the particle size distribution of the synthesized powder. In order to limit the coarsening effects and attain nanopowders with a narrow particle size distribution, it is then necessary that the synthesis process somehow lowers the reaction temperature of the precursor, reduces the initial particle or agglomerate size of the precursor, reduces the time required at elevated temperature, limits the total number of cations that can combine into a given crystallite, or ideally achieves some combination of these things. An optimized heat treatment would therefore limit the powder's exposure to high temperatures to just as long as it takes to fully form the garnet phase.

The sol-gel, co-precipitation and polymeric precursor techniques have each been used to produce garnet powders with average crystallite sizes as small as ~20 nm [2-6,10-13], whereas the solid-state reaction and high-energy ball-milling methods struggle to make powders with average crystallite sizes smaller than ~100 nm [4,7]. The main difference that makes the chemical methods capable of producing smaller crystallites is that their precursor powders distribute the cations in an organic matrix. The organic matrix both reduces the number of cations in near enough proximity of each other to react into a single crystallite and creates more space between individual crystallites, thus reducing the amount of interparticle diffusion, coarsening and sintering that takes place during the heat treatment. Though the organic part of the precursor burns off in an exothermic reaction during the calcining step, it usually occurs at too low of a temperature and doesn't produce enough thermal energy to initiate the garnet phase formation. As such, the burning of the organic matrix doesn't do much to directly decrease the

temperature required to fully form garnet, but its impact on the precursor's atomic structure during the initial stages of synthesis does ultimately affect the final reaction temperature.

Solid-state reaction, or the ceramic method as it's more commonly called, is a challenging method to synthesize garnet nanopowders with. In this method, nanopowders of the constituent oxides, A_2O_3 and B_2O_3, are carefully mixed according to the ratio of 3 A_2O_3:5 B_2O_3. The goal of mixing is to carefully coat particles of one oxide with the other, such that a coated particle has the overall 3 A:5 B cation ratio of garnet. Mixing is commonly achieved through ball-milling, sometimes leading to mechanosynthesis of the perovskite phase in between the two oxide layers when the milling procedure provides sufficient energy.[15] The mixed oxide powders then need to be heat treated for the type of cations concentrated near the core of the particles to diffuse to the surface where the other type is concentrated and vice versa, and to subsequently crystalize the powder into the garnet phase. The characteristic size of the resulting powder is therefore dependent on the initial particle size of the milled powder prior to heat treatment. Larger initial particles will require higher temperatures or hold times since the cations will need to diffuse over longer distances than for smaller ones, creating conditions that favor coarsening and sintering. Several issues make it difficult to attain single phase garnet nanopowders through a solid-state reaction method, including but not limited to the size and uniformity of the starting oxide powders, agglomeration of the mixed oxides, and interparticle bonding of the milled powders. The ceramic method does excel, however, as a straight-forward way of making micron sized garnet powders if the mixed oxides are simply heat-treated for a long time at high temperatures.

High-energy ball-milling can also be used to break down a coarser garnet powder into a finer one. There are several limitations to high-energy ball-milling, however, and the high-

energy ball-milled powder always requires a heat treatment to remove any structural changes or unwanted phases introduced by the milling process. Due to the amount of energy required to break apart the garnet powder, the milling process regularly causes mechanosynthesis of the perovskite phase since it is typically slightly denser and more stable at the higher pressures experienced during high-energy ball-milling.[7,14,15] The ultimate size of the milled powder is also limited by the fact that thermal energy produced from collisions during the high-energy ball-milling can cause smaller particles to bond with other particles. The milling conditions such as the ratio of media to powder, size and shape of the media, media material, rotational speed and milling duration can all be optimized to create as small of particles as possible, but after heat treatment, the garnet powders attained through this method still possess larger features than those attainable through chemical routes. One other drawback to high-energy ball-milling is that the milling media and jar are likely to introduce contaminants to the powder.

The sol-gel and polymer precursor routes share a lot of similarities with each other. For both methods, the first step is to prepare a cation solution by dissolving nitrates in stoichiometric 3 A:5 B ratio in water. After this, the two methods start to differentiate. For the sol-gel method, citric acid is next added to the nitrate solution before then drying it to form a precursor. Sometimes for the sol-gel technique, a complexing agent such as ethanediol is also added to the nitrate solution before the drying step. In a similar fashion to the use of citric acid in the sol-gel technique, a polymerizing agent such as polyvinyl alcohol is added to the nitrate solution before then drying it and reacting it at low temperature, typically between 200-300°C, to form the precursor according to the polymer precursor method. For both routes, the pH might be maintained at a low value by adding more citric acid or nitric acid, respectively. After their respective drying steps, the precursors from both routes are subsequently broken down by

grinding and then calcined in air at high temperature to form the garnet powders. Despite the many similarities, there are certain benefits provided by choosing one over the other. It is usually easier to get very small average crystallite sizes using the polymer precursor method when compared to the sol-gel method, however, the sol-gel method tends to provide a more uniform morphology and distribution of crystallite sizes. In addition, the polymer precursor method is very good at forming a completely amorphous powder.[18]

The co-precipitation technique has several substantial differences from both the sol-gel and polymer precursor routes. There is also far more variation of the chemicals used by different co-precipitation recipes, with potential benefits or drawbacks to each unique recipe. For the co-precipitation route, a common first step is to prepare a cation solution by dissolving nitrates or chlorides in stoichiometric ratio in water. Different complexing agents, such as ammonia, NaOH or dimethylformamide are next added to the solution. A certain pH is maintained in the solution for a prolonged period of time in order to form a gelatinous cation containing precipitate. The precipitate is then separated from the remaining solution and cleaned via centrifugation and rinsing, and then dried to form a metal-organic precursor. The precursor is then ground and finally calcined in air at high temperature to form the garnet powders. Extra chemicals and chemical steps are occasionally required according to specific recipes, but in general, co-precipitation synthesis follows the steps outlined above.

Each of the successful garnet nanopowder synthesis techniques discussed so far ultimately depends on the thermal energy provided in a heat treatment as the driving force for the atomic diffusion of cations. Aside from the diffusivity of the constituent cations, the characteristic sizes and elemental distribution of the precursor material are other important factors that determine the exact heat treatment conditions required to fully form garnet. Due to

the fact that intermediary oxide phases typically form during the synthesis of garnet, methods that either produce very small particles during the initial stages of the reaction of the precursor, or in which the precursor consists of very small particles to begin with don't need as high of temperatures or hold times to fully form garnet. This is due to the simple reason that cations in these types of precursors don't need to diffuse over as long of distances. Methods that produce an amorphous precursor or in which the precursor is atomically homogeneous also tend not to require as high of temperatures or hold times for similar reasons. Bearing the above factors in mind, the resulting morphology and microstructure of a garnet nanopowder is intimately linked to the initial state of the precursor and the heat treatment it undergoes. To illustrate the extent to which these factors affect the resulting powder's microstructure, representative micrographs of garnet powders as synthesized by the different methods discussed and with average crystallite sizes close to 100 nm are shown in **Fig. 2.5**.

The three chemical routes presented, namely the sol-gel, polymer precursor and co-precipitation methods, are all capable of yielding finely structured precursors with uniform atomic mixing. Because of this, the chemical routes also produce finer structured garnet nanopowders than the traditional ceramic processing techniques of high-energy ball-milling and solid-state reactions. In addition to being inexpensive, the chemical synthesis routes also have the added benefits of being less time-consuming and introducing far fewer contaminants than traditional ceramic processing techniques. Of the three chemical routes discussed, both the sol-gel and polymer precursor methods have fewer steps and simpler procedures than co-precipitation. For these reasons, we chose to use the sol-gel and polymer precursor methods for the synthesis of rare earth iron garnet nanopowders. In cases where we wanted very fine garnet powders, we employed a polymer precursor route, namely the polymeric-steric entrapment

method. In cases where we sought both a more uniform crystallite size distribution and powder morphology, we instead used a citrate sol-gel synthesis method.

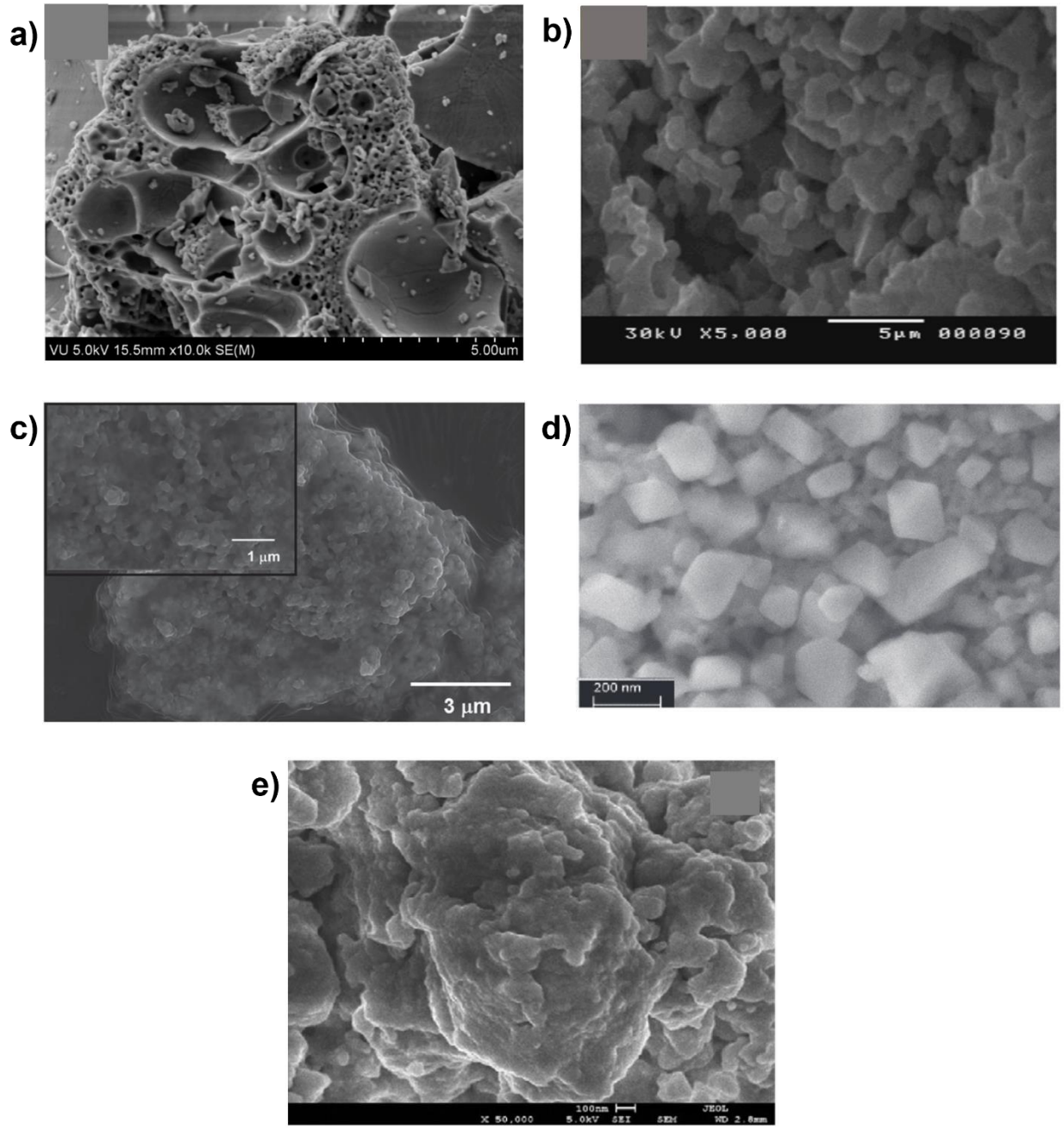

Fig. 2.5: SEM micrographs of garnet powders synthesized by different routes. a) Sol-gel synthesized LuIG with an average crystallite size of 115 nm[2], b) co-precipitated YIG with an average crystallite size of 115 nm[8], c) polymeric precursor synthesized Bi:YIG with an approximate average crystallite size of 120 nm[6], d) solid-state reacted YIG with an average crystallite size of 102 nm[4], and e) high-energy ball-milled YIG with submicron features[15].

2.1.2. Polymeric-Steric Entrapment Synthesis of Rare Earth Iron Garnets

The polymeric precursor route used for the synthesis of $Y_3Fe_5O_{12}$ and $Y_{3X}Tm_{3(1-X)}Fe_5O_{12}$ powders is the polymeric-steric entrapment method. This method bears many similarities to the Pechini or polyol synthesis method, except that it uses simpler long-chain polymers such as poly(vinyl alcohol) (PVA) or poly(ethylene glycol) to form the ceramic precursor. For our specific method, we used PVA as our long-chain ceramic precursor carrier.

The first step of our polymeric-steric entrapment method is to prepare three separate aqueous solutions of yttrium nitrate, iron nitrate and PVA. In the case of $Y_{3(1-X)}Tm_{3X}Fe_5O_{12}$ powder synthesis, an additional aqueous solution of thulium nitrate is also prepared. For the aqueous nitrate solutions, a 1:1 mass ratio of the fully hydrated nitrate crystals to deionized water is combined, sealed, and then stirred for a minimum of 12 hours with a magnetic stirrer. The various cation nitrate materials used in these solutions were $Y(NO_3)_3{\cdot}6H_2O$ (Aldrich, 99.8%), $Tm(NO_3)_3{\cdot}5H_2O$ (Aldrich, 99.9%), and $Fe(NO_3)_3{\cdot}9H_2O$ (Aldrich, 99.95%). A 5 wt% aqueous solution of PVA is then prepared by combining PVA powder (Aldrich) in deionized water, sealing the solution, and stirring it for a minimum of 12 hours with a magnetic stirrer until the PVA is completely dissolved. The PVA used had a molecular weight in the range of 9,000-10,000 g/mol.

Once the various aqueous solutions are prepared, they can then be combined in the correct ratios. Given a target mass of garnet powder to synthesize, the nitrate solutions are carefully weighed and combined in a stoichiometric 3 RE:5 Fe cation ratio, where RE stands for a rare earth element or yttrium. The mass of PVA solution needed depends on the total charge of the cations in solution. The desired ratio is such that each negative valence from the $-OH^-$ groups along the PVA molecules is balanced with 4 positively charged valences from the cations.[18]

For PVA, this means that each vinyl alcohol molecule (CH_2CH_2O) in the long PVA chains should be balanced with a total charge of +4 from the cations. Based on this ratio, a mass of the 5 wt% PVA solution is weighed and then combined with the solution containing the iron and rare earth nitrates. The pH of the solution is verified to be <1 to ensure that gelation does not occur in the subsequent steps. If the pH is too high, some additional nitric acid may be added in order to lower the pH. The resulting solution is sealed and stirred for a minimum of 12 hours with a magnetic stirrer.

The cation and PVA containing solution is then unsealed and heated to 80°C while stirring for a minimum of 12 hours until the majority of the water has evaporated and the solution is a dark, nearly opaque brown-black color. At this point, the solution is then heated to approximately 230°C while stirring for about 30 minutes. During this step, even more water and volatile NO_X molecules will evaporate from the solution, and the solution will become progressively more viscous. As less evaporates from the solution, the solution can then be heated to approximately 300°C. At around 250°C, decomposition of the PVA molecules occurs due to dehydration [5] and there is a large outgassing of the remaining NO_X in the form of brown colored fumes. As the decomposition reaction progresses, the solution will become more and more viscous.

To attain nanosized powders, it is best to remove the resin from the heat when it is near the viscosity of honey. At this point, it can be directly placed into a vacuum oven set at a temperature of 125°C to complete the drying process. Drying in the vacuum oven will have created and expanded pores in the resin, resulting in a crispy, aerated brown resin. A more aerated and expanded resin with fine bubble structures throughout it will yield smaller crystallite sizes in the final powder. The volume expansion that results from vacuum drying can be quite

dramatic. Due to practical considerations such as the size of the equipment being used, this means that there may be a tradeoff between the mass of powder that can be synthesized in a single batch and the crystallite size of the resulting powder. The vacuum drying step plays a critical role in the characteristic size, particle size distribution and repeatability of the resulting powder.

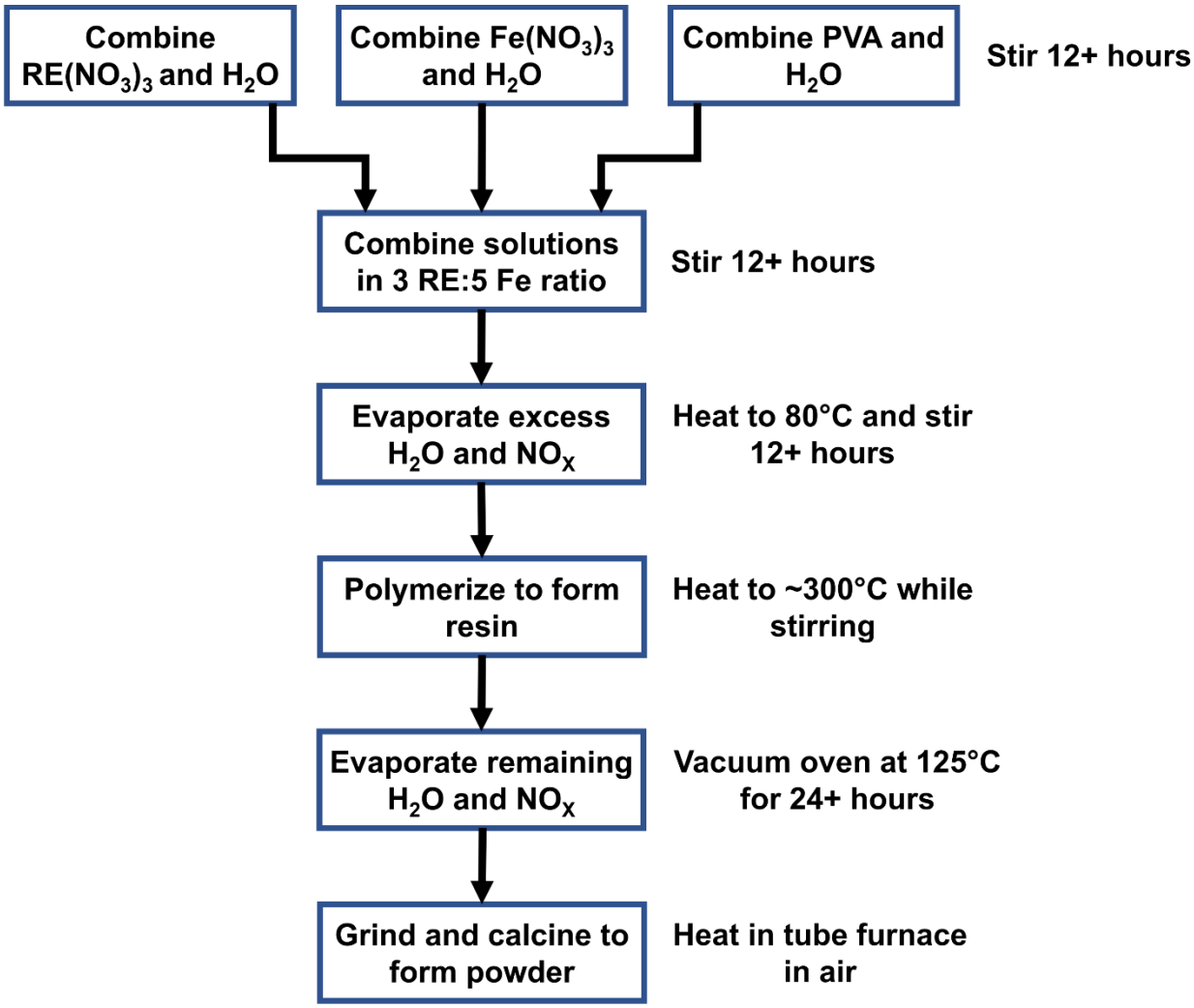

Fig. 2.6: Flow chart of the polymeric-steric entrapment method used in the synthesis of rare earth iron garnet powders.

The vacuum dried resin is then broken apart and ground with mortar and pestle to from the preceramic powder. The powder is then calcined in air to remove the organic material and

oxidize the powder. A fully amorphous powder results if the heat treatment is done below the crystallization point. At higher temperatures, the powder will start to crystallize and eventually form garnet. The calcined powder is then usually reground using a mortar and pestle or ball-milled to break apart agglomerations and particles that had begun to neck together. The entire polymeric-steric entrapment process followed here is summarized in a flow-chart in **Fig. 2.6**.

2.1.3. Citrate Sol-Gel Synthesis of Rare Earth Iron Garnets

A citrate sol-gel method was used in the synthesis of Y-Fe-O and Eu-Fe-O powders in a 3 RE:5 Fe cation ratio characteristic of the rare earth iron garnets. There are significant overlaps between the citrate sol-gel method employed here, and the polymeric-steric entrapment method previously described. These differences arise from the use of citric acid as a gelling agent in the ceramic precursor solution instead of the use of long-chain PVA as a ceramic precursor carrier.

The first step of our citrate sol-gel method is to prepare three separate aqueous solutions of citric acid, iron nitrate, and yttrium or europium nitrate. For the aqueous yttrium and iron nitrate solutions, a 1:1 mass ratio of the fully hydrated nitrate crystals to deionized water is combined, sealed, and then stirred for a minimum of 12 hours with a magnetic stirrer. The nitrate materials used in these two solutions were $Y(NO_3)_3 \cdot 6H_2O$ (Aldrich, 99.8%) and $Fe(NO_3)_3 \cdot 9H_2O$ (Aldrich, 99.95%). The europium nitrate solution was prepared by first preparing anhydrous europium nitrate crystals. The europium nitrate crystals were prepared by dissolving Eu_2O_3 powder (Alfa Aesar, 99.9%) in 70% nitric acid (Sigma Aldrich), such that there were at least 6 $(NO_3)^-$ molecules in solution per every Eu^{3+} ion. After the Eu_2O_3 fully dissolved, all water and excess $(NO_3)^-$ was evaporated from the solution by stirring with a magnetic stirrer and heating the solution to 125°C, leaving behind solid white crystals of pure $Eu(NO_3)_3$. The aqueous europium nitrate solution was then made by adding deionized water to the as prepared anhydrous

europium nitrate crystals, sealing it, and then stirring it for a minimum of 12 hours with a magnetic stirrer. A ratio of approximately 20 g of deionized water per gram of dissolved Eu_2O_3 was used in the europium nitrate solution. The exact amount of water used in the various nitrate solutions does not drastically affect this synthesis method since the water is evaporated in a later step. For the citric acid solution, a 1:2 mass ratio of citric acid (Sigma Aldrich, 99.5%) to deionized water is combined, sealed, and then stirred for a minimum of 12 hours or until the citric acid is fully dissolved.

Once the various aqueous solutions are prepared, they can then be combined in the correct ratios. Given a target mass of garnet powder to synthesize, the nitrate solutions are carefully weighed and combined in a stoichiometric 3 RE:5 Fe cation ratio, where RE stands for a rare earth element or yttrium. The mass of citric acid solution needed depends on the total number of cations in solution. The desired ratio is such that each cation in solution is balanced with three citric acid ($HOC(CH_2CO_2H)_2$) molecules. Based on this ratio, a mass of citric acid solution is weighed and then combined with the solution containing the iron and rare earth nitrates. The resulting solution is sealed and stirred for a minimum of 12 hours with a magnetic stirrer.

The cation and citric acid containing solution is then unsealed and heated to 80°C while stirring for a minimum of 12 hours in order to evaporate out the excess water and volatile NO_X compounds and begin forming a metal-organic complex. The end result of this step is the production of a brown colored cation containing gel, i.e., the namesake citrate sol-gel. This gel is then directly placed in a vacuum oven at 110°C for a minimum of 36 hours, or until the gel has fully dried and hardened into a solid, orange colored, cation impregnated ceramic precursor xerogel. The xerogel is then broken apart and ground with mortar and pestle to form the

preceramic powder. This powder is then calcined in air at high temperature for 12 hours to remove the organic material, oxidize it, and ultimately crystallize it into a ceramic. We chose a 12 hour heat treatment for the powders synthesized via this method because it produced desirable and repeatable results, but this time period can obviously be adjusted for different outcomes. The calcined powder is then reground using a mortar and pestle or ball-milled to break apart agglomerations and particles that had begun to neck together. The entire citrate sol-gel process followed here is summarized in a flow-chart in **Fig. 2.7**.

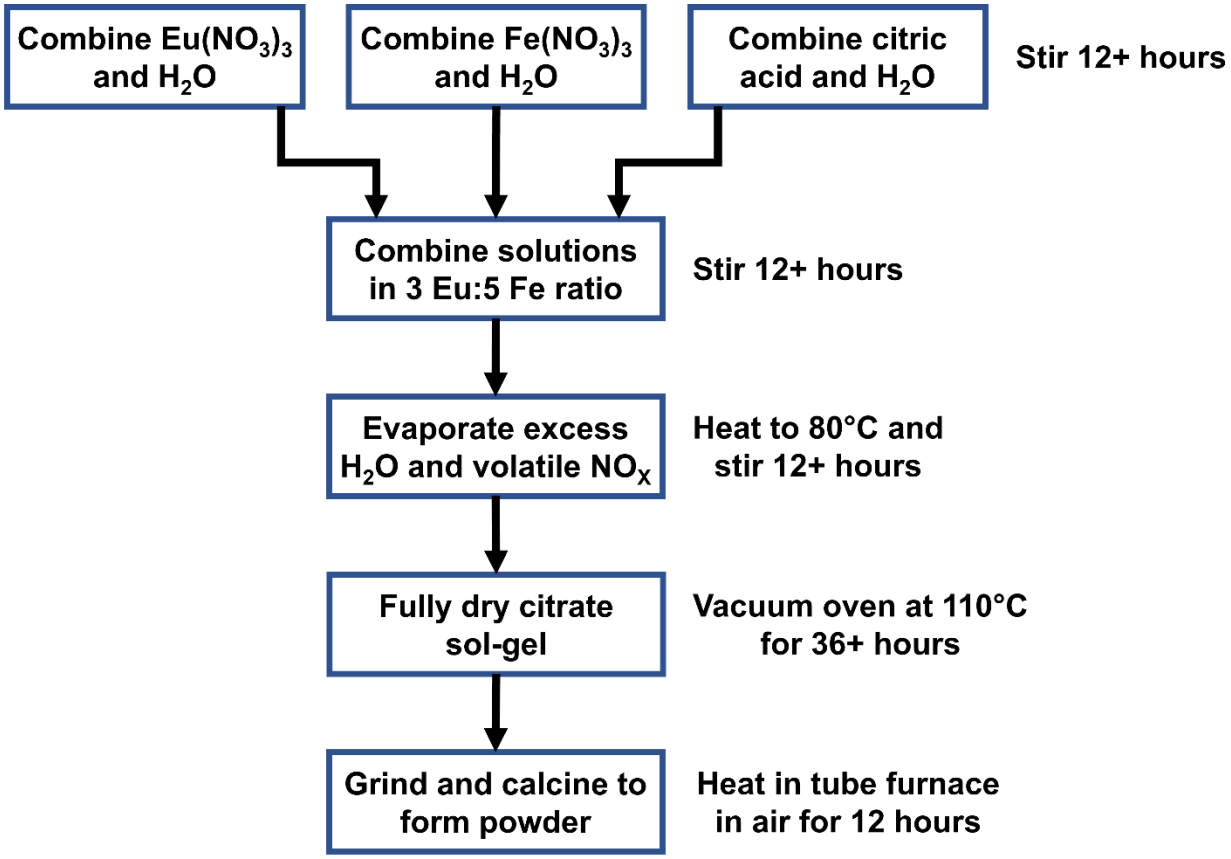

Fig. 2.7: Flow chart of the citrate sol-gel method used in the synthesis of rare earth iron garnet nanopowders.

2.2. Current-Activated, Pressure-Assisted Densification (CAPAD) of Bulk Ceramics

2.2.1. Introduction to CAPAD Processing

Current-activated, pressure-assisted densification (CAPAD) is a method of densifying powders using the simultaneous application of pressure and an electrical current. The high heating rates used in CAPAD, typical on the order of 100's of °C/min, make it possible to consolidate powders to full density much faster and at lower temperatures than traditional methods such as hot pressing and pressureless sintering.[9] A typical CAPAD experiment only takes approximately 20 minutes from beginning to end, as compared to the many hours required by more traditional methods. Moreover, CAPAD processing can produce highly dense, nanostructured materials that are nearly impossible to make using other methods, as will be discussed later.

The CAPAD method has gone by several different names, such as spark plasma sintering (SPS), field-assisted sintering technique (FAST), or pulsed-electric current sintering (PECS). Each term ultimately describes the same form of processing whereby mechanical loads and high electrical currents are simultaneously applied to densify powders. However, there is no concrete evidence of the formation of sparks or plasma during CAPAD processing, and there are likely other densification mechanisms involved besides just sintering. The term CAPAD more accurately describes the two key components involved in this process, without omitting any key densification mechanisms such as particle rearrangement.

Aside from the drastically reduced processing times of CAPAD, the high heating rates provide other useful benefits by altering the dominant diffusion mechanisms involved in sintering. Sintering is driven by a reduction in surface energy and involves both particle coarsening and densification. One of the primary grain coarsening mechanisms, surface diffusion, is more active at intermediary CAPAD processing temperatures than grain or volume

diffusion. By quickly heating to the processing temperatures at which grain and volume diffusion are more active, the material spends less time during which grain coarsening is the dominant sintering mechanism.[9] This makes it possible to retain nanosized grains and features in bulk samples processed using CAPAD.

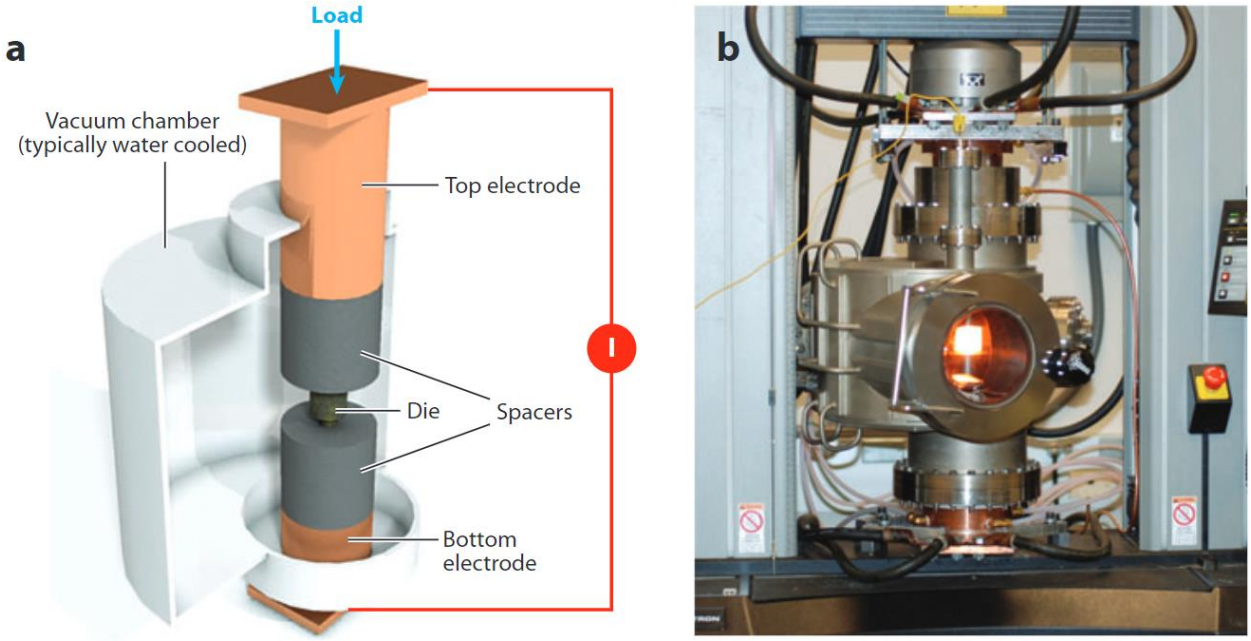

Fig. 2.8: (a) A schematic of the custom built current-activated, pressure-assisted densification (CAPAD) apparatus, and (b) a photograph of the CAPAD apparatus during a densification experiment.[9]

A typical CAPAD apparatus involves a die and plunger set placed between two electrodes which simultaneously apply pressure and electrical current. Powder is placed inside the die and plunger prior to consolidation, which is densified into a bulk sample during an experiment. The wide range of temperatures, pressures and heating rates experienced during CAPAD processing places high demand on the die and electrode materials. Microstructured graphite with a yield strength between 100 – 150 MPa is often the material of choice for both the die and electrodes since it has high electrical and thermal conductivity, and its yield strength actually increases at the temperatures experienced during CAPAD processing. Graphite is a brittle material that reacts with atmospheric oxygen at elevated temperatures, so therefore the die

and electrodes are housed within a water-cooled vacuum chamber to protect both the die and user. A schematic of a typical CAPAD apparatus is shown in **Fig. 2.8**, and a schematic of a graphite die and plunger set is shown in **Fig. 2.9**.

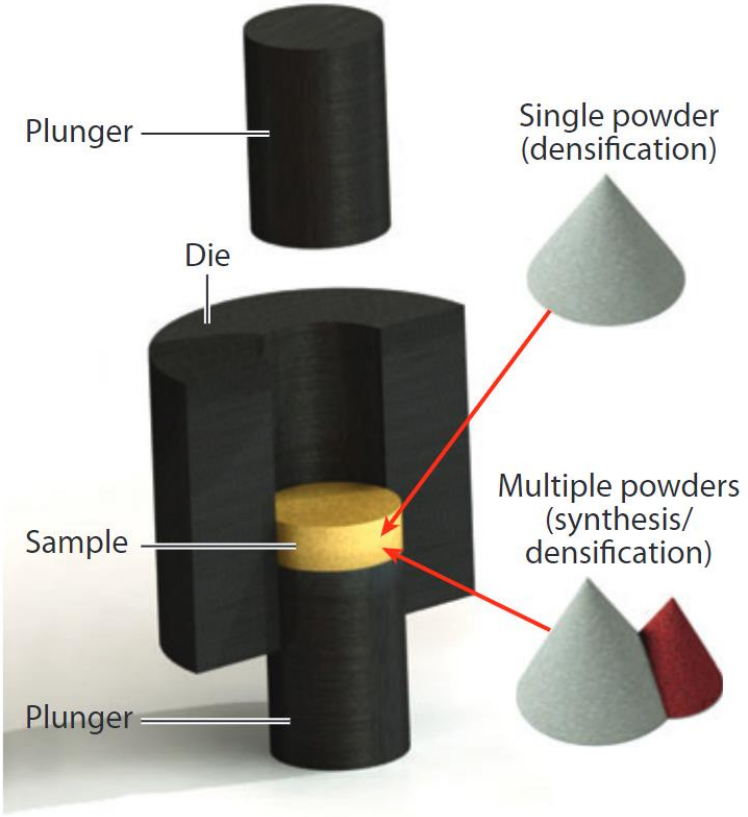

Fig. 2.9: A cross-sectional schematic of a typical graphite die and plunger setup used to densify powders using CAPAD.[9]

Once the powder filled die is loaded into the CAPAD apparatus and the vacuum chamber's atmosphere is evacuated, the CAPAD experiment can begin. First, the mechanical load is applied at a constant rate until reaching the maximum load. The maximum load is then held while an electrical current is applied to heat the die and sample at a constant rate. Once the maximum temperature is reached, the temperature is held for a duration of time during which most of the densification occurs. At the end of the hold time, the electrical current is decreased or turned off and the die and sample cool. Once the die and sample have cooled to ~200°C or less,

the load is then removed at a constant rate. The six main user defined parameters are heating rate, hold temperature, cooling rate, loading rate, hold pressure, and load removal rate. A schematic of a typical CAPAD experiment illustrating the main user defined parameters is shown in **Fig. 2.10**.

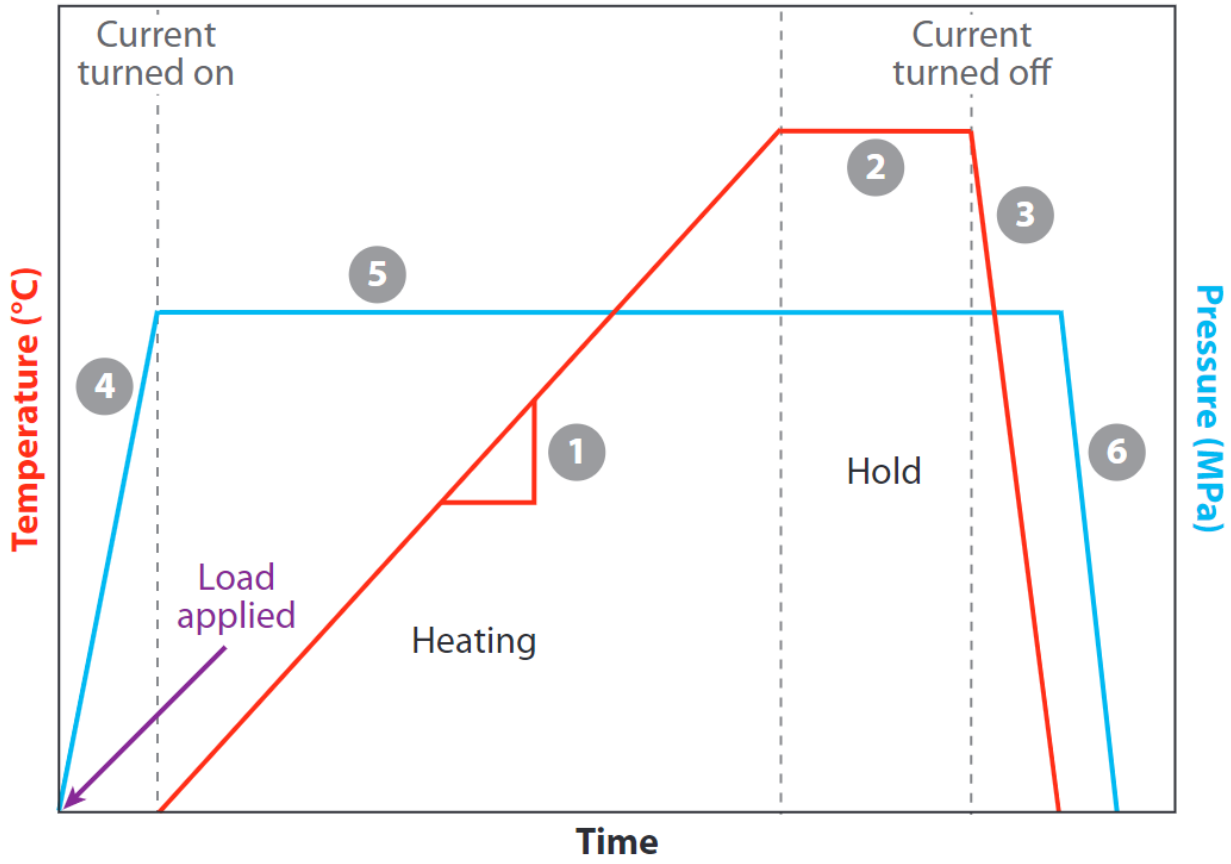

Fig. 2.10: A graphical overview of a typical CAPAD experiment illustrating the six main user defined processing parameters: (1) heating rate, (2) hold temperature, (3) cooling rate, (4) loading rate, (5) hold pressure, and (6) load removal rate.[9]

2.2.2 CAPAD Processing of Rare Earth Iron Garnets

Several different die setups were used to consolidate rare earth iron garnet powders. For larger samples with a diameter of 0.750 in., a graphite die with an internal diameter of 0.760 in. was used in conjunction with plungers that had a diameter of 0.750 in. To facilitate sample extraction and prevent damage to the die and plunger set, the inside of the die and plunger

surfaces adjacent to the powder were lined with graphite foil with a thickness of 0.005 in. YIG and EuIG samples were processed from ~2.00 – 3.00 g of powder at applied loads of 100 and 105 MPa using the 0.760 in. diameter graphite die. The powder was always prepressed inside the die at 100 or 105 MPa for 5 minutes prior to the consolidation experiment. Loading rates of 35 MPa/min, heating and cooling rates of 100 - 200°C/min, hold temperatures of 800 – 1100°C and hold times of 5 minutes were used with the 0.760 in. die. Because the 0.760 in. die used a relatively large amount of powder, it was primarily used for PLD target fabrication. Most of the PLD targets were fabricated by other lab members and are not discussed in this dissertation. The only 0.750 in. diameter sample processed in this manner was an EuIG sample fabricated by P. Sellappan that was used as a PLD target for fabricating the films of Ch. 6.

The majority of the bulk samples presented in Ch. 5 were processed using smaller dies with an internal diameter of 0.385 in. The smaller die produced samples with a diameter of 0.375 in., and used plungers with a diameter of 0.375 in. The inside surface of the 0.385 in. diameter die and its plungers' surfaces were lined with graphite foil in a similar fashion to the larger 0.760 in diameter die. The smaller die had an outer diameter of 0.750 in. and the whole setup was inserted inside the 0.76 in." diameter die for processing. The inside of the 0.760 in. diameter die was lined in graphite foil in order to protect both die setups and facilitate extraction. Two different 0.385 in. diameter dies were used. One was made of graphite, and one was made of tungsten carbide cemented with Co. When using the graphite 0.365 in. die, 0.750 in. diameter steel diffusion plates were inserted between the smaller plungers of the 0.385 in. die setup and the 0.750 in plungers of the larger outer die. Similarly, cemented tungsten carbide diffusion plates were used with the cemented tungsten carbide die setup.

YIG samples were processed from ~0.30 – 0.35 g of powder at applied loads of 100 MPa using the 0.385 in. diameter graphite die. The powder was always prepressed inside the die at 100 MPa for 5 minutes prior to the consolidation experiment. Loading rates of 28 MPa/min, heating and cooling rates of 100 - 200°C/min, hold temperatures of 800 – 1100°C and hold times of 5 minutes were used with the 0.385 in. graphite die. The primary benefit of the cemented carbide die is that it could apply much higher processing pressures. Its maximum temperature was limited to 750°C, however, to prevent the onset of thermal creep deformation. YIG samples were processed from ~0.30 – 0.35 g of powder at applied loads of 100 – 500 MPa using the 0.385 in. diameter cemented tungsten carbide die. The powder was always prepressed inside the die at 100 – 500 MPa for 5 minutes prior to the consolidation experiment. Loading rates of 28 MPa/min, heating and cooling rates of 100 °C/min, hold temperatures of 600 – 700°C and hold times of 5 minutes were used with the 0.385 in. cemented tungsten carbide die.

2.3. Ferromagnetic Resonance (FMR) Measurement Techniques

2.3.1. Introduction to FMR

Ferromagnetic resonance is a method of measuring magnetic properties of a ferromagnetic or ferrimagnetic material based on the processional motion of the unpaired electrons bound within it. It is closely related to the technique of paramagnetic resonance and bears many similarities to nuclear magnetic resonance as well. In a typical FMR measurement, the sample is placed within a uniform applied field H. The total magnetic moment of the sample then aligns along the direction of the effective field experienced by the sample, which depends on its orientation and magnetic anisotropy. The external H field simultaneously causes Zeeman splitting of the energy levels between the two spin states of the unpaired electrons according to

$$\Delta E = g\mu_B m_J B, \tag{2.1}$$

where g is the Landé g-factor, μ_B is the Bohr mangeton, m_J is the component of the total angular momentum lying in the direction of the applied field, and B is the magnetic flux density, defined as

$$\mathbf{B} = \mu_0(\mathbf{H} + \mathbf{M}), \tag{2.2}$$

where μ_0 is the permeability of free space and **M** is the magnetization of the sample.

A second magnetic field is then applied perpendicular to the applied field H. The perpendicular field usually comes from microwave frequency radiation or an electronic signal. When the energy of the microwave matches the energy difference caused by the Zeeman splitting, the microwave is absorbed by an unpaired electron, causing it to align parallel to the perpendicular field direction. The energy of the resonant frequency f_R is related to the Zeeman splitting caused by the applied (resonant) field H according to

$$E = hf_R, \tag{2.3}$$

where h is Planck's constant. The torque experienced from the external field then causes the electron's moment to start returning to its original position along a spiral path. As the moment realigns to the equilibrium position, there is a damping force involving the transfer of energy from spin angular momentum to microscopic thermal motion in the material.[19]

It is practically more difficult to vary the frequency of the microwaves while keeping the microwave intensity the same, so in practice the microwave frequency is fixed during an FMR measurement as the applied field is swept. The microwave absorption is observed as a Lorentzian peak, which has a certain width that depends on both the magnetic uniformity of the sample and its intrinsic spin damping. The lower the damping, the faster the moment returns to its equilibrium position and can reabsorb, which results in a narrower FMR linewidth. Conversely, wider linewidths result from higher damping in which the moment takes longer to

return to equilibrium. Wider linewidths also result from more magnetic inhomogeneity within a sample, which can possibly interfere with measuring the intrinsic properties of the material. For this reason, FMR samples are typically prepared from spheres and films, for which the shape anisotropy has a trivial solution.

The motion of the magnetization is described by the Landau-Lifshitz-Gilbert (LLG) equation according to

$$\frac{\partial \mathbf{M}}{\partial t} = \gamma(1+\alpha^2)\mathbf{M}\times\mathbf{H} - \frac{\alpha}{M_S}\mathbf{M}\times\frac{\partial \mathbf{M}}{\partial t}, \tag{2.4}$$

where γ is the gyromagnetic ratio and α is the Gilbert spin damping constant.[19] The intrinsic spin damping of a material can be calculated from first principles in accordance with eq. (2.4), however, this can be difficult for many materials since it combines several different mechanisms, such as magnon-phonon scattering, magnon-magnon scattering, eddy currents and interactions with itinerant electrons. Furthermore, many materials contain defects, grain boundaries and other microstructural variations which might make it behave differently than models. It is often simpler to indirectly measure a material's Gilbert damping through a series of FMR measurements conducted at different frequencies. In samples with high magnetic uniformity, the linewidth increases linearly with frequency according to

$$\Delta H = \frac{2\pi\alpha}{\gamma} f_R + \Delta H_0, \tag{2.5}$$

where ΔH is the FMR linewidth and ΔH_o is the inhomogeneous contribution to broadening.[20] The damping is then determined from the slope that results from plotting the FMR linewidth as a function of resonant frequency f_R, and the inhomogeneous broadening is determined from the y-axis intercept.

As briefly mentioned earlier, the effective field experienced by a sample depends on its magnetic anisotropy, meaning that the resonant condition of a sample also depends on its

magnetic anisotropy. The simplest case is for the resonance of a spherically shaped sample, in which the shape anisotropy is equal in all directions. The resonant condition for a sphere is given by

$$f_R = \frac{\gamma H_R}{2\pi}, \tag{2.6}$$

where H_R is the resonant field.[21] The above equation is functionally equivalent to the Larmor condition for resonant absorption. The case of an infinite planar sample, i.e., a film, is more complicated than for a sphere since its shape anisotropy is directed entirely along the out-of-plane direction. The resonant condition for a planar sample is given by

$$f_R = \frac{\gamma}{2\pi}\sqrt{BH}. \text{ [22]} \tag{2.7}$$

It is important to note that B and H vary with position and orientation within the sample depending on its magnetic anisotropy. For samples in which the magnetization lies fully within the plane of the film, eq. (2.7) reduces to

$$f_R = \frac{\gamma}{2\pi}\sqrt{H_R(H_R+4\pi M_{eff})}, \tag{2.8}$$

where M_{eff} is the effective magnetization, given by

$$4\pi M_{eff} = 4\pi M_S - \frac{2K_1}{M_S}. \text{ [22]} \tag{2.9}$$

For samples in which the magnetization is directed fully out-of-plane of the film, such as for epitaxially strained films with large perpendicular anisotropy fields, eq. (2.7) reduces to

$$f_R = \frac{\gamma}{2\pi}(H_R - 4\pi M_{eff}). \text{ [23]} \tag{2.10}$$

In addition to the Gilbert damping and inhomogeneous broadening of a sample, FMR measurements can be used to determine many other magnetic properties. The magnetocrystalline anisotropy coefficients can be determined from angle dependent FMR measurements, and the stress induced anisotropy fields and g-factor can be extracted from frequency dependent FMR measurements [25,26], to name a few examples. FMR analysis can also precisely determine the

magnetization direction in films. Because of its wide-ranging versatility, FMR is a popular characterization method for the study of magnetic materials.

2.3.2. FMR Measurements Using a Microwave Cavity

Cavity type FMR apparatuses irradiate the sample with microwaves, typically within the frequency range of 1 – 35 GHz. The sample is suspended within a microwave cavity under vacuum, located between the poles of an electromagnet. The intensity of transmitted microwaves is measured and recorded, and the absorption of the sample is measured from the change in transmission. The raw collected signal is Lorentzian in shape, although typically the data is output as the derivative of the raw absorption curve. From the derivative of the absorption, the resonant field position can immediately be identified from the horizontal intercept, and the linewidth can be measured from the difference between the maximum and minimum derivative values. For well-behaved materials with clear resonances, the data from cavity type FMR's is often the simplest to analyze. Cavity type FMR setups do have some limitations, however. The sample size is limited to what can fit within the microwave cavity, and furthermore, the available frequencies are limited by the resonant frequencies of the microwave cavity itself. Thus, not all cavity type FMRs are capable of performing frequency dependent FMR measurements, but they can usually perform angle dependent FMR measurements. Cavity type FMR's can also measure any shaped sample that fits inside of it, and not just flat samples like co-planar waveguide setups can.

2.3.3. FMR Measurements Using a Co-Planar Waveguide

Co-planar waveguide FMR apparatuses expose the sample to a magnetic field arising from a high frequency electric signal, typically within the range of 1 – 70 GHz. Samples need to have a flat surface in order to measure them with co-planar waveguides. As such, this method is

almost exclusively used for the analysis of films. The flat face of the sample is placed flush with the surface of the waveguide. Typically, a thin electrically insulating layer such as Kapton tape is inserted between the waveguide and the face of the sample to prevent any current from entering the sample. The waveguide and sample setup is then oriented within the poles of an electromagnet. A high frequency signal is applied across the waveguide as the external field is swept, and the resulting signal is collected with a vector network analyzer. The FMR absorption is measured as an attenuation of the transmitted signal. The signal background is carefully subtracted from the raw data and the resulting absorption signal is fit with the sum of a Lorentzian and an antilorentzian function representing the real and imaginary components of the FMR signal, respectively.[24] The resonant field position and linewidth are then extracted from the fit parameters. While the data analysis is more complicated when using co-planar waveguide type FMRs, the benefit of these setups is that they can typically perform both angular and frequency dependent FMR measurements. Waveguides can also be manufactured over a wide range of dimensions, making it possible to measure different sized films using this technique.

2.4. High-Resolution X-Ray Diffraction of Single-Crystal Films

2.4.1. Introduction to X-Ray Diffraction

X-ray diffraction (XRD) is one of the primary ways of identifying and characterizing the crystal structure of material. Specifically, XRD is sensitive to the interplanar spacings withing a crystal. When a crystal is oriented within a focused beam of x-rays such that the diffraction conditions are met, a portion of the beam is diffracted which can be collected as an intensity signal. The interplanar spacing that diffracted the light can then be precisely calculated from that signal. Provided that the material does not fully absorb a given frequency of light, any wavelength of light can satisfy the diffraction condition. Diffraction is maximized when the

wavelength of light is less than or equal to the aperture width. The main reason that x-rays are used is that their wavelengths are on the same size scale as atoms (i.e., ~10^{-10} m = 1 Å), thus giving them a high degree of spatial resolution with respect to interplanar spacings.

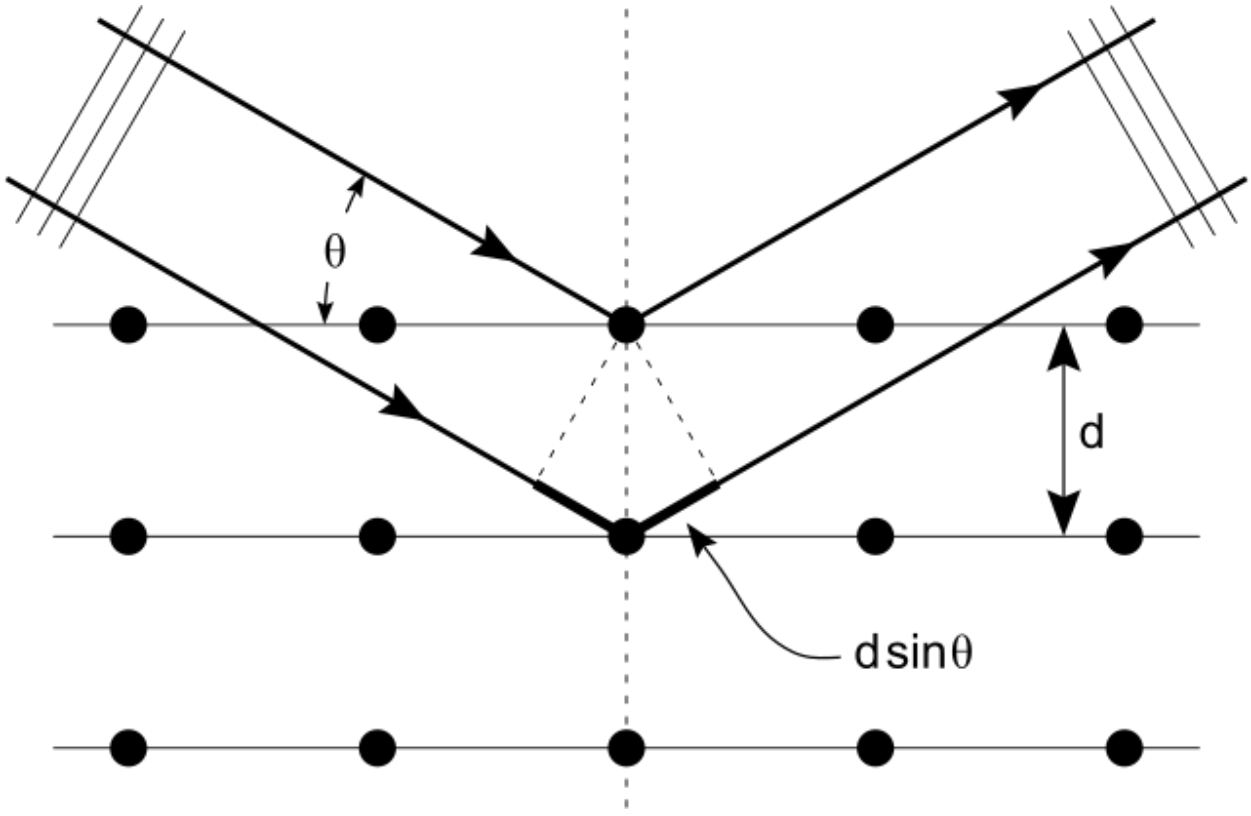

Fig. 2.11: A two-dimensional schematic of first-order x-ray diffraction occurring from a crystallographic plane according to Bragg's law.[27]

The x-ray diffraction condition is known as Bragg's law, and is expressed as

$$n\lambda = 2d\sin\theta, \tag{2.11}$$

where n is the diffraction order, λ is the wavelength of light, d is the interplanar spacing, and θ is the angle made between the crystal plane and the diffracted light. A two-dimensional schematic of first-order x-ray diffraction by a crystalline plane in accordance with Bragg's law is presented in **Fig. 2.11**. Modern cabinet style X-ray diffractometers are geometrically designed around Bragg's law. A schematic representation of an x-ray diffractometer equipped with a goniometer that has five principal axes of rotation is shown in **Fig. 2.12**. Essentially, the five angles are

controlled to achieve diffraction from crystallographic planes with different orientations within a sample. These angles are necessary for performing a variety of structural measurements on single crystal samples, and they have standard names and definitions that are used to quantify and compare measurement results.

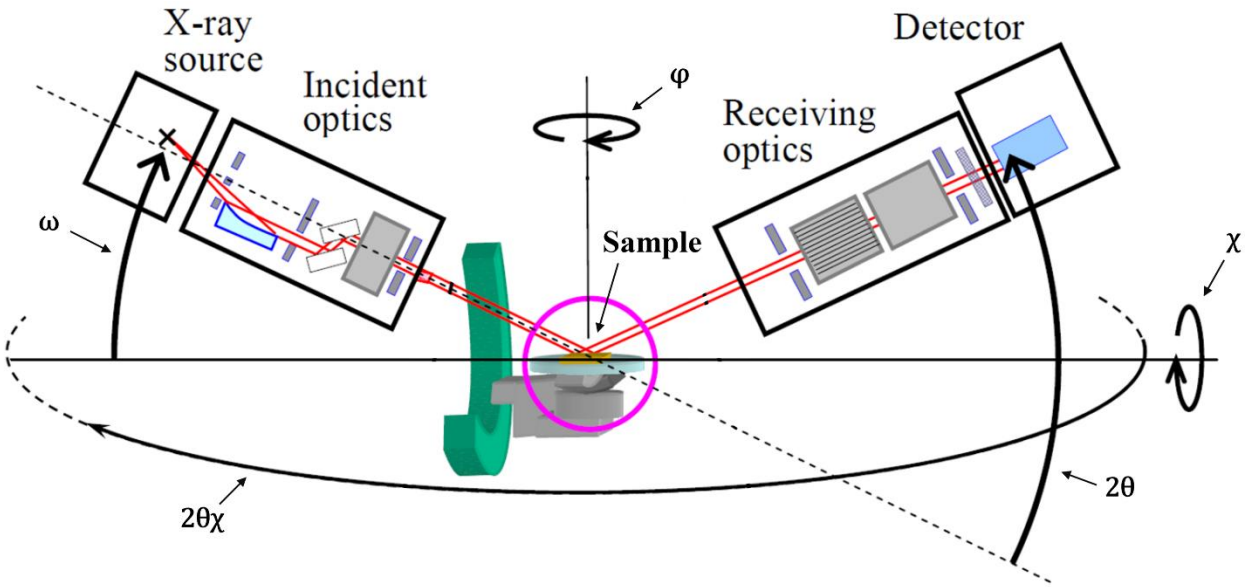

Fig. 2.12: A three-dimensional schematic of a sample in an x-ray diffractometer equipped with a goniometer that has five principal axes of rotation, similar to the set-up of a Rigaku SmartLab diffractometer.[28]

The five axes' angles are 2θ (or θ), ω, φ, 2θχ, and χ. The 2θ angle is simply two times the diffraction angle θ, which was previously defined as the angle made between the crystal plane and diffracted beam. Standardized XRD measurements use the angle 2θ because earlier detectors were designed using 2θ as the detector angle. ω is the angle made between the incident beam and the focal plane of the XRD detector. Note that the focal plane is independent of the sample and is defined by the common plane that results from an incident beam that is diffracted and then received by the detector. The focal plane will contain a component of both the incident and diffracted beams, and then a second shared plane will contain an orthogonal component of both the incident and diffracted beams. φ is the azimuthal rotation angle of the sample around a

vertical axis that pierces the center of the focal plane. $2\theta\chi$ is analogous to the 2θ angle, but with a key difference. Specifically, $2\theta\chi$ is used to measure interplanar spacings that are aligned in-plane of a sample. $2\theta\chi$ is then defined as the angle made between an in-plane oriented crystallographic plane and the diffracted light. The $2\theta\chi$ angle is most useful for in-plane measurements of flat samples, i.e., films and substrates. Finally, the χ angle is analogous to the φ angle except that it rotates around a horizontal central axis that pierces the center of the focal plane. Unlike φ, however, the χ angle is usually manipulated by rotating the optics of the detector with respect to the sample.

For powder or bulk polycrystalline samples with randomly oriented grains, some of these angles are redundant and don't provide any extra information. Single crystals, films, and textured samples, however, have higher degrees of symmetry that require more control over the XRD optics. Aside from the five goniometer angles just discussed, there are also physical detector parameters that can be independently adjusted. Examples of these parameters include sample stage tilt angles R_X and R_Y, and sample stage height Z. R_X, R_Y and Z-position are specifically used to better align the sample, and to compensate for differences in sample height and substrate miscut angles.

As previously mentioned, x-rays are chosen for crystal diffraction because their wavelengths are on the same size scale as atoms. Characteristic x-rays can be emitted from a variety of source materials, such as Mo, Cu, Co, Fe or Cr, each with a unique emission spectrum of their own. The most commonly used x-ray source for inorganic materials characterization is elemental copper. A graphical representation of the x-ray emission intensity as a function of wavelength is shown in **Fig. 2.13** for a typical Cu target. The high intensity and nearly monochromatic Cu $K\alpha_1$ radiation is the specific emission used in XRD experiments. As **Fig. 2.13**

shows, however, there are other high intensity wavelengths near the $K\alpha_1$ peak emitted from the $K\beta$ and $K\alpha_2$ absorption edges. Oftentimes in powder diffractometry, most of the lower wavelength emissions are absorbed by inserting a Ni-filter in the path of the beam. This method of monochromating produces diffraction patterns with split peaks resulting from the slight difference in wavelength from the $K\alpha_1$ and $K\alpha_2$ emissions. For high resolution XRD measurements more typically used on epitaxial films, the beam is narrowly monochromated around the $K\alpha_1$ wavelength. One method of achieving better levels of monochromation is to use pairs of highly polished single crystal (220)-oriented Ge mirrors. While using mirror-based monochromators results in higher precision XRD measurements than Ni-filters, their use also results in a dramatic reduction of signal intensity.

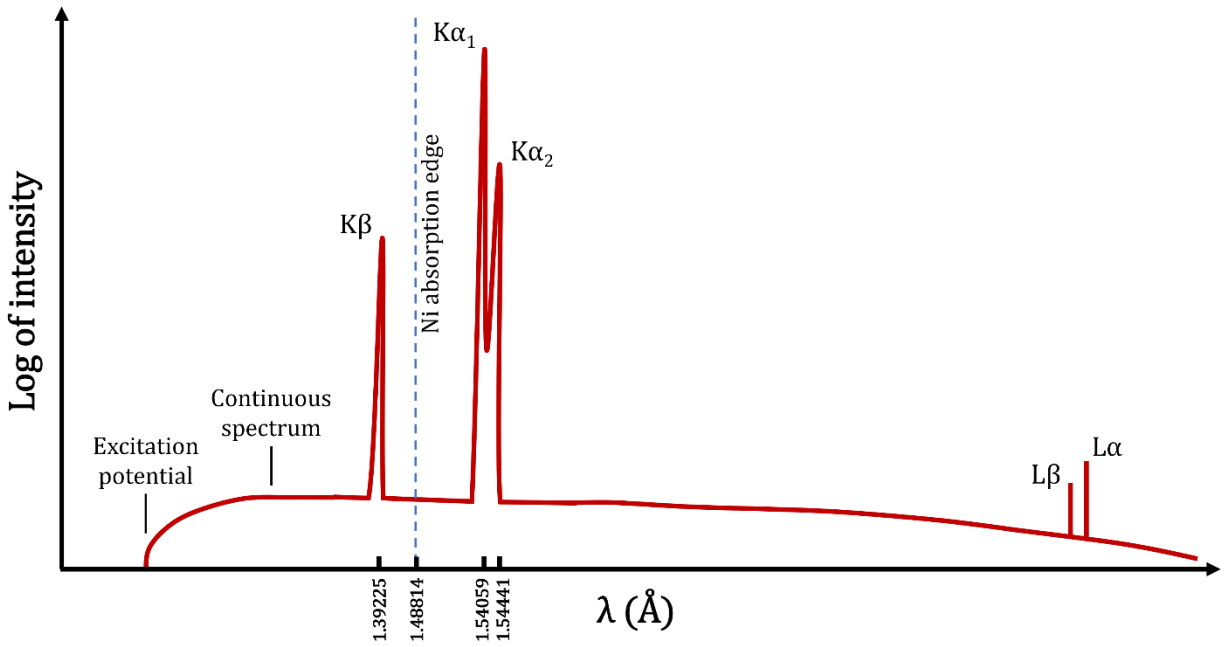

Fig. 2.13: A graphical representation of the typical x-ray emission emitted by a Cu target plotted as a function of wavelength. Axes are not drawn to scale.

For an ideal crystal, the diffraction peak intensity curves possess a Lorentzian shape with respect to θ and the analysis of interplanar spacings according to Bragg's law is straightforward. However, real physical materials always contain some level of disorder from things like grain

boundaries, free surfaces, strain, point defects, or dislocations. XRD is sensitive to all forms of structural disorder that lead to changes in the distributions of interplanar spacings. The statistical nature of XRD makes it a versatile method of materials analysis beyond just phase identification. For example, the size of nanopowders can be correlated with XRD peak FWHM measurements [30], the level of residual stress in milled powders can be analyzed and compared with XRD FWHM's [31], the texturing of metal alloys can be quantified with relative changes in XRD peak intensities [32], and strain relaxation can be precisely measured in epitaxially strained films and correlated to a gradient in density of dislocations by using techniques like reciprocal space mapping.[33] The breadth of XRD analysis is so vast that comprehensive books exist for many of the specific applications just mentioned.

2.4.2. 2θ-θ Measurements

2θ-θ scans are a specific form of 2θ-ω scan in which the incident angle ω is made identical to the diffracted beam angle θ through careful alignment of the sample. Once the sample is aligned, the measurement is performed by sweeping the incident and receiving optics up and around the sample at the same angular rate while measuring the intensity of collected x-rays. The experimental setup for this form of measurement is geometrically analogous to the representation of diffraction according to Bragg's law in **Fig. 2.11**, and it specifically measures interplanar d-spacings that are directed out-of-plane of the focal plane of the detector. For powders, the alignment process is a straightforward manner of preparing a flat sample and placing its top surface flush with the focal plane of the detector. The sample alignment is more involved for an epitaxial single crystal film. In the case of the film, the upper crystallographic planes near the surface of the film and parallel to the interface with the substrate must be aligned to the focal plane of the detector. Since the film is often much smaller by volume than the

substrate and it may contain a broad range of interplanar d-spacings, it is practically easier to achieve good alignment by aligning to the substrate itself.

To align to the single crystal substrate parallel with the focal plane of the XRD, you first need to determine the 2θ position given by its out-of-plane oriented interplanar d-spacing which is closest to the d-spacing you wish to measure in the film. With the incident and receiving optics in the zero positions, first sweep the sample stage height Z-position to identify and set the Z-position for the top surface of the sample. Then set the receiving angle to the given 2θ position of the substrate, and the incident angle to the corresponding $\omega = \theta$ position. Proceed to align the sample by performing sweeps across the sample stage tilt angles R_X and R_Y, adjusting their values to the maximum peak value after each sweep. The purpose of optimizing the R_X and R_Y angles is to compensate for any miscut angle present on the substrate itself. Iterate through this process of optimizing the Z-position, R_X and R_Y until the signal from the substrate is maximized and highly symmetric in shape. If it isn't very symmetric, then the actual 2θ value of the substrate is likely slightly different than the reference value, and you may need to sweep and optimize the 2θ value in addition to the stage alignment values.

After the epitaxial film is aligned, the 2θ-θ scan can be collected. 2θ-θ scans of single crystalline films are collected in much the same way as they are for powder samples. The largest difference is that all possible planes can be measured in a powder sample with randomly oriented crystallites, whereas only those crystallographic planes parallel to the alignment plane can possibly be measured in a single crystal. Therefore, it is usually only necessary to measure relatively narrow 2θ ranges around the possible peaks. It is generally a good idea to measure across both the film and substrate peaks, and to measure each of the peaks that are present given the type of sample and its orientation.

2.4.3. Rocking Curve Measurements

Rocking curve measurements are performed by aligning the diffraction angle 2θ of the receiving optics to the location of a diffraction peak, and then measuring the intensity of collected x-rays by sweeping the incident angle ω while keeping the 2θ angle fixed. While this measurement provides information about the out of-plane d-spacings in a film, it is fundamentally different information than a 2θ-θ scan. Furthermore, rocking curves aren't typically performed on powder or bulk polycrystalline specimens like 2θ-θ scans because they wouldn't provide much useful information about their structures.

Rocking curves are a method of measuring the distribution of tilt angles, i.e., mosaic tilt, within highly oriented samples such as epitaxial films. The crystallographic d-spacings that are aligned out-of-plane with respect to the focal plane of the diffractometer coincide with the peak center of a rocking curve at $\omega = \theta$. Any intensity of diffracted x-rays measured at positions other than $\omega = \theta$ result from crystallographic d-spacings that have an additional tilt angle. Wider rocking curve peaks indicate a higher degree of mosaicity. The primary figure of merit for a rocking curve is the FWHM of the peak, which is used as a convenient way to quantify the degree of mosaic tilt within a material.

To collect a rocking curve of an epitaxial film's peak, the sample must first be aligned in the same way as done for a 2θ-θ measurement in the previous section. Then a 2θ-θ scan is collected across the given film peak from which its 2θ peak position is determined. The diffraction angle 2θ of the receiving optics is aligned to the film's peak position, and then the rocking curve is collected by measuring the intensity of collected x-rays while keeping the 2θ angle fixed on the film's peak center and sweeping the incident optics angle ω across the peak

position. Typically, the ω range of a rocking curve is small and a scan range from θ – 0.4° to θ + 0.4° is large enough to fully capture it.

2.4.4. Reciprocal Space Mapping

Reciprocal space mapping is a technique that is exclusively used to study the structure of epitaxial films. There are two types of reciprocal space maps, symmetric and asymmetric, and their interpretations and uses are both complimentary and distinct to each other. Both types of measurements are two-dimensional space maps about a given crystallographic peak, both are collected by iteratively performing several coupled 2θ-ω scans at different ω offsets, and both are plotted and analyzed in reciprocal Q-space according to the same transformation matrix. The differences result from the fact that symmetric reciprocal space maps are collected about diffraction peaks arising from planes with the same orientation as the substrate, i.e., diffraction peaks that can be measured with a standard 2θ-θ measurement, whereas asymmetric reciprocal space maps are collected about peaks arising from planes with a different orientation than the substrate and cannot be measured with a standard 2θ-θ measurement.

The processes of collecting symmetric and asymmetric reciprocal space maps are mostly similar, except that asymmetric scans require extra alignment steps. For both techniques, the first step is to align the substrate of the sample parallel to the XRD focal plane according to the method described in the 2θ-θ measurement section. At this point, the symmetric scan is ready to be collected, however, the asymmetric scan needs subsequent alignment to the offset peak position before it can be collected. To align to the asymmetric peak position, the diffraction angle 2θ is set to the position corresponding to the d-spacing of the asymmetric peak, and the incident angle ω is set to a position that is offset by an angle τ as determined by the angle between the symmetric and asymmetric planes, i.e. $\omega = \theta + \tau$. Depending on the crystallographic

system, the equation for determining τ is different. For a cubic system, the relationship for τ is given by

$$\cos\tau = \frac{h_1h_2+k_1k_2+l_1l_2}{\sqrt{h_1{}^2+k_1{}^2+l_1{}^2}\sqrt{h_2{}^2+k_2{}^2+l_2{}^2}}, \tag{2.12}$$

where (h_1 k_1 l_1) and (h_2 k_2 l_2) are given by the Miller indices of the symmetric and asymmetric places, respectively. It is important to note that the possible asymmetric planes are limited by the physical constraints of the XRD system being used, and to those mutual planes shared between the film and substrate that are both detectable to XRD, i.e., that aren't hidden planes. With 2θ and ω set to the asymmetric position, perform a full sweep of the sample rotation angle φ and set φ to the highest intensity peak. Depending on the n-fold rotational symmetry of the asymmetric plane in question, there should be a total of n peaks with respect to φ. Iteratively sweep the sample stage tilt angles R_X and R_Y, and rotational angle φ one at a time, setting their position to the highest intensity position after each sweep. Once the peaks become symmetric and stop changing intensity, the sample is fully aligned. If the peaks aren't very symmetric, then the actual lattice parameter of the substrate is likely different than the reference value, and the 2θ and ω angles will need to be iteratively swept and optimized in addition to R_X, R_Y, and φ.

Once the sample is aligned to the symmetric or asymmetric peak, the reciprocal space map is collected by taking a series of coupled 2θ-ω scans that each cover the same 2θ range but have a different ω offset value ω'. A coupled 2θ-ω scan is performed by sweeping the incident and receiving optics up and around the sample at the same angular rate much like a 2θ-θ scan, the only difference is that the incident angle ω need not equal θ, and has a value given by ω = θ + ω'. The offset values used should be evenly spaced, such that uniformly spaced points are collected within the entire two-dimensional space produced from the range of 2θ values and ω' values. The specific ranges of 2θ and ω are determined by the positions of the substrate and film

peaks and should be made large enough to capture the entire peaks. Equivalently, the reciprocal space map can be collected as a series of rocking curve measurements at evenly spaced 2θ steps over the desired range. The resulting data is then mapped to reciprocal Q-space using the following relationships:

$$Q_X = \frac{1}{\lambda}(\cos(2\theta-\omega)-\cos\omega); \quad (2.13)$$

$$Q_Z = \frac{1}{\lambda}(\sin(2\theta-\omega)+\sin\omega), \quad (2.14)$$

where λ is the wavelength of x-rays.[29] Alternatively, Q_X and Q_Z can be expressed in reciprocal lattice units by multiplying the expressions in (3.13) and (3.14) by the bulk lattice parameter of the film material. A two-dimensional representation of the accessible peak positions for an epitaxial (0001)-oriented hexagonal film in reciprocal space is shown in **Fig. 2.14**. Examples of the two-dimensional scan regions are highlighted in red and blue for symmetric and asymmetric reciprocal space maps, respectively.

To create the reciprocal space maps, the Q-mapped intensity data is then plotted in log scale as a function of Q_X on the x-axis and Q_Z on the y-axis. In both the symmetric and asymmetric reciprocal space maps, Q_Z is interpreted in a similar way. Q_Z is a projection of the out-of-plane component of the interplanar spacing along the out-of-plane direction of the sample. However, Q_X has a somewhat different interpretation depending on whether it's from a symmetric or asymmetric measurement. In both cases, Q_X is a projection of the in-plane component of the interplanar spacing onto the symmetric plane, i.e., the plane that is oriented with the substrate. For an asymmetric scan, the projection corresponds to an individual direction and interplanar spacing within the symmetric plane. However, for a symmetric scan, there is not a corresponding interplanar spacing within the symmetric plane. Instead, the Q_X component of a symmetric peak is related to the degree of tilt in the growth direction of the film with respect to

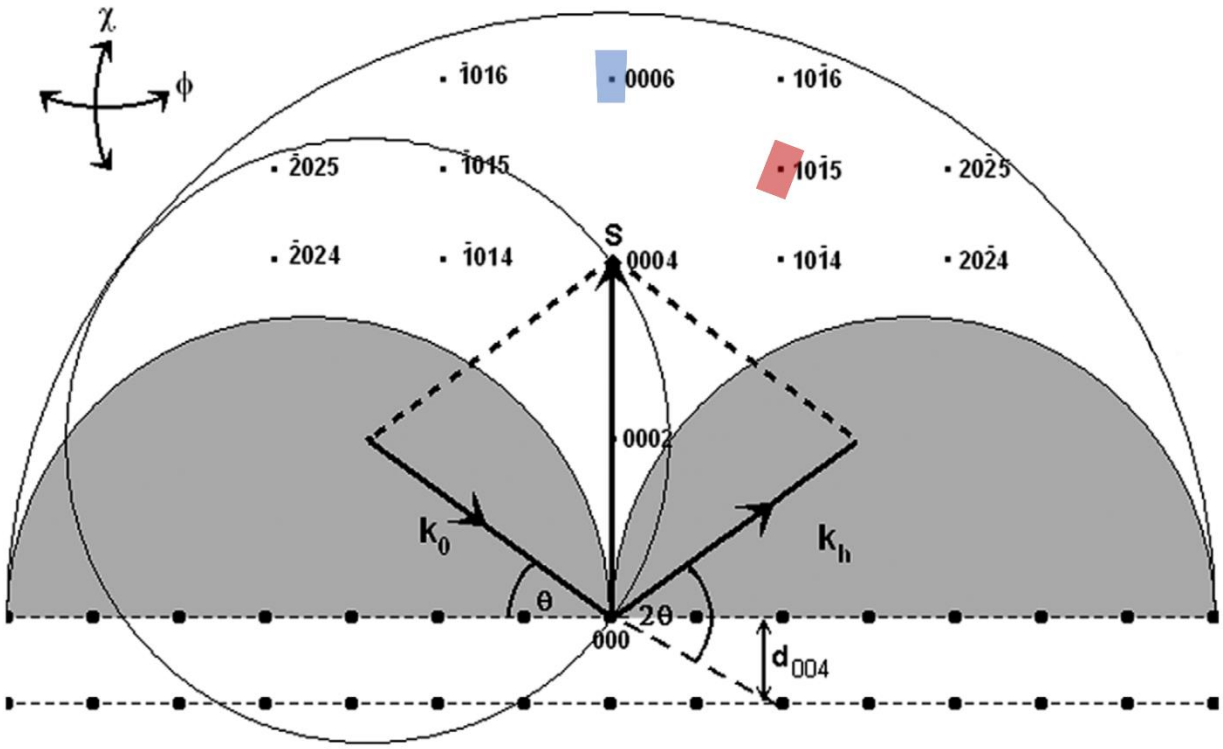

Fig. 2.14: A cross section through reciprocal space for an epitaxial (0001)-oriented hexagonal film. The diffractometer is aligned to the symmetric 2θ-θ position of the (0004) peak, as evidenced by the position of the scattering vector S and the edge of the Ewald sphere. The bottom plane of atoms represents the plane of atoms in regular space. The space bound between the greyed-out regions and the outer semicircle represents the reciprocal space mapping accessible peaks. The blue region is an example of the two-dimensional space measured by a symmetric scan about the (0006) peak position, and the red region is an example of the two-dimensional space measured by an asymmetric scan about the $(10\bar{1}5)$ peak position.[29]

the substrate. In this way, Q_X of a symmetric scan can be interpreted in a similar manner as ω from a rocking curve. Deviation from $Q_X = 0$ in a symmetric scan indicates variation in the mosaic tilt angle of the film. Unlike a rocking curve, however, a symmetric reciprocal space map measurement contains tilt information for a wide range of d-spacings within the film.

Symmetric reciprocal space maps are useful for understanding how the mosaic tilt angle changes with out-of-plane d-spacing. Given enough information about the strain relaxation in a film, the tilt angle and out-of-plane d-spacings can then be correlated to a depth from the film's surface. Asymmetric reciprocal space maps directly measure both the in-plane and out-of-plane

lattice parameters of the film and are useful for understanding the strain and relaxation behavior in a film. When combined, symmetric and asymmetric reciprocal space maps provide large quantities of information about the structure of a film. The major drawback to reciprocal space maps is that they are time intensive to collect and analyze, but due to their two-dimensional nature, they contain much more information than standard 2θ-θ and rocking curve measurements provide. While the Q_Z of symmetric scans and both the Q_X and Q_Z of asymmetric scans correspond to individual interplanar spacings in reciprocal space, determining the exact planes can be tricky and depends on the exact crystallographic plane that was aligned to. It is often more straightforward and less error prone to determine the strain from a film's Q-position in relation to the theoretical Q-position calculated for the identical plane in an unstrained material with a known lattice parameter, i.e., the reference material. From these strain values, the physical length of a film's in-plane and out-of-plane d-spacings or lattice parameters can easily be determined.

REFERENCES

[1] A. V. Rane, K. Kanny, V. K. Abitha, and S. Thomas. Chapter 5 – Methods for Synthesis and Fabrication of Nanoparticles and Fabrication of Nanocomposites. Synthesis of Inorganic Nanomaterials (Woodhead Publishing 2018) 121-139.

[2] O. Opuchovik, A. Kareiva, K. Mazeika, and D. Batrunas. Magnetic nanosized rare earth iron garnets $R_3Fe_5O_{12}$: Sol-gel fabrication, characterization and reinspection. J. Magn. Magn. Mater. 422 (2017) 425-433.

[3] S. Hosseini Vajargah, H. R. Madaah Hosseini, and Z. A. Nemati. Synthesis of nanocrystalline yttrium iron garnets by sol-gel combustion process: The influence of pH of precusrsor solution. Mater. Sci. Eng. B 129 (2006) 211-215.

[4] M. N. Akhtar, M. A. Khan, M. Ahmad, G. Murtaza, R. Raza, S. F. Shaukat, M. H. Asif, N. Nasir, G. Abbas, M. S. Nazir, and M. R. Raza. $Y_3Fe_5O_{12}$ nanoparticulate garnet ferrites: Comprehensive study on the synthesis and characterization fabricated by various routes. J. Magn. Magn. Mater. 368 (2014) 393-400.

[5] M. H. Nguyen, S. J. Li, and W. M. Kriven. Synthesis of oxide powder by way of a polymeric steric entrapment precursor route. J. Mater. Res. 14, 8 (1999) 3417-3426.

[6] P. Sellappan, C. Tang, J. Shi, and J. E. Garay. An integrated approach to doped thin films with strain-tunable magnetic anisotropy: powder synthesis, target preparation and pulsed laser depositioin of Bi:YIG. Mater. Res. Lett. 5, 1 (2017) 41-47.

[7] H. M. Widatallah, C. Johnson, S. H. Al-Harthi, A. M. Gismelseed, A. D. Al-Rawas, S. J. Stewart, M. E. Elzain, I. A. Al-Omari, and A. A. Yousif. A structural and Mössbauer study of $Y_3Fe_5O_{12}$ nanoparticles prepared with high energy ball milling and subsequent sintering. Hyperfine Interact. 183 (2008) 87-92.

[8] M. M. Rashad, M. M. Hessien, A. El-Midany, and I. A. Ibrahim. Effect of synthesis conditions on the preparation of YIG powders via co-precipitation method. J. Magn. Magn. Mater. 321 (2009) 3752-3757.

[9] J. E. Garay. Current-Activated, Pressure-Assisted Densification of Materials. Annu. Rev. Mater. Res., 40 (2010) 445-468.

[10] H. Yu, L. Zeng, C. Lu, W. Zhang, and G. Xu. Synthesis of nanocrystalline yttrium iron garnet by low temperature solid state reaction. Mater. Charact. 62 (2011) 378-381.

[11] S. Hosseinzadeh, M. Behboudnia, L. Jamilpanah, M. H. Sheikhi, E. Mohajerani, K. Tian, A. Tiwari, P. Elahi, and S. M. Mohseni. High saturation magnetization, low coercivity and fine YIG nanoparticles prepared by modifying co-precipitation method. J. Magn. Magn. Mater. 476 (2019) 255-360.

[12] M. Rajendran, S. Deka, P. A. Joy, and A. K. Bhattacharya. Size-dependent magnetic properties of nanocrystalline yttrium iron garnet powders. J. Magn. Magn. Mater. 301 (2006) 212-219.

[13] R. Godoi, M. Jafelicci Jr., R. Marques, L. C. Balcony, and R. C. Lima. Nanometric particles of yttrium ferrite. Chem Nova 22, 6 (1999).

[14] C. V. Stan, J. Wang, I. S. Zouboulis, V. Prakapenka, and T. S. Duffy. High-pressure phase transition in $Y_3Fe_5O_{12}$. J. Phys. Condens. Matter. 27 (2015) 405401.

[15] F. Sanchez-De Jesús, C. A. Cortés, R. Valenzuela, S. Ammar, and A. M. Bolarín-Miró. Synthesis of $Y_3Fe_5O_{12}$ (YIG) assisted by high-energy ball-milling. Ceram. Int. 38 (2012) 5257-5263.

[16] K. Momma, and F. Izumi. VESTA for three-dimensional visualization of cystals, volumetric and morphology data. J. Appl. Crystallogr. 44 (2011) 1272-1276.

[17] J. Cassedanne, and C. R. Hebd. Iron-Oxygen-Yttrium Ternary Alloy Phase Diagram. Seances. Acad. Sci. 252 (1961) 3261-3262.

[18] M. A. Gülgün, M. H. Nguyen, and W. M. Kriven. Polymerized Organic-Inorganic Synthesis of Mixed Oxides. J. Am. Ceram. Soc. 82 (1999) 556-560.

[19] T. L. Gilbert. A Phenomenological Theory of Damping in Ferromagnetic Materials. IEEE Trans. Magn., 40 (2004) 6.

[20] B. Buford, P. Dhagat, and A. Jander. A technique for error estimation of linewidth and damping parameters extracted from ferromagnetic resonance measurements. J. Appl. Phys., 117 (2015) 17E109.

[21] C. Kittel. Ferromagnetic resonance. J. Phys. Radium, 12 (1951) 291-302.

[22] C. Kittel. On the Theory of Ferromagnetic Resonance Absorption. 73 (1948) 2.

[23] B. Samantaray, A. K. Singh, A. Perumal, R. Ranganathan, and P. Mandal. Spin dynamics and frequency dependence of magnetic damping study in soft ferromagnetic FeTaC film with a stripe domain structure. AIP Adv., 5 (2015) 067157.

[24] S. Tamaru, S. Tsunegi, H. Kubota, and S. Yuasa. Vector network analyzer ferromagnetic resonance spectrometer with field differential detection. Rev. Sci. Instrum., 89 (2018) 053901.

[25] V. H. Ortiz, B. Askook, J. Li, M. Aldosary, M. Biggerstaff, W. Yuan, C. Warren, Y. Kodera, J. E. Garay, I. Barsukov, and J. Shi. First- and second-order magnetic anisotropy and damping of europium iron garnet under high strain. Phys. Rev. Mater., 5 (2021) 124414.

[26] I. Barsukov, Y. Fu, A. M. Gonçalves, M. Spasova, M. Farle, L. C. Sampaio, R. E. Arias, and I. N. Krivorotov. Field-dependent perpendicular magnetic anisotropy in CoFeB thin films. Appl. Phys. Lett., 105 (2014) 152403.

[27] Hydrargyrum. “Bragg diffraction 2” [Online]. Wikipedia Commons, Dec. 1, 2011. Available from: https://commons.wikimedia.org/wiki/File:Bragg_diffraction_2.svg

[28] K. Inaba, S. Kobayashi, K. Uehara, A. Okada, S. L. Reddy, and T. Endo. High Resolution X-Ray Diffraction Analyses of (La,Sr)MnO_3/ZnO/Sapphire(0001) Double Heteroepitaxial Films. AMPC, 3 (2013) 72-89.

[29] M. A. Moram, and M. E. Vickers. X-ray diffraction of III-nitrides. Rep. Prog. Phys., 72 (2009) 036502.

[30] A. L. Patterson. The Scherrer Formula for X-Ray Particle Size Determination. Phys. Rev., 56 (1939) 978.

[31] P. S. Prevéy. X-ray Diffraction Residual Stress Techniques. Metals Handbook. 10. Metals Park: American Society for Metals, (1986) 380-392.

[32] M. D. Vaudin. Crystallographic Texture in Ceramics and Metals. J. Res. Natl. Inst. Stand. Technol., 106 (2001) 1063-1069.

[33] H. Heinke, M. O. Möller, D. Hommel and G. Landwehr. Relaxation and mosaicity profiles in epitaxial layers studied by high resolution X-ray diffraction. J. Cryst. Growth, 135 (1994) 41-52.

CHAPTER 3

CAPAD Processing of Bulk YIG Ceramics

3.1. Background and Motivation

The growing body of research of epitaxial rare earth iron garnet films requires high quality PLD and sputtering targets in addition to a variety of single crystal garnet substrates. Many types of rare earth iron garnets are simply not available in target form, forcing those wanting to create and study films to fabricate ceramic targets of their own from commercially available powders. While individually made targets can be used to produce highly crystalline epitaxial films, the microstructure of a target impacts both the quality of the resulting films and the degree of control over the deposition process. Anecdotally, thin film researchers claim that targets with higher relative densities and smaller grain sizes produce higher quality films. Many commercial companies specializing in equipment related to thin film deposition and fabricating targets make the same claims on their websites. However, there aren't many systematic studies proving these claims in the available scientific literature. One study by Reza at al. shows that using a sputtering target with smaller grain sizes produces films with larger grain sizes.[14] These results suggest that using targets with small grain sizes should enhance the ability to grow epitaxial films.

Yttrium iron garnet (YIG) is the quintessential low spin-damping material. The crystal and magnetic structure of YIG is analogous to the rare earth iron garnets, and yttrium itself is chemically very similar to the rare earth elements. There is also a vast amount of scientific literature on the properties of YIG in both bulk and thin film form, making YIG the ideal candidate for demonstrating a new method of fabricating a dense, finely structured rare earth iron garnet target. While there exists a large amount of scientific literature on the synthesis of

nanograined YIG powder, there are few studies published on the fabrication of bulk nanograined YIG. Many of the difficulties faced when synthesizing nanograined YIG powder previously discussed in the methods section not only carry over to the fabrication of bulk nanograined YIG ceramics but are exacerbated by the high temperatures and hold times need to create them. This type of processing invariably leads to a high degree of grain growth, making it difficult to retain nano-sized features in bulk form.

To date, one of the most successful attempts at producing a bulk nanograined YIG resulted from reactive spark plasma sintering (SPS) of an amorphous precursor synthesized via a polymeric precursor method at a processing temperature of 750°C.[2] The best sample that came out of this study was phase pure garnet according to XRD, had a relative density of ~94%, an average grain size of ~100 nm, and a M_S value of 26.6 emu/g, which is only about 5% lower than what's typically reported for bulk YIG. These samples were very close to realizing a fully dense, single phase, bulk nanograined YIG, but as the SEM image in **Fig. 3.1** shows, this method also resulted in some trapped porosity located within the interiors of grains. Unfortunately, the magnetic properties of these samples were not thoroughly characterized beyond VSM and Mössbauer, and as of early 2019, there are no other published reports on the fabrication of bulk nanograined YIG of similar or better quality.

Aside from the potential applications as a PLD or sputtering target, a dense, bulk nanograined YIG would be scientifically interesting in itself. This is especially true since it has proven so difficult to produce, and as such, there are very few reports containing property measurements for such a material. Of particular interest are the effects of small grain size on both the spin dynamics and spin transport in YIG. Perhaps magnon confinement, analogous to phonon confinement, could be observed at or near room temperature where the magnon thermal

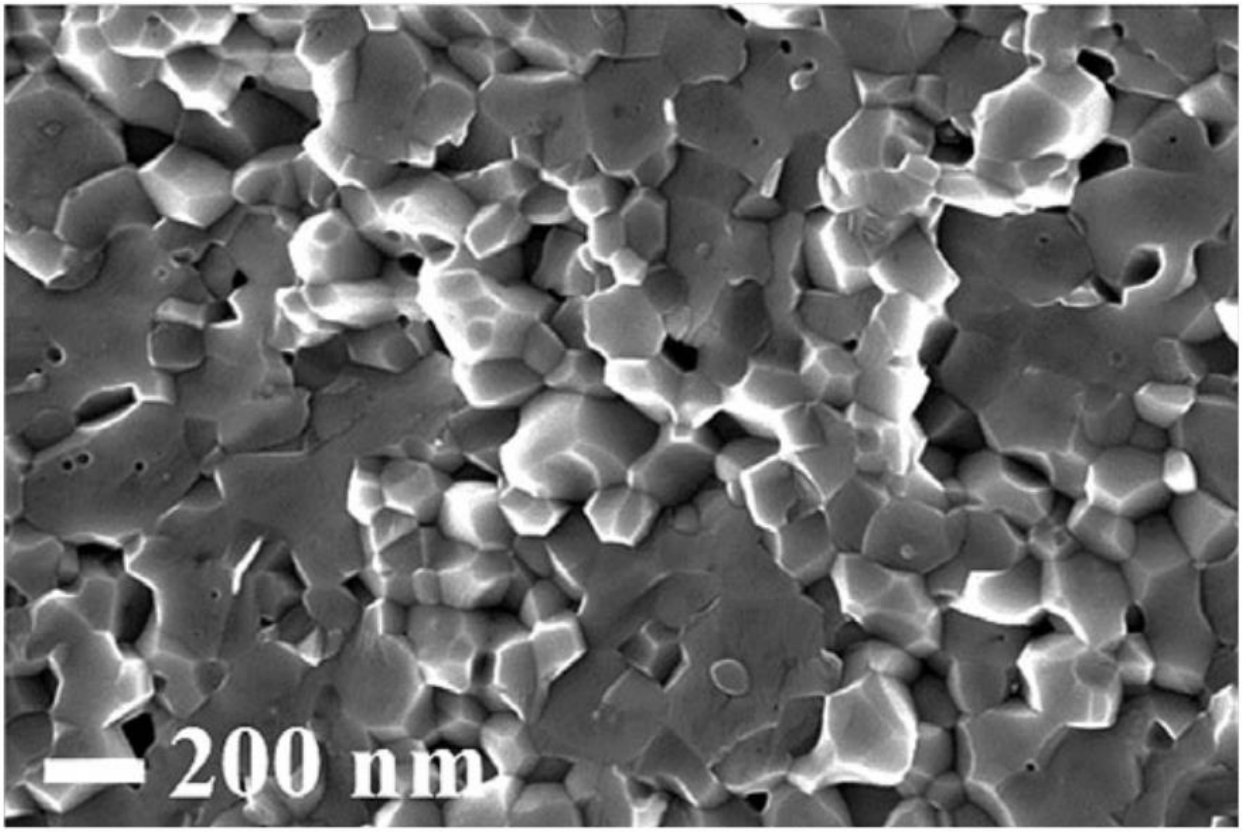

Fig. 3.1: A representative SEM micrograph of a fractured surface of the bulk nanograined YIG produced via reactive SPS at 750°C by Gaudisson et al.[2]

mean free path is on the order of tens of nanometers.[1] Similarly, the thermal transport of magnons can be further investigated when phonon confinement plays a role at reducing the thermal conductivity due to phonons. Other phenomena involving standing spin waves within nano-sized grains might also emerge in samples with narrow grain size dispersions. While the technological importance of such studies is not yet known, the results would be worthy of investigation.

3.2. Synthesis and Consolidation of YIG Powders at 100 MPa

The objective of this study is to fabricate a dense, single phase and finely structured polycystalline YIG via CAPAD of powders synthesized via the polymeric steric entrapment method. YIG powders were first synthesized according to the polymeric-steric entrapment

method as described in the powder synthesis portion of the methods section. The resulting metal-organic preceramic powder underwent simultaneous thermogravimetric and differential scanning calorimetry (TGA/DSC) in air using a TA Instruments SDT-600, which is shown in **Fig. 3.2**. The TGA-DSC analysis revealed several low temperature exothermic reactions centered at approximately 280°C, 330°C and 380°C as evidenced by upwards pointing peaks in the red colored heat flow curve. In the black colored curve that pertains to the percentage of the initial weight of the measured sample, the largest weight loss occurs in the region from approximately 230-390°C where the sample decreases from ~91% of its initial mass to ~57%. These results indicate that the majority of the organic material burns off before 400°C. After 500°C, the mass remains nearly constant, only dropping from ~56% of its weight at 500°C to ~54% at ~770°C where another exothermic reaction is observed in the heat flow curve. From this point on, the mass remains at a constant value up through the maximum measurement temperature of 1100°C, indicating that all organic material has been fully removed.

The sharpest peak in the heat flow curve is centered at 763.5°C, which was later confirmed by XRD to be the crystallization point of this powder. A calcining temperature sweep was then performed on the preceramic powder to evaluate the phase evolution of the powder and determine the proper calcining conditions. A small amount of precursor was first calcined in an alumina boat in a tube furnace in air at 1300°C for 12 h, which is both a higher temperature and longer hold time than is necessary to fully react the powder. This step was taken to verify that stoichiometry of the precursor was in the correct 3 Y:5 Fe ratio since YIG is a line compound and secondary phases would appear alongside the garnet if the powder was stoichiometrically off. A certain degree of interdiffusion took place between the powder in direct contact with the alumina boat as evidenced by a red discoloration of the boat, however, according to XRD and

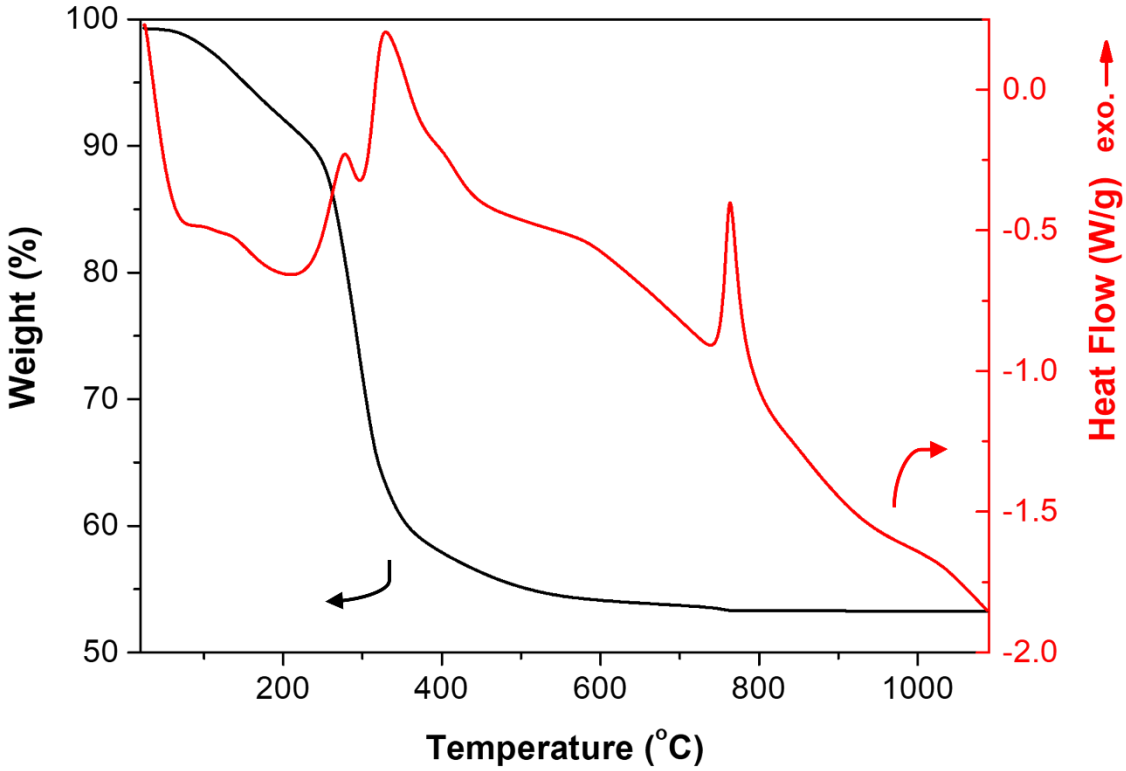

Fig. 3.2: Simultaneous TGA-DSC analysis of the metal-organic YIG precursor powder synthesized according to the polymeric-steric entrapment method. The black curve pertains to the percentage of the initial weight of the sample, whereas the red curve pertains to the net heat flow in and out of the sample.

VSM analysis, this did not significantly affect the structure or magnetic properties of the calcined powder. After repeated usage of the boat to calcine YIG powders, the color of the interior of the boat remained constant and the interdiffusion of aluminum and iron was assumed to have slowed and to not significantly impact the quality of the calcined powders. After verifying that the fully reacted precursor only forms garnet, small portions of precursor were then calcined in the same alumina boat in a tube furnace in air from 700°C to 1200°C in 100°C increments for 30 minutes each, using a heating rate of 10°C/min.

The structural compositions of the powders calcined at different conditions were evaluated with XRD analysis using a PANalytical Empyrean Series 2 diffractometer. The results

of the powder XRD measurements are shown in **Fig. 3.3**. Powder calcined below the crystallization temperature of 763.5°C resulted in amorphous powder, as clearly shown by the near total lack of crystalline peaks in the XRD pattern collected for the powder heat treated at 700°C. As expected, the powders calcined above the crystallization temperature were fully crystalline and exhibited diffraction peaks consistent with the Y-Fe-O ternary system. The diffraction pattern of all powders calcined below 1200°C contained peaks consistent with the garnet phase in addition to relatively small peaks consistent with the perovskite phase, YIP, indicating that these powders are composites comprised primarily of YIG with a lesser amount of YIP.

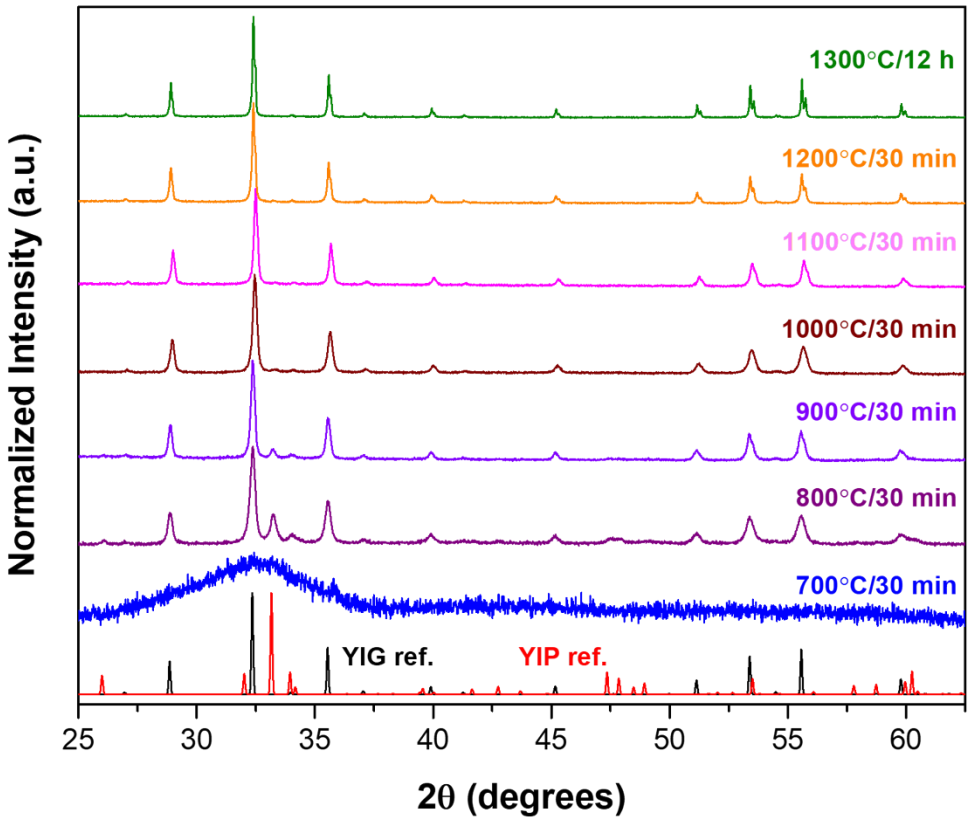

Fig. 3.3: XRD measurements of YIG powders synthesized via the steric-entrapment method and calcined in air at various conditions. Published XRD patterns for the garnet phase (ICSD coll. code 33931) and perovskite phase (ICSD coll. code 258501) are shown at the bottom of the graph for reference.

Since the XRD of the fully reacted powder proves that the overall cation ratio is nearly identical to 3 Y:5 Fe, the presence of YIP indicates that there should also be some iron oxide present, likely in the form of α-Fe_2O_3. For every three formula units of $YFeO_3$ (YIP) there should be one formula unit of Fe_2O_3 in order to maintain the correct overall stoichiometry. Since $YFeO_3$ and Fe_2O_3 have similar volumes per formula unit, this means that diffraction peaks from Fe_2O_3 should be observed at approximately one third the overall intensity of the YIP peaks, however, clear Fe_2O_3 peaks are not observed for two reasons. The first reason is that the overall volume of any Fe_2O_3 phases and thus their diffraction intensities would be very small in these powders since the overall volume of the YIP phase was shown to be small according to XRD. The second reason is that the primary diffraction peak position of Fe_2O_3 ($2\theta = 33.180°$) overlaps very closely with that of YIP's ($2\theta = 33.171°$), and similarly, the secondary diffraction peak position of Fe_2O_3 ($2\theta = 35.641°$) overlaps closely with that of YIG's ($2\theta = 35.510°$). As a result, it is difficult to detect any Fe_2O_3 present in the as-synthesized powders from XRD alone.

According to the XRD results of **Fig. 3.3**, the powder calcined at 800°C contains the largest fraction of the intermediary YIP phase by volume. As the calcining temperature increases, the peaks associated with the perovskite phase decrease in area, indicating that relative amount of YIP phase decreases with calcining temperature. The primary YIP peak is still barely visible in the 1100°C treated powder, but it is no longer detectable with XRD in the 1200°C or 1300°C powder, meaning that the garnet phase was fully formed by calcining at 1200°C or higher. The diffraction peaks also become narrower as the calcining temperature increases. This observation is to be expected because higher calcining temperatures produce larger grain sizes and higher levels of crystallinity, both of which result in narrower diffraction peaks.

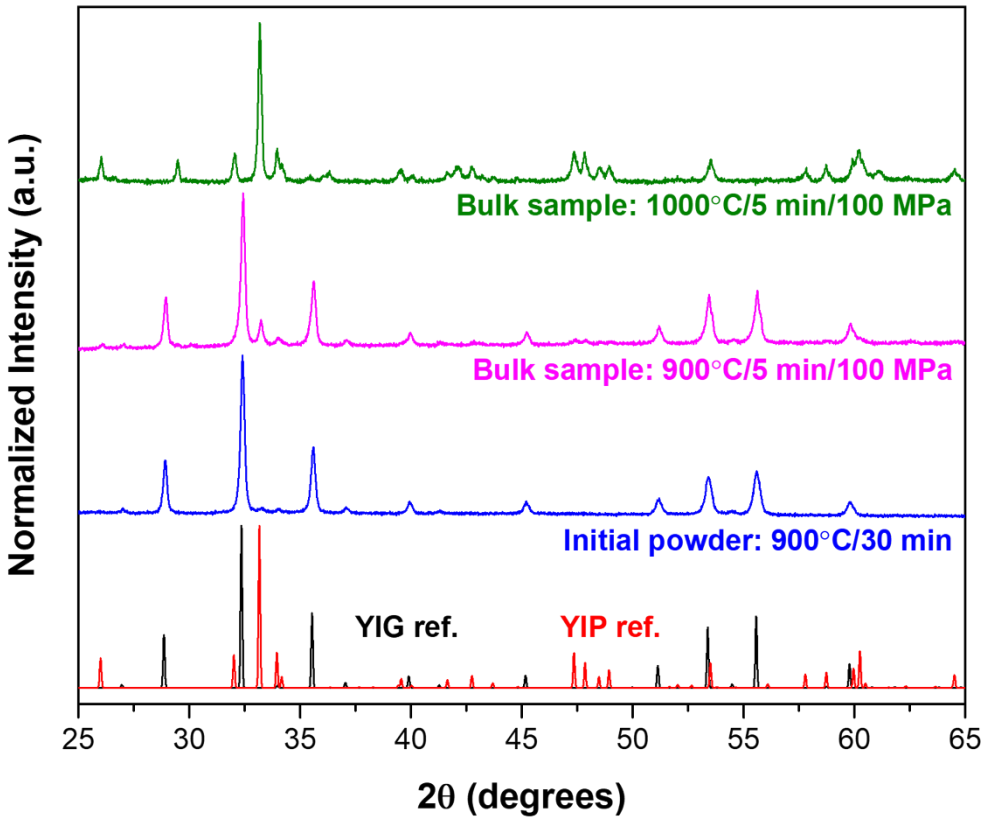

Fig. 3.4: XRD measurements of bulk YIG samples consolidated using CAPAD at an applied pressure of 100 MPa from powders synthesized via the polymeric-steric entrapment technique. The XRD pattern of the as-synthesized powder prior to densification is also presented for comparison. Published XRD patterns for the garnet phase (ICSD coll. code 33931) and perovskite phase (ICSD coll. code 258501) are shown at the bottom of the graph for reference.

YIG powder calcined at 900°C for 30 minutes was chosen to be consolidated into bulk form in a 3/8 in. graphite die using CAPAD processing according to the method described in the current-activated, pressure-assisted densification portion of the methods section. This powder was chosen as a trade-off between phase purity and small grain size, since according to XRD it is nearly single phase garnet, and its grains didn't grow as large as for the powder calcined at higher temperatures. All samples were processed with a hold time of 5 minutes at the target densification temperature, with heating and cooling rates of 200°C/min, and a uniaxially applied

pressure of 100 MPa. Prior to consolidation, the powder was pre-pressed at 100 MPa for 10 minutes. Processing temperatures of 900°C and 1000°C were each used because 900°C was the lowest temperature at which high density YIG was consolidated in prior CAPAD studies.

XRD measurements of the bulk samples and the powder used in their consolidation are presented in **Fig. 3.4**. The XRD results show that the sample consolidated at 900°C has partially converted into the perovskite phase, and that the sample consolidated at 1000°C is mostly perovskite phase, with smaller amounts of YIG and iron oxide phases present. Prior to deposition, the powder was a bright green color consistent with pure YIG, however, both of the consolidated samples are black in appearance. Several pieces of evidence indicate that both the change in physical appearance and the conversion to the perovskite phase are related to oxygen vacancies. The environment created during CAPAD processing is highly reducing and has been documented to reduce Fe^{3+} ions in ferrites to Fe^{4+} via oxygen vacancy formation.[3-5] In other internal studies, black colored bulk YIG samples containing the unwanted YIP phase were restored to green and converted back to YIG by high temperature heat treatments in air. XRD of the sample before and after annealing is presented in **Fig. 3.23**. The densities of the samples were measured using the hydrostatic weighing technique. Both of the consolidated samples had relative densities in the range of 90-96%, although a precise value is difficult to determine due to the mixed phase composition of the samples. An SEM micrograph of a fractured surface of the sample consolidated at 900°C is shown in **Fig. 3.5**. The micrograph shows several grains with sizes in the range of 300-400 nm, and several regions of trapped porosity within the grains.

The magnetic hysteresis loops of the two samples in addition to the initial powder were measured using a Lakeshore 7400 Series VSM. The hysteresis data is normalized by mass and presented in **Fig. 3.6**. All samples had small coercivity values increasing from 9.9 Oe in the

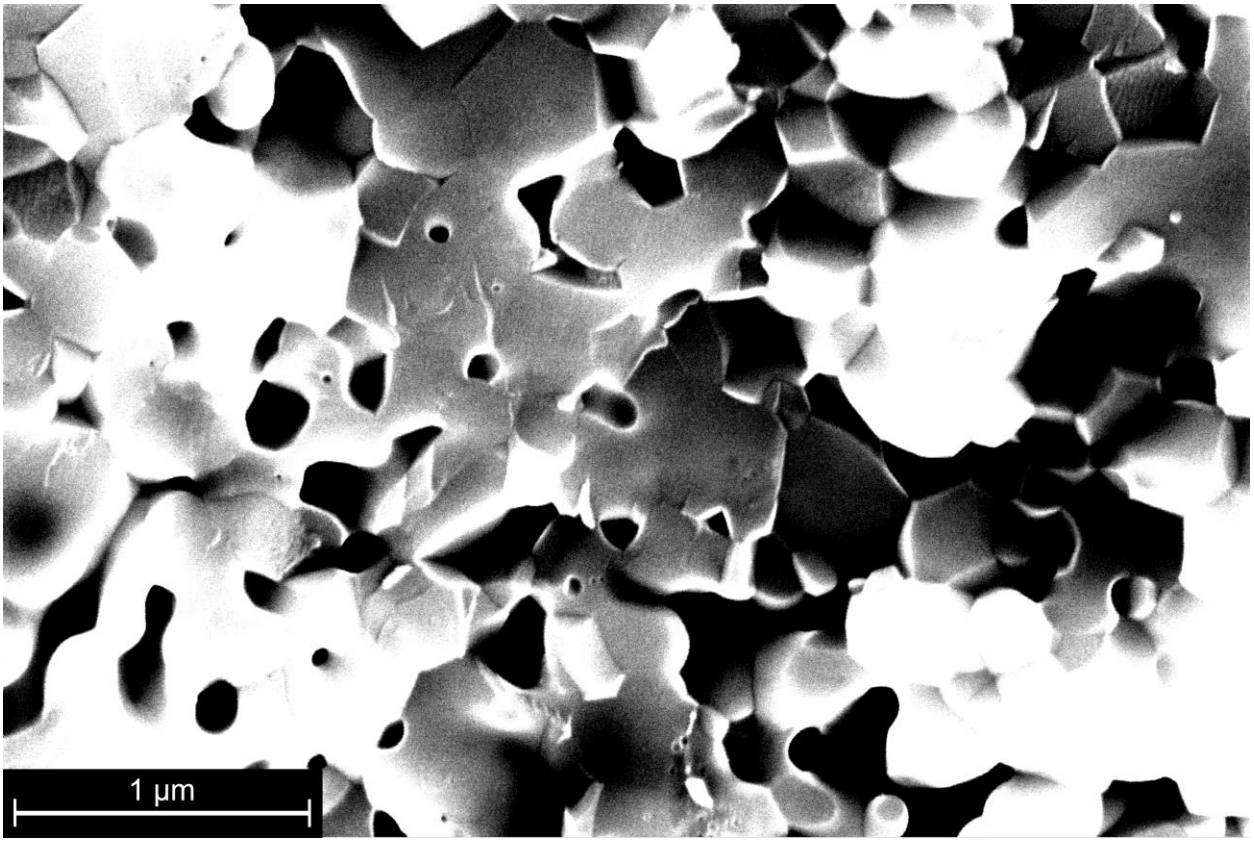

Fig. 3.5: An SEM micrograph taken of a fractured surface of a bulk sample consolidated using CAPAD from powder synthesized via the polymeric steric entrapment technique. The initial powder was heat treated at 900°C for 30 min in air, and sample was processed at 900°C with CAPAD with a hold time of 5 minutes and applied pressure of 100 MPa.

powder to 51.6 Oe in the bulk sample processed at 1000°C. Aside from this, the magnetic behavior of the samples varied continually with increasing perovskite content. The hysteresis of the as-synthesized powder matches that of other pure YIG powders, and has an M_S value of 26.5 emu/g and classic soft magnet shape. The bulk sample that was consolidated at 900°C has a slightly lower M_S value of 23.5 emu/g and still has a soft magnet shape, but it also possesses an unsaturated slope at applied fields greater than 2000 Oe. The sample consolidated at 1000°C has the lowest M_S value of 17.2 emu/g and has a decidedly less square shaped hysteresis than the other two samples, with an even steeper unsaturated slope than the 900°C sample. The change in hysteretic behavior is well explained by the different compositions. The perovskite crystal is a

canted antiferromagnet with weak magnetic behavior that requires very high field to saturate.[6] Samples with more perovskite phase therefore have a lower M_S and a larger unsaturated slope to their hysteresis curves. A summary of the magnetic and physical properties of the samples is provided in **Table 3.1**.

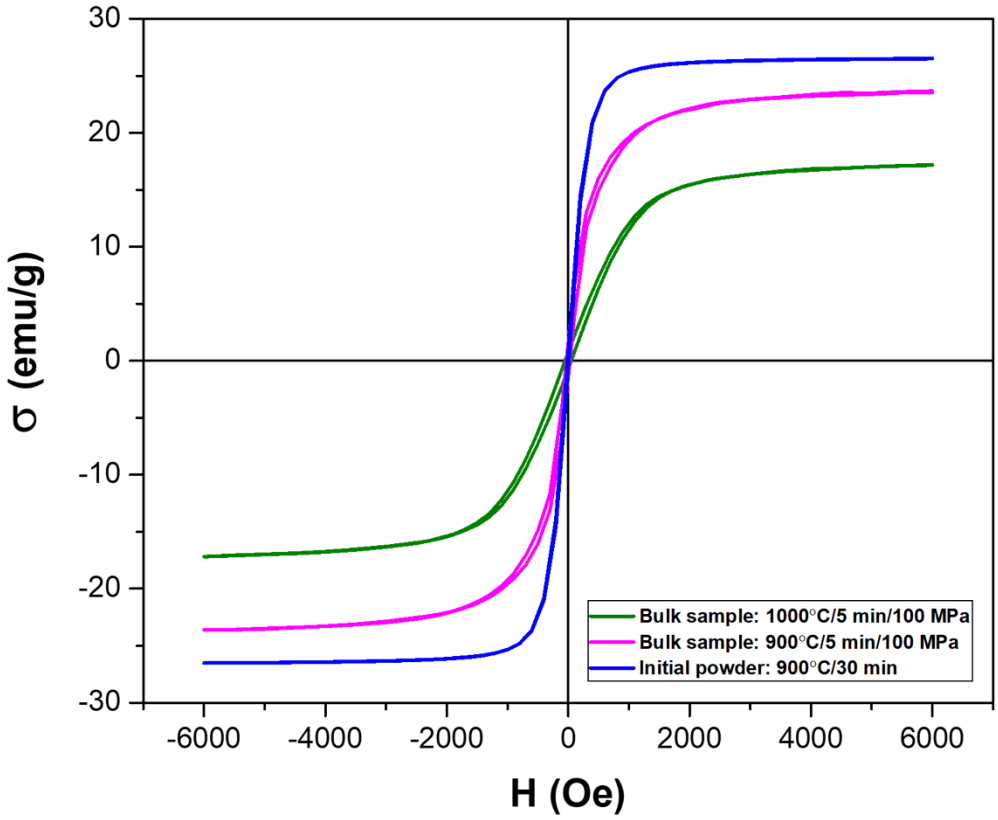

Fig. 3.6: Magnetic hysteresis measurements of two bulk YIG samples consolidated using CAPAD at an applied pressure of 100 MPa from powders synthesized via the polymeric-steric entrapment technique, in addition to the as-synthesized powder prior to densification.

This study revealed two key issues with producing a dense, single phase and finely structured polycystalline YIG via CAPAD of powders synthesized via the polymeric steric entrapment method. Both of these issues revolve around the formation of the unwanted YIP phase. The first problem is that the synthesis method requires high calcining temperatures in

excess of 1100°C in order to fully convert the intermediary oxide phases into garnet, resulting in substantial grain growth in the attained powder. The other major issue is that the reduction of YIG during CAPAD processing converts YIG into an oxygen deficient perovskite phase. High temperature annealing of a CAPAD processed sample in air can reoxygenate it and convert it back into the desired YIG phase, however, this results in additional grain growth of the bulk sample as well. Adjusting the CAPAD processing conditions to densify at a lower temperature would both mitigate the reduction of YIG during processing and lessen the grain growth of the resulting samples. Similarly, adjusting powder processing conditions to produce a finer-structured YIG powder would also result in smaller grain sizes in CAPAD processed samples.

3.3. Consolidation of Commercial YIG Powders at 100 – 500 MPa

The purpose of this study is to determine whether the application of higher pressures can reduce the densification temperature of YIG during CAPAD processing. In many ceramics, the use of higher pressures during CAPAD processing has been demonstrated to lower the temperature required to attain highly dense bulk nanometric ceramics.[7,8] For the case of CAPAD processing of YIG, a lower consolidation temperature would reduce the rate of grain growth during processing and also help mitigate the reduction of YIG that occurs at higher processing temperatures. The grain size of the initial powder does not play as significant of a role at affecting the densification temperature for monodispersed ceramic powders with comparable morphologies, meaning that our in-house synthesized powder should densify at comparable temperatures to most commercial YIG powders. Therefore, we chose to use commercially available Alfa Aesar (99.9% REO) YIG powder for this study.

Before consolidation, the powder was low-energy ball milled for 10 h using 7.5 mm YSZ cylinders in a mass ratio of 1 powder: 10 media. Ultra-high purity water was used as a milling

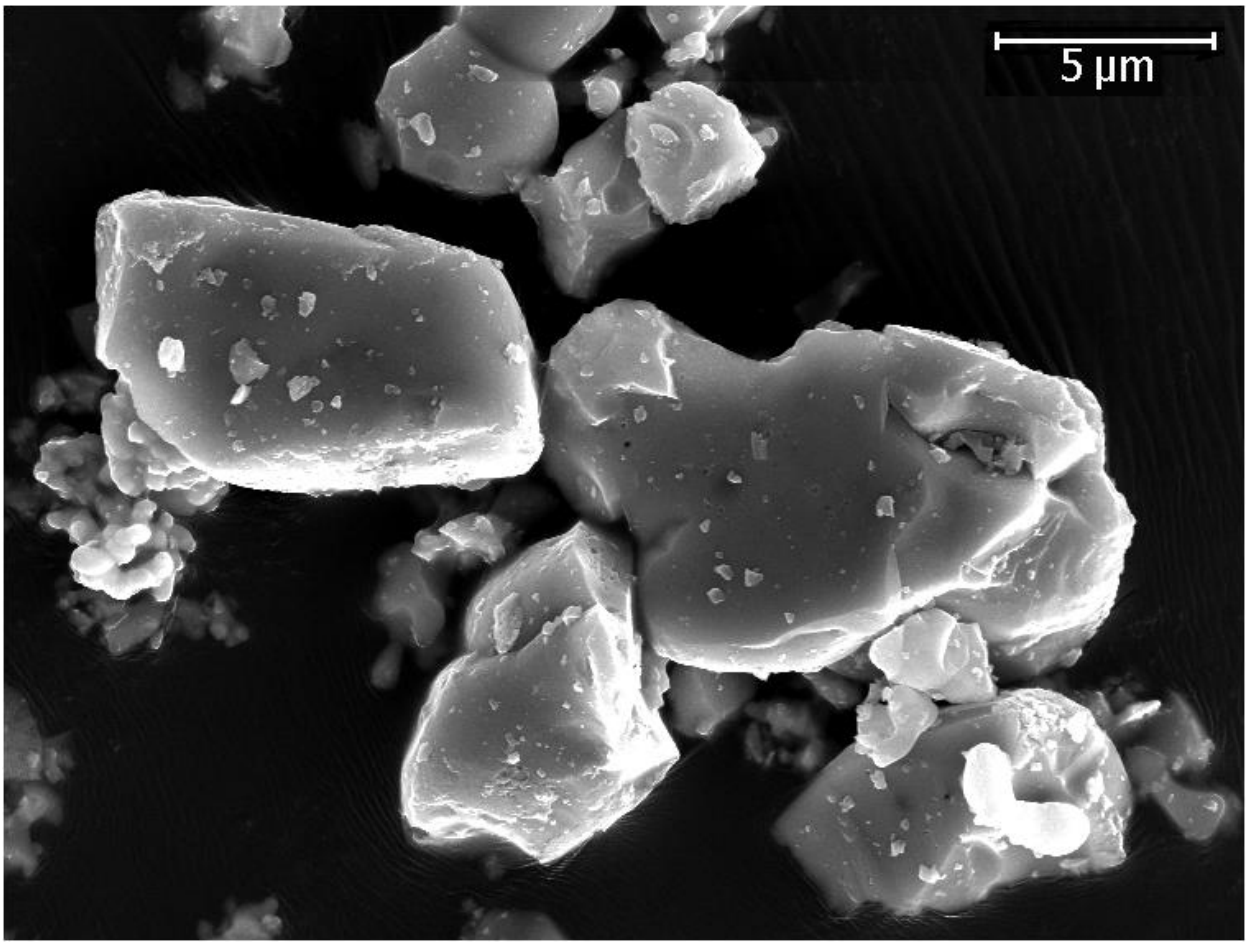

Fig. 3.7: A representative SEM micrograph of the ball milled, sieved and 450°C annealed Alfa Aesar YIG powder prior to CAPAD consolidation.

medium in a mass ratio of 2 powder: 1 H_2O. The milled powder was then centrifuged, dried at 125°C, and then sieved with no. 100 mesh (150 µm). The sieved powder was then briefly annealed at 450°C in air for just 1 minute. A representative SEM micrograph of the as milled, sieved and annealed YIG powder is shown in **Fig. 3.7**. The average grain size of this powder was found to be 2.96 ± 1.74 µm through manually measuring SEM micrographs using ImageJ software. The YIG powder was then consolidated in a 3/8 in. cemented tungsten carbide die setup using CAPAD processing according to the method described in the current-activated, pressure-assisted densification portion of the methods section. Nine separate YIG samples were fabricated at processing temperatures of 600°C, 650°C or 700°C with applied pressures of 100

MPa, 300 MPa or 500 MPa, hold times of 5 minutes, and heating and cooling rates of 100°C/min. Prior to densification, the powder was pre-pressed at the respective processing pressure for each sample for a duration of 10 minutes.

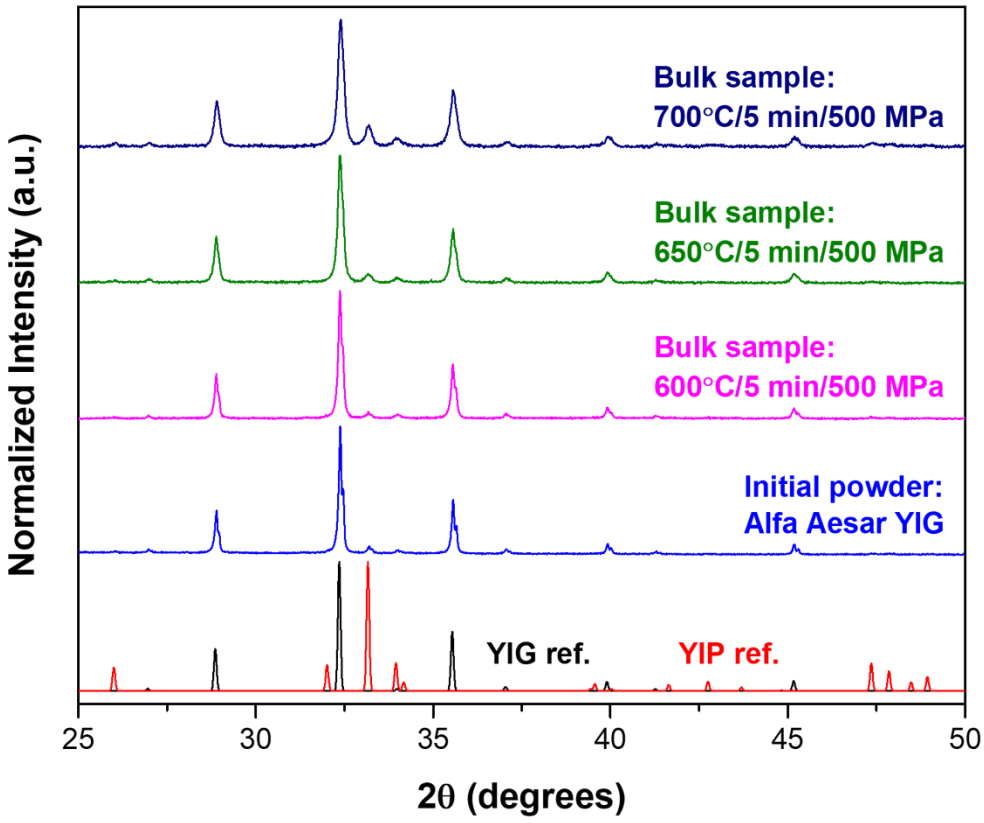

Fig. 3.8: XRD measurements of bulk YIG samples consolidated using CAPAD at an applied pressure of 500 MPa from ball milled, sieved and annealed Alfa Aesar powder. The XRD pattern of the as-processed powder prior to densification is also presented for comparison. Published XRD patterns for the garnet phase (ICSD coll. code 33931) and perovskite phase (ICSD coll. code 258501) are shown at the bottom of the graph for reference.

The structural compositions of the bulk samples and the as-processed Alfa Aesar powder were evaluated with XRD analysis using a PANalytical Empyrean Series 2 diffractometer. The results of the powder XRD measurements for the samples processed at 500 MPa are shown in **Fig. 3.8**. The composition of the sample processed at 600°C and 500 MPa did not change from

the initial powder, which according to XRD is mostly YIG phase with a barely detectable amount of the impurity YIP phase. As the processing temperature of the 500 MPa samples increased, so did the relative amount of YIP phase detected with XRD. The XRD plot reveals one more interesting thing about these samples. Typically for stable materials, as the CAPAD processing temperature of a sample increases the average grain size also increases, and as a result, XRD peaks will tend to narrow. However, these samples exhibit the opposite trend, where the XRD peaks grew broader as the processing temperature increased. This phenomenon is likely caused by phase decomposition of the garnet phase during higher temperature CAPAD processing. A photograph of the three samples processed at 500 MPa is shown in **Fig. 3.9**. The

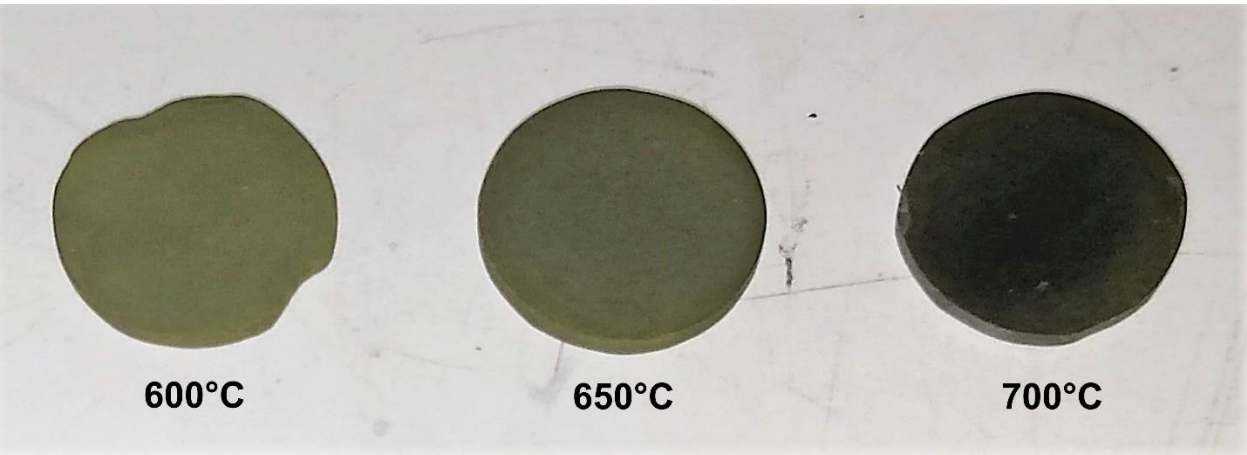

Fig. 3.9: A photograph of the three bulk YIG samples consolidated at an applied pressure of 500 MPa from ball milled, sieved and annealed Alfa Aesar powder at processing temperatures of 600°C, 650°C and 700°C, respectively.

600°C sample is the same bright green color as the initial powder, but the other samples became darker as the processing temperature increased. In contrast to the 600°C sample, the 700°C one is nearly black in appearance. Since these samples retain a mostly garnet phase, this likely means that the darkening is a result of oxygen deficiency caused by the reducing environment of CAPAD at higher temperatures.

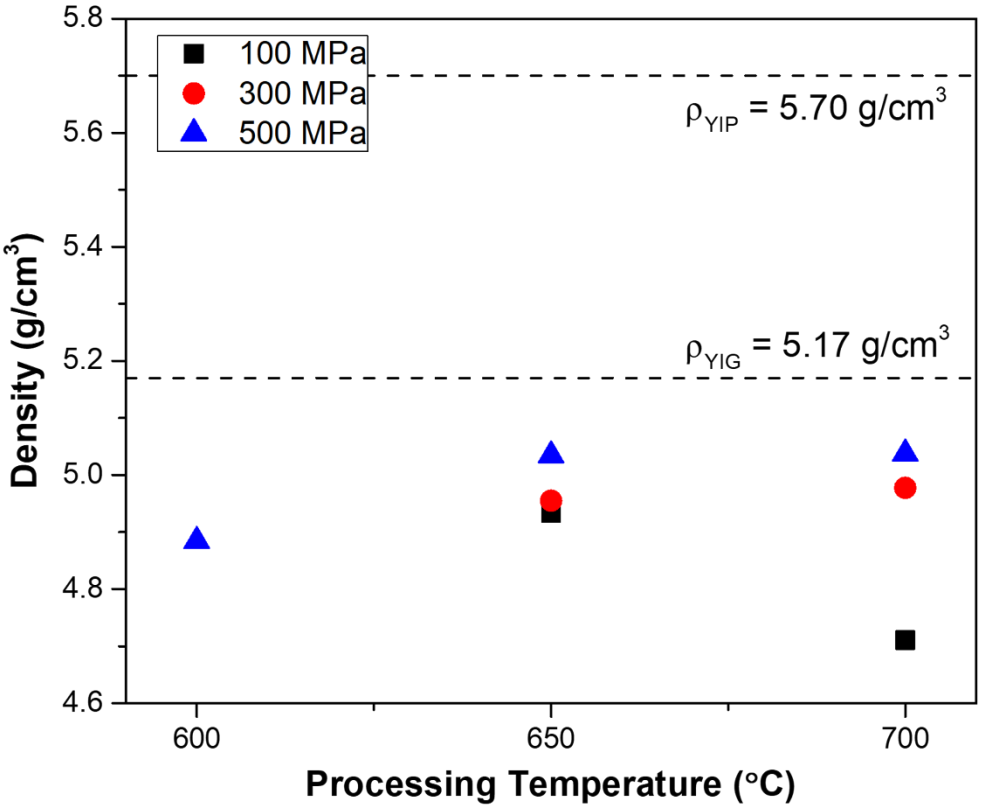

Fig. 3.10: A plot of the measured densities versus processing temperature of the bulk YIG samples consolidated with CAPAD processing from ball milled, sieved and annealed Alfa Aesar powder. The densities of the YIG and YIP phases are plotted as straight lines for reference. The 600°C processed samples attained at pressures of 100 MPa and 300 MPa did not have the handling strength to be measured.

The densities of all CAPAD processed samples were measured using the hydrostatic weighing technique, except for the two that were processed at 600°C for 100 MPa and 300 MPa. The densities of the two samples just mentioned couldn‘t be properly measured because they did not densify at those conditions, and as a result they lacked the necessary handling strength. A plot of the density of the samples versus processing temperature is shown in **Fig. 3.10**. In general, the samples show positive trends between density and processing temperature, and between density and processing pressure, however, the sample processed at 700°C and 100 MPa

is somewhat of an outlier, with a density ~3.5% less than the one processed at 650°C and 100 MPa. It's unclear why this sample doesn't follow the same density trends as the other samples, but it may simply be the case that this sample wasn't prepared as well as the other samples in this study.

The phase compositions of the samples were quantified via the XRD peak area integral ratios between the primary YIP peaks ($2\theta = 33.171°$) and primary YIG peaks ($2\theta = 32.327°$), such that an integral value of 0 represents a fully garnet material according to XRD. For samples containing more perovskite phase, the peaks were deconvoluted and fit with Lorentzians in order to accurately determine the peak areas. For most samples, however, the peaks were sufficiently separated to simply subtract the measurement background and then integrate them. The YIP/YIG integral ratios of all samples in addition to the Alfa Aesar powder are plotted versus processing temperature in **Fig. 3.11**. This plot reveals several key trends about the phases of these samples. First, it shows that all samples processed at 600°C possess the exact same composition as the starting powder, but all samples processed at higher temperatures contain a higher fraction of YIP phase. The plot also reveals positive trends between the relative amount of YIP phase and the processing temperature, and between the relative amount of YIP phase and the processing pressure. It is also interesting to notice that the separation distance between the integral ratios at a fixed temperature increases with the processing temperature, indicating that the decomposition of the garnet phase during CAPAD increases with both the processing temperature and pressure.

This study successfully demonstrated the application of higher pressures to lower the densification temperature of YIG powders using CAPAD. From XRD analysis and density measurements, it was determined that CAPAD processing of YIG at 650°C and 500 MPa for a hold time of five minutes and using a heating rate of 100°C/minute can yield bulk samples in

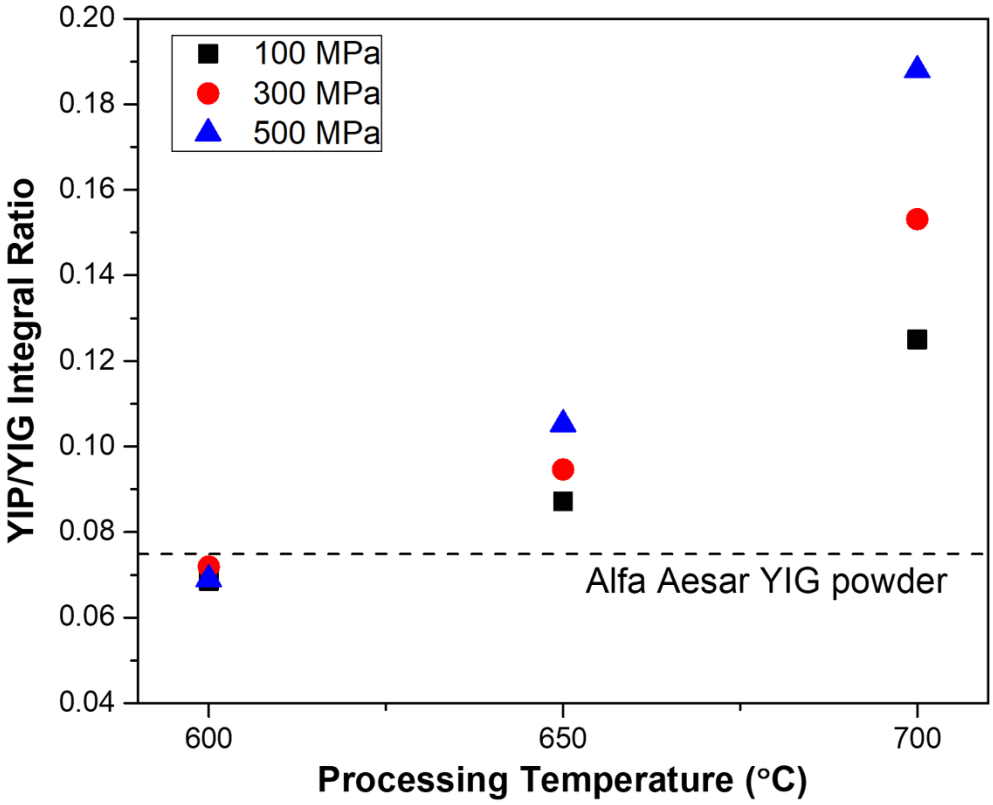

Fig. 3.11: A plot of the XRD peak area integral ratios between the primary YIP and YIG peaks versus processing temperature of the bulk YIG samples consolidated with CAPAD processing from ball milled, sieved and annealed Alfa Aesar powder. The integral ratio of the Alfa Aesar YIG powder is plotted as a straight line for reference.

excess of 95% relative density, while simultaneously not significantly increasing the amount of YIP phase in the resulting sample. This processing temperature is much lower than the 900°C needed to consolidate YIG powders at 100 MPa, and should be beneficial at reducing grain growth during processing. In a somewhat surprising result, XRD analysis of these bulk samples revealed that in addition to higher processing temperatures, higher processing pressures also lead to a higher rate of YIP phase formation during CAPAD processing.

3.4. Synthesis and Consolidation of YIG Powders at 500 MPa

As an extension of the previous two studies on CAPAD processing of YIG, namely the consolidation of YIG powder synthesized via the polymeric-steric entrapment route at 100 MPa and the consolidation of commercial YIG powder at 100-500 MPa, the purpose of this study is to fabricate a dense, single phase and finely structured polycystalline YIG using 500 MPa CAPAD processing of powder synthesized via the polymeric-steric entrapment route. While the latter study determined a lower temperature CAPAD processing condition at 500 MPa that can produce bulk samples in excess of 95% relative density while not significantly increasing the amount of YIP phase, the commercial powder used to make the bulk samples for that study contained a small amount of the impurity YIP phase and had a relatively large average grain size of 2.96 μm. The former study showed, however, that we can synthesize phase pure garnet powder with much finer features than the commercially available powder using the polymeric-steric entrapment method. Therefore, we chose to use our in-house synthesized powder as the starting material from which to fabricate dense, single-phase, finely structured bulk YIG.

In previous attempts to synthesize phase pure YIG powders using the polymeric-steric entrapment technique, a small portion of the intermediary YIP phase persisted in the heat-treated powders until high calcining temperatures were used. The XRD plot of the synthesized powders calcined at different conditions in **Fig. 3.3** shows that a calcining temperature of 1300°C was required in order for no YIP phase to be detected by XRD. Even after calcining at 1200°C, the primary YIP peak is still barely visible to XRD. This means that the powder must be heat treated at high temperatures in order to remove any intermediary phases and form phase-pure powder, which has the unintended consequence of coarsening the powder and growing its grains. To mitigate this effect, we decided to further refine the as-synthesized powder through water

quenching and subsequent ball-milling. The purpose of the water-quenching is two-fold. First, the quenching will rapidly lower the temperature of the powder, thus decreasing the amount of time it spends at elevated temperatures at which grain growth occurs more rapidly. The second reason is that stresses resulting from the rapid thermal contraction experienced by the powder as it is submerged in water should enhance its ability to break down using ball-milling.

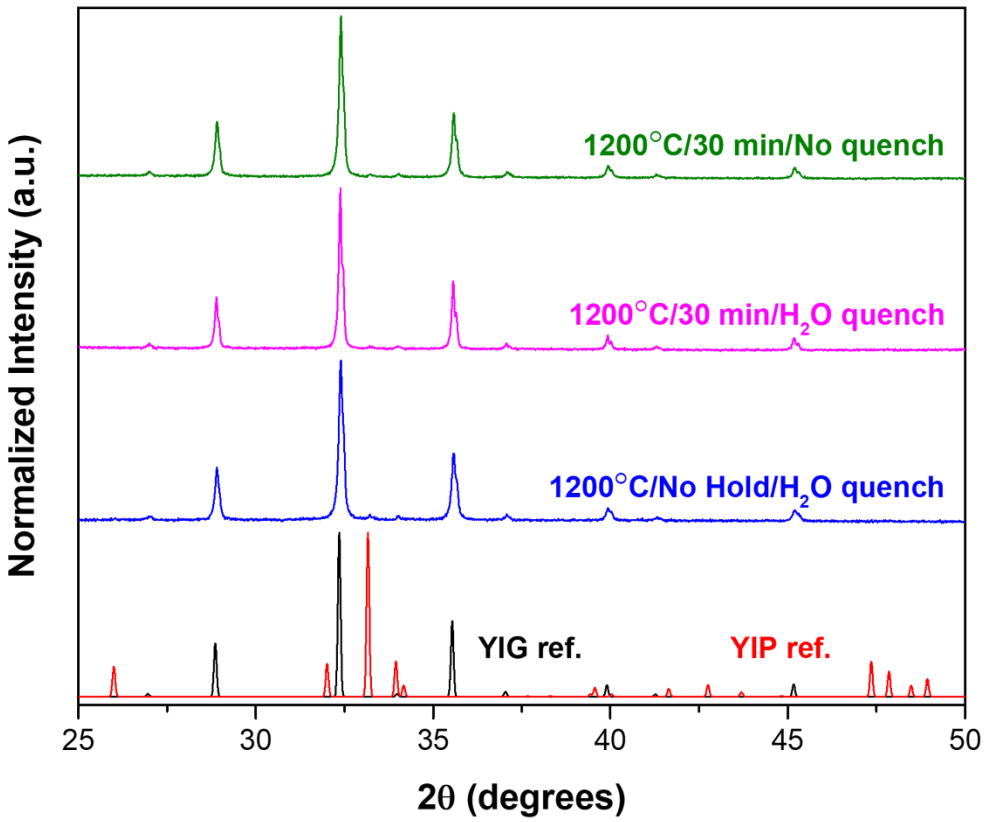

Fig. 3.12: XRD measurements of YIG powder synthesized via the polymeric-steric entrapment technique and given different heat treatments with a calcining temperature of 1200°C. Published XRD patterns for the garnet phase (ICSD coll. code 33931) and perovskite phase (ICSD coll. code 258501) are shown at the bottom of the graph for reference.

Powders calcined at temperatures ranging from 800-1300°C underwent water quenching and XRD analysis. The structural compositions of the powders heat treated at different conditions were evaluated with XRD analysis using a PANalytical Empyrean Series 2

diffractometer. It was experimentally determined from the XRD results that powder that had been heated to 1200°C and then immediately poured into room temperature water yielded nearly phase pure powder. An XRD plot containing powders with three different heat treatments at a calcining temperature of 1200°C is shown in **Fig. 3.12**. The three XRD patterns presented are nearly identical, and the primary YIP peak at $2\theta = 33.171°$ remained very small and did not noticeably change in intensity for any of the three powders. The XRD pattern from the powder that had no hold time and was water quenched has noticeably wider diffraction peaks than the other two powder samples. The wider peaks are an indication of lower crystallinity, which is likely due to smaller grain sizes or residual stresses resulting from the quenching process. SEM micrographs of the YIG powder that was heat treated to 1200°C and immediately water quenched are shown in **Fig. 3.13**. The micrographs show sintered, polycrystalline ceramics with open porosity and a uniform grain size distribution with an average size of approximately 600 nm.

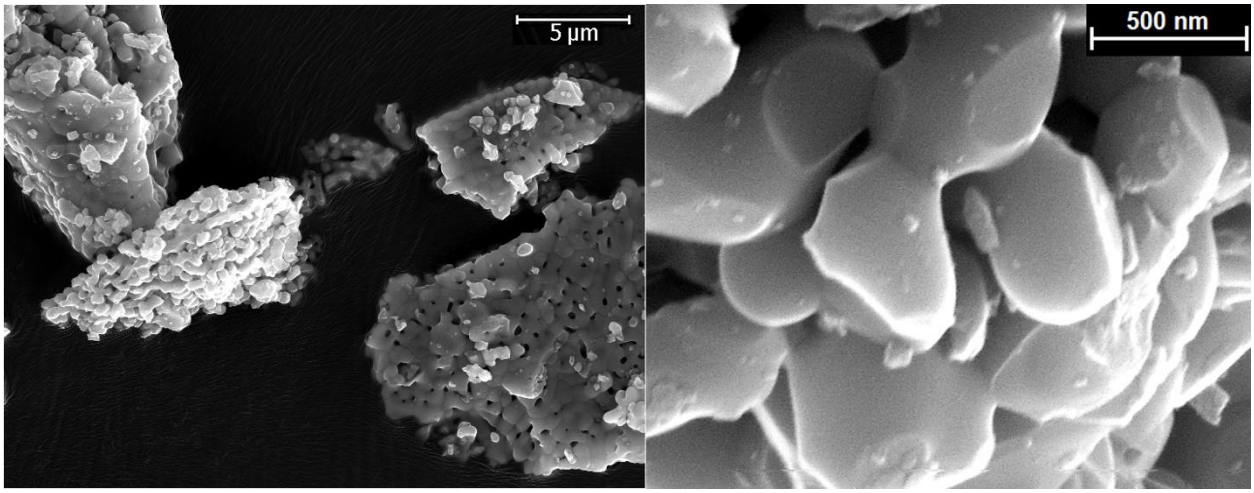

Fig. 3.13: SEM micrographs of the YIG powder synthesized via the polymeric-steric entrapment route that was heat treated to 1200°C in air for no hold time and immediately water quenched.

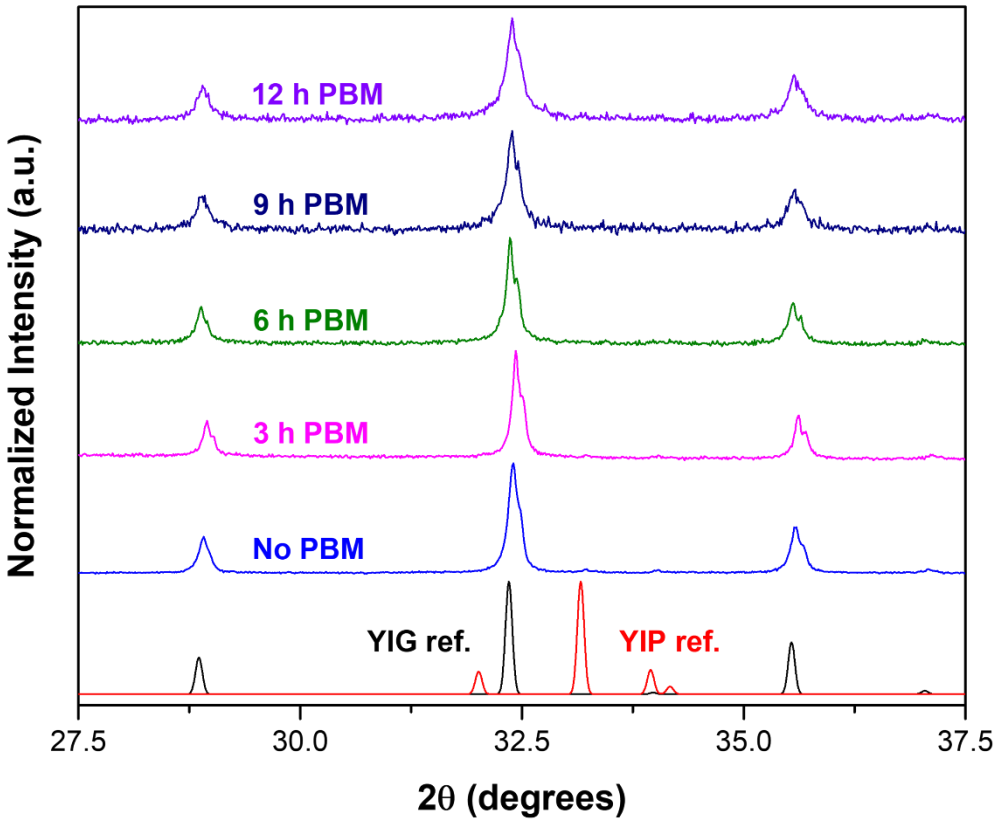

Fig. 3.14: XRD measurements of the YIG powder synthesized via the polymeric-steric entrapment route that was heat treated to 1200°C in air for no hold time, water quenched and then planetary ball-milled for different lengths of time. Published XRD patterns for the garnet phase (ICSD coll. code 33931) and perovskite phase (ICSD coll. code 258501) are shown at the bottom of the graph for reference.

The water quenched YIG powder was then refined with planetary ball-milling. It was milled in stainless steel jars using spherical 5 mm Si_3N_4 media with a mass ratio of 20 media: 1 powder, and ultra-high purity water as a medium with a mass ratio of 2 H_2O: 1 powder. The powder was milled at 200 rpm for 12 hours, with small powder samples for XRD analysis being collected every 3 hours. XRD patterns of the planetary ball-milled YIG powders are shown in **Fig. 3.14**. The intensities and positions of the XRD peaks remain consistent across the samples with different milling times, although the peaks become broader as the milling time was increased. As previously mentioned, wider peaks are an indication of lower crystallinity, which

can be a consequence of smaller grain sizes or residual stresses resulting from the milling process. Fortunately, the milling process did not cause the formation of more perovskite phase, as has been reported in the case of higher energy ball-milling of YIG powders.[9-11] SEM micrographs of the water quenched YIG powders after ball-milling are shown in **Fig. 3.15**. It can be seen from these images that the ball-milling process did indeed separate the grains from each other and refine the grain size of the powder.

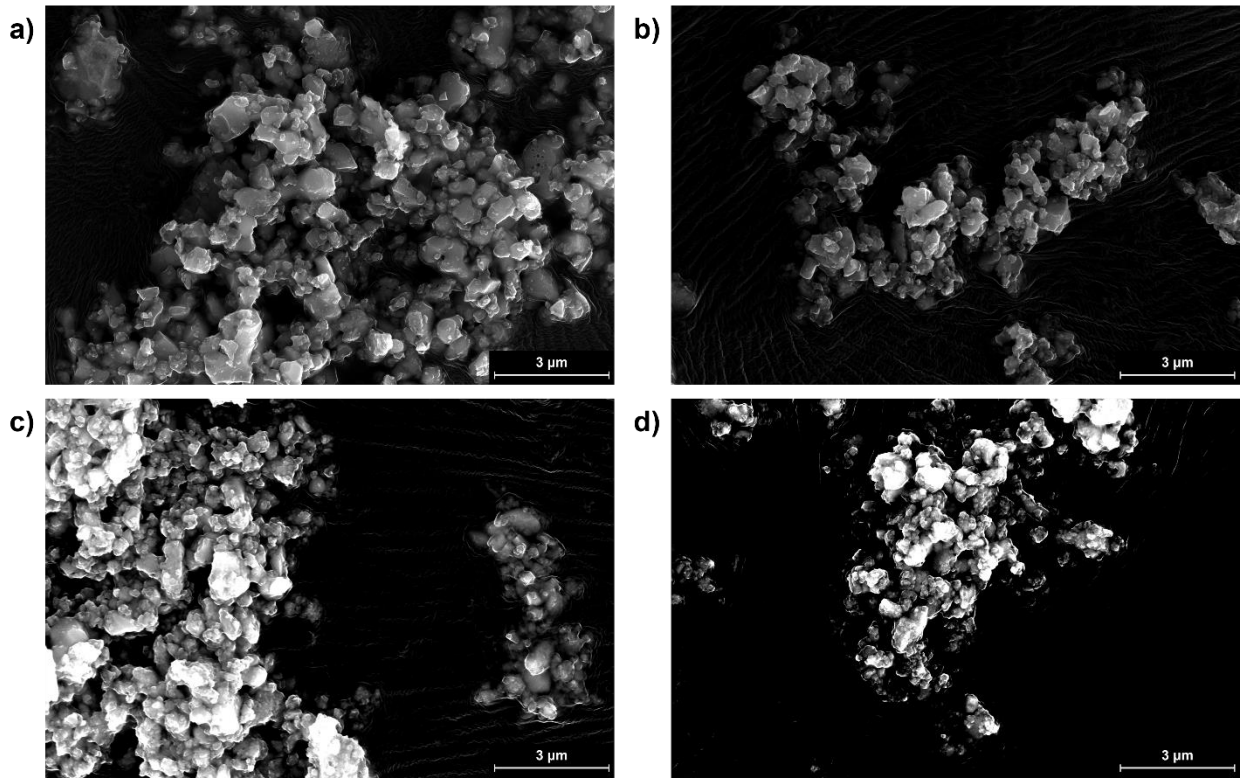

Fig. 3.15: SEM micrographs of the YIG powder synthesized via the polymeric-steric entrapment route that was heat treated to 1200°C in air, immediately water quenched and then planetary ball-milled for a) 3 hours, b) 6 hours, c) 9 hours and d) 12 hours.

After 12 hours of ball-milling, the powder was centrifuged and dried at 125°C. The as-processed powder was then consolidated in a 3/8 in. cemented tungsten carbide die setup using CAPAD processing according to the method described in the current-activated, pressure-assisted densification portion of the methods section. It was processed at 650°C and 500 MPa for a hold time of five minutes and using a heating rate of 100°C/minute. Prior to consolidation, the powder

was pre-pressed at 500 MPa for a duration of 10 minutes. XRD measurements of the bulk sample in comparison to the YIG powder at various stages in its processing are plotted in **Fig. 3.16**. The XRD pattern of the bulk sample contains only peaks attributable to garnet, and interestingly, the XRD peaks are broader for the bulk sample than for the 12 hour planetary ball-milled powder it was fabricated from. Although XRD of the bulk sample shows no detectable perovskite phase, the bulk sample that was CAPAD processed from commercial YIG powder at the exact same conditions did show decomposition into the YIP phase accompanied with the broadening of the diffraction peaks. For these reasons, it seems likely that the peak broadening observed in this

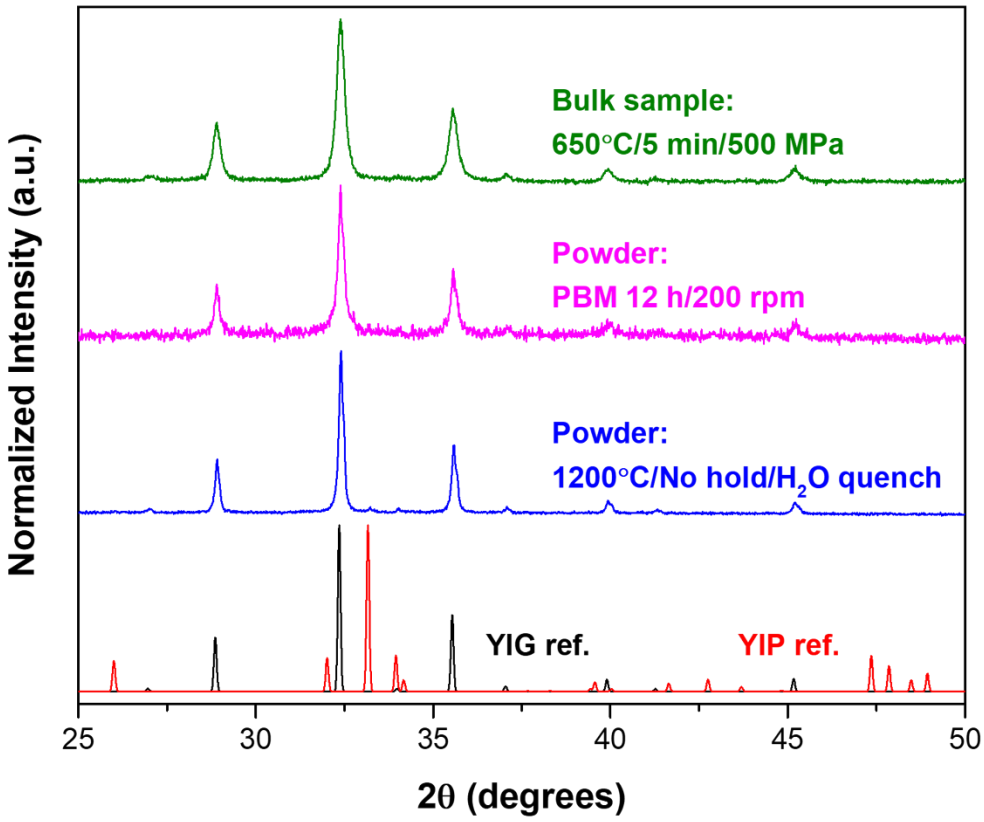

Fig. 3.16: XRD measurements of the 500 MPa CAPAD processed bulk sample produced from water quenched and 12 hour ball-milled YIG powder synthesized via the polymeric-steric entrapment route and the initial powder before and after ball-milling. Published XRD patterns for the garnet phase (ICSD coll. code 33931) and perovskite phase (ICSD coll. code 258501) are shown at the bottom of the graph for reference.

sample is also due to a small amount of phase decomposition that occurred during processing, even though there is not enough YIP phase in this sample to be detectable with XRD.

The density of the bulk sample was measured to be 4.76 g/cm^3 using the hydrostatic weighing technique, which gives a relative density of 92%. An SEM micrograph of a fractured surface from this sample is shown in **Fig. 3.17**. This image shows many nanosized features, but the grains in this sample are not monodispersed. The structure of the sample can be described as larger grains on the order of a few hundred nanometers embedded in a matrix of sub-100 nm grains. The volumetric portions of the two different sized groups of grains appear to be roughly comparable. The magnetic hysteresis of this sample and the initial powder were both measured

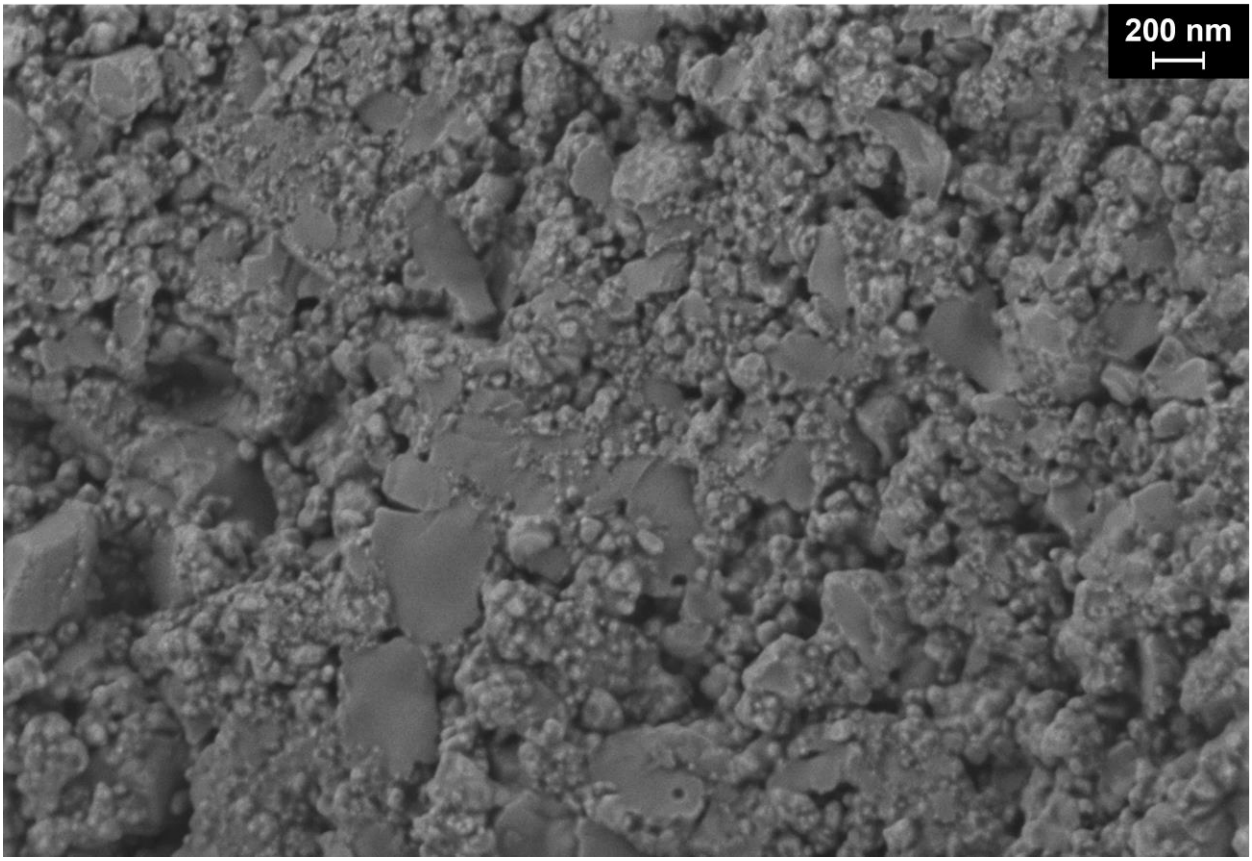

Fig. 3.17: An SEM micrograph of a fractured surface of the bulk YIG sample consolidated with CAPAD at 650°C and 500 MPa from the water quenched and ball-milled powders synthesized via the polymeric-steric entrapment route.

using a Lakeshore 7400 Series VSM. The VSM data was mass normalized and plotted in **Fig. 3.18**. The magnetic behavior of the bulk sample is nearly identical to the initial powder, but the bulk sample has a slightly lower M_S and a slightly higher coercivity. A summary of the magnetic and physical properties of the samples is provided in **Table 3.1**.

In this study we were able to successfully fabricate a bulk, single phase YIG ceramic with a fine microstructure and high density by refining YIG powder synthesized via the polymeric-steric entrapment route using a combination of water quenching and planetary ball-milling and subsequently subjecting it to CAPAD processing at 500 MPa. The composition of the resulting sample was confirmed to be single phase garnet by using XRD, and its magnetic properties were

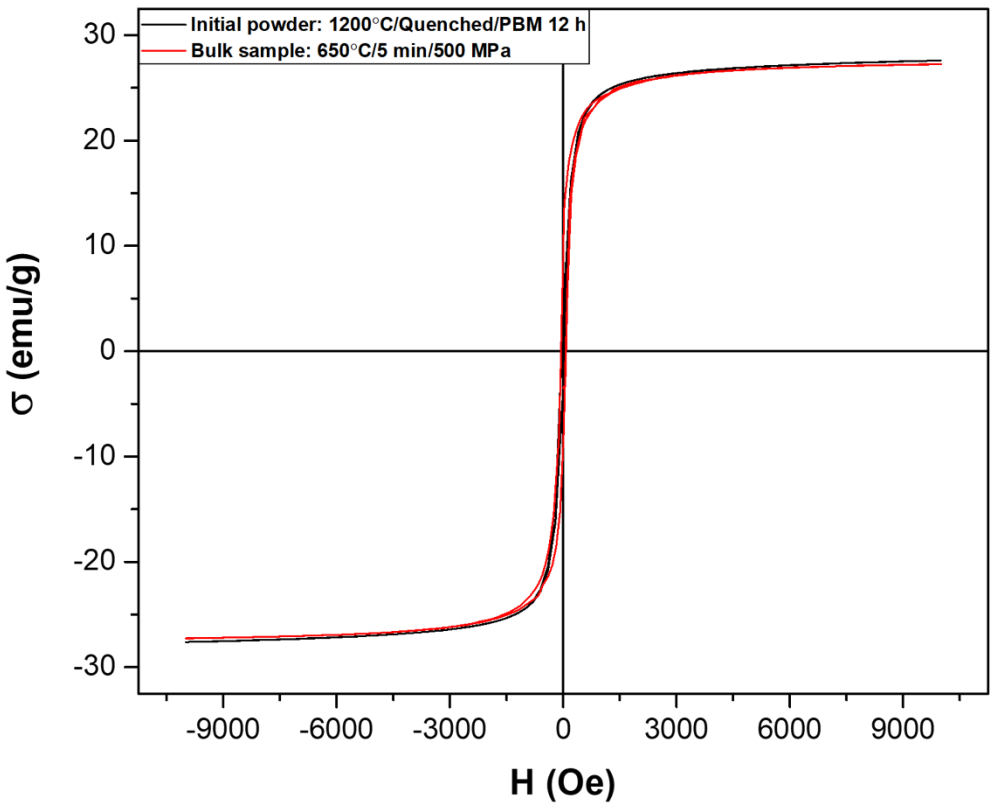

Fig. 3.18: Magnetic hysteresis measurements of the water quenched and ball-milled YIG powder synthesized via the polymeric-steric entrapment route and the bulk sample fabricated from this powder using CAPAD processing at 650°C and 500 MPa.

confirmed to be very similar to other YIG materials by using VSM. The structure of the sample was evaluated with SEM analysis of a fractured surface and the average grain size of the resulting sample is below 100 nm, but this value does not fully approximate its microstructure. The sample's grains are not monodispersed and it has several grains with sizes of approximately 300-400 nm which don't appear to have been fully broken down by the planetary ball-milling. It is possible that a longer milling time could better refine the initial powder, thus enhancing its densifiability and yielding bulk samples with a more homogeneous microstructure.

3.5. Reactive Consolidation of Bulk YIG from an Amorphous Precursor

The goal of this study is to fabricate a bulk, nanostructured YIG ceramic through the reactive consolidation of an amorphous precursor using CAPAD processing. Reactive processing has already been demonstrated as an effective way to reduce the densification temperature needed for the CAPAD processing of dense garnets when compared to the consolidation of pre-reacted powders.[2,12] Because of the enhanced atomic rearrangement that happens during a chemical reaction in addition to the particle rearrangement that occurs during CAPAD processing, reactive processing can lead to samples with relative densities over 98%, and because of the lower temperatures involved with this technique, smaller average grain sizes are also possible. The powder we chose to use as the starting material for the reactive consolidation of YIG is a fully amorphous YIG precursor synthesized via the polymeric-steric entrapment route.

To attain a fully amorphous powder, the as-synthesized metal-organic preceramic powder was calcined at 600°C in air for 30 minutes. It was known from the XRD patterns of powders attained from previous calcining experiments that a calcining temperature of 700°C or lower would yield amorphous powder, as clearly evident in **Fig. 3.3**. It was additionally known from

the TGA-DSC measurements performed on the metal-organic precursor that the majority of all organic material burns off by the time the powder reaches 550°C, as shown in **Fig. 3.2**. An SEM micrograph of the powder calcined at 600°C is shown in **Fig. 3.19**. The image shows irregular submicron powder with nanometric features and no clear grains, which is consistent with an amorphous material.

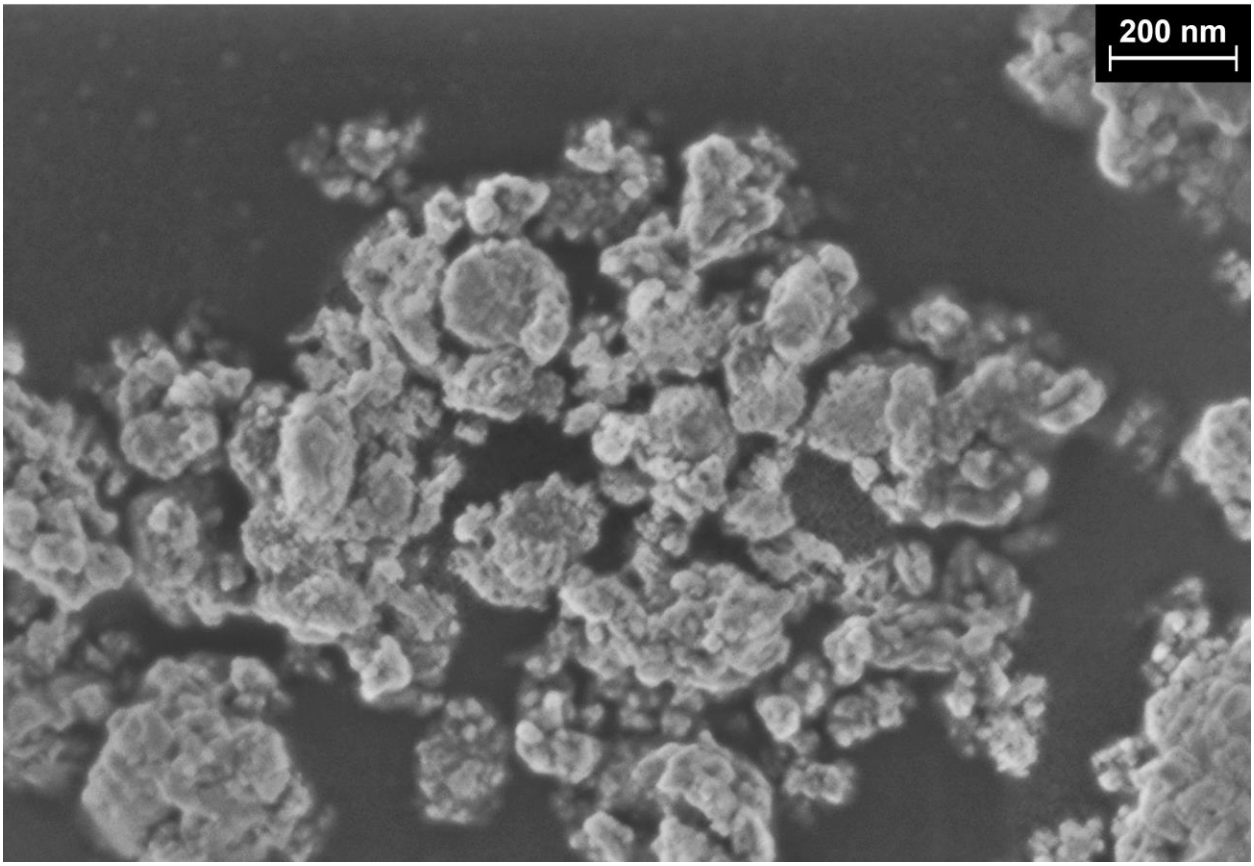

Fig. 3.19: An SEM micrograph of the amorphous YIG precursor synthesized via the polymeric-steric entrapment route and calcined in air at 600°C for 30 minutes.

The calcined amorphous powder was then refined using planetary ball-milling to break down any larger particles or agglomerates and enhance its densifiability. It was milled in stainless steel jars using spherical 5 mm Si_3N_4 media with a mass ratio of 20 media: 1 powder, and ultra-high purity water as a medium with a mass ratio of 2 H_2O: 1 powder. The amorphous powder was milled at 200 rpm for 6 hours, and then centrifuged and dried at 125°C. Similar

milling parameters were previously used to refine fully garnet powder, and in that instance, the milling process was shown through XRD analysis to not introduce any unwanted phases. Therefore, we assumed that these parameters would be low enough energy to not fully crystallize the powder.

The as-processed powder was then consolidated in a 3/8 in. cemented tungsten carbide die setup using CAPAD processing according to the method described in the current-activated, pressure-assisted densification portion of the methods section. Three samples were fabricated at 100 MPa, 300 MPa, and 500 MPa, respectively. They were each processed at 700°C for a hold

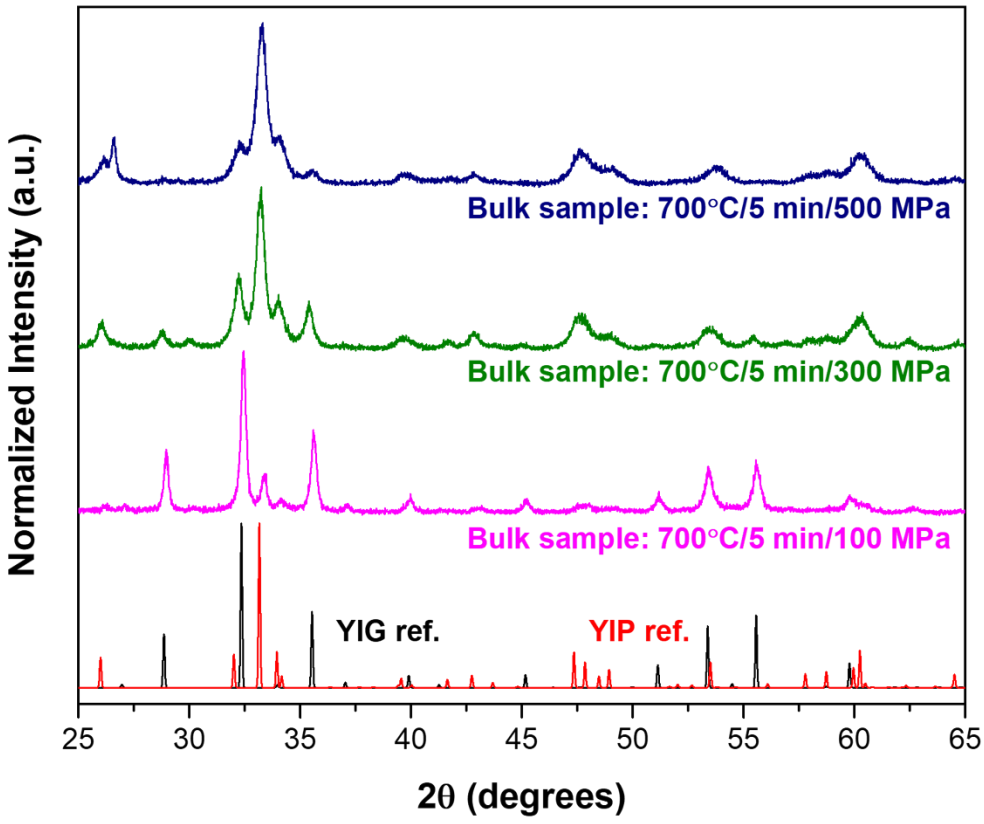

Fig. 3.20: XRD measurements of the CAPAD processed bulk samples fabricated from ball-milled amorphous YIG precursor synthesized via the polymeric-steric entrapment route. Published XRD patterns for the garnet phase (ICSD coll. code 33931) and perovskite phase (ICSD coll. code 258501) are shown at the bottom of the graph for reference.

time of five minutes and using a heating rate of 100°C/minute. Prior to consolidation, the powder was pre-pressed at 500 MPa for a duration of 10 minutes. The structural compositions of the bulk samples were evaluated with XRD analysis using a PANalytical Empyrean Series 2 diffractometer. XRD patterns of the three samples are shown in **Fig. 3.20**. The plot shows that the sample processed at 100 MPa is mostly garnet phase, but as the processing pressure increased, more YIP phase resulted. The sample processed at 500 MPa is mostly perovskite phase, with very little YIG phase detectable to XRD, seeming to indicate that the YIP phase is preferred at higher pressure processing conditions over YIG. Smaller peaks not attributed to these two phases are visible in the diffraction patterns of these samples, but they aren't well associated with specific phases from the Y-Fe-O ternary system.

Due to both the small size of these samples (~0.3 g) and the limited sensitivity of the CAPAD apparatus, it is difficult to locate the exact point at which the powder crystallized. However, by removing the compliance of the entire CAPAD apparatus itself from the vertical extension length of a sample as it was being processed, any changes to a sample's thickness as it was being processed could be determined. By taking the derivative of this value, a change in densification rate could then be found in the densification curves of all three samples at ~610°C. There was also a sharp spike in outgassing detected by the system's vacuum sensor at ~630°C. Both pieces of information seem to indicate that the powder began crystallizing at ~610°C. Due to both noise and experimental error, it is difficult to say with certainty whether the processing pressure had any influence on the crystallization temperature.

The densities of the samples were measured using the hydrostatic weighing technique. Since the samples all have a mixed phase composition, it is difficult to ascertain their exact level of porosity, however, the two samples processed at 300 MPa and 500 MPa appear to have a

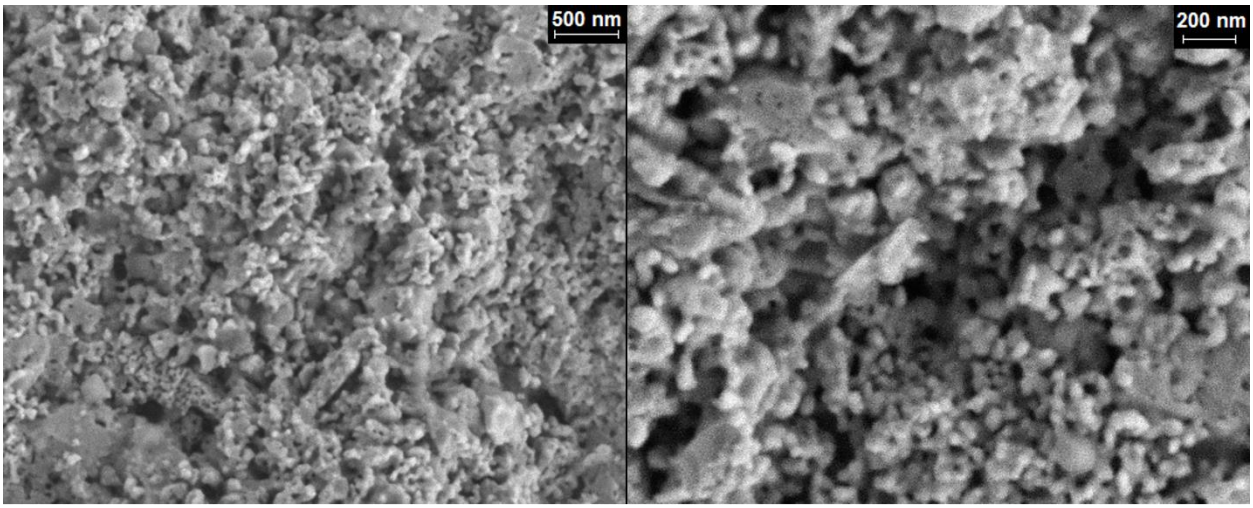

Fig. 3.21: SEM micrographs taken of a fractured surface of the bulk YIG sample that was reactively consolidated using CAPAD processing at 100 MPa from an amorphous powder synthesized via the polymeric-steric entrapment route.

relative density of at least 90%, and the sample processed at 100 MPa could be better approximated to ~77%. An SEM micrograph of a fractured surface of the sample processed at 100 MPa is shown in **Fig. 3.21**. The image shows a slightly porous microstructure with sub-100 nm grains. The average grain size of this sample was found to be 62.3 ± 13.9 nm through manually measuring SEM micrographs using ImageJ software. The magnetic hysteresis loops of the three samples were measured using a Lakeshore 7400 Series VSM. The VSM data was mass normalized and plotted in **Fig. 3.22**. The sample produced at 100 MPa has a similar shaped hysteresis to YIG, albeit with a slightly larger coercivity and an M_S of 22.1 emu/g, which is about 20% lower than what is typically measured for YIG. The sample processed at 300 MPa has an even higher coercivity and lower M_S value, and the hysteresis is wasp-waisted, indicating that it has two distinct magnetic phases. The 500 MPa processed sample, however, has very weak magnetism, with an M_S of just 1.80 emu/g. A summary of the magnetic and physical properties of the samples is provided in **Table 3.1**.

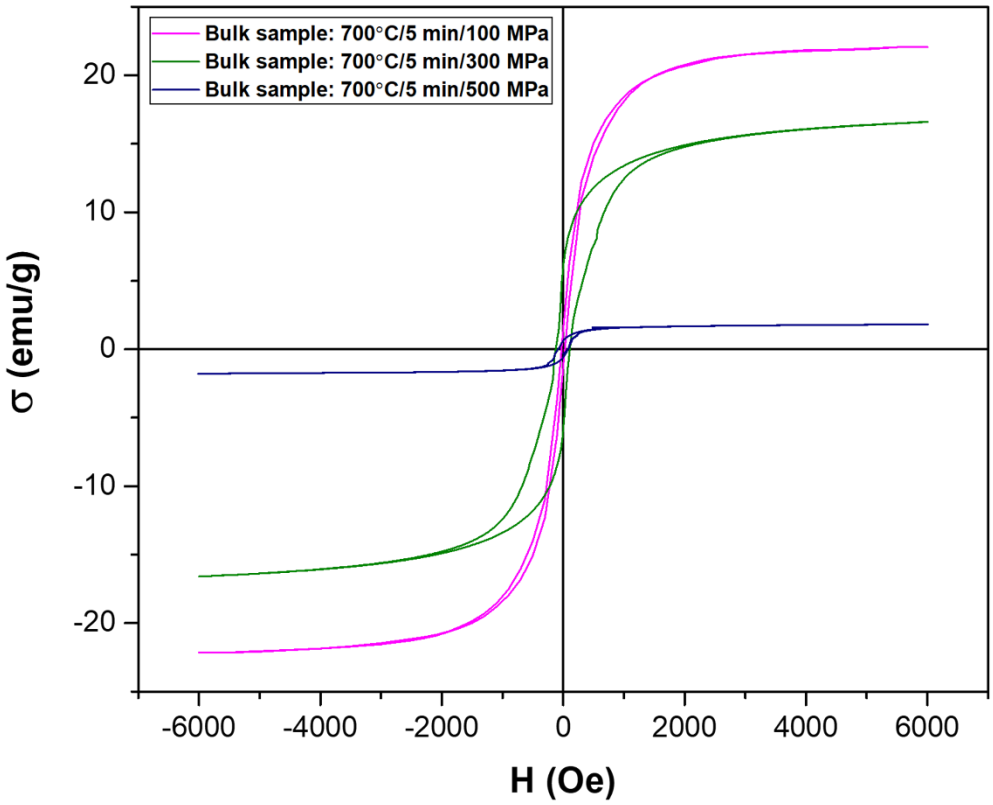

Fig. 3.22: Magnetic hysteresis measurements of the bulk samples that were reactively consolidated using CAPAD processing at 700°C and different applied pressures from an amorphous YIG precursor synthesized via the polymeric-steric entrapment route.

We successfully fabricated a nanostructured YIG ceramic through the reactive consolidation of an amorphous precursor using CAPAD processing for this study. The best sample produced using this method was consolidated at 700°C with an applied pressure of 100 MPa and had an average grain size of 62 nm and a relative density of ~77%. XRD characterization of this sample showed that in addition to the garnet phase, it also contains the impurity perovskite phase. VSM characterization revealed that because of its secondary phase, its M_S was 20% lower than for other YIG ceramics. The samples processed at 700°C with applied pressures of 300 MPa and 500 MPa had a significantly higher phase fraction of YIP that

also increased with pressure, suggesting that the YIP phase is preferred at higher pressure processing conditions over YIG.

Table 3.1: A summary of the magnetic and physical properties of the various powder and bulk YIG specimens investigated for the study on the CAPAD processing of YIG.

Section	Sample	Phase	M_S (emu/g)	M_R (emu/g)	H_C (Oe)	ρ (g/cm^3)	Ave. grain size (nm)
3.2	Starting powder: 900°C/30 min	YIG, YIP	26.5	0.72	9.9	--	--
3.2	Bulk sample: 900°C/5 min/100 MPa	YIG, YIP	23.5	1.46	22.0	4.87 (~93%)	~300 - 400
3.2	Bulk sample: 1000°C/5 min/100 MPa	YIP, YIG	17.2	0.75	51.6	5.50 (90-95%)	--
3.3	Alfa Aesar Powder	YIG, YIP	27.4	1.40	18.0	--	2960 ± 1740
3.4	Starting powder: 1200°C/Quenched/PBM	YIG	27.6	3.52	39.1	--	--
3.4	Bulk sample: 650°C/5 min/500 MPa	YIG	27.3	9.03	63.4	4.76 (92%)	< ~100
3.5	Bulk sample: 700°C/5 min/100 MPa	YIG, YIP	22.1	1.59	27.3	4.05 (~77%)	62.3 ± 13.9
3.5	Bulk sample: 700°C/5 min/300 MPa	YIP, YIG	16.6	5.96	115.9	5.17 (90 - 95%)	--
3.5	Bulk sample: 700°C/5 min/500 MPa	YIP, YIG	1.80	0.63	80.9	5.30 (90 - 95%)	--

3.6. Conclusions

While CAPAD has proven effective at producing other types of nanoceramics, it proves to be a challenging method of fabricating a highly dense, nanostructured YIG. Most attempts we made to produce a bulk YIG using CAPAD processing resulted in a composite of YIG and YIP. All of the gathered evidence seems to indicate that the transformation from YIG into YIP is closely related to the reducing environment of CAPAD processing. It is an unsurprising result that the YIG phase is unstable in this type of environment. It is well documented that ferrites are reduced by CAPAD processing through the formation of oxygen vacancies [3-5], and YIG is a ferrite.

This work shows that longer hold times and higher processing temperatures during the CAPAD processing of YIG results in more conversion into the perovskite phase, as evidenced by XRD measurements and the visual color appearance of the sample. A CAPAD processed sample with a high phase fraction of YIP can be fully converted back to garnet with a high temperature heat treatment in air and its color will become green again, as the XRD results in **Fig. 3.23** show. The difficulty arises from the fact that the high temperature heat treatment coarsens the grains of the sample, such that they cannot remain nanosized.

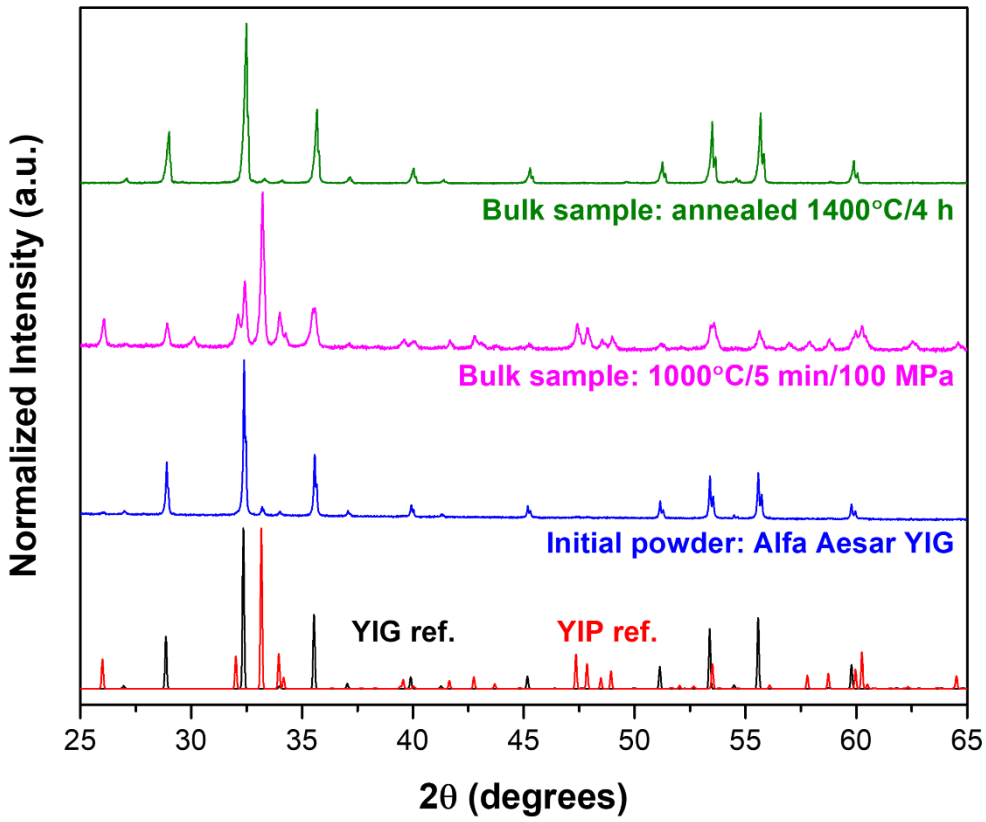

Fig. 3.23: XRD measurements of a bulk sample as it emerged from CAPAD processing in a 3/4 in. graphite die (magenta) and after it was heat treated in air at high temperature (green) in comparison to the initial powder the sample was consolidated from (blue). Data was provided by P. Sellappan. Published XRD patterns for the garnet phase (ICSD coll. code 33931) and perovskite phase (ICSD coll. code 258501) are shown at the bottom of the graph for reference.

Another finding from our work is that when YIG decomposed into YIP during CAPAD processing, no additional phases could be found with XRD analysis. This is an unexpected result because YIG ($Y_3Fe_5O_{12}$) and YIP ($YFeO_3$) are both line compounds and have dissimilar cation ratios, meaning that there should also be additional iron oxide phases present in order to maintain the same overall stoichiometry of YIG. It is possible that the phase decomposition YIG experiences during CAPAD processing converts it into an oxygen deficient, disordered perovskite. Previous reports of high pressure experiments on YIG have shown that it's possible to convert stoichiometric YIG into a disordered perovskite phase with the formula $(Y_{0.75}Fe_{0.25})FeO_3$ with the application of enough heat and pressure.[13]

Despite not being able to produce a highly dense, pristine, single-phase garnet nanoceramic for spin transport measurements, our work yielded many other interesting results. As far as I'm aware, we are the first to consolidate YIG ceramics using high pressure CAPAD processing conditions of up to 500 MPa. The use of high pressures allowed us to consolidate micron sized commercial YIG powder at lower temperatures, with much less phase decomposition than is possible when using more typical pressures of 100 MPa or less. Using those same high pressure processing parameters, we were then able to fabricate a nanofeatured single-phase bulk YIG with a relative density of 92% from in-house synthesized powders. This sample is unique in the fact that it was the first CAPAD processed YIG sample to be consolidated at 650°C and without any decomposition into the perovskite phase as detectable by XRD. This sample also has high enough density and small enough features to be used as a high-quality PLD or sputtering target.

We then applied the use of high pressure to reactively consolidate YIG ceramics from an in-house synthesized amorphous precursor using CAPAD. In this instance, however, the use of

high pressures was detrimental to the formation of the garnet phase in the resulting ceramic. More perovskite phase formed from the amorphous precursor as the processing pressure increased. A similar finding was already seen in the YIG ceramics we consolidated at high pressure from micron sized commercial YIG powders, but to a much lesser extent. This suggests that the YIP phase is more favorable than YIG at high pressure CAPAD processing conditions.

Using the more traditional 100 MPa processing pressure, we were then able to reactively consolidate a nanostructured YIG ceramic with an average grain size of 62 nm and a relative density of ~77%. To date, this sample has the smallest reported grain size for a bulk YIG ceramic. While the density of this sample is ultimately not very high, it is likely dense enough to produce high-quality films when used as a target. Another remarkable feature of this sample is its highly uniform nanoporous structure. Overall, the use of high pressures during the CAPAD processing of YIG is a unique contribution of this work. The high processing pressures proved beneficial at mitigating the phase decomposition of fully reacted garnet powders, but then led to more YIP formation when reactively consolidating amorphous precursor powders.

Acknowledgements

Chapter 3 contains unpublished material. The dissertation author was the primary researcher and author of this chapter. Pathikumar Sellappan provided the data used to make **Fig. 3.23**.

REFERENCES

[1] S. R. Boona, and J. P. Heremans. Magnon thermal mean free path in yttrium iron garnet. Phys. Rev. B 90 (2014) 064421.

[2] T. Gaudisson, U. Acevedo, S. Nowak, N. Yaacoub, J.-M. Greneche, S. Ammar, and R. Valenzuela. Combining Soft Chemistry and Spark Plasma Sintering to Produce Highly Dense and Finely Grained Soft Ferrimagnetic $Y_3Fe_5O_{12}$ (YIG) Ceramics. J. Am. Ceram. Soc. 96 (2013) 3094-3099.

[3] J. R. Morales, S. Tanju, W. P. Bayermann, and J. E. Garay. Exchange bias in large three dimensional iron oxide nanocomposites. Appl. Phys. Lett. 96 (2010) 013102.

[4] A. D. Volodchenkov, Y. Kodera, and J. E. Garay. Synthesis of strontium ferrite/iron oxide exchange coupled nano-powders with improved energy product for rare earth free permanent magnet applications. J. Mater. Chem. C 4 (2016) 5593-5601.

[5] D. Giuntini, E. Torresani, K. T. Chan, M. Blankenburg, L. Saviot, B. Bor, B. Domènech, M. Shachar, M. Müller, E. A. Olevsky, J. E. Garay, and G. A. Schneider. Iron oxide-based nanostructured ceramics with tailored magnetic and mechanical properties: development of mechanically robust, bulk superparamagnetic materials. Nanoscale Adv. 1 (2019) 3139-3150.

[6] H. Shen, J. Xu, A. Wu, J. Zhao, and M. Shi. Magnetic and thermal properties of perovskite $YFeO_3$ single crystals. Mater. Sci. Eng. B 157 (2009) 77-80.

[7] Y. Kodera, C. L. Hardin, and J. E. Garay. Transmitting, emitting and controlling light: Processing of transparent ceramics using current-activated pressure-assisted densification. Scr. Mater. 69 (2013) 149-154.

[8] U. Anselmi-Tamburini, J. E. Garay, and Z. A. Munir. Fast low-temperature consolidation of bulk nanometric ceramic materials. Scr. Mater. 54 (2006) 823-828.

[9] H. M. Widatallah, C. Johnson, S. H. Al-Harthi, A. M. Gismelseed, A. D. Al-Rawas, S. J. Stewart, M. E. Elzain, I. A. Al-Omari, and A. A. Yousif. A structural and Mössbauer study of $Y_3Fe_5O_{12}$ nanoparticles prepared with high energy ball milling and subsequent sintering. Hyperfine Interact. 183 (2008) 87-92.

[10] C. V. Stan, J. Wang, I. S. Zouboulis, V. Prakapenka, and T. S. Duffy. High-pressure phase transition in $Y_3Fe_5O_{12}$. J. Phys. Condens. Matter. 27 (2015) 405401.

[11] F. Sanchez-De Jesús, C. A. Cortés, R. Valenzuela, S. Ammar, and A. M. Bolarín-Miró. Synthesis of $Y_3Fe_5O_{12}$ (YIG) assisted by high-energy ball-milling. Ceram. Int. 38 (2012) 5257-5263.

[12] E. H. Penilla, Y. Kodera, and J. E. Garay. Simultaneous synthesis and densification of transparent, photoluminescent polycrystalline YAG by current activated pressure assisted densification (CAPAD). Mater. Sci. Eng. B 177 (2012) 1172-1181.

[13] C. V. Stan, J. Wang, I. S. Zouboulis, V. Prakapenka, and T. S. Duffy. High-pressure phase transition in $Y_3Fe_5O_{12}$. J. Phys. Condens. Matter. 27 (2015) 405401.

[14] M. Reza, Z. Sajuri, Y. Yunas, and J. Syarif. Effect of sputtering target's grain size on the sputtering yield, particle size and coercivity (H_C) of Ni and $Ni_{20}Al$ thin films. IOP Conf. Ser.: Mater. Sci. Eng., 114 (2016) 012116.

CHAPTER 4

Structural and Magnetic Properties of $Y_{3(1-X)}Tm_{3X}Fe_5O_{12}$ Solid Solution Powders

4.1. Background and Motivation

The rare earth iron garnets have garnered a lot of scientific interest over the last ten years due to the growing body of research in the field of spintronics. Yttrium iron garnet (YIG), as the quintessential low damping synthetic garnet, has been the primary focus of fundamental magnonic research due to its wide availability and unusually low spin damping. Other rare earth iron garnets also exhibit low levels of damping, but never quite as low as is possible for YIG or the similarly behaved lutetium iron garnet (LuIG). In general, less is known about the spin-damping of the other rare earth iron garnets than for YIG. This is largely due to YIG's commercial successes, and the fact that commercial PLD and sputtering targets are not widely available for most other types of rare earth iron garnets. One often must fabricate a target from raw materials if they want to create and study new types of garnet films.

While the Gilbert damping of the best YIG films is typically as low as a 1-3 $x10^{-4}$ [10-13], robust perpendicular magnetic anisotropy (PMA) has proven difficult to produce in YIG. This is because YIG's magnetostriction constants are quite low (λ_{100} = -1.30 $x10^{-6}$; λ_{111} = -2.25 $x10^{-6}$ [9]), such that the in-plane strain required to produce PMA in YIG usually creates enough stress energy in the film to cause nonuniform strain relaxation via dislocation formation. On the other hand, thulium iron garnet (TmIG) has displayed PMA in epitaxial films of ~10-30 nm thick[14-18], owing in part to its larger magnetostriction value (λ_{111} = -5.10 $x10^{-6}$ [9]). There is even one report that shows PMA in a 350 nm thick epitaxial TmIG film.[19] The highest quality TmIG films, however, have 1-2 orders of magnitude worse damping than YIG.[17,18] It may be possible that a solid solution of YIG and TmIG would retain the low damping properties of YIG,

but also inherit the ability to produce films with PMA from TmIG. A similar phenomenon was observed in a 30 nm thick epitaxial Bi-substituted YIG ($Bi_1Y_2Fe_5O_{12}$) film that had a low damping of 3.1 $x10^{-4}$ in addition to robust PMA.[20]

Generating PMA in a material depends on more physical properties than just the magnetostriction constant. Properties such as the elastic stiffness constants, its first order magnetic anisotropy constant, and its magnetic saturation all play a role in producing PMA. Since this method of generating PMA depends on the in-plane strain in the film, the amount of lattice mismatch between film and substrate is another determining factor. Therefore, the unstrained lattice parameter size of the film also plays a role in producing PMA. The magnetostriction constant, elastic stiffness constants, first order magnetic anisotropy constant, and lattice parameter of a YIG-TmIG solid solution each depend on its composition. Thus, the composition of a YIG-TmIG solid solution can allow further tuning of PMA beyond what is possible for a pure YIG or pure TmIG film.

Rare earth iron garnets typically have a high degree of solubility with one another owing to their non-close-packed structures. One can synthesize rare earth iron garnet solid solutions by the conventional solid state reaction method whereby oxides of iron and two different rare earth metals are carefully mixed and reacted at high temperature, but it is difficult to ensure that the composition of the reacted powder is uniform when using this method. A much simpler method to ensure compositional uniformity is to synthesize the solid solution using a wet chemical route. Therefore, we propose to synthesize a full compositional range of $Y_{3(1-X)}Tm_{3X}Fe_5O_{12}$ solid solution powders using the previously employed polymeric-steric entrapment route, and to characterize their magnetic and structural properties using XRD, VSM and FMR analysis techniques.

4.2. Sample Preparation

Metal-organic preceramic powders of $Y_{3(1-X)}Tm_{3X}Fe_5O_{12}$ solid solutions with compositions of X = 0, 0.25, 0.5, 0.75 and 1 were each synthesized via the polymeric-steric entrapment route as described in the powder synthesis portion of the methods section. A total mass of ~3 g of powder was synthesized for each different composition, with half of it calcined in air in a furnace at 1300°C for 1 h, and the other half at 1300°C for 12 h. These calcining conditions were chosen because the individual combination of 1300°C for 1 h yielded fully reacted, phase pure YIG for previously synthesized powders, and then the extra calcining condition of 1300°C for 12 h was used to produce a coarser powder with larger grain and particle sizes, such that for each composition there are two chemically identical sets of powder with different sized features. This resulted in ten distinctive batches of powder encompassing all combinations of composition and calcining duration with a mass of ~1.5 g each. All ten powders were then manually ground using an agate mortar and pestle for ~30 minutes each.

XRD, SEM, VSM and FMR samples were then prepared of the as-synthesized powders. The XRD and SEM samples were both prepared as is typical for powder samples. VSM and FMR samples required a more specific preparation method. For these samples, the powder was first well dried at 80°C in air. While the powder was still warm, a small portion of it was measured and placed in the bottom of an open polycarbonate capsule with an inner diameter of 4 mm. The capsule and powder were then maintained at a constant 60-65°C as n-eicosane (Alfa Aesar, 99%) crystals were placed in the capsule on top of the powder where they would then melt. Eicosane was continually added until ~2 mm of liquid eicosane covered the powder. The capsule and its contents were then allowed to cool to room temperature and the eicosane would solidify such that the powder was rigidly held in place, and then the capsule was capped. All

VSM samples were prepared in this method with a mass of powder in the range of 0.012-0.015 g, and all FMR samples were similarly prepared but with a mass of powder in the range of ~0.001-0.003 g.

4.3. Results and Discussion

4.3.1. Structure and Morphology of $Y_{3(1-X)}Tm_{3X}Fe_5O_{12}$ Powders

The structural compositions of the different powders were evaluated with XRD analysis using a PANalytical Empyrean Series 2 diffractometer with a Ni filter for monochromatization. The results of the XRD measurements for the powders calcined at 1300°C for 1 h, and for those calcined at 1300°C for 12 h are shown in **Fig. 4.1 and Fig. 4.2**, respectively. Both figures show sharp, clear diffraction peaks associated with the garnet phase for all compositions of powder. A very small diffraction peak associated with the primary perovskite peak is barely visible near $2\theta = 33.2°$ for X = 0, 0.25, 0.5 and 1 in the 1 h heat treated powders, and for X = 0, 0.25 and 0.5 in the 12 h heat treated powders. Since both phases are line compounds and the perovskite phase has a higher rare earth to iron cation ratio, this is an indication that the powders with these specific compositions have a slightly higher overall rare earth content than stoichiometric garnet. The XRD peaks are all narrow, and do not noticeably change in width or relative intensity between the powders calcined for the different times, indicating that all powders are fully reacted and highly crystalline. The fact that the XRD patterns for all compositions show a majority garnet phase and no additional unwanted oxide phases other than the barely detectable amounts of the perovskite phase means that YIG and TmIG are fully soluble with each other. Changes in the relative intensities of specific XRD peaks can also be seen as the composition varies from YIG to TmIG as is normal for different elemental compositions, which corroborates that we successfully synthesized solid solutions.

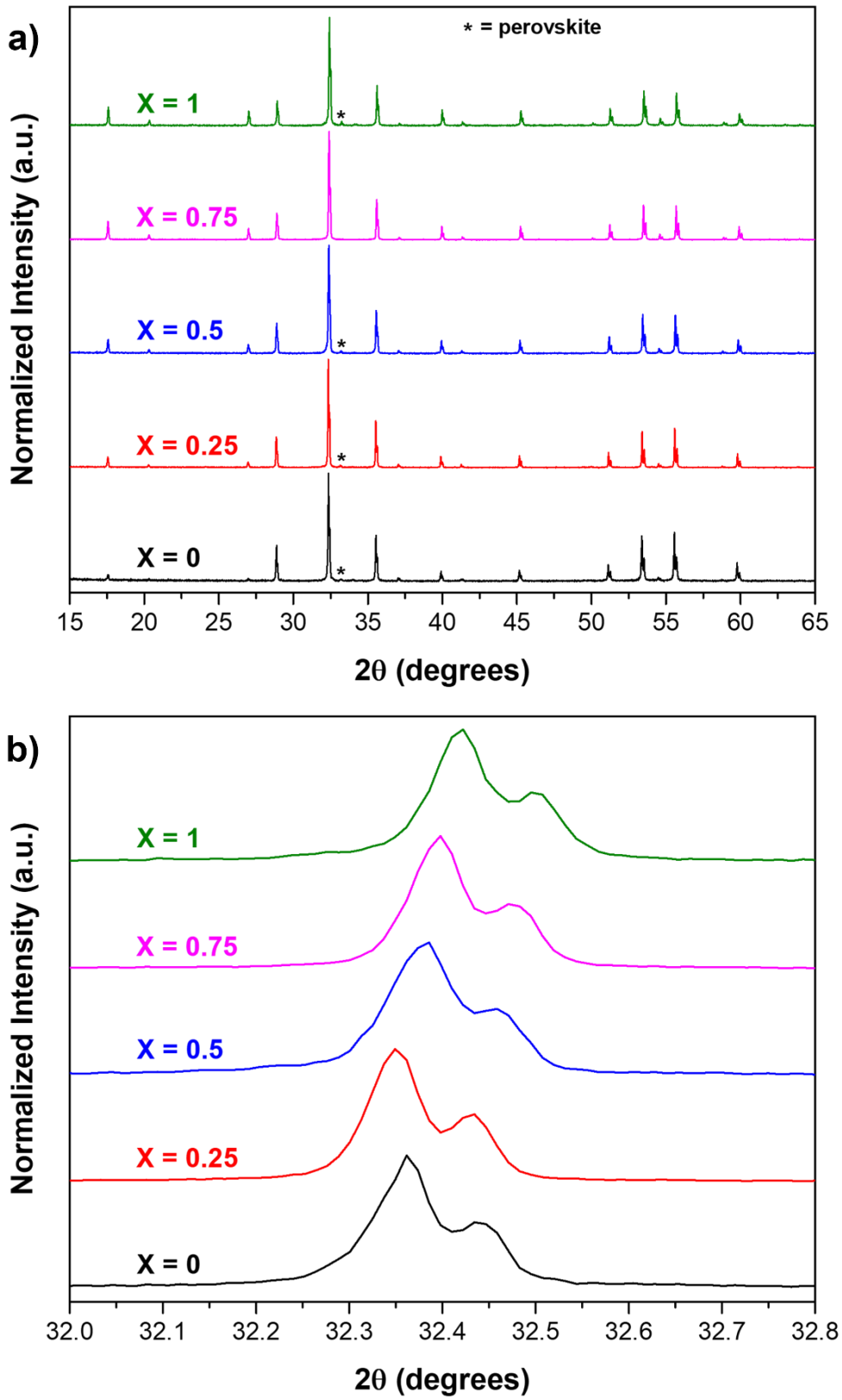

Fig. 4.1: XRD measurements of the $Y_{3(1-X)}Tm_{3X}Fe_5O_{12}$ powders synthesized via the polymeric-steric entrapment method and calcined in air at 1300°C for 1 h. A wide range of 2θ is shown in a) and a zoomed region of the primary peak (420) is plotted in b).

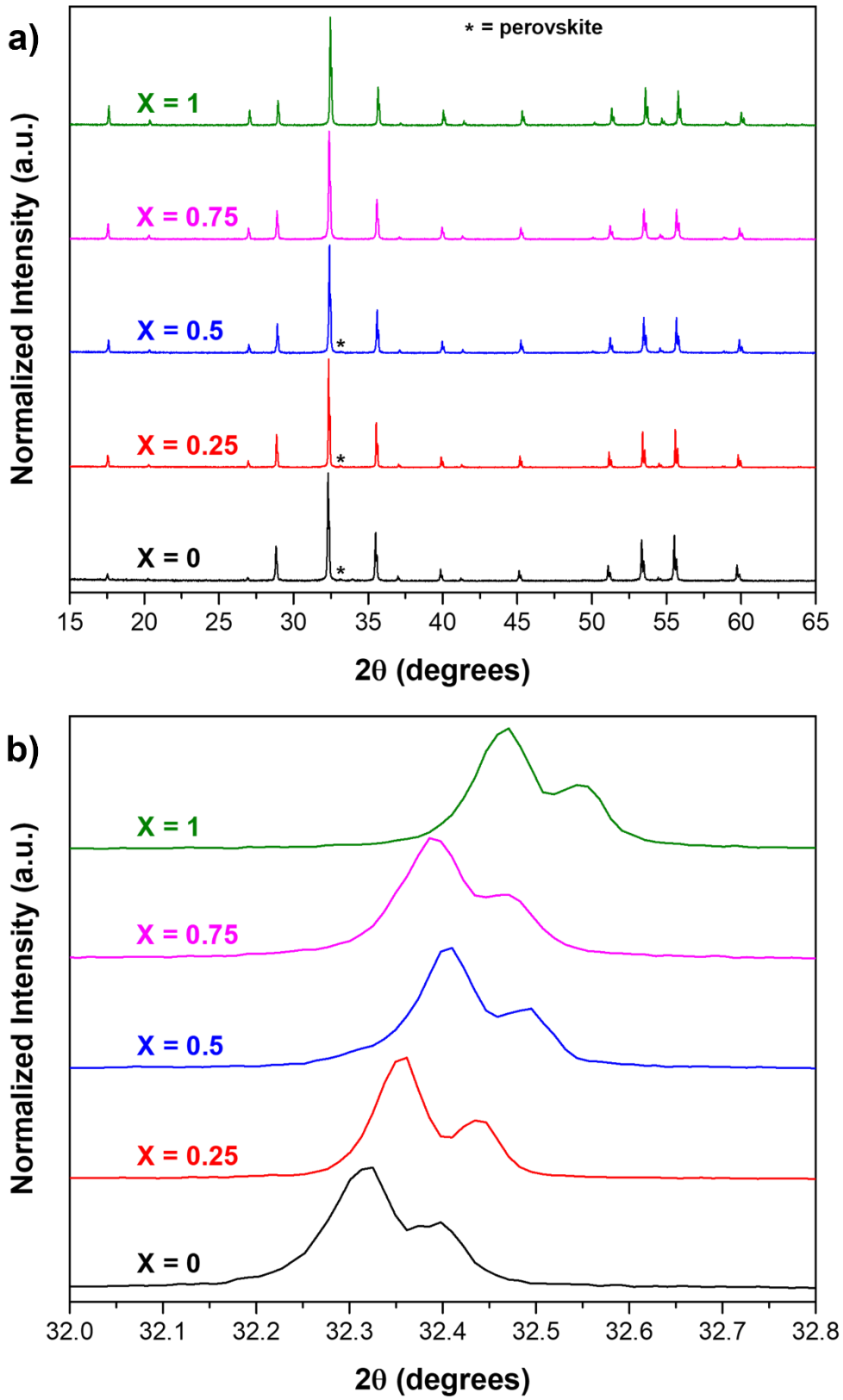

Fig. 4.2: XRD measurements of the $Y_{3(1-X)}Tm_{3X}Fe_5O_{12}$ powders synthesized via the polymeric-steric entrapment method and calcined in air at 1300°C for 12 h. A wide range of 2θ is shown in a) and a zoomed region of the primary peak (420) is plotted in b).

YIG and TmIG have very similar reported lattice parameters of a_{YIG} = 12.375 Å (ICSD collection code #33931) and a_{TmIG} = 12.324 Å[1]. Because of this similarity, it can be difficult to detect changes in their 2θ diffraction peak positions, however, shifts in their positions are easily seen at higher resolutions. In the XRD plots of the zoomed-in region (**Fig. 4.1b and 4.2b**) around the primary garnet peak (420), the peaks of the various compositions of powder clearly shift towards higher 2θ values with increasing Tm content as expected from TmIG's smaller lattice size. There is a level of experimental error in these measurements that results from the flatness of a given powder specimen and its vertical alignment within the diffractometer that may cause a slight shift in peak position for a given XRD curve, but overall, this trend holds well for these samples. One other thing worth noting is that a secondary peak of roughly half the intensity of the primary peak can be seen on the right side of all peaks in the zoomed-in regions. This feature occurs on all peaks of the measured samples but is only apparent at higher resolutions. It is the result of Cu-Kα_2 radiation in the incident x-ray beam that is not absorbed by the Ni filter, whereas the higher intensity peak we used for structural analysis is due to the shorter wavelength Cu-Kα_1 radiation.

The (420) d-spacings of all samples were calculated from their primary peaks' 2θ positions according to Bragg's law, expressed as

$$n\lambda = 2d\sin\theta, \tag{4.1}$$

where λ is the wavelength of the diffracted light and n is the diffraction order. In this instance, an adjusted wavelength of λ = 1.5418 Å was used to account for other x-ray emissions near the wavelength of Cu-Kα_1. The lattice parameters were then calculated according to the following relationship for the d-spacing of a cubic system:

$$a = d_{hkl}\sqrt{h^2 + k^2 + l^2}, \tag{4.2}$$

where h, k and l are the Miller indices of a given plane. For each composition, the calculated lattice parameters for the 1 h and 12 h heat treated samples were then averaged. The theoretical lattice parameters of the different compositions were calculated as a linear combination of the two constituent garnets, YIG and TmIG, and their theoretical densities were calculated from unit cells comprised of the theoretical lattice parameters. A summary of the experimentally determined lattice parameters, and the theoretically determined lattice parameters and densities are provided in **Table 4.1**.

The experimental lattice parameters of the powder samples are plotted versus composition in comparison to the theoretical lattice parameters in **Fig. 4.3**. A linear fit of the

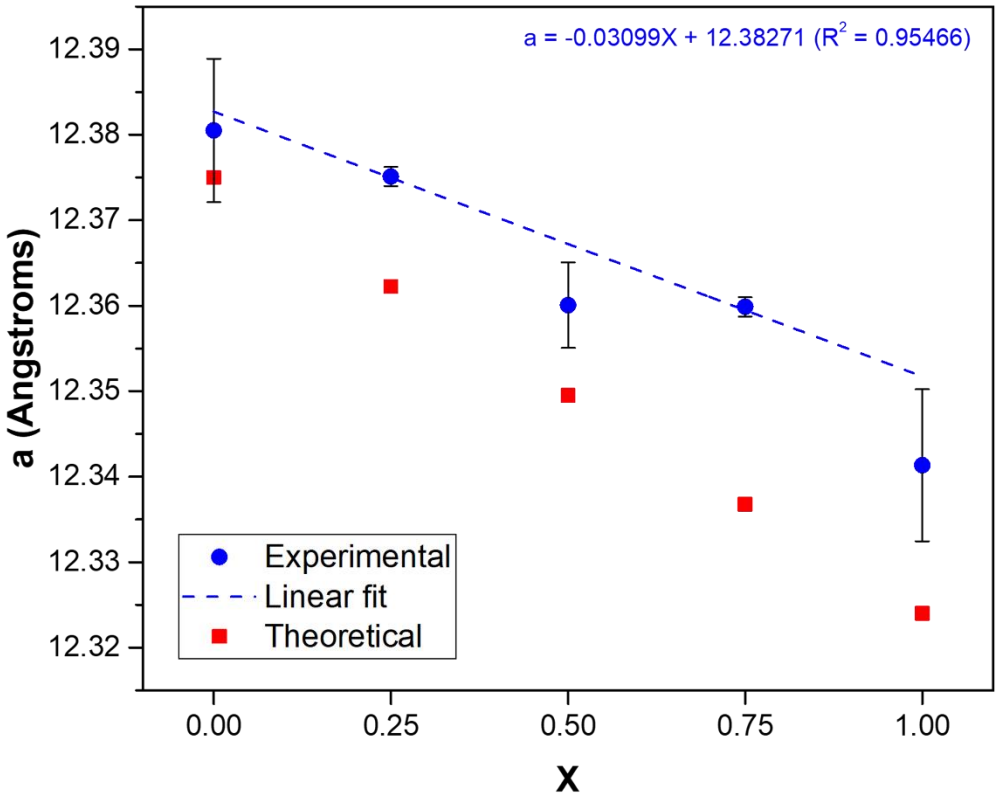

Fig. 4.3: The average lattice parameters of the $Y_{3(1-X)}Tm_{3X}Fe_5O_{12}$ powders synthesized via the polymeric-steric entrapment route (blue) plotted versus composition in comparison to the theoretical lattice parameters (red).

experimental lattice parameters yielded an $R^2 = 0.95466$, indicating a highly linear relationship between lattice size and composition. The linear relationship of the lattice parameter length with composition is further evidence of the successful formation of solid solutions. The lattice parameters of the $Y_{3(1-X)}Tm_{3X}Fe_5O_{12}$ powders are overall slightly larger than the expected values. Some of this could simply be caused by systematic error in either the measuring or calculating of the lattice parameters, but it might also be that the synthesis method used to make these powders introduced higher levels of thermal oxygen vacancies which resulted in larger than expected lattice parameters. It's also important to note that there is little structural data published on TmIG, so it is within the realm of possibility that the reference lattice parameter value used here is smaller than it truly is.

SEM micrographs of the 1 h and 12 h heat treated powders are shown in **Fig. 4.4 and Fig. 4.5**, respectively. The micrographs show irregularly shaped micrometer sized powders with comparable morphologies. The grain sizes and particle sizes of the powders were each evaluated by manually measuring their SEM images using ImageJ software. A cutoff size of ~0.3 μm was implemented when measuring the images since below this size there were mostly very fine nano-sized particulates. The powders calcined for 1 h were found to have comparable average grain sizes of 1.80 ± 0.64 μm, and comparable particle sizes of 1.85 ± 1.40 μm. Similarly, the powders calcined for 12 h were found to have comparable average grain sizes of 2.90 ± 0.84 μm, and comparable particle sizes of 2.96 ± 2.50 μm. For a given calcining duration, no significant differences were observed in particle sizes across compositions, however, some differences were observed with respect to grain size. In both the 1h and 12 h heat treated powders, the pure TmIG (X = 1) had a slightly higher average grain size than pure YIG (X = 0) with a difference of ~0.2 μm, whereas the average grain sizes of the solid solutions were very comparable to each other.

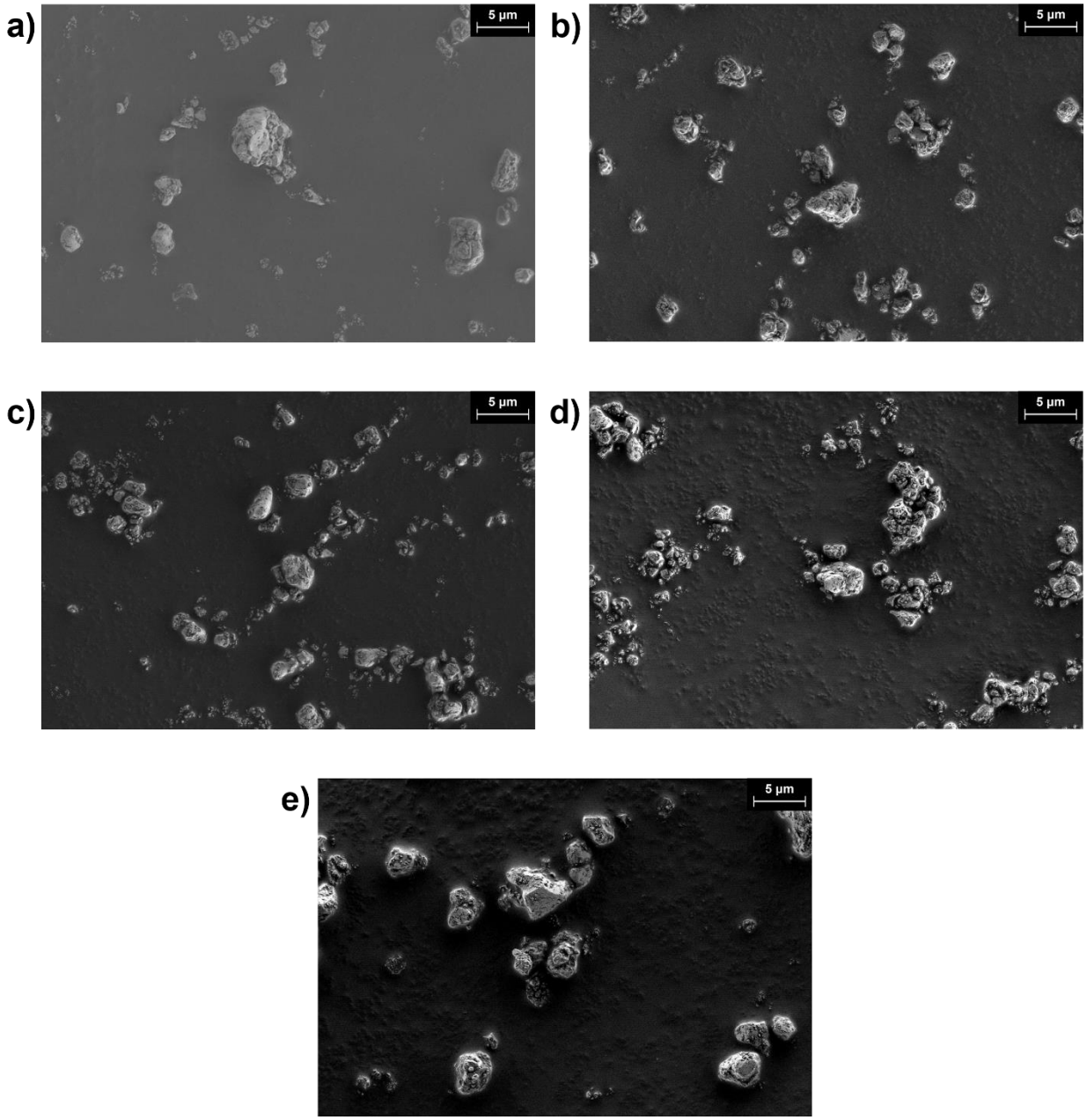

Fig. 4.4: Representative SEM micrographs of the $Y_{3(1-X)}Tm_{3X}Fe_5O_{12}$ powders synthesized via the polymeric-steric entrapment route and calcined in air at 1300°C for 1 h. The composition of the powder in each image is as follows: a) X = 0, b) X = 0.25, c) X = 0.5, d) X = 0.75 and e) X = 1.

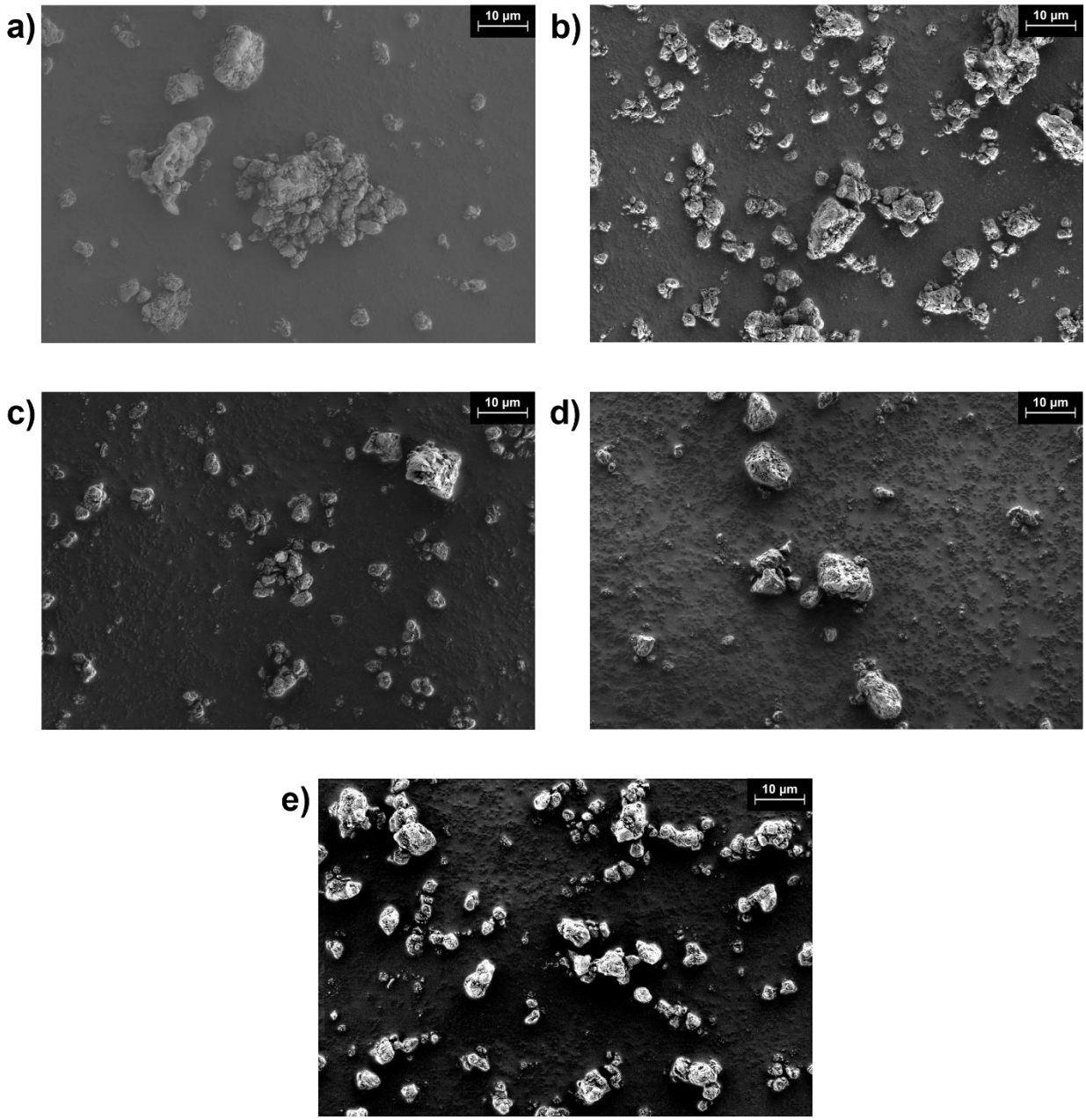

Fig. 4.5: Representative SEM micrographs of the $Y_{3(1-X)}Tm_{3X}Fe_5O_{12}$ powders synthesized via the polymeric-steric entrapment route and calcined in air at 1300°C for 12 h. The composition of the powder in each image is as follows: a) X = 0, b) X = 0.25, c) X = 0.5, d) X = 0.75 and e) X = 1.

Table 4.1: A summary of the physical and magnetic properties of the $Y_{3(1-X)}Tm_{3X}Fe_5O_{12}$ powders synthesized via the polymeric-steric entrapment route as experimentally and theoretically determined.

X	$a_{Theor.}$ (Å)	$a_{Exp.}$ (Å)	$\rho_{Theor.}$ (g/cm^3)	$4\pi M_{S\text{-}Theor.}$ (G)	$4\pi M_{S\text{-}Exp.}$ (G)	$g_{Theor.}$	$g_{Exp.}$	$H_{R\text{-}Theor.}$ (Oe)	$H_{R\text{-}Exp.}$ (Oe)
0	12.375	12.380	5.17	1780	1783	2.00	2.06	3329	3235
0.25	12.362	12.375	5.61	1680	1620	1.89	1.96	3528	3398
0.5	12.350	12.360	6.05	1580	1643	1.78	1.87	3751	3558
0.75	12.337	12.359	6.49	1480	1658	1.66	1.79	4004	3719
1	12.324	12.341	6.94	1380	1500	1.55	1.66	4295	4011

4.3.2. Magnetic Behavior of $Y_{3(1-X)}Tm_{3X}Fe_5O_{12}$ Powders

The magnetizations of the powder samples were measured using a Lakeshore 7400 Series VSM. The magnetic hysteresis plots are shown in **Fig. 4.6**. All samples possess small coercivities and exhibit the soft magnetic behavior characteristic of ferrimagnetic rare earth iron garnets. For both the 1 h and 12 h heat treated samples, the pure YIG (X = 0) powder has the highest saturation magnetization value of ~27.5 emu/g, and then the net magnetization decreases with increasing thulium content until it reaches its lowest measured value for pure TmIG (X = 1) which had a saturation magnetization of ~17.2 emu/g. The M_S value we measured for our TmIG powder is ~8% higher than the 15.9 emu/g that was previously reported for bulk TmIG.[2] It's unclear why the M_S values of our TmIG samples are higher, but as is the case with structural information about TmIG, there aren't many reports on its magnetic properties in bulk or powder form either. The M_s of the samples with the compositions X = 0, 0.5 and 1 remain mostly unchanged when comparing the 1 h to the 12 h heat treated powders, but an interesting phenomenon occurred in those samples with a composition of X = 0.25 and 0.75. The M_S of the X = 0.25 samples decreased from 23.2 emu/g for the 1 h heat treated powder to 22.7 emu/g for the 12 h heat treated powder, and the M_S of the X = 0.75 samples increased from 19.7 emu/g for the 1 h heat treated powder to 21.0 emu/g for the 12 h heat treated powder, such that they are both closer to the M_S of the X = 0.5 powders of ~21.6 emu/g than their 1 h heat treated

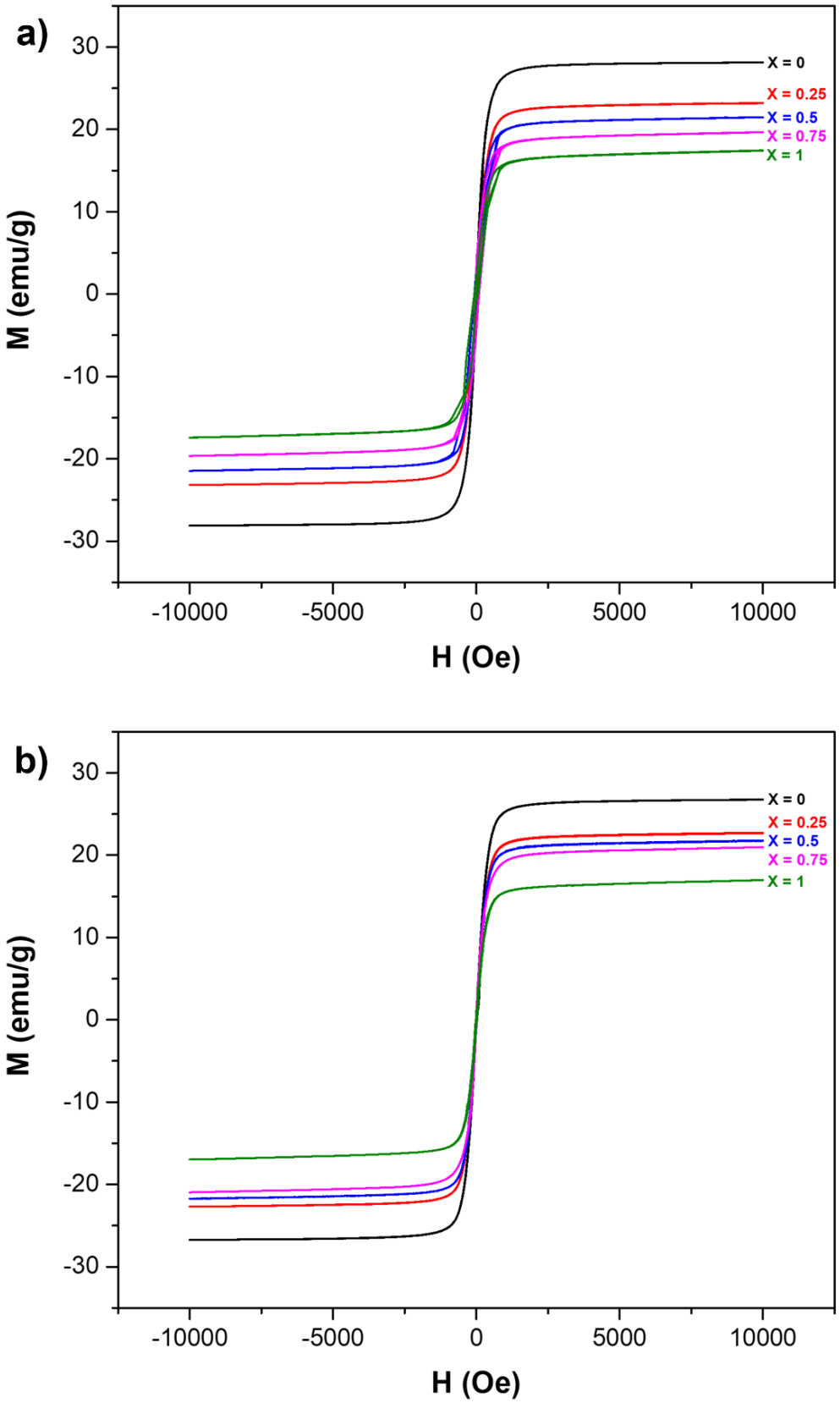

Fig. 4.6: Magnetic hysteresis measurements of the $Y_{3(1-X)}Tm_{3X}Fe_5O_{12}$ powders synthesized via the polymeric-steric entrapment route and calcined in air at 1300°C for a) 1 h and b) 12 h.

counterparts. It is unclear why these changes occurred to the powders heat treated for 12 h, but this difference cannot solely be explained by experimental error.

The mass normalized M_S values of the various samples as determined using VSM analysis were then converted into the volumetric magnetization $4\pi M_S$ values using the theoretical density as a conversion factor. For each composition, the $4\pi M_S$ values of the 1 h and 12 h heat treated samples were then averaged. The theoretical $4\pi M_S$ values of the different compositions were calculated as a linear combination of the two constituent garnets, YIG and TmIG. A linear approximation makes sense in this case because structurally, the nonmagnetic Y^{3+} ions are being replaced with magnetic Tm^{3+} ions as the thulium concentration of the solid solutions increases. Both the experimentally derived and theoretically calculated $4\pi M_S$ values are listed in **Table 4.1**, and they are plotted versus composition in **Fig. 4.7**. The $4\pi M_S$ of the $Y_{3(1-X)}Tm_{3X}Fe_5O_{12}$ samples decreases with increasing thulium content in a somewhat nonlinear fashion. A linear fit of the experimental values yielded an $R^2 = 0.57000$. This low R^2 value is a result of the fact that the $4\pi M_S$ values for the X = 0.25 and 0.75 samples don't coincide well with a linear trend. As previously noted, the magnetic saturation of our TmIG samples is higher than was previously reported for TmIG, but this plot also reveals that the solid solutions with compositions of X = 0.5 and X = 0.75 also have higher magnetic saturations than expected.

Room temperature FMR measurements were performed on the as-prepared samples using a Bruker EMX cavity based EPR at a fixed frequency of 9.32 GHz. The FMR samples were very small due to the high sensitivity of the EPR, with masses of only a few micrograms. The collected FMR spectra were normalized by their maximum intensities due to variation in the individual sample's absorption intensities resulting from their different masses, and then plotted together in **Fig. 4.8**. The figure shows relatively broad absorption linewidths on the order of

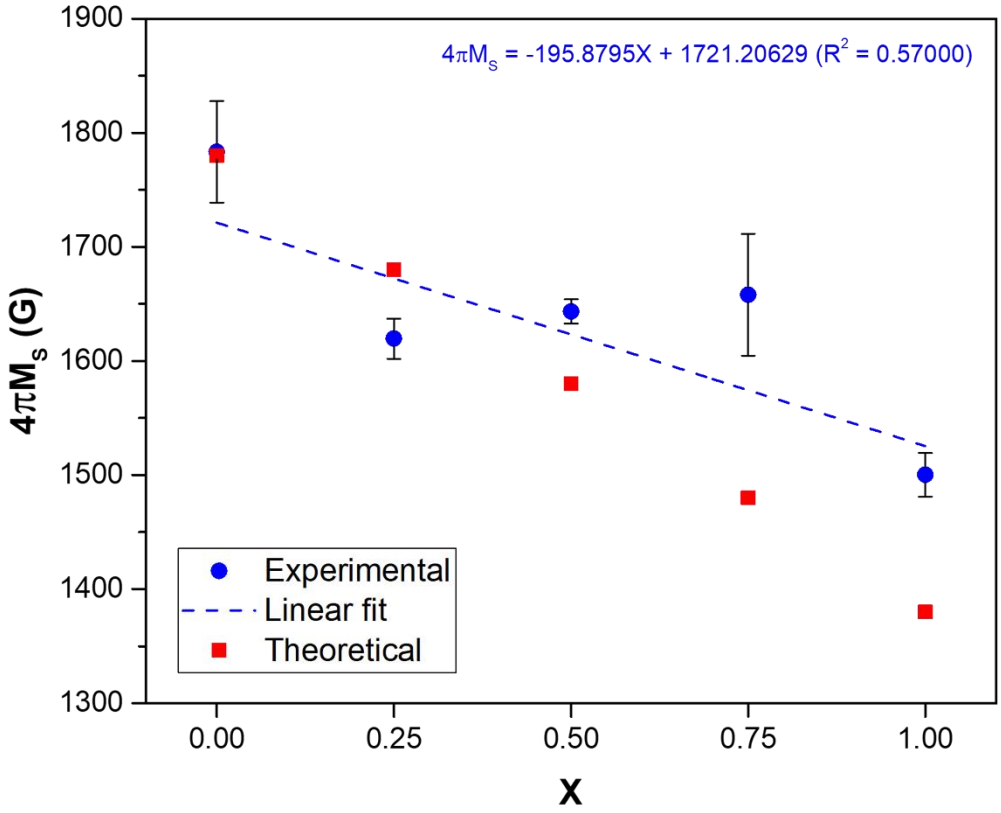

Fig. 4.7: The average $4\pi M_S$ values of the $Y_{3(1-X)}Tm_{3X}Fe_5O_{12}$ powders synthesized via the polymeric-steric entrapment route (blue) plotted versus composition in comparison to the theoretical $4\pi M_S$ values (red).

~600 Oe for all measured samples, and that the resonant field position increases with thulium content for both the 1 h and 12 h heat treated powders. The resonant fields of each sample were determined by taking the integral of the absorption derivative and fitting the resulting absorption peak with a bigaussian function. The peaks were initially fit with Lorentzian functions as well since the absorption should theoretically be a Lorentzian, however, the bigaussian function more reliably fit this specific data set. For each composition, the resonant field was found to be virtually identical between the 1 h and 12 h heat treated samples.

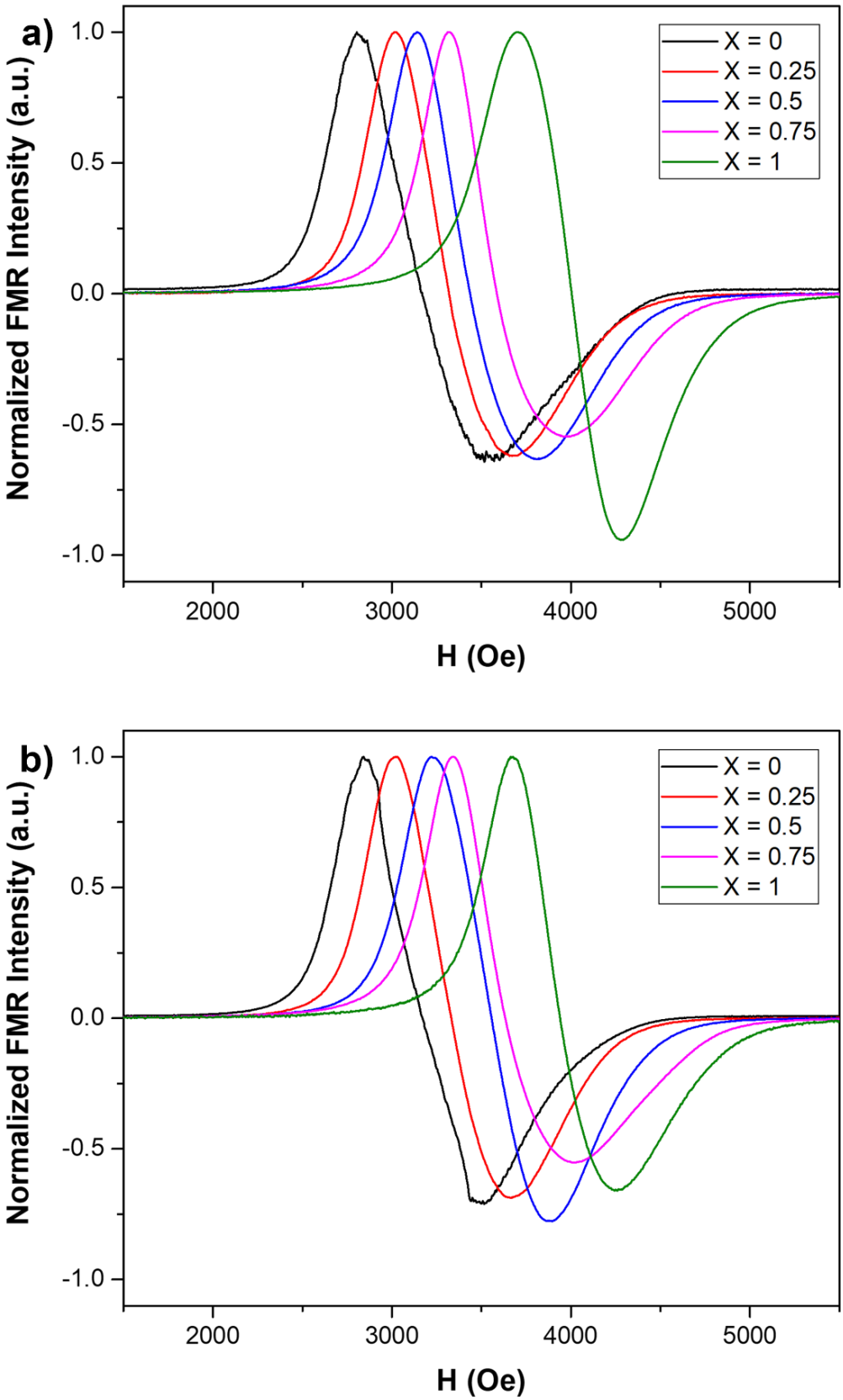

Fig. 4.8: FMR measurements taken at a frequency of 9.32 GHz of the $Y_{3(1-X)}Tm_{3X}Fe_5O_{12}$ powders synthesized via the polymeric-steric entrapment route and calcined in air at 1300°C for a) 1 h and b) 12 h.

In order to calculate the theoretical resonant fields, it was assumed that the powders could be treated as collections of approximately spherical particles with varying degrees of magnetic anisotropy. This assumption seems valid since SEM analysis revealed no net aspect ratio in the particles for any of the as-synthesized powders. The resonant equation of a sphere can be expressed as

$$f_R = \frac{\gamma_{eff} H_R}{2\pi}, \tag{4.3}$$

where f_R is the resonant frequency, γ_{eff} is the effective gyromagnetic ratio, and H_R is the resonant field.[3] The effective gyromagnetic ratio is defined as

$$\gamma_{eff} = \frac{g_{eff}\mu_B}{\hbar}, \tag{4.4}$$

where g_{eff} is the effective Landé g-factor, μ_B is the Bohr magneton, and $\hbar$ is the reduced Planck's constant. Combining eq. (4.3) and (4.4) into an expression for the resonant field of a sphere gives the following relationship:

$$H_R = \frac{h f_R}{\mu_B g_{eff}}, \tag{4.5}$$

where h is Planck's constant.

The above expression for the resonant field of a sphere depends on its effective g-factor. A simple relationship exists over a wide range of temperatures between the g_{eff} of a rare earth iron garnet and its M_S, which can be expressed as follows:

$$g_{eff} = \frac{g_{YIG} M_{REIG}}{M_{YIG}}, \tag{4.6}$$

where g_{YIG} is the g-factor of YIG, M_{REIG} is the magnetic saturation of the given rare earth iron garnet, and M_{YIG} is the magnetic saturation of YIG.[4] The theoretical g-factors of the different compositions of $Y_{3(1-X)}Tm_{3X}Fe_5O_{12}$ were calculated using eq. (4.6) with the previously determined theoretical $4\pi M_S$ values. The theoretical resonant field values were then calculated

using eq. (4.5) and the theoretical g_{eff} values just determined. Finally, the experimental g_{eff} values of the synthesized powders were calculated using the expression in eq. (4.5) with the previously measured average resonant field values. All of the theoretically and experimentally determined g-factors and resonant field values are summarized in **Table 4.1**.

The experimental and theoretical resonant field values are plotted together versus composition in **Fig. 4.9**. A linear fit of the experimental values yielded an $R^2 = 0.99826$, indicating nearly perfect linearity. The high degree of linearity implies that the resonance of the powder samples closely follows the relationship described in eq. (4.3) for a sphere, suggesting no net shape anisotropy in the as-synthesize powders. For all compositions, the experimentally determined resonant field values are ~100-300 Oe lower than the theoretical values. The magnitude of this difference increases with the thulium content of the composition in a uniform fashion, i.e., the slope of the theoretically calculated resonant field is higher than the slope produced by the experimental data. The discrepancy in slopes can be explained quite neatly by the difference between the reported M_S value of TmIG which was used to calculate the theoretical g_{eff} values, and our measured M_S for TmIG. Using our experimental $4\pi M_S$ value of TmIG in eq. (4.6) yields a $g_{eff} = 1.69$, which is both close to our experimentally found value of 1.66, and the previously reported g_{eff} for bulk TmIG of 1.63[5,6]. However, that still leaves a difference of up to ~100 Oe between the experimental and theoretical resonant field values for the other compositions, which we believe is evidence of somewhat higher g-factors in our synthesized powders.

The peak-to-peak linewidths from the FMR measurements are plotted versus composition in **Fig. 4.10** for both the 1 h and 12 h heat treated powders. Looking at the individual data points, there doesn't appear to be a strong trend between linewidth and composition, nor does there

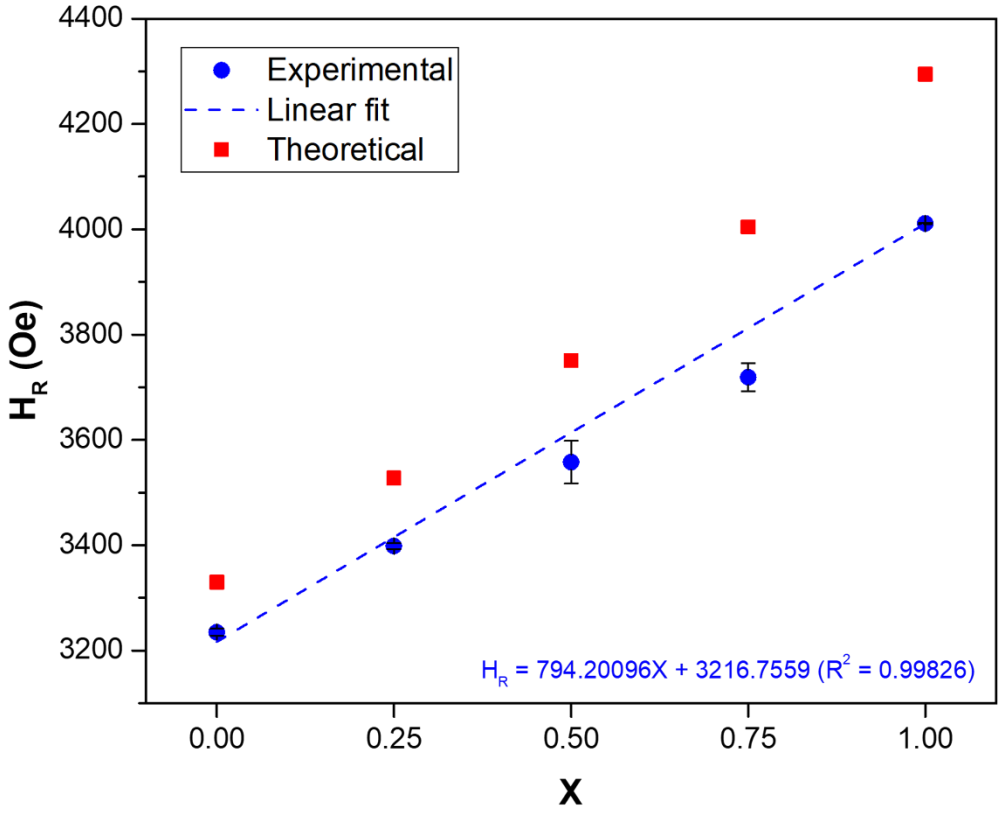

Fig. 4.9: The average resonant field position of the $Y_{3(1-X)}Tm_{3X}Fe_5O_{12}$ powders synthesized via the polymeric-steric entrapment route (blue) plotted versus composition in comparison to the theoretical resonant field (red).

appear to be a clear difference between the 1 h and 12 h heat treated powders. Perhaps the most surprising things shown by this plot are that the linewidth of the TmIG (X = 1) samples were lower than for all other compositions, and the linewidth of the YIG sample (X = 0) heat treated for 1 h was the largest in this sample set. These results were unexpected when considering the many physical similarities of these powders, and that pure YIG has a reported linewidth of ≤ 0.5 Oe[7,8], and TmIG has a reported linewidth of 135 Oe[6]. This indicates that the pure YIG powders have the highest level of magnetic inhomogeneity, whereas the TmIG powders have the least. The exact reasons why the TmIG samples had lower levels magnetic inhomogeneity than

the other compositions aren't entirely clear, but it may be related to the fact that the average grain sizes of the TmIG powders are slightly larger than the others. A linear fit of the averaged linewidth values yielded a negative slope with an $R^2 = 0.90121$, seeming to indicate that there is a strong linear trend for decreasing linewidth with increasing thulium content. The goodness of this fit is somewhat questionable, however, because seven out of the ten measured linewidths are clustered between a relatively small range of 620 to 660 Oe. Considering that pristine YIG and TmIG have much narrower linewidths, the as-prepared powder samples all have large inhomogeneous contributions to their linewidths somewhere in the range of ~430-680 Oe.

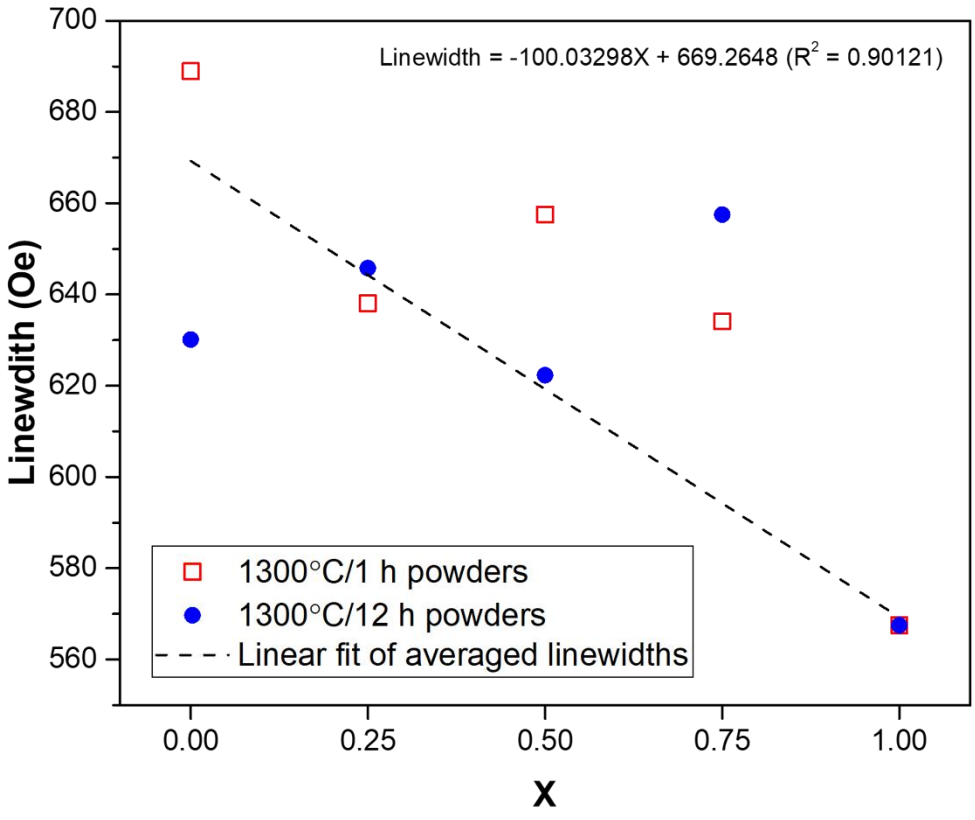

Fig. 4.10: The measured peak-to-peak FMR linewidths of the $Y_{3(1-X)}Tm_{3X}Fe_5O_{12}$ powders synthesized via the polymeric-steric entrapment route plotted against composition. The linear fit to the averaged linewidth values of each composition of powder in this study is also plotted.

4.4. Conclusions

Over the course of this study we successfully synthesized a full compositional range of $Y_{3(1-X)}Tm_{3X}Fe_5O_{12}$ powders using the polymeric-steric entrapment method. We are also the first to report on the synthesis of $Y_{3(1-X)}Tm_{3X}Fe_5O_{12}$ powders using this method. We selectively synthesized two different sized groups of powders by calcining them at 1300°C in air for 1 h and 12 h, respectively, and then characterized each powder sample with XRD, SEM, VSM and FMR. XRD analysis showed that the lattice parameters of the synthesized garnets varied linearly with composition, and VSM measurements of the powders showed that their M_S decreased nonlinearly with increasing thulium content. Since PMA in a film depends on both M_S and the lattice mismatch between film and substrate, this demonstrates the possibility of tuning PMA of a YIG-TmIG solid solution using composition as a variable.

FMR measurements showed that the resonant field position varied linearly with composition. This implies that there is no net shape anisotropy in the as-synthesize powders, and that their effective g-factors also vary linearly with composition. Unsurprisingly, the FMR results didn't yield much information about the inherent spin-damping of the $Y_{3(1-X)}Tm_{3X}Fe_5O_{12}$ powders. The irregular shaped morphology of the powder samples lead to high amounts of inhomogeneous broadening in the FMR absorptions which completely overshadowed the intrinsic linewidth of the underlying garnet. Being able to estimate the intrinsic linewidths of the powder samples using FMR would have greatly accelerated the process of discovering low damping solid solution compositions. The inhomogeneous broadening in the FMR measurements likely could have been reduced if the morphology of the powder had been highly spherical, or completely removed had we fabricated small bulk spheres of the various solid solutions.

The magnetic and structural property measurements of the pure TmIG samples are also important contributions from this work. There are very few published reports on the properties of bulk or powder TmIG, let alone for TmIG synthesized via the polymeric-steric entrapment route. As of 2023, there isn't even a crystallographic reference on file in ICSD's database for TmIG. Furthermore, one of the only identifiable references for the lattice parameter of TmIG is in a difficult to find book originally published in 1978.[1] These properties are especially important to report because both our measured lattice parameter and magnetic saturation are slightly larger than the previously reported values for TmIG. It may be the case that the synthesis method we used is partly responsible for these discrepancies, but it could also indicate that the properties of pristine TmIG are currently not well known.

Acknowledgements

Chapter 4 contains unpublished material. The dissertation author was the primary researcher and author of this chapter.

REFERENCES

[1] K.-H. Hellwege, and A. M. Hellwege. Landolt-Börnstein – Group III Crystal and Solid State Physics Vol. 12a, Springer-Verlag, Berlin/Heidelberg 1978.

[2] C. N. Wu, C. C. Tseng, K. Y. Lin, C. K. Cheng, S. L. Yeh, Y. T. Fanchiang, M. Hong, and J. Kwo. High-quality single-crystal thulium iron garnet films with perpendicular magnetic anisotropy by *off-axis* sputtering. AIP Adv. 8 (2018) 055904.

[3] C. Kittel. Ferromagnetic resonance. J. Phys. Radium, 12 (1951) 291-302.

[4] C. Kittel. Theory of Ferromagnetic Resonance in Rare Earth Garnets. I. *g* Values. Phys. Rev., 113 (1959) 6.

[5] T. Miyadi. Ferrimagnetic Resonance in polycrystalline Thulium-Iron Garnet ($Tm_3Fe_5O_{12}$). J. Phys. Soc. Japan, 17 (1962) 870-871.

[6] T. Miyadi. Ferrimagnetic Resonance in a Single Crystal of Thulium-Iron Garnet ($Tm_3Fe_5O_{12}$). J. Phys. Soc. Japan, 17 (1962) 1899-1900.

[7] R. C. LeCraw, E. G. Spencer, and C. S. Porter. Ferromagnetic Resonance Line Width in Yttrium Iron Garnet Single Crystals. Phys. Rev., 110 (1958) 6.

[8] S. Bornmann, E. Glauche, P. Görnhert, R. Hergt, and C. Becker. Preparation and Properties of YIG Single Crystals. Kristall und Technik, 9 (1974) 895-904.

[9] S. Iida. Magnetostriction Constants of Rare Earth Iron Garnets. J. Phys. Soc. Japan, 22 (1967) 5.

[10] C. Tang, M. Aldosary, Z. Jiang, H. Chang, B. Madon, K. Chan, M. Wu, J. E. Garay, and J. Shi. Exquisite growth control and magnetic properties of yttrium iron garnet thin films. Appl. Phys. Lett., 108 (2016) 102403.

[11] Y. Sun, Y. Song, H. Chang, M. Kabatek, M. Jantz, W. Schneider, M. Wu, H. Schultheiss, and A. Hoffman. Growth and ferromagnetic resonance properties of nanometer-thick yttrium iron garnet films. Appl. Phys. Lett., 101 (2012) 152405.

[12] M. C. Onbasli, A. Kehlberger, D. H. Kin, G. Jakob, M. Klaui, A. V. Chumak, B. Hillebrands, and C. A. Ross. Pulsed laser deposition of epitaxial yttrium iron garnet films with low Gilbert damping and bulk-like magnetization. APL Mater., 2 (2014) 106012.

[13] O. d'Allivy Kelly, A. Anane, R. Bernard, B. Youssef, C. Hahn, A. H. Molpeceres, C. Carrétero, E. Jacquet, C. Deranlot, P. Bortolotti, R. Lebourgeois, J.-C. Mage, G. de Loubens, O. Klein, V. Cros, and A. Fert. Inverse spin Hall effect in nanometer-thick yttrium iron garnet/Pt system. Appl. Phys. Lett., 103 (2013) 082408.

[14] C. Tang, P. Sellappan, Y. Liu, Y. Xu, J. E. Garay, and J. Shi. Anomalous Hall hysteresis in $Tm_3Fe_5O_{12}$/Pt with strain-induced perpendicular magnetic anisotropy. Phys. Rev. B, 140403(R) (2016).

[15] C. O. Avci, A. Quindeau, M. Mann, C.-F. Pai, C. A. Ross, and G. S. D. Beach. Spin transport in as-grown and annealed thulium iron garnet/platinum bilayers with perpendicular magnetic anisotropy. Phys. Rev. B, 95 (2017) 115428.

[16] C. N. Wu, C. C. Tseng, K. Y. Lin, C. K. Cheng, S. L. Yeh, Y. T. Fanchiang, M. Hong, and J. Kwo. High-quality single-crystal thulium iron garnet films with perpendicular magnetic anisotropy by *off-axis* sputtering. AIP Adv., 8 (2018) 055904.

[17] C. N. Wu, C. C. Tseng, Y. T. Fanchiang, C. K. Cheng, K. Y. Lin, S. L. Yeh, S. R. Yang, C. T. Wu, T. Liu, M. Wu, M. Hong, and J. Kwo. High-quality thulium iron garnet films with perpendicular magnetic anisotropy by *off-axis* sputtering – correlation between magnetic properties and film strain. Sci. Rep., 8:11087 (2018).

[18] A. Quindeau, C. O. Avci, E. Liu, C. Sun, M. Mann, A. S. Tang, M. C. Onbasli, D. Bono, P. M. Voyles, Y. Xu, J. Robinson, G. S. D. Beach, and C. A. Ross. $Tm_3Fe_5O_{12}$/Pt Heterostructures with Perpendicular Magnetic Anisotropy for Spintronics Applications. Adv. Electron. Mater., 3 (2017) 1600376.

[19] M. Kubota, A. Tsukazaki, F. Kagawa, K. Shibuya, Y. Tokunaga, M. Kawasaki, and Y. Tokura. Stress-Induced Perpendicular Magnetization in Epitaxial Iron Garnet Thin Films. Appl. Phys. Express, 5 (2012) 103002.

[20] L. Souhmah, N. Beaulieu, L. Qassym, C. Carrétero, E. Jacquet, R. Lebourgeios, J. B. Youssef, P. Bortolotti, V. Cros, and A. Anane. Ultra-low damping insulating magnetic thin films get perpendicular. Nat. Commun., 9:3355 (2018).

CHAPTER 5

Structural Analysis of PLD Grown Epitaxial EuIG Films with Varying Strain

5.1. Background and Motivation

The perpendicular magnetic anisotropy of epitaxial rare earth iron garnets has been extensively studied owing to their ability to produce strain induced anisotropy and wide range of magnetostriction coefficients at room temperature, ranging from -8.5 x 10^6 to +21x10^6.[10] This property makes it possible to control the magnetic anisotropy through the in-plane strain of a film. Since strain relaxes over much longer distances in oxides than in metals, thickness can be used as a means to control the average strain of a rare earth iron garnet. This phenomenon was previously reported in (100)-oriented europium iron garnet (EuIG) films grown on GGG, where films with thicknesses ranging from 4 to 180 nm had anisotropy fields $H_{2\perp}$ ranging from +33 KOe in the thinnest film to -5 KOe in the thickest.[12] Other means of controlling the perpendicular magnetic anisotropy include lattice mismatch with substrates, substrate orientation, and chemical substitution.

While much of the work on tailoring perpendicular magnetic anisotropy revolves around the first-order anisotropy field $H_{2\perp}$ that depends exclusively on the first-order magnetocrystalline anisotropy coefficient K_1 and varies linearly with in-plane stress, other higher-order anisotropy terms exist. For example, there is a second-order anisotropy field $H_{4\perp}$ that emerges at higher strains and depends on the second-order magnetocrystalline anisotropy coefficient K_2. While higher in-plane strains lead to larger anisotropy fields, it generally increases the magnetic inhomogeneity and spin-damping of the film as well. The potential role of higher order anisotropy terms on spin-damping is currently not well understood, despite its contribution to the overall magnetic anisotropy.

The damping of EuIG compared to other rare earth iron garnets is also uniquely interesting. The lowest damping rare earth iron garnets, yttrium iron garnet (YIG) and lutetium iron garnet (LuIG), have similar intrinsic damping of ~10^{-5}.[13] One thing that unites these two materials is that their magnetic structures are virtually identical. Furthermore, the Y^{3+} and Lu^{3+} ions in the dodecahedral sites have fully occupied electron orbitals yielding no net contribution to the magnetic moment. EuIG has a very similar magnetic structure, and despite the Eu^{3+} having 6 unpaired 4f electrons, they are in a J = 0 state that does not contribute to the net magnetic moment of the garnet.[1] The damping in bulk EuIG is two orders of magnitude higher than either YIG or LuIG at room temperature, yet FMR linewidths as narrow as YIG or LuIG have been observed in EuIG single crystals at temperatures of ~42 K.[14] Therefore, we chose to fabricate a range of epitaxial EuIG films with different amounts of substrate lattice mismatch in order to study the effects of strain on damping, in addition to possible mechanisms responsible for its increased room temperature damping.

5.2. Sample Fabrication

An EuIG target was prepared by densifying in-house synthesized powders. The EuIG powders were first synthesized according to the polymeric-steric entrapment route as previously described in the methods section. The as-synthesized powders were then consolidated into bulk form in a 3/4 in. (19 mm) diameter graphite die using the CAPAD processing procedure detailed in the methods section at a processing pressure of 105 MPa, a processing temperature of 900°C, and for a hold time of 5 minutes. Our collaborators then grew (111)-oriented epitaxial EuIG films from the target using pulsed laser deposition (PLD).

The films were grown on a variety of single crystal garnet substrates with different lattice parameters $a_{substrate}$ such that the lattice mismatch η, defined as

$$\eta = \frac{a_{substrate} - a_{EuIG}}{a_{EuIG}}, \quad (5.1)$$

ranged from +0.456% to -3.945% when using a lattice parameter of a_{EuIG} = 12.497Å as reference. In order of decreasing lattice parameter, the individual substrates that were used are $Gd_3Sc_2Ga_3O_{12}$ (GSGG), $Nd_3Ga_5O_{12}$ (NGG), $Gd_{2.6}Ca_{0.4}Ga_{4.1}Mg_{0.25}Zr_{0.65}O_{12}$ (GSGG), $Y_3Sc_2Ga_3O_{12}$ (YSGG), $Gd_3Ga_5O_{12}$ (GGG), $Tb_3Ga_5O_{12}$ (TGG), and $Y_3Al_5O_{12}$ (YAG). The substrates were each annealed inside the PLD chamber prior to deposition at 220°C for 5 h with a base pressure of $<10^{-6}$ Torr, and then subsequently heated to a temperature of 600°C for 30 minutes in an atmosphere of 1.5 mTorr oxygen mixed with 12% ozone by weight. The target was then ablated with a pulsed 248 nm KrF excimer laser with a power of 156 mJ at a 1 Hz repetition rate while the substrates were maintained at 600°C in the oxygen rich atmosphere.

EuIG films with a thickness of 50 nm were grown on each of the different substrates, except for the film grown on YAG which had a thickness of 20 nm. For thicker films grown on YAG, the strain is almost completely relaxed to the bulk value due to the large lattice mismatch η = -3.945%. A thinner sample was therefore grown on YAG in order to preserve more of the compressive strain in the film. Similarly, a second 25 nm thick film was grown on GSGG which had the largest lattice mismatch η = +0.456% out of the films grown with tensile strain. Immediately after deposition, reflection high-energy electron diffraction (RHEED) measurements were performed, showing no crystalline order in any of the films. The films were

Table 5.1: A summary of various structural and magnetic properties for the epitaxial (111)-oriented EuIG films grown with PLD. Strain values marked with an * were determined from asymmetric reciprocal space maps.[1]

Substrate	$a_{subs.}$ (Å)	t (nm)	η (%)	$\varepsilon_{//}$ (%)	$\varepsilon_{\perp}$ (%)	$H_{2\perp}$ (Oe)	$H_{4\perp}$ (Oe)	α ($x10^{-2}$)	ΔH_0 (Oe)
GSGG	12.554	25	0.456	0.456*	-0.213	-1543.6 ± 39.7	709.5 ± 27.5	1.58 ± 0.06	10.2 ± 1.7
GSGG	12.554	50	0.456	0.341	-0.160	-1394.2 ± 44.9	339.8 ± 6.6	2.46 ± 0.03	21.4 ± 1.3
NGG	12.505	50	0.064	0.119*	-0.064	-1224.4 ± 5.7	18.3 ± 0.1	2.41 ± 0.01	8.9 ± 0.7
SGGG	12.480	50	-0.136	-0.129	0.060	-909.6 ± 15.2	164.8 ± 1.4	2.13 ± 0.01	5.6 ± 0.4
YSGG	12.426	50	-0.568	-0.321*	0.123	-709.4 ± 22.0	377.3 ± 5.1	2.47 ± 0.03	9.9 ± 1.8
GGG	12.383	50	-0.912	-0.400*	0.210	-1015.0 ± 81.3	887.2 ± 37.3	2.20 ± 0.14	412.2 ± 8.4
TGG	12.355	50	-1.136	-0.382	0.179	-393.4 ± 53.6	245.0 ± 10.0	2.29 ± 0.20	253.4 ± 11.8
YAG	12.004	20	-3.945	-0.423	0.198	-36.8 ± 47.1	424.8 ± 20.9	1.86 ± 0.20	217.0 ± 22.6

then crystallized using rapid thermal annealing (RTA) at 800°C for 200 s under a steady flow of oxygen. The lattice parameters of the substrates, the resulting lattice mismatch, and the thicknesses of the various samples are all provided in **Table 5.1**.

5.3. Results and Discussion

5.3.1. Strain Behavior of Epitaxial EuIG

The structures of the films were evaluated by high-resolution x-ray diffraction using a Rigaku SmartLab diffractometer with Cu $K\alpha_1$ radiation and a double bounce Ge-(220) mirror set-up as a monochromator. 2θ-θ scans of the (444) peaks were collected for each of the samples and are plotted together in comparison to the fully relaxed EuIG (444) position in **Fig. 5.1**. The film peak position is observed at lower 2θ positions relative to the relaxed value for films grown on substrates with a lattice mismatch $\eta < 0$, indicating larger out-of-plane d-spacings and therefore compressive in-plane strain. The films grown on substrates with a lattice mismatch $\eta > 0$ show peak positions at higher 2θ values than the relaxed position, indicating smaller out-of-plane d-spacings and therefore tensile in-plane strain. The only exception to this is the XRD curve collected for the film grown on NGG ($\eta = +0.064\%$) which shows the film peak to the left of the relaxed value, seeming to imply that the film is experiencing compressive in-plane strain. However, in previous 2θ measurements using a Ni filter monochromator and then also in follow up reciprocal space mapping (RSM) measurements, the film was shown to be under tensile in-plane strain as expected from its slightly larger lattice parameter ($a_{NGG} = 12.505$ Å vs. $a_{EuIG} = 12.497$ Å). The fact that the film peak is observed at lower 2θ values in this individual measurement is thought to be due to both experimental misalignment and the very small difference in d-spacing of the film and substrate (444) planes. The collected 2θ scans also contain Laue oscillations for most of the samples. These oscillations indicate a high degree of

crystalline order and conformal growth, in addition to smooth interfaces. Notably, fringes are not visible for samples with the largest lattice mismatch, namely the films grown on GGG, TGG and YAG, implying that these films have nonuniform strain relaxation. The (444) peaks of these three samples also appear very close to the bulk value, indicating significantly relaxed strain.

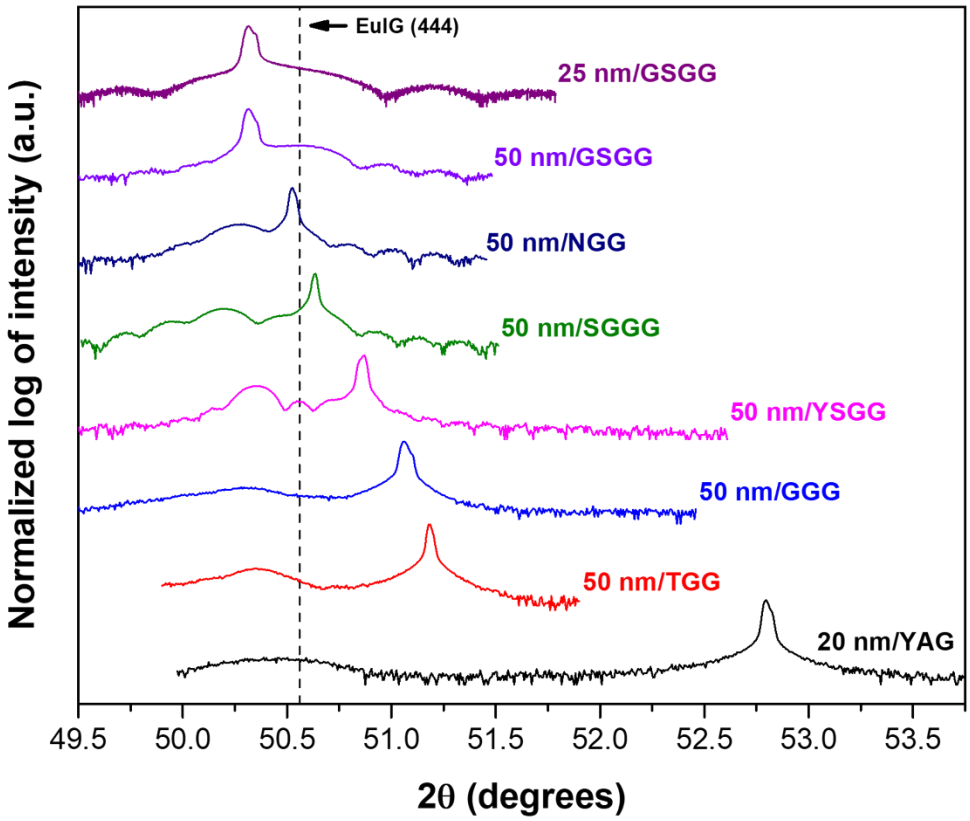

Fig. 5.1: 2θ XRD scans of the (444) peak of the epitaxial EuIG films grown by PLD. The dashed line represents the fully relaxed 2θ position of the EuIG (444) peak.

The in-plane strain $\varepsilon_{//}$ of epitaxial films is often inferred from the out-of-plane strain $\varepsilon_{\perp}$ since this value is relatively easy to obtain from a standard 2θ-θ XRD measurement. For an elastically isotropic (111)-oriented cubic film, the in-plane and out-of-plane strains are related according to the following equation:

$$\varepsilon_{//} = -\frac{c_{11}+2c_{12}+4c_{44}}{2c_{11}+4c_{12}-4c_{44}}\varepsilon_{\perp}, \tag{5.2}$$

where c_{ij} are the elastic stiffness constants of the given material, and the out-of-plane strain is defined as

$$\varepsilon_{\perp} = \frac{a_{\perp} - a_0}{a_0}, \tag{5.3}$$

where a_0 is the relaxed lattice parameter of the bulk material, and $a_{\perp}$ is the out-of-plane lattice parameter of the strained film.[2] The out-of-plane lattice parameter $a_{\perp}$ is readily attainable from the 2θ peak position of the film according to

$$a_{\perp} = d_{hkl}\sqrt{h^2 + k^2 + l^2}, \tag{5.4}$$

where d_{hkl} is calculated according to Bragg's law, expressed as

$$n\lambda = 2d_{hkl}\sin\theta, \tag{5.5}$$

where λ is the wavelength of diffracted x-ray and n is the diffraction order.

This approach assumes that both the lattice parameter and elastic stiffness constants of the deposited material match the bulk values. However, these properties could differ from the bulk values given the presence of crystalline point defects or deviation from stoichiometry in the as-grown films. Since the deposition process itself can potentially introduce these types of changes, the only way to know the exact lattice parameter of the deposited material is to grow a sufficiently thick enough film to be considered as bulk. This is often not very practical, so there exists an inherent level of uncertainty in the intrinsic lattice parameter of all epitaxially strained films. The in-plane lattice parameter $a_{//}$, however, can be precisely measured from an asymmetric reciprocal space map (RSM), thus allowing for a direct measurement of the in-plane strain, and by extension, the elastic response of the film to strain.

Asymmetric RSMs were collected about the (642) peak position for the 25 nm film grown on GSGG (η = +0.456%), and for the 50 nm films grown on NGG (η = +0.064%), YSGG (η = -0.568%) and GGG (η = -0.912%). The RSMs are presented in **Fig. 5.2-5.5** in order of

decreasing η. The Q-coordinates of both the film and substrate (642) peaks were identified and are listed in **Table 5.2** in comparison to the theoretical coordinates as calculated according to the following relationships:

$$Q_X = \frac{1}{\lambda}(\cos(2\theta-\omega)-\cos\omega); \quad (5.6)$$

$$Q_Z = \frac{1}{\lambda}(\sin(2\theta-\omega)+\sin\omega), \quad (5.7)$$

where θ is the angle of the diffracted beam relative to the crystalline plane and ω is the angle of the incident beam relative to the focal plane of the XRD.[3] The experimentally found Q-coordinates of all substrates are found to be in good agreement with the theoretical positions calculated using their reference lattice parameters. The Q_X positions of the films grown on GSGG, NGG and YSGG are also found to be nearly identical to the Q_X positions of their respective substrates, which is a clear indication of well conformed films. However, the film that was grown on GGG which has the largest lattice mismatch out of the samples studied with RSMs shows an elongated peak region with one peak top centered almost exactly along the vertical Q_X position of the film at (0.22856 $Å^{-1}$, 0.55025 $Å^{-1}$), and a second more diffuse peak top centered at (0.22724 $Å^{-1}$, 0.55322 $Å^{-1}$) that more generally spreads in the direction of the relaxed EuIG (642) peak position of (0.22633 $Å^{-1}$, 0.55439 $Å^{-1}$). This indicates nonuniform relaxation of strain with two structurally distinct regions of the film, the first being a highly strained epitaxial region of the film near the interface with GGG, and the second being a relaxed region closer to the free surface of the film. The Q_Z values of all four films closely match the out-of-plane strain information determined from the 2θ-θ measurements. One other thing worth noting about the RSMs collected for the samples grown on NGG and YSGG is that these measurements used a larger experimental ω step value, resulting in a visibly lower resolution than for the other two mapped samples.

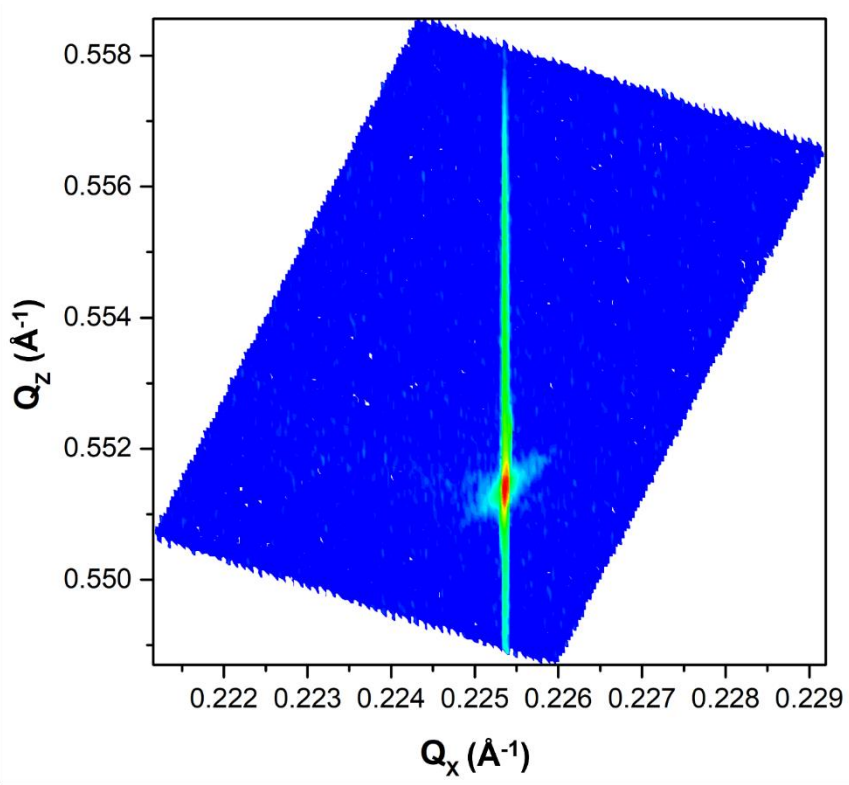

Fig. 5.2: Asymmetric RSM around the (642) peak of the (111)-oriented 25 nm EuIG/GSGG film.

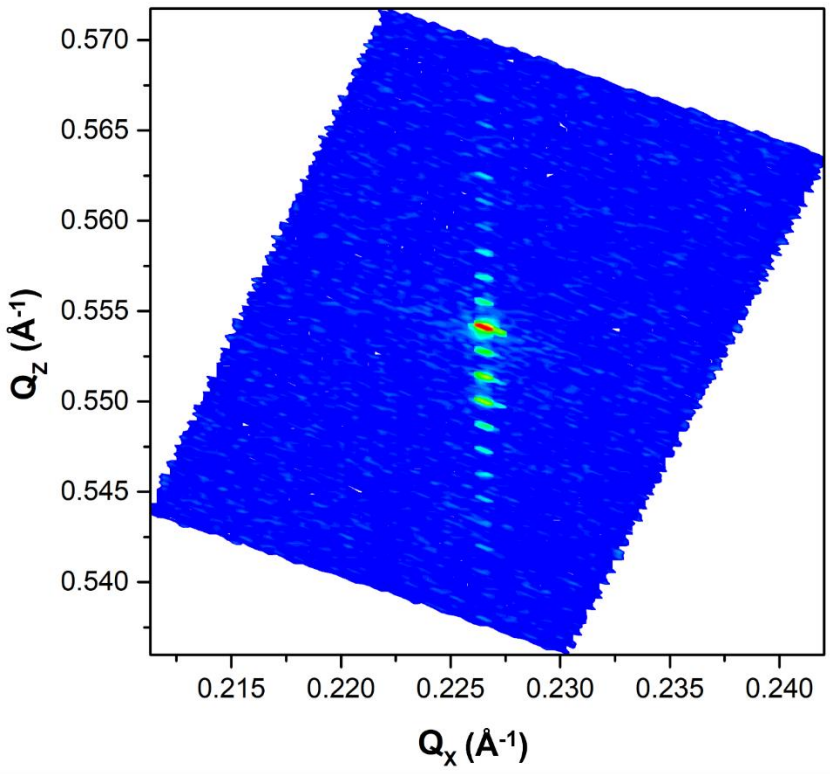

Fig. 5.3: Asymmetric RSM around the (642) peak of the (111)-oriented 50 nm EuIG/NGG film.

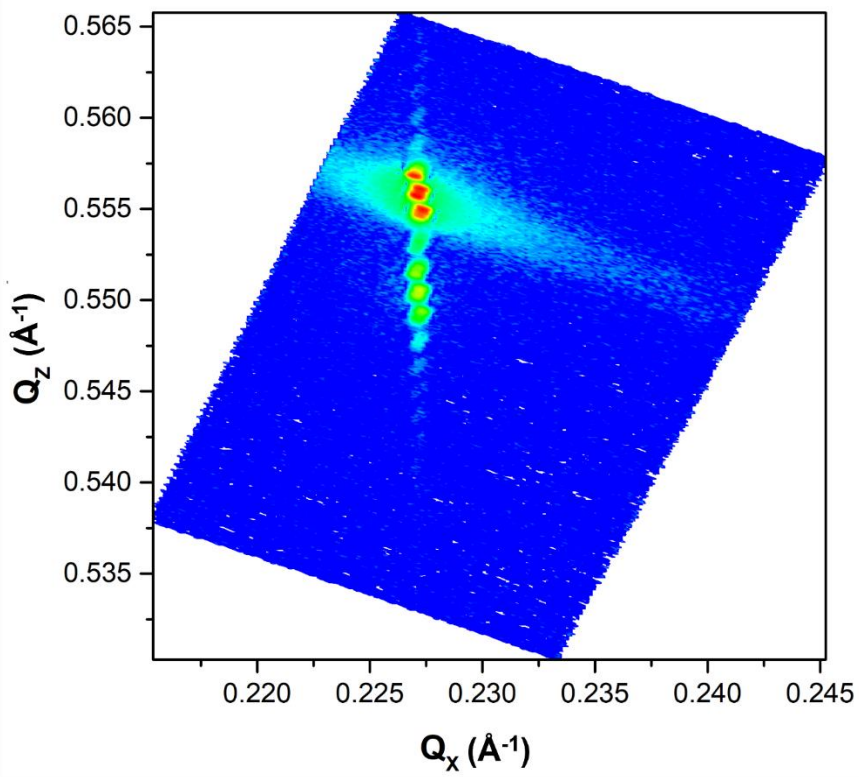

Fig. 5.4: Asymmetric RSM around the (642) peak of the (111)-oriented 50 nm EuIG/YSGG film.

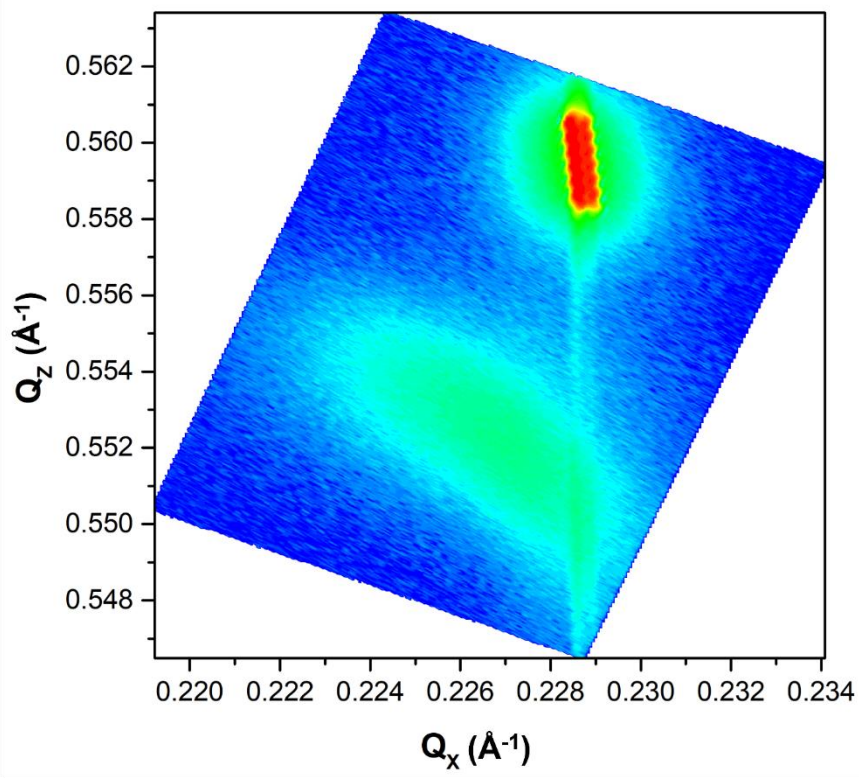

Fig. 5.5: Asymmetric RSM around the (642) peak of the (111)-oriented 50 nm EuIG/GGG film.

The in-plane strain values of the same four films were also calculated from the out-of-plane 2θ-θ measurements using eq. (5.2) and the following elastic stiffness values found in literature: c_{11} = 25.10 x 10^{11} dyn/cm^2, c_{12} = 10.70 x 10^{11} dyn/cm^2, and c_{44} = 7.62 x 10^{11} dyn/cm^2.[4] The in-plane strain predicted by the elastic equations is plotted versus the in-plane strain directly measured by the asymmetric RSMs in **Fig. 5.6**. The strain values determined by the two methods are shown to be directly proportional to each other, although the in-plane strain predicted by the elastic equation is ~42% lower than the true strain of the film. This indicates that the elastic stiffness constants of the as-grown EuIG are different from the literature values, which could mean that the films are nonstoichiometric or contain atomic point defects. For the

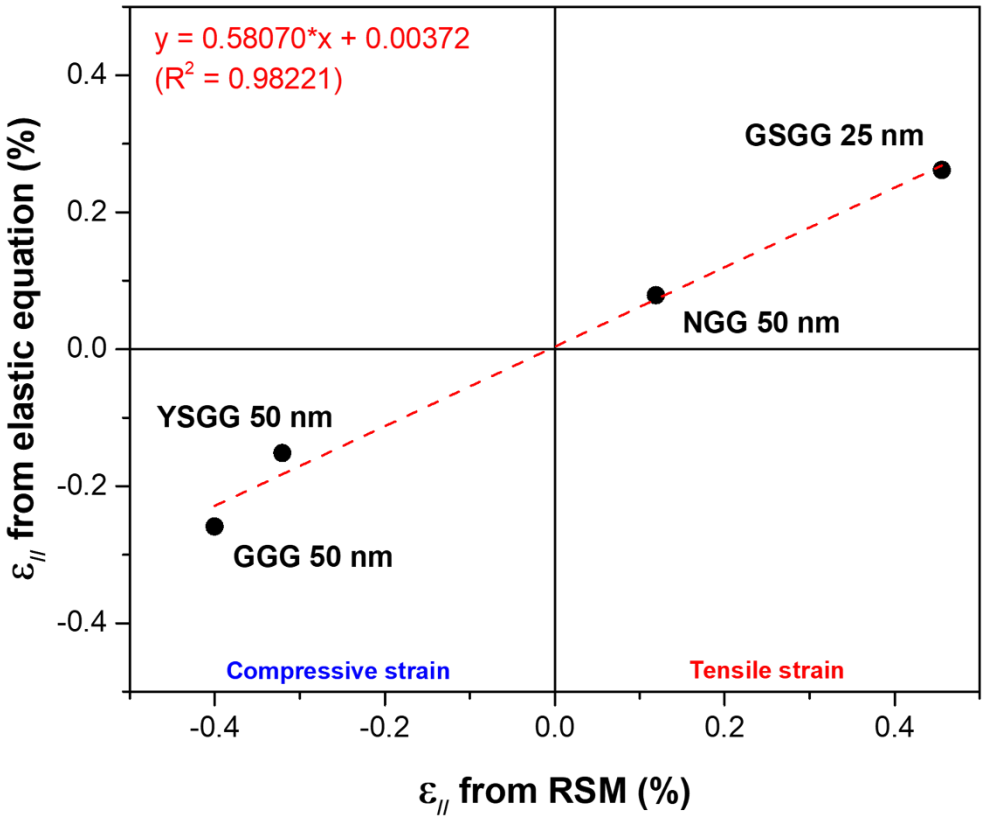

Fig. 5.6: The in-plane strain calculated from elastic equations using the out-of-plane strain determined from 2θ-θ measurements plotted versus the in-plane strain directly measured from asymmetric reciprocal space maps for a subset of (111)-oriented epitaxial EuIG films.

films that weren't measured with RSM, the in-plane strain was calculated from the out-of-plane strain using a modified eq. (5.2) that was multiplied by a constant scaling factor as determined from the slope of the fitted line in **Fig. 5.6**. The out-of-plane strain as determined by the 2θ-θ measurements, and the in-plane strain as determined by either RSM or the modified eq. (5.2) are provided for all films in **Table 5.1**.

Table 5.2: A summary of the film and substrate (642) peak positions in Q-coordinates for the epitaxial (111)-oriented EuIG samples measured with asymmetric reciprocal space maps.

Sample	Substrate Q_X ($Å^{-1}$)		Substrate Q_Z ($Å^{-1}$)		EuIG Q_X ($Å^{-1}$)	EuIG Q_Z ($Å^{-1}$)
	Theor.	Exp.	Theor.	Exp.		
25 nm on GSGG	0.22530	0.22538	0.55187	0.55140	0.22530	0.55557
50 nm on NGG	0.22618	0.22656	0.55404	0.55407	0.22606	0.55474
50 nm on YSGG	0.22762	0.22711	0.55756	0.55575	0.22706	0.55371
50 nm on GGG	0.22841	0.22855	0.55949	0.55950	0.22724	0.55322
Bulk EuIG Ref.	--	--	--	--	0.22633	0.55439

5.3.2. Magnetic and Magnetoelastic Properties of Epitaxial EuIG

The magnetic properties of the epitaxial EuIG films were extensively studied by our collaborators who grew them using VSM, frequency dependent FMR, and polar angle dependent FMR measurement techniques. For all films in this study, the $4\pi M_S$ was found using VSM to be nearly 920 G, which is ~23% lower than the literature value of 1193 G.[5] VSM also showed that the magnetic easy axes lie in-plane for all of the films. Frequency dependent FMR measurements were then carried out using a co-planar waveguide set-up with the field applied in-plane. $4\pi M_{eff}$ values were determined from the frequency dependence of H_R by fitting to the resonant equation as follows:

$$f_R = \frac{\gamma}{2\pi}\sqrt{H_R(H_R+4\pi M_{eff})}, \quad (5.8)$$

where f_R is the resonant frequency, H_R is the resonant field, and γ is the gyromagnetic ratio.[6]

In order to extract the Gilbert damping and inhomogeneous contribution to linewidth for each of the samples, the FMR linewidths are plotted as a function of frequency and fit with a

straight line, as shown in **Fig. 5.7a**. Assuming that the broadening due to two-magnon scattering is negligible, the Gilbert damping parameter is extracted from the slope of the fit and the intercept is the inhomogeneous broadening, according to

$$\Delta H = \frac{2\pi\alpha}{\gamma} f_R + \Delta H_0, \quad (5.9)$$

where α is the gilbert damping and ΔH_0 is the inhomogeneous broadening.[7] For the samples with moderate lattice mismatches, the linewidths follow a very linear trend with frequency and have low levels of inhomogeneous broadening on the order of ~10 Oe. The samples with larger lattice mismatches, namely the films grown on GGG (η = -0.912%), TGG (η = -1.136%) and YAG (η = -3.945%), have somewhat less linear frequency dependence with respect to linewidth and much larger inhomogeneous broadening in the range of ~200-400 Oe. The increased amount of magnetic inhomogeneity in these samples can be explained by their large epitaxial strain which resulted in nonuniform strain relaxation. The inhomogeneous broadening and Gilbert damping values are plot versus in-plane strain in **Fig. 5.7b**. Despite the observed differences in broadening, the damping is unaffected by magnetic inhomogeneity and has an average value of 2.17×10^{-2}. The experimental α and ΔH_0 are included in **Table 5.1**.

In order to evaluate the magnetic anisotropy of the films, angle dependent FMR measurements were performed across a polar angle range of 0° to 180° in 10° steps using a microwave cavity type FMR at a fixed frequency of 9.32 GHz. The obtained H_R values were fit as a function of polar angle by considering the first-order $-K_1\cos^2\theta$ and the second-order $-\frac{1}{2}K_2\cos^4\theta$ crystalline anisotropy energy terms.[8] Values for $4\pi M_{eff}$, $H_{2\perp}$ and $H_{4\perp}$, where $4\pi M_{eff} = 4\pi M_S - H_{2\perp}$, $H_{2\perp} = \frac{2K_1}{M_S}$, and $H_{4\perp} = \frac{2K_2}{M_S}$, were extracted from the fits. It is important to note that $H_{2\perp}$ and $H_{4\perp}$ are the first- and second-order anisotropy fields, respectively, and that they favor an out-of-plane magnetization direction when they are positive and an in-plane magnetization when

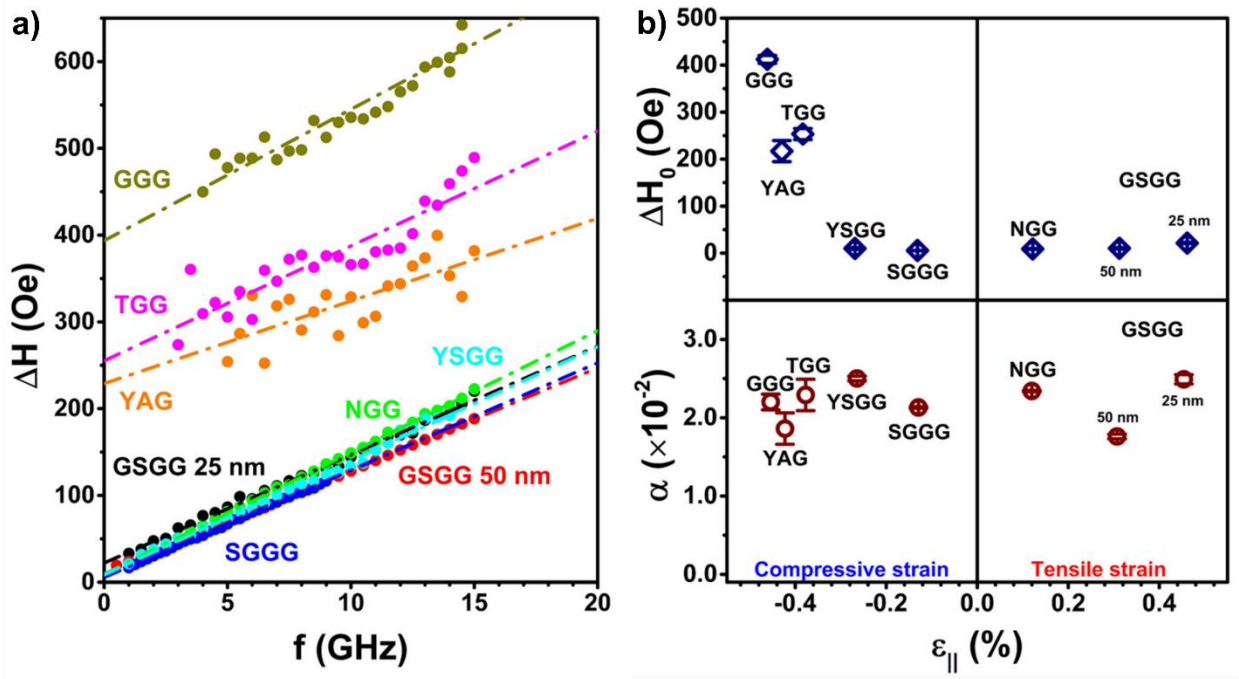

Fig. 5.7: Results of the frequency dependent FMR measurements of the PLD grown EuIG plotted as (a) linewidths as a function of frequency, and (b) inhomogeneous broadening and gilbert damping as a function of in-plane strain.[1]

they are negative. The $4\pi M_{eff}$ values found from the fits agree well with the previously determined $4\pi M_{eff}$ values from the frequency dependent FMR measurements. All extracted $H_{2\perp}$ values were found to be negative, while all $H_{4\perp}$ were positive. $H_{2\perp}$ and $H_{4\perp}$ are plotted as a function of strain in **Fig. 5.8**. This figure clearly shows that $H_{2\perp}$ depends linearly on in-plane strain, whereas $H_{4\perp}$ has a quadratic dependence, as is expected for each term. These results also show that the second order-anisotropy field is quite significant for in-plane strains with magnitudes ≥0.2 - 0.3%. The experimentally determined $H_{2\perp}$ and $H_{4\perp}$ values are included in **Table 5.1** for all samples.

It was expected from theory that some of the more strained films would have exhibited signs of perpendicular magnetic anisotropy, however all films in this study have in-plane magnetic easy axes. The first-order anisotropy field of a strained (111)-oriented film is well described by the following relationship which depends linearly on stress:

$$H_{2\perp} = \frac{-4K_1 - 9\lambda_{111}\sigma_{//}}{3M_S}, \tag{5.10}$$

where K_1 is the first-order cubic anisotropy constant, λ_{111} is the magnetostriction constant for the (111) direction and $\sigma_{//}$ is the in-plane stress.[9] For films grown with a (111)-orientation, the in-plane stress is related to the out-of-plane strain $\varepsilon_\perp$ by the elastic stiffness constants according to

$$\sigma_{//} = -6c_{44}\frac{c_{11}+2c_{12}}{2c_{11}+4c_{12}-4c_{44}}\varepsilon_\perp.[2] \tag{5.11}$$

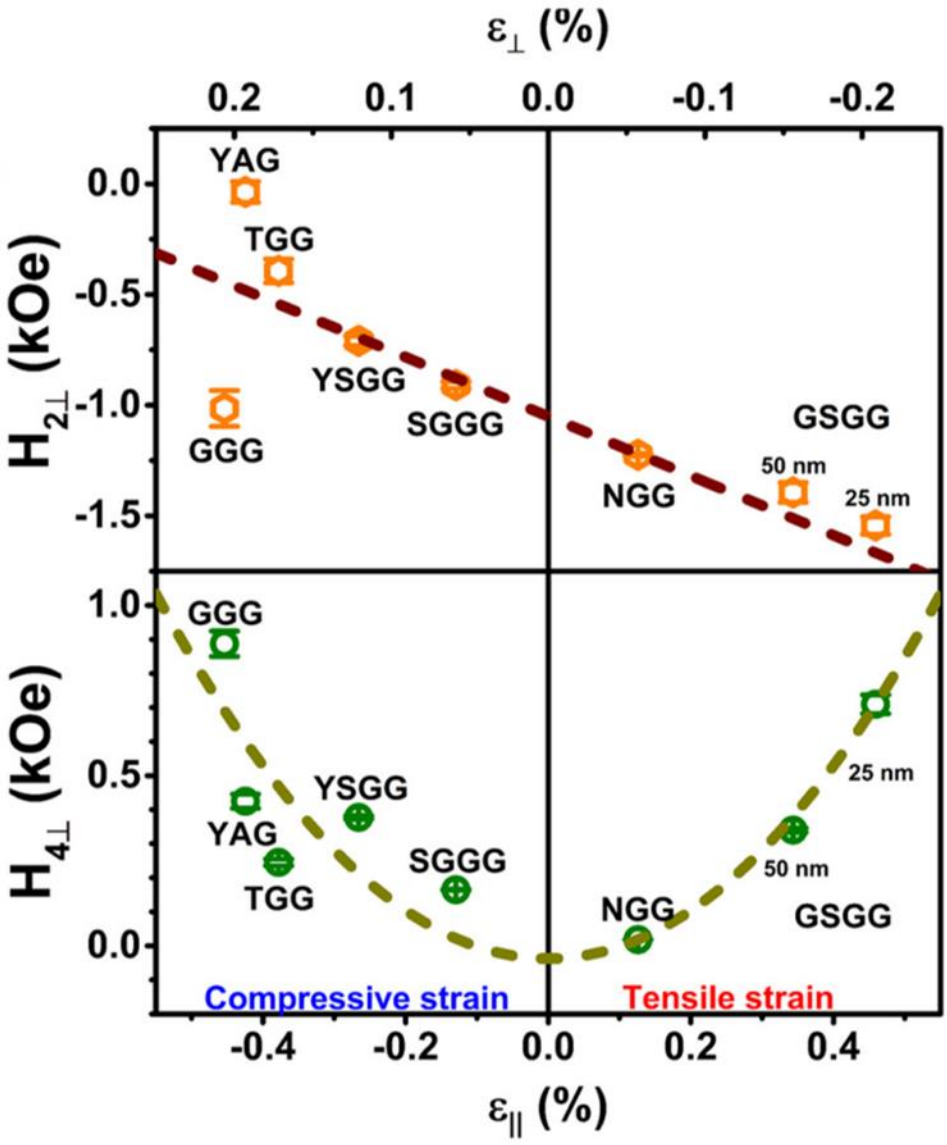

Fig. 5.8: The first-order magnetic anisotropy $H_{2\perp}$ and the second-order magnetic anisotropy $H_{4\perp}$ plotted as a function of strain for the epitaxial (111)-oriented EuIG films grown with PLD.[1]

Using the elastic stiffness values found in literature (c_{11} = 25.10 x 10^{11} dyn/cm^2, c_{12} = 10.70 x 10^{11} dyn/cm^2, and c_{44} = 7.62 x 10^{11} dyn/cm^2) [4], an unstrained a_{EuIG} = 12.497 Å, and λ_{111} = 1.8 x 10^{-6} [10], eq. (5.10) and (5.11) dictate that perpendicular magnetic anisotropy is expected to dominate for out-of-plane strains greater than +0.341%, or for in-plane strains less than -0.419%.

To better understand why the $H_{2\perp}$ of the films differed from theory, the experimental $H_{2\perp}$ values were plotted versus the out-of-plane strain $\varepsilon_\perp$ and then fit with a linear equation, as shown in **Fig. 5.9**. Aside from the two data points for the films grown on GGG and YAG that also have nonuniform strain relaxation, the fit matches the experimental data reasonably well. The first-order anisotropy constant was found from the intercept according to eq. (6.10) to be K_1 = +57.2 ± 1.6 x 10^3 erg/cm^3, which has a different magnitude and opposite sign as the K_1 = -35 x 10^3 erg/cm^3 that was previously reported for single crystal EuIG.[11] The large difference in K_1 likely indicates that the EuIG films deviate from stoichiometry and could contain atomic point defects. A magnetoelastic term combining the magnetostriction constant with the elastic stiffness constants was defined as $\Lambda = (\lambda_{111}\sigma_{//})/\varepsilon_\perp$. This magnetoelastic term was extracted from the slope of the fit and has a value of $\Lambda_{Exp.}$ = -6.89 ± 0.91 x 10^4 dyne/cm^2. The same term was calculated from literature values as $\Lambda_{Lit.}$ = -6.12 x 10^4 dyne/cm^2, which is ~11% lower in magnitude than the experimentally derived value. It is worth pointing out that even though the in-plane strain calculated using elastic equations is ~42% lower than the true strain of these films, their magnetoelastic response to strain is not nearly as affected. The necessary out-of-plane strain required for these films to produce perpendicular magnetic anisotropy was then determined from the fit to be greater than +0.695%, or for in-plane strains less than -1.47%.

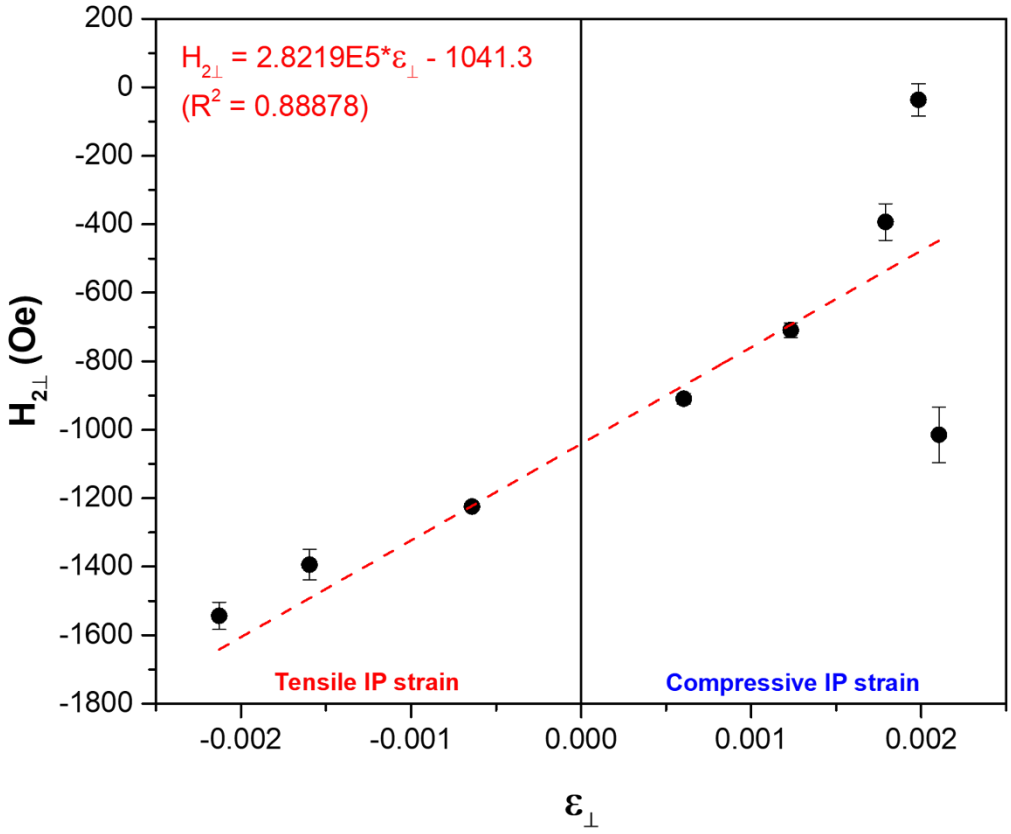

Fig. 5.9: The first order-anisotropy field $H_{2\perp}$ of the epitaxial (111)-oriented EuIG films grown with PLD plotted as a function of out-of-plane strain $\varepsilon_\perp$ and then fit with a linear function.

5.4. Conclusions

Stress induced magnetic anisotropy was systematically controlled and characterized in epitaxial (111)-oriented EuIG films grown using PLD by depositing them on various garnet substrates with lattice mismatches ranging from η = +0.456% to η = -3.945%. The in-plane and out-of-plane strain of the films were characterized through a combination of high-resolution x-ray diffraction 2θ-θ measurements and asymmetric reciprocal space maps. The elastic equation relating in-plane strain to out-of-plane strain was shown to systematically underestimate the in-plane strain by ~42% when compared to the strain directly measured from the reciprocal space maps. For samples grown with a lattice mismatch of less than ~0.6% in magnitude, the films

were shown to be well-conformed to the substrate, however, the films grown with larger magnitudes of lattice mismatch showed evidence of nonuniform strain relaxation.

The first-order magnetic anisotropy $H_{2\perp}$ and second-order magnetic anisotropy $H_{4\perp}$ values of the films were determined using polar angle dependent FMR. All $H_{2\perp}$ values were found to be negative, preferring an in-plane magnetization direction, whereas all $H_{4\perp}$ values were found to be positive, preferring an out-of-plane magnetization direction. All of the samples have magnetic easy axes lying in the plane of the films as well. When plotted against strain, $H_{2\perp}$ was shown to have a linear dependence and $H_{4\perp}$ was shown to have a quadratic dependence, as expected for each term. For films with small in-plane strains, $H_{4\perp}$ is small and the magnetic anisotropy is well described by $H_{2\perp}$, but for magnitudes of strain of ~0.2 - 0.3% or larger, $H_{4\perp}$ cannot be ignored. The first-order anisotropy constant of the films was determined from the $H_{2\perp}$ data as $K_1 = +57.2 \pm 1.6 \times 10^3$ erg/cm^3, which is quite different from the literature value of $K_1 = -35 \times 10^3$ erg/cm^3.[11] Despite the observed ~42% difference in elastic behavior from theory, the theoretical magnetoelastic response to in-plane strain is only ~11% lower than the observed magnetoelastic behavior of the films.

The Gilbert damping and inhomogeneous broadening of the films were also characterized with frequency dependent FMR measurements. The inhomogeneous contribution to broadening is only ~10 Oe in the well conformed films grown with smaller lattice mismatches but is as large as ~425 Oe in the films with larger lattice mismatches. The large inhomogeneous broadening of the films with higher epitaxial strain is explained by their nonuniform strain relaxation. Despite the large differences in magnetic inhomogeneity, the damping remains unaffected and has a nearly constant value of $\sim 2.2 \times 10^{-2}$ for all films.

In addition to the observed differences in elasticity, magnetoelasticity and K_1 from the literature values, the $4\pi M_S$ of the films is ~920 G, which is ~23% lower than what's reported for bulk EuIG. The large number of physical differences between these samples and references from literature implies that the as-grown material is chemically different from pristine EuIG. Stoichiometric differences could manifest as deviation in the chemical ordering of the garnet structure, constitutional vacancies, or both. To identify exact reasons why the properties are different would require elemental analysis of both the initial target and as-grown films, and perhaps supporting evidence from Mössbauer spectroscopy. Without this information, it is difficult to determine whether the deposition process changed the stoichiometry of the target material. Regardless, these results show that the in-plane strain cannot accurately be inferred from the out-of-plane strain if the deposited material has different elastic stiffness constants than the reference material. Since one typically cannot know the stiffness constants of an as-grown epitaxial film a priori, it is therefore prudent to perform asymmetric reciprocal space maps in order to directly measure the in-plane structure. Combining elemental analysis with reciprocal space mapping could also provide useful insight into how the elastic behavior of rare earth iron garnets depends on stoichiometry, thus enhancing the ability to tailor perpendicular magnetic anisotropy in rare earth iron garnets.

Acknowledgements

Chapter 5 contains data and figures as they were published in V. H. Ortiz, B. Askook, J. Li, M. Aldosary, M. Biggerstaff, W. Yuan, C. Warren, Y. Kodera, J. E. Garay, I. Barsukov, and J. Shi. First- and second-order magnetic anisotropy and damping of europium iron garnet under high strain. Phys. Rev. Mater., 5 (2021) 124414. The dissertation author was a co-author and co-researcher on this paper.

REFERENCES

[1] V. H. Ortiz, B. Askook, J. Li, M. Aldosary, M. Biggerstaff, W. Yuan, C. Warren, Y. Kodera, J. E. Garay, I. Barsukov, and J. Shi. First- and second-order magnetic anisotropy and damping of europium iron garnet under high strain. Phys. Rev. Mater., 5 (2021) 124414.

[2] E. Annastassakis. Strained supperlattices and heterostructures: elastic considerations. J. Appl. Phys., 68 (1990) 4561.

[3] M. A. Moram, and M. E. Vickers. X-ray diffraction of III-nitrides. Rep. Prog. Phys., 72 (2009) 036502.

[4] T. B. Bateman. Elastic Moduli of Single-Crystal Europium Iron Garnet and Yttrium Iron Garnet. J. Appl. Phys., 37 (1966) 2194.

[5] G. Winkler. *Magnetic Garnets* (Vieweg, Braunschweig, 1981).

[6] C. Kittel. On the Theory of Ferromagnetic Resonance Absorption. Phys. Rev., 73 (1948) 2.

[7] B. Buford, P. Dhagat, and A. Jander. A technique for error estimation of linewidth and damping parameters extracted from ferromagnetic resonance measurements. J. Appl. Phys., 117 (2015) 17E109.

[8] I. Barsukov, Y. Fu, A. M. Gonçalves, M. Spasova, M. Farle, L. C. Sampaio, R. E. Arias, and I. N. Krivorotov. Field-dependent perpendicular magnetic anisotropy in CoFeB thin films. Appl. Phys. Lett., 105 (2014) 152403.

[9] D. M. Heinz, P. J. Besser, J. M. Owens, J. E. Mee, and G. R. Pulliam. Mobile Cylindrical Magnetic Domains in Epitaxial Garnet Films. J. Appl. Phys., 42 (1971) 1243.

[10] S. Iida. Magnetostriction Constants of Rare Earth Iron Garnets. J. Phys. Soc. Japan, 22 (1967) 5.

[11] T. Miyadi. Ferrimagnetic Reasonance in Europium-Iron Garnet. J. Phys. Soc. Japan, 15 (1960) 12.

[12] V. H. Ortiz, M. Aldosary, J. Li, Y. Xu, M. I. Lohmann, P. Sellappan, Y. Kodera, J. E. Garay, and J. Shi. Systematic control of strain-induced perpendicular magnetic anisotropy in epitaxial europium and terbium iron garnet thin films. APL Mater., 6 (2018) 121113.

[13] M. Sparks. *Ferromagnetic-Relaxation Theory* (McGraw-Hill, New York, 1964).

[14] R. C. LeCraw, W. G. Nilsen, J. P. Remeika, and J. H. Van Vleck. Ferromagnetic Relaxation in Europium Iron Garnet. Phys. Rev. Lett., 11 (1963) 490-493.

CHAPTER 6

Off-axis Sputtered Epitaxial EuIG Films with Robust Perpendicular Magnetic Anisotropy

6.1. Background and Motivation

Ferrimagnetic insulators play a significant role in spintronics research as magnon spin current sources [25-29], static exchange coupling sources [30-33] and low dissipation spin current media [34,35]. The Gilbert damping in ferrimagnetic insulators such as YIG or LuIG is two to three orders of magnitude lower than that in metals. The low magnetic damping of ferrimagnetic insulators makes it possible for spin waves to propagate over long distances in them. Another important feature that ferromagnetic insulators can have is perpendicular magnetic anisotropy, which causes the magnetization of a film to be directed out-of-plane. The perpendicular magnetic anisotropy in a ferrimagnetic layer breaks the time-reversal symmetry in an adjacent nonmagnetic layer with no applied field and can induce ferromagnetism through exchange interactions, which is a requisite for the anomalous Hall effect that supports dissipationless chiral edge channels.[36,37] Perpendicular magnetic anisotropy is therefore useful for fundamental studies as well as spintronics devices.

Normally, the shape anisotropy of a film causes its magnetization to be directed in-plane. A successful strategy for overcoming shape anisotropy is to induce perpendicular magnetic anisotropy by taking advantage of the magnetostriction caused by interfacial strain. The rare earth iron garnets, which includes both YIG and LuIG, are one class of ferrimagnetic insulators in which perpendicular magnetic anisotropy can be systematically tuned using interfacial strain. Some work so far has explored tuning film strain by changing the substrate type, substrate orientation, and film thickness in the TmIG, TbIG and EuIG systems.[2,18,23,38-42] A small

fraction of studies have also used cation substitution as an effective means of controlling the strain in Bi:YIG films.[40,41]

Most of the work on producing perpendicular magnetic anisotropy in rare earth iron garnet films has been accomplished using pulsed laser deposition (PLD). PLD provides important benefits for growing epitaxial films, such as a high degree of control over the deposition rate and producing films with high compositional uniformity. However, one major drawback of this method limiting its use in industry is its small coverage area. Larger films are instrumental for translating the films into technologically useful devices and facilitate characterization.

Magnetron sputtering is a widely available technology for growing thin films that has a much larger coverage area when compared to PLD, but is a difficult method to use for producing epitaxy when used in a standard configuration. Using an off-axis configuration reduces the bombardment rate on the substrate while maintaining a larger coverage area, making it easier to grow larger area epitaxial films with sputtering.[42] Additionally, using a sputtering target with smaller grain sizes has been shown to increase the grain size of the resulting films [1], which should further enhance the ability to grow epitaxial films with sputtering. This effect happens because it is easier to eject clusters of atoms from along the grain boundaries where there is more structural disorder than it is from the exposed interior regions of grains. For related reasons, a compacted nanopowder target might further improve on the quality of the films when compared to sintered targets since powders have much higher surface areas than their bulk counterparts.

There are practical difficulties associated with using a compacted powder target over a sintered one, namely that they can break apart and expose the underlying material to plasma during sputtering, or otherwise contaminate the sputtering gun and vacuum chamber. Such

difficulties could be worth the extra efforts should compacted sputtering targets facilitate the growth of large area epitaxial films in a significant way. To demonstrate the feasibility of this method to produce epitaxial films with strain induced perpendicular magnetic anisotropy, we decided to grow EuIG films from compacted powder targets using off-axis magnetron sputtering.

6.2. Sample Fabrication

A compacted powder sputtering target was fabricated from in-house synthesized Eu-Fe-O nanopowders. The Eu-Fe-O powders were synthesized with the same 3 Eu:5 Fe cation ratio of pure garnet according to the citrate sol-gel method as previously described in the methods section. In order to evaluate the phase purity and morphology of the resulting powders, a small portion of the metal-organic preceramic powders were calcined for 12 h in air over temperatures ranging from 800 – 1000°C inside of quartz boats placed in a box furnace. XRD 2θ-θ measurements were performed on the as-synthesized powders using a Rigaku SmartLab diffractometer with Cu Kα radiation in conjunction with a Ni filter monochromator. The collected XRD patterns were normalized and plotted together in **Fig. 6.1**. The XRD profile of the powder calcined at 800°C shows diffraction peaks almost entirely consistent with the perovskite phase EuIP, but as the calcining temperatures increased, the relative intensity of peaks associated with the garnet phase also increased. At a calcining temperature of 950°C or higher, the resulting powders are single phase garnet according to XRD.

In addition to the correct stoichiometric composition, we also sought uniformly sized powders with a fine microstructure. Uniformly sized powders are important to target fabrication because they aid in compacting a uniform and dense green body pellet, meanwhile sputtering targets with smaller grain sizes have been shown to have higher yields and produce films with larger grain sizes.[1] Provided that the overall stoichiometry of the powder is correct, its actual

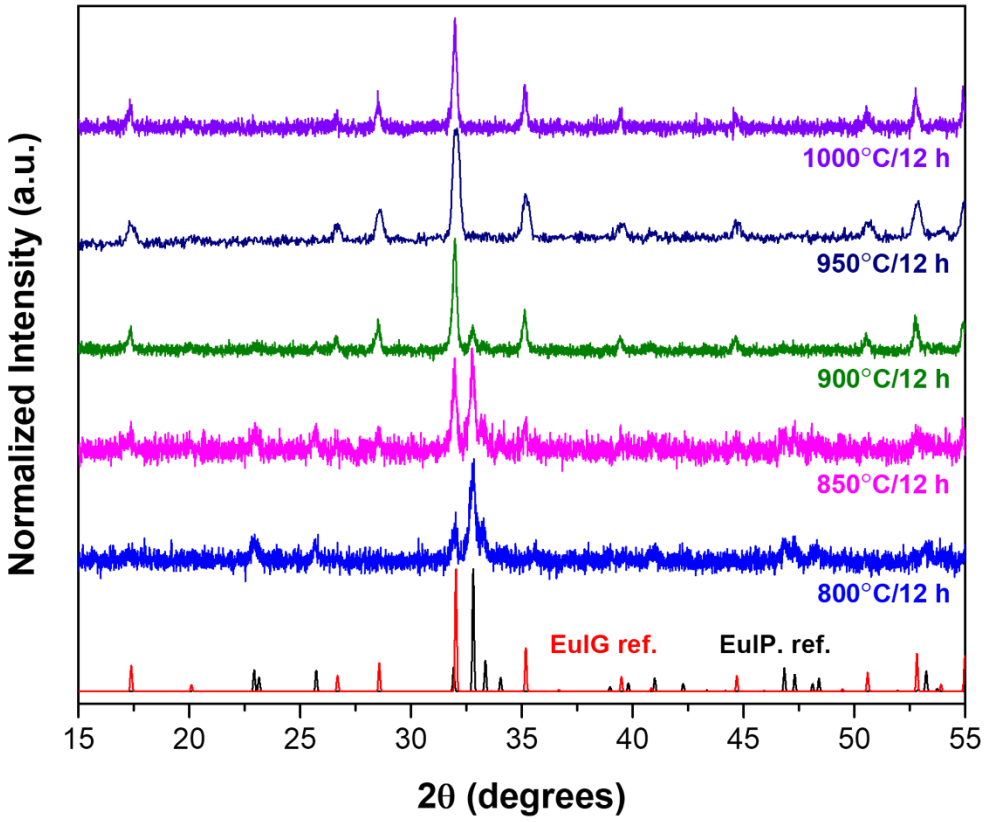

Fig. 6.1: XRD 2θ-θ measurements of EuIG powders synthesized via the citrate sol-gel route and calcined at different temperatures in air. Published XRD patterns for the garnet phase (ICSD coll. code 9232) and perovskite phase (ICSD coll. code 27277) are shown at the bottom of the graph for reference.

phase composition is a less important consideration because the subsequent deposition and growth conditions favor formation of the garnet phase. With these considerations in mind, the morphology of the calcined powders was then evaluated using SEM, and the grain sizes were manually measured using ImageJ software. The powder calcined at 800°C had a fine, granular morphology with an average grain size of 102.2 ± 30.0 nm. Representative SEM micrographs of the Eu-Fe-O powders calcined at 800°C for 12 h are shown in **Fig. 6.2**. Based on these results, the remainder of the metal-organic precursor powder was calcined at 800°C in air for 12 h. The calcined powder was then manually ground with an agate mortar and pestle for ~30 minutes. A

target was prepared by compacting ~13 g of the as-synthesized powder into a 2 in. diameter copper backing plate under an applied load of 50 MPa in a hydraulic uniaxial press.

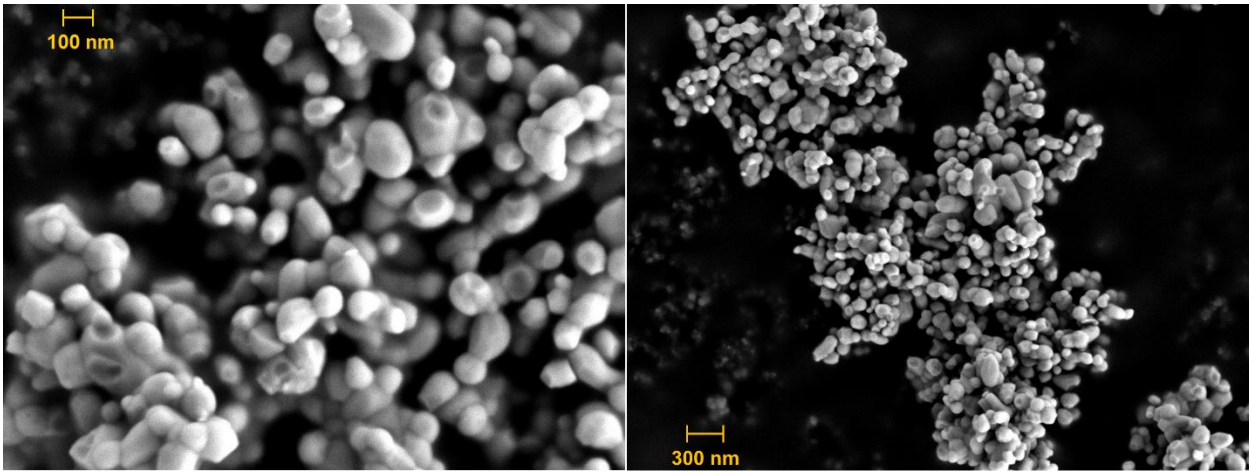

Fig. 6.2: Representative SEM micrographs of the Eu-Fe-O powders synthesized via the citrate sol-gel route and calcined at 800°C in air for 12 h.

The compacted powder target and 10 mm x 10 mm $Gd_3Ga_5O_{12}$ (GGG) substrates with (100) orientation were placed in a sputtering chamber with a 45° off-axis geometry, where the center of the target face was 5 cm from the substrate rotation axis and 5 cm below the substrate surface. A schematic representation of the sputtering configuration is shown in **Fig. 6.3**. The substrates were annealed at 220°C for 5 h with a base pressure of $<10^{-6}$ Torr before deposition. After this annealing process, the substrate temperatures were then raised and maintained at 600°C. Films were deposited at a pressure of 5 mTorr in an atmosphere of 95% Argon and 5% Oxygen by weight with a sputtering power of 100 W and an attained sputtering rate of 1.84 nm/min. Using this process, we deposited 6 films with thicknesses varying from 6 – 102 nm using this process. A representative photograph of three of the films is shown in **Fig. 6.4**. The dimensions of all films in this study are ~8 mm x 8 mm. The film does not cover the whole surface of the 10 mm x 10 mm substrate due to the clamping method involved in securing the substrates during deposition, however, we believe that our deposition method can produce larger

area films with modification to the set-up. The off-axis sputtering technique employed in this study for the growth of epitaxial films appears to have an advantage in terms of coverage area when compared to the more conventional pulsed laser deposition (PLD) technique.

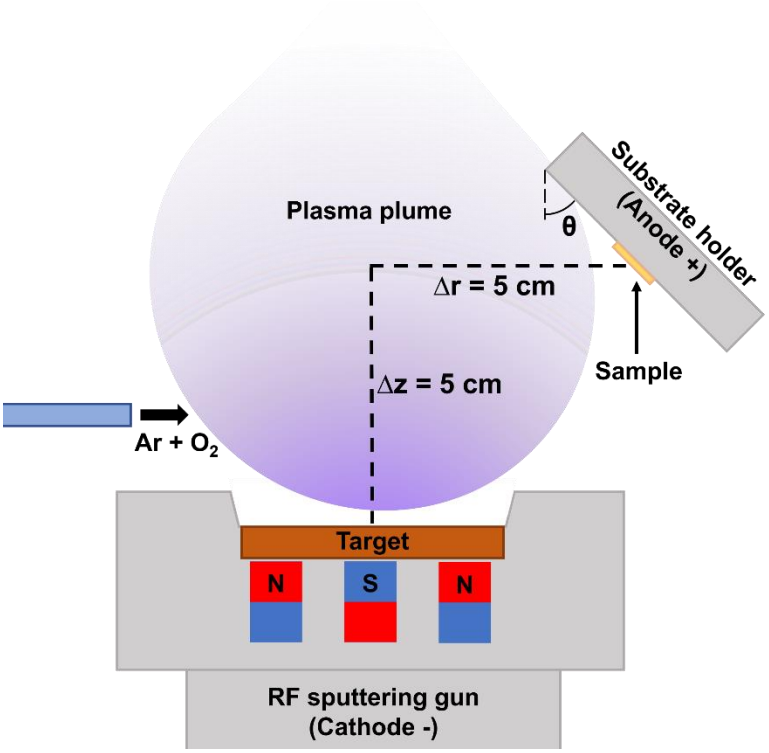

Fig. 6.3: A schematic representation of the off-axis sputtering configuration used to fabricate the epitaxial (100)-oriented EuIG/GGG films.

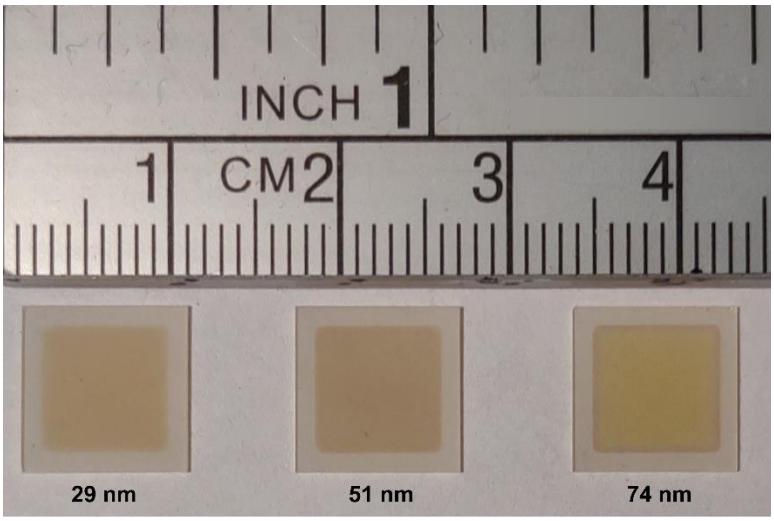

Fig. 6.4: A representative photograph of the epitaxial off-axis sputtered (100)-EuIG/GGG films with thicknesses of 29, 51 and 74 nm.

6.3. Results and Discussion

6.3.1. Structural Characterization of Off-axis Sputtered EuIG

The thicknesses of the as-prepared EuIG films were measured using a Bruker Dektak XT stylus profilometer. They were all found to be within ~2 nm of the intended thickness, indicating that the deposition rate remained nearly constant during the sputtering of all samples. The thicknesses determined through profilometry range from 6 to 102 nm and are listed in **Table 6.1**. The structures of the as-prepared films were then investigated using high resolution x-ray diffraction. 2θ-θ measurements were collected about the (400) and (800) peak positions for each sample using a Rigaku SmartLab diffractometer with Cu $K\alpha_1$ radiation that was monochromated with a double bounce Ge-(220) mirror set-up on the incident beam.

The 2θ-θ scans collected around the (800) peak are plotted together in **Fig. 6.5a**. Clear periodic Laue fringes are visible on either side of the (800) peaks of the films with thicknesses of 51 nm or less and are just barely visible on the 74 nm thick film. The presence of such fringes indicates smooth, flat interfacial and free-surface boundaries. The 2θ-θ measurements also show that the (800) peak positions associated with the out-of-plane interplanar spacing d_{800} are nearly constant across all films, suggesting successful heteroepitaxy up to 102 nm in thickness. In all samples, the film peaks are observed at lower 2θ values than that of an unstrained EuIG which indicates larger out-of-plane d_{800} interplanar spacings and therefore compressive interfacial strain. This is consistent with the difference in lattice parameters between EuIG (a_{EuIG} = 12.497 Å) and GGG (a_{GGG} = 12.376 Å). The out-of-plane d_{800} values were calculated for each of the samples from their 2θ positions according to Bragg's law, expressed as

$$n\lambda = 2d_{hkl}\sin\theta, \tag{6.1}$$

where λ is the wavelength of diffracted light. The experimentally derived $2\theta_{800}$ and d_{800} values are listed for each of the samples in **Table 6.1**.

Since the strategy for producing perpendicular magnetic anisotropy relies on interfacial strain, it is particularly important to quantify the strain of these films. Because the materials comprising the films and substrates are single crystals with a cubic crystal structure, and we assume that the EuIG of our films is elastically isotropic, the in-plane strain can be considered as a single biaxial strain $\varepsilon_{//}$. For films grown with a (100)-orientation, the out-of-plane strain $\varepsilon_{\perp}$ is related to $\varepsilon_{//}$ through the elastic stiffness coefficients c_{ij} by

$$\varepsilon_{\perp} = -\frac{2c_{12}}{c_{11}}\varepsilon_{//}, \tag{6.2}$$

$$\varepsilon_{\perp} = \frac{a_{\perp}-a_0}{a_0}, \text{ and} \tag{6.3}$$

$$\varepsilon_{//} = \frac{a_{//}-a_0}{a_0}, \tag{6.4}$$

where $a_{\perp}$ is the out-of-plane lattice parameter of the strained film, $a_{//}$ is the in-plane lattice parameter of the strained film and a_0 is the unstrained lattice parameter of the film material.[4] The out-of-plane lattice parameter is easily obtained from 2θ-θ measurements according to

$$a_{\perp} = d_{hkl}\sqrt{h^2 + k^2 + l^2}. \tag{6.5}$$

In epitaxially strained films, there are two thickness regimes describing typical strain relaxation behavior. For films below a certain critical thickness t_c, the film has a single pseudomorphic structure and its in-plane strain is given by the lattice mismatch between the film material and substrate. Once the film is thicker than t_c, dislocation formation occurs in order to minimize the total stress energy of the film and both the in-plane and out-of-plane interplanar spacings approach the unstrained value as the film thickness increases, i.e. strain relaxation.[3] However, this relaxation behavior is not observed in these films. This phenomenon is best

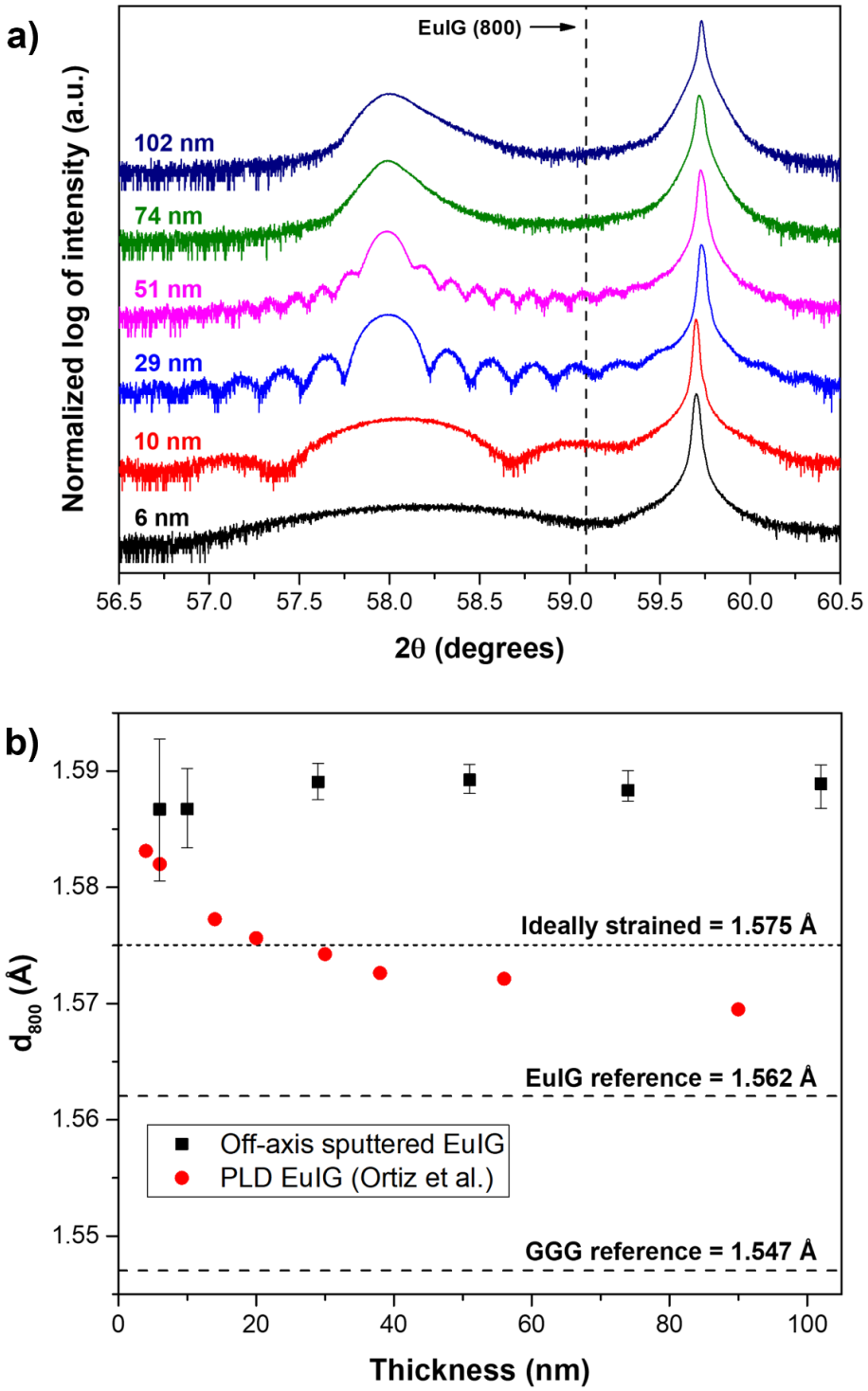

Fig. 6.5: XRD structural characterization of the off-axis sputtered epitaxial (100)- EuIG/GGG films. a) 2θ-θ measurements around the (800) peak position of EuIG films with varying thicknesses, and b) interplanar spacing of the (800) peaks d_{800} plotted as a function of thickness in comparison to PLD films frown by Ortiz et al.[2]

illustrated in **Fig. 6.5b** where the (800) interplanar spacings d_{800} are plotted versus film thickness for both the sputtered films from this study and the PLD grown films reported by Ortiz et al.[2] The error bars on the d_{800} values of the sputtered films represent the full width of the film peak at 95% of its maximum intensity. The dashed horizontal lines represent the reference (800) interplanar spacings of unstrained EuIG, GGG, and an ideally strained EuIG that does not relax as calculated according to eq. (6.2) and (6.3) by setting the in-plane strain equal to the lattice misfit strain and using elastic stiffness constants found in literature of $c_{11} = 25.10 \times 10^{11}$ dyne/cm^2 and $c_{12} = 10.70 \times 10^{11}$ dyne/cm^2.[5] The ideally strained interplanar spacing value also provides a useful approximation for the maximum out-of-plane d_{800} expected for an epitaxially strained (100)-oriented EuIG film grown on GGG.

Fig. 6.5b shows that the out-of-plane interplanar spacings of the PLD grown films [2] are thickness dependent and relax towards the bulk value whereas the off-axis sputtered films of the present study stay at a nearly constant value up to a thickness of 102 nm, which was the thickest film studied. The measured d_{800} values of the off-axis-sputtered films also have an average value of 1.588 Å which is much larger than the value calculated for an ideally strained EuIG of 1.575 Å. Since we were able to determine with XRD measurements that the GGG substrates have a lattice parameter of 12.378 Å which closely matches the manufacturer provided value of 12.376 Å, the larger than expected out-of-plane interplanar spacings of these samples likely indicates that either their intrinsic (unstrained) lattice parameters, elastic stiffness coefficients, or both, are different from the values reported in literature for EuIG. This could be an indication that the films contain atomic point defects, or that the stoichiometry of the films has been altered by the off-axis sputtering technique.

To better understand the structure of the films, reciprocal space maps were taken of the 102 nm thick sample about the symmetric (800) and asymmetric ($84\bar{2}$) peak positions, as shown in **Fig. 6.6a and 6.6b**, respectively. The symmetric reciprocal space map of the film in **Fig. 6.6a** exhibited a single peak near the higher intensity (800) peak of GGG. The observed peak position of the film at Q_Z =0.62944 $Å^{-1}$ matches closely with the 0.62937 $Å^{-1}$ calculated from the peak position in the 2θ-θ measurements. There is a spread in the film along the surface normal direction towards larger Q_Z, suggesting that the strain gradient is not entirely symmetric in the out-of-plane direction and relaxes toward the small intrinsic interplanar spacing of EuIG. However, the bulk of the peak is centered on the fully strained position. There is also a significant triangle-shaped mosaic region surrounding the film peak which results from the horizontal spread of the film in the Q_X direction being asymmetric along the surface normal, where any deviations from the central Q_X value are interpreted as mosaicity and variation in the growth direction.

Unlike 2θ-θ and symmetric reciprocal space map measurements, asymmetric reciprocal space maps contain information on the in-plane lattice component and therefore provide a direct measurement of the in-plane strain. **Fig. 6.6b** shows an asymmetric reciprocal space map of the ($84\bar{2}$) peak. The peak maxima of the film and substrate share a common Q_X value, confirming that the film and substrate share a common in-plane lattice parameter. The film is well strained with respect to the substrate and maintains strong coherency, indicating successful heteroepitaxy at a thickness of 102 nm. The film peak also shows a small degree of relaxation towards the unstrained lattice position of EuIG. This is consistent with the data obtained from the 2θ-θ and symmetric reciprocal space map measurements because the maximum of the film peak has not shifted towards the unstrained position.

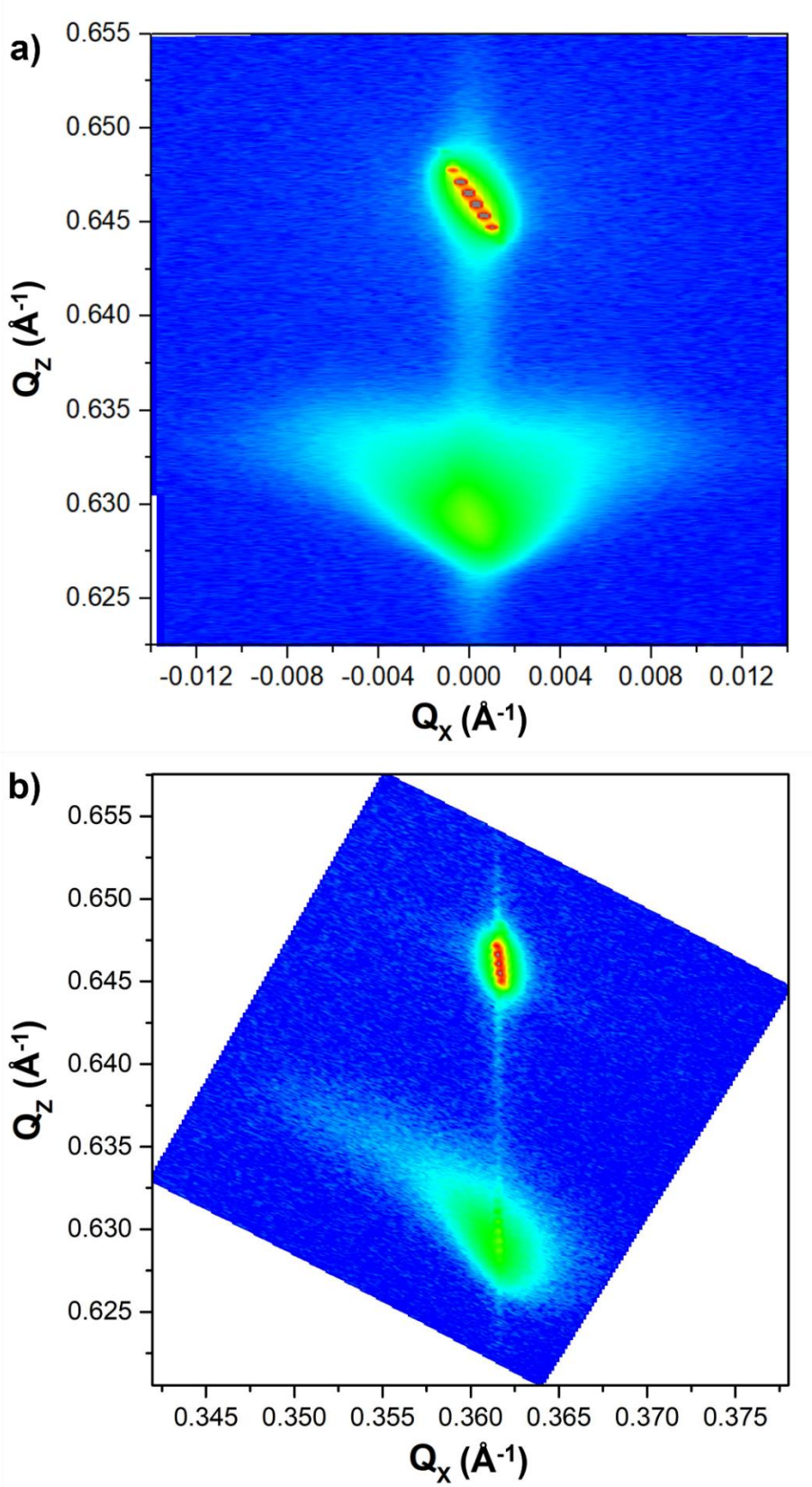

Fig. 6.6: Reciprocal space maps of the 102 nm off-axis sputtered EuIG film grown on (100)-oriented GGG about the a) symmetric (800) and b) asymmetric ($84\bar{2}$) peak positions.

The XRD results of **Fig. 6.5 and 6.6** collectively show low levels of strain relaxation and that the in-plane lattice parameters of the films match the substrate. This indicates that the strain in the films is approximately ideal and that the films possess a nearly uniform structure with an in-plane strain equal to the lattice mismatch strain. In the asymmetric reciprocal space map of **Fig. 6.6b**, the film peak relaxes in a direction that points to a slightly lower Q_X and Q_Z position than what is predicted for the reference lattice parameter of a_{EuIG} = 12.497 Å. This implies that the unstrained lattice parameter a_0 is in fact larger than the reference value. Seeing as the difference in lattice parameter could result from point defects or deviation from stoichiometry, it might also be the case that the elastic stiffness coefficients differ from the reported values. The elastic (6.2), (6.3) and (6.4) can be combined into a single equation with two unknown values, namely the unstrained lattice parameter of the film a_0, and a single combined constant containing the elastic stiffness constants. Knowing one of these values would allow us to determine the other from the available XRD data, however, there isn't a straightforward way to measure either of these values from the films. It would also be practically very difficult to grow a sufficiently thick enough film to obtain a_0 from. In the following analysis, we assumed that the stiffness constants of the films are similar to the literature values because we have no clear evidence to suggest otherwise, yet we have evidence that the intrinsic lattice parameter of the films are larger than reference.

By combining eq. (6.2), (6.3) and (6.4) and rearranging for a_0, we obtain the following expression for determining the intrinsic lattice parameter of the film:

$$a_0 = \frac{c_{11}a_{\perp}+2c_{12}a_{//}}{c_{11}+2c_{12}}. \quad (6.6)$$

Using an average $a_{\perp}$ determined from the 2θ-θ peak positions of the films, an in-plane strain $a_{//} = a_{GGG}$ according to the asymmetric reciprocal space map results, and the elastic stiffness constants

from literature (c_{11} = 25.10 x 10^{11} dyne/cm^2 and c_{12} = 10.70 x 10^{11} dyne/cm^2)[5] yields an intrinsic lattice parameter a_0 = 12.555 Å. This value is 0.5% larger than the reference value for EuIG. The slight relaxation observed in **Fig. 6.6b** also appears directed more closely toward the relaxed reciprocal lattice position calculated for a lattice parameter of 12.555 Å (0.35620 Å^{-1}, 0.63720 Å^{-1}) than it does for the position calculated for a lattice parameter of 12.497 Å (0.35786 Å^{-1}, 0.64015 Å^{-1}), which suggests that the elastic stiffness constants of the sputtered films are close to the reference values. The strains calculated using the reference lattice parameter of 12.497 Å are $\varepsilon_{//}$ = -0.95% and $\varepsilon_{\perp}$ = 1.67%. However, using the calculated lattice parameter of 12.555 Å yields more accurate strain values of $\varepsilon_{//}$ = -1.33% and $\varepsilon_{\perp}$ = 1.20%.

We believe that the differences between the lattice parameters of the films grown here and that of reference values can be explained by small differences in stoichiometry. Our fabrication process might cause a change in the cation ratio of Eu and Fe compared to the starting material, and it could also lead to oxygen deficiency. A recent work on the off-axis sputtering of EuIG on GGG by Guo et al. [6] demonstrates an approximately linear increase in out-of-plane lattice parameter with increasing Eu/Fe ratio. Specifically, the Eu/Fe ratio increased as the longitudinal target to substrate distance increased. It was reasoned that lighter Fe ions are more easily scattered away from the central sputtering axis than the heavier Eu ions. A similar relationship between the cation ratios and longitudinal substrate distance was also shown in off-axis sputtered TmIG films, which also reported an increasing lattice parameter with Tm concentration.[7] The lattice parameter measured in the present work, however, is larger than that reported by Guo et al [6], which we believe is because our films are also oxygen deficient as will be discussed next.

Oxygen deficient ferrites have been shown to have up to a 3.6% larger lattice parameter than their stoichiometric counterparts.[8-10] It was argued that oxygen vacancies donate electrons to the empty 3d orbitals of nearby Fe^{3+}, reducing them to Fe^{2+}.[8,11] Because Fe^{2+} has a larger ionic radius than Fe^{3+}, the lattice parameter of rare earth iron garnets is directly related to the level of oxygen vacancies.[8,12] It is likely that some oxygen may have come out of the lattice during film growth due to the sputtering conditions. Specifically, the deposition occurred in a low-pressure environment with a much lower partial pressure of oxygen than the ambient atmosphere. Furthermore, the substrate was heated to a temperature of 600°C during the deposition process, which likely increased the rate of oxygen vacancy formation in the films. It is important to mention that unlike the EuIG films by Guo et al [6] or Ortiz et al [2], the films of this study were never annealed post deposition.

As previously discussed, the 2θ-θ data of **Fig. 6.5** show that the strain in the films does not substantially relax with thickness. Typically, as an epitaxial film grows thicker, a depth dependent strain profile develops that correlates with a gradient of misfit dislocations.[13] Because the strain energy in a film is proportional to its strained volume, these misfit dislocations develop as a mechanism to reduce the total strain energy of a film as it becomes thicker. In the asymmetric reciprocal space map of **Fig. 6.6b** we observed that most of the 102 nm thick film remains in a fully strained state, and in the symmetric reciprocal space map of **Fig. 6.6a** we saw that most of the film shares the same out-of-plane (800) d-spacing. The dramatically lower strain relaxation compared to PLD grown films might be explained by a different strain relaxation method that is less thickness dependent than strain accommodated by the typical gradient in density of dislocations.

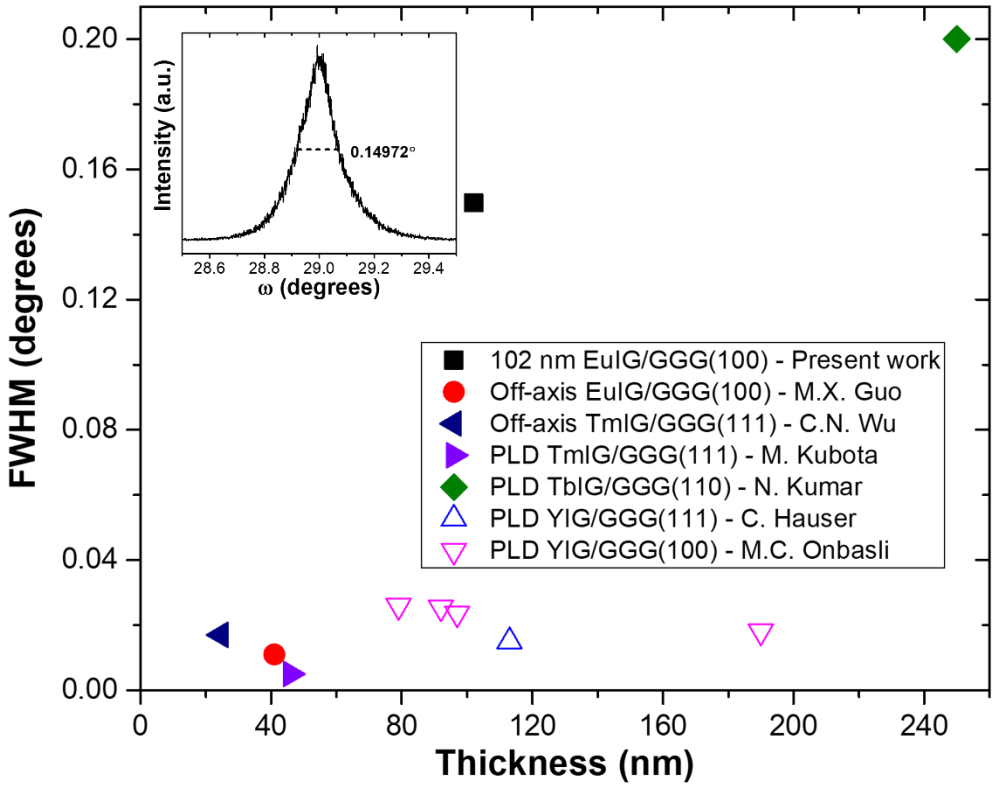

Fig. 6.7: A comparison of XRD rocking curve FWHM measurements of various epitaxial rare earth iron garnet films. Open symbols represent films with in-plane magnetic easy axes [14,15], whereas the closed symbols represent films with out-of-plane magnetic easy axes [6,7,16,17]. The inset is the rocking curve of the (800) peak of the 102 nm EuIG/GGG-(100) film from the present study.

The triangular shaped spread near the film peak in **Fig. 6.6a** reveals that there is mosaicity in the structure of the film. Unfortunately, there are few reports of asymmetric reciprocal space maps of epitaxial rare earth iron garnet films in literature to compare with, let alone for the $(84\bar{2})$ peaks of (100)-oriented films. However, there are reports of XRD rocking curve measurements from which comparisons can be made. In particular, the FWHM value of a rocking curve is a convenient way to quantify the spread in mosaic tilt angle within an oriented film. A rocking curve was collected for the (800) peak of the 102 nm thick sample and its FWHM is plotted in comparison to other epitaxial rare earth iron garnet films from literature in

Fig. 6.7. The majority of the films from literature have very low FMHM values of less than ~0.03°, yet our 102 nm off-axis sputtered film and a ~250 nm thick PLD grown TbIG film reported by Kumar et al [17] have FWHM's of ~0.15° and ~0.2°, respectively. Furthermore, both our film and the film grown by Kumar et al [17] exhibit stress-induced perpendicular easy axes of magnetization, indicating that the in-plane strains of these films are significant.

In comparison to the other epitaxial films, **Fig. 6.7** clearly shows that our sample has a larger distribution of mosaic tilt angles. We believe that this mosaicity plays a role in accommodating the elastic strain energy in our films. It is possible that their larger lattice parameters also affect the dislocation formation since dislocation formation energy is proportional to the square of the Burgers vector, and the Burgers vector scales with lattice size. Thus, the dislocation formation energy of our films is likely higher than a pristine EuIG, which is a contributing factor for making mosaicity the dominant strain accommodation method as compared to the more usual dislocation formation method. In addition, the point defects related to non-stoichiometry might also contribute to the high degree of mosaicity.

Table 6.1: Structural and magnetic properties of the epitaxially strained EuIG films with perpendicular magnetic anisotropy grown on (100)-oriented GGG with thicknesses ranging from 6 to 102 nm.

Thickness (nm)	**$2\theta_{800}$ (degrees)**	**d_{800} (Å)**	**$4\pi M_S$ (G)**	**H_C (G)**
6	58.090	1.5867	1339	540
10	58.085	1.5867	1336	641
29	57.992	1.5891	1296	185
51	57.985	1.5892	1084	1124
74	58.021	1.5883	1069	524
102	58.004	1.5889	1047	684

6.3.2. Magnetic Characterization of Off-axis Sputtered EuIG

Our method of producing perpendicular magnetic anisotropy was verified using VSM measurements. All samples had their magnetization curves measured with the field applied both in-plane and out-of-plane to the film using a Lakeshore 7400 Series VSM. The linear

paramagnetic background of the substrate was subtracted from the measurement data and then they were normalized by M_S before being plotted in **Fig. 6.8**. The VSM analysis of **Fig. 6.8** shows that all samples exhibit in-plane paramagnetic-like and square out-of-plane magnetic hystereses, indicating that the easy axes of magnetization are directed out-of-plane for all samples. The out-of-plane coercivities of our samples range from 185 Oe in the 29 nm thick film to 1124 Oe in the 51 nm thick film, with most near ~600 Oe. The $4\pi M_S$ values of the films decreased with thickness, and range from 1047 to 1339 G. The measured coercivities and $4\pi M_S$ values are included in **Table 6.1**.

The measured $4\pi M_S$ values are close to what has been reported for other EuIG films [2,6,18,19,23], and are comparable to the 1193 G reported for bulk EuIG.[20] Specifically, these $4\pi M_S$ values are somewhat higher than reported by Ortiz et al [2,23], and similar but lower to Rosenberg et al, Bauer et al and Guo et al [6,18,19]. It is likely that these differences are caused by slight differences in stoichiometry. For example, in other off-axis sputtered films with thicknesses of ~30 nm, the $4\pi M_S$ was shown to decrease from 1565 to 904 G as the Eu/Fe ratio was decreased from 0.586 to 0.498.[6] It is likely that oxygen vacancies play a role in the slightly lower $4\pi M_S$ values as well. The reason for the substantial variation in coercivity is not well understood, but it may be related to differences in the magnetic asymmetry in the crystal structure of the films or variation in the domain behavior with thickness. There are also step-like features in all of the measured hysteresis curves at applied fields of approximately ±300 Oe. We believe that these features are due to the substrate and are not present in the films themselves. A measurement of a bare GGG substrate revealed similar features, and similar step-like features are visible in the hysteresis curves of other rare earth iron garnet films grown on GGG substrates.[2,18]

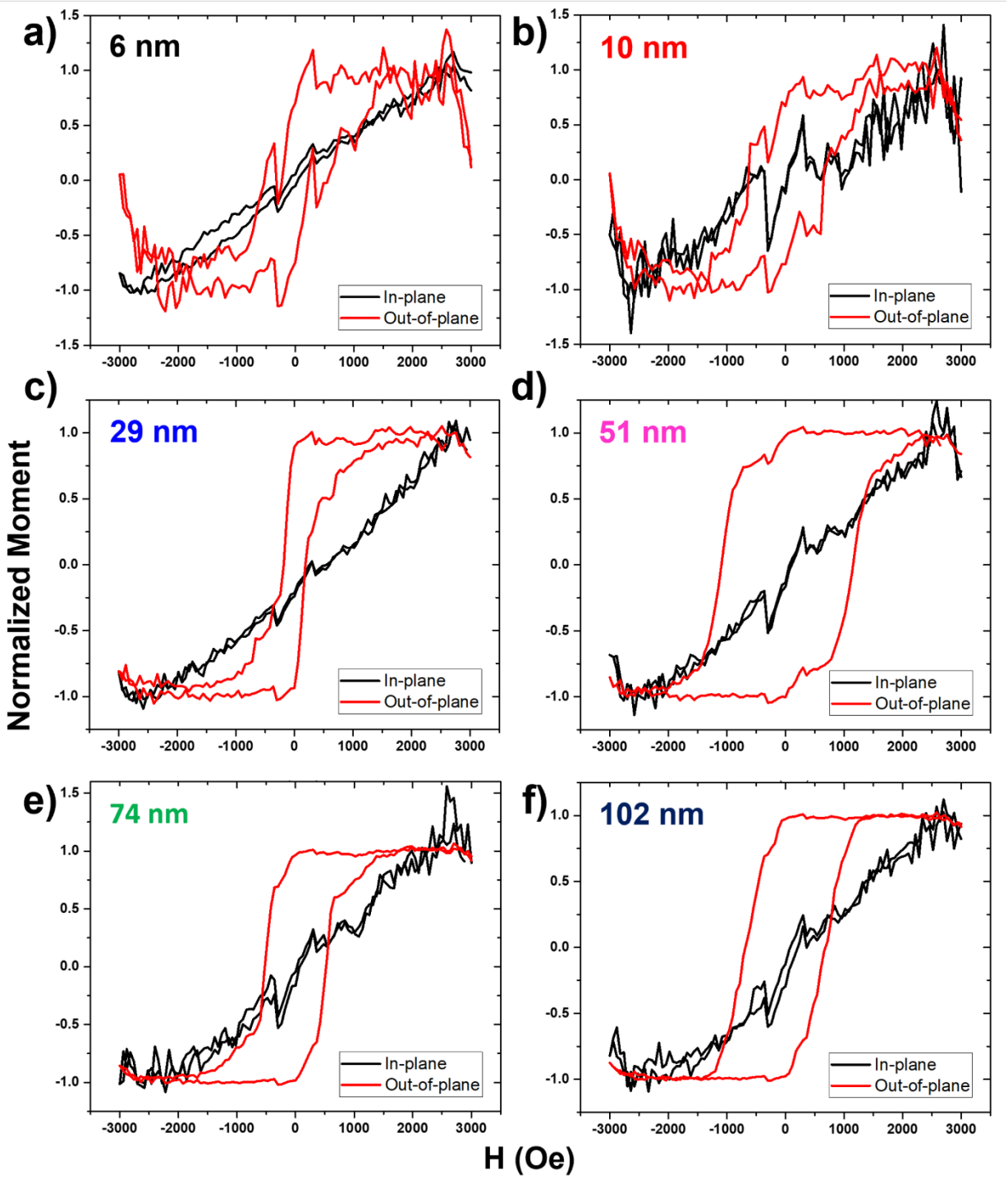

Fig. 6.8: In-plane (black) and out-of-plane (red) magnetic hysteresis curves normalized by M_S for the a) 6 nm, b) 10 nm, c) 29 nm, d) 51 nm, e) 74 nm and f) 102 nm off-axis sputtered epitaxial EuIG films.

Most notably, the thickest sample in this study exhibits robust perpendicular magnetic anisotropy at a thickness of 102 nm. Earlier work on EuIG films have so far only reported PMA

at a maximum thickness of 56 nm.[2,18] The robust perpendicular magnetic anisotropy observed at such a large thickness is a direct consequence of the as-synthesized films having less strain relaxation than is typically expected. While the low levels of strain relaxation in these samples are remarkable, it is possible that the underlying structural differences resulting in this phenomenon could lead to increased spin damping.

In order to determine their spin damping, frequency dependent FMR measurements were carried out on the 74 nm and 102 nm thick samples using a co-planar waveguide set-up with the field applied out-of-plane and collected with a vector network analyzer. The nonlinear backgrounds were subtracted from the collected signals and the resulting absorption curves were then fit with the sum of a Lorentzian, antilorentzian and gaussian function. The purpose of the gaussian function was to compensate for a smaller secondary resonance that overlapped with the primary signal, possibly related to the presence of Eu^{2+} or Fe^{2+} ions. The resonant field H_R and linewidth ΔH_0 values were extracted from the Lorentzian portion of the fits and were plotted versus frequency for both samples in **Fig. 6.9**.

The resonant field values are highly linear with frequency, matching the relationship for FMR in films with an out-of-plane magnetization given by

$$f_R = \frac{\gamma}{2\pi}(H_R - 4\pi M_{eff}), \tag{6.7}$$

where γ is the gyromagnetic ratio.[21] Remarkably, the resonant field positions are virtually identical between the two samples, indicating that both their gyromagnetic ratios and $4\pi M_{eff}$ values are nearly identical. The resonant fields were fit with a linear function and the $\frac{\gamma}{2\pi}$ values were determined from the slope to be $2.33 \pm 0.09 \times 10^{-3}$ GHz/Oe and $2.19 \pm 0.08 \times 10^{-3}$ GHz/Oe for the for the 74 nm and 102 nm samples, respectively. This is somewhat larger than the literature value of 1.95×10^{-3} GHz/Oe, indicating that the g-factor of the off-axis sputtered

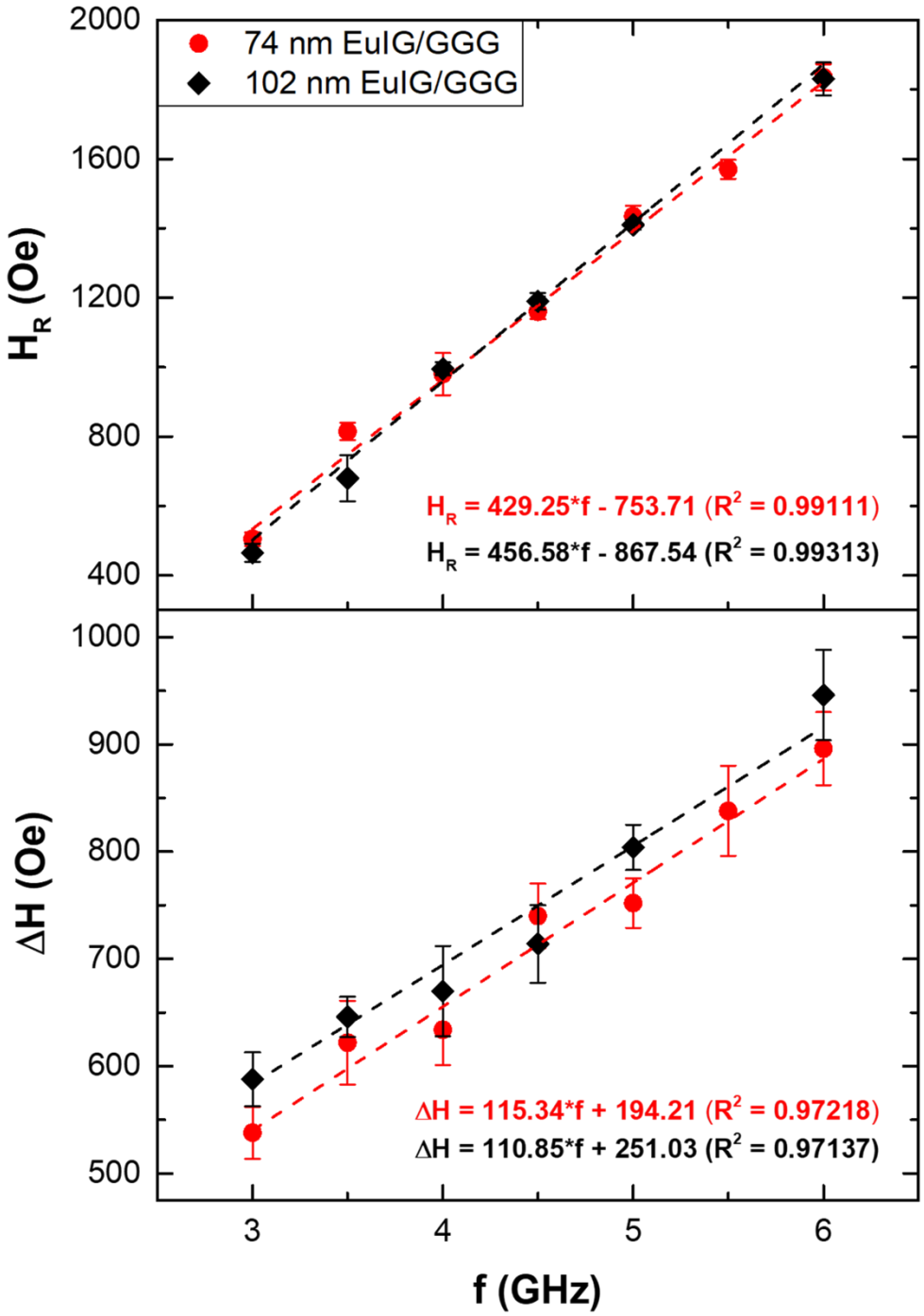

Fig. 6.9: Out-of-plane FMR measurement results of the 74 nm (red) and 102 nm (black) off-axis sputtered epitaxial EuIG films. The resonant fields H_R (top panel) and FMR linewidths ΔH_0 (bottom panel) are plotted as a function of the resonant frequency.

samples is ~10% larger than the reference value of 1.40.[22,23] The larger gyromagnetic ratio of our samples is likely caused by deviation from the ideal stoichiometry. The anisotropy fields $H_\perp$ were extracted from the intercepts according to

$$4\pi M_{eff} = 4\pi M_S - H_\perp, \tag{6.8}$$

and had values of 1823 ± 72 Oe and 1915 ± 76 Oe for the 74 nm and 102 nm films, respectively. The fact that the anisotropy fields are so similar is consistent with the XRD results which showed very similar strains in these samples.

The Gilbert damping and inhomogeneous contribution to linewidth were found for the two samples by plotting their linewidths as a function of frequency and fitting them with a straight line. Assuming that the broadening due to two-magnon scattering is negligible, the Gilbert damping parameter α is extracted from the slope of the fit and the intercept is the inhomogeneous broadening, according to

$$\Delta H = \frac{2\pi\alpha}{\gamma} f_R + \Delta H_0.[24] \tag{6.9}$$

The damping was found to be very similar in both samples, with the 74 nm film having a damping of 0.269 ± 0.021 and the 102 nm film having a damping of 0.243 ± 0.020. These values are an order of magnitude larger than the 0.020 to 0.025 that's been reported in other epitaxial EuIG films.[18,23] It is likely that point defects related to nonstoichiometry play a role in the increased damping, especially oxygen vacancies which can change the oxidation state of nearby Fe and Eu ions, thereby changing their magnetic state.[8,11] In particular, an Eu^{3+} ion occupying a dodecahedral site normally has a J = 0 ground state that contributes no net magnetic moment, but if reduced to Eu^{2+} it then has a J = 7/2 ground state which has a significant contribution to the overall magnetic moment.[23]

The inhomogeneous broadening of the two samples were also found to be fairly large and similar to each other, with values of 194.2 ± 35.7 Oe and 251.0 ± 35.4 Oe in the 74 nm and 102 nm samples, respectively. It is unsurprising that the inhomogeneous broadening was slightly larger in the 102 nm film since the 2θ-θ measurements of **Fig. 6.5a** showed the broadest XRD peak for this sample, implying there is more variation in d-spacing in the 102 nm film than in any other sample. This also suggests that the 102 nm film has more dislocations than the 74 nm film and thus has a higher degree of structural and magnetic inhomogeneity. Together, the 2θ-θ and reciprocal space mapping results imply that there was little to no non-uniform strain relaxation in these films, therefore the large amounts of magnetic inhomogeneity are likely explained by the presence of point defects and significant levels of mosaicity. It is unclear whether the magnetic inhomogeneity resulting from structural inhomogeneity affected the spin damping of these films. In highly strained EuIG films grown with PLD that had inhomogeneous broadening as large as 412 Oe, the damping was unaffected by the amount of magnetic inhomogeneity.[23]

6.4. Conclusions

We demonstrated a novel off-axis sputtering technique for growing epitaxially strained rare earth iron garnet films from a compacted powder target. Compared to PLD, off-axis sputtering has clear benefits with regards to growing larger coverage area films, and the wider industrial support for sputtering at large. Our method stands out compared to other reports of off-axis sputtering because it resulted in single crystal garnet films with stress-induced perpendicular magnetic anisotropy that required no post-deposition annealing step. Most notably, the EuIG films produced in this study exhibited robust perpendicular magnetic anisotropy as confirmed by

VSM analysis at a maximum thickness of 102 nm, the thickest reported EuIG film with perpendicular anisotropy to date.

The structures of the films were analyzed using high-resolution x-ray diffraction 2θ-θ and reciprocal space mapping techniques and it was discovered that the lattice mismatch strain from the (100)-oriented GGG substrates did not relax appreciably with thickness. The films maintained near complete heteroepitaxy up to a thickness of 102 nm, the thickest film in this study. From the structural data, it was also discovered that the intrinsic (unstrained) lattice parameter of the films was ~0.5% larger than the reference value, and that the films had significant levels of mosaicity. Based on this larger lattice parameter, the in-plane strain of the films is $\varepsilon_{//} = -1.33\%$ and the out-of-plane strain is $\varepsilon_{\perp} = 1.20\%$. The larger lattice parameter is likely explained by point defects related to nonstoichiometry of the films. In particular, oxygen vacancies likely developed during the growth of the films, and have been previously shown to increase the lattice parameter of ferrites by up to 3.6%.[8-10] Furthermore, the spatial separation from target to substrate can significantly alter the cation ratios of off-axis sputtered rare earth iron garnet films, additionally affecting their lattice parameter.[6,7] The dramatically lower strain relaxation compared to PLD grown films might be explained by a different strain relaxation method that is less thickness dependent than the more typical strain accommodation through a gradient in the density of dislocations. We believe that the mosaicity of our films plays a role in accommodating the elastic strain energy, and it is possible that point defects related to nonstoichiometry also contribute to the mosaicity.

The robust perpendicular magnetic anisotropy of these films at such large thicknesses is a direct consequence of their low levels of strain relaxation. Thicker films with perpendicular magnetic anisotropy are potentially useful for their larger magnetic interaction with adjacent

layers, however, the mosaicity and point defects that we believe are responsible for the reduced strain relaxation of our films likely have negative consequences on their spin damping. Using frequency dependent FMR analysis, we found that the films had damping of ~0.25, almost exactly one order of magnitude higher than the damping of PLD grown EuIG.[18,23] While magnetic inhomogeneity due to structural inhomogeneity could potentially affect their spin damping, the damping of other EuIG films was shown to be unrelated to the inhomogeneous contribution broadening.[23] It is likely that point defects are the primary reason for the increased damping of these films. More specifically, oxygen vacancies can impact the magnetization of neighboring Eu and Fe ions and could potentially have a large impact on the overall damping due to oxygen's role in mediating superexchange.

This work highlights the fact that the compositions of rare earth iron garnet films, and therefore their physical properties, can be altered by deposition and growth conditions. The field of rare earth iron garnet films would benefit from a more systematic approach of quantifying strain, defects, and how to selectively control them. Techniques such as reciprocal space mapping and x-ray photoelectron spectroscopy are two such methods that could help explain differences in elastic and magnetic behavior and pave the way for tailoring properties not yet seen in stoichiometric bulk rare earth iron garnets. In particular, atomic point defects haven't received much attention, yet they could dramatically impact the properties of rare earth iron garnet films. The off-axis sputtering method employed here resulted in defected films with unusually low strain relaxation and increased spin damping, yet it also demonstrated one possible method of controlling the defects in garnet films.

Acknowledgements

Chapter 6, in part, is a reprint of the material as it appears in C. R. Warren, V. Ortiz, L. Scipioni, J. Greer, J. Shi, Y. Kodera, and J. E. Garay. Robust perpendicular magnetic anisotropy in off-axis sputtered europium iron garnet (EuIG) thin films. J. Magn. Magn. Mater., 560 (2022) 169513. The dissertation author was the primary researcher and author of this material.

REFERENCES

[1] M. Reza, Z. Sajuri, Y. Yunas, and J. Syarif. Effect of sputtering target's grain size on the sputtering yield, particle size and coercivity (H_C) of Ni and $Ni_{20}Al$ thin films. IOP Conf. Ser.: Mater. Sci. Eng., 114 (2016) 012116.

[2] V. H. Ortiz, M. Aldosary, J. Li, Y. Xu, M. I. Lohmann, P. Sellappan, Y. Kodera, J. E. Garay, and J. Shi. Systematic control of strain-induced perpendicular magnetic anisotropy in epitaxial europium and terbium iron garnet thin films. APL Mater., 6 (2018) 121113.

[3] M. T. Johnson, P. J. H. Bloemen, F. J. A. den Broeder, and J. J. de Vries. Magnetic anisotropy in magnetic multilayers. Rep. Prog. Phys., 59 (1996) 1409-1458.

[4] E. Anastassakis. Strained superlattices and heterostructures: elastic considerations. J. Appl. Phys., 68 (1990) 4561.

[5] T. B. Bateman. Elastic Moduli of Single-Crystal Europium Iron Garnet and Yttrium Iron Garnet. J. Appl. Phys., 37 (1966) 2194.

[6] M. X. Guo, C. K. Cheng, Y. C. Liu, C. N. Wu, W. N. Chen, T. Y. Chen, C. T. Wu, C. H. Hsu, S. Q. Zhou, C. F. Chang, L. H. Tjeng, S. F. Lee, C. F. Pai, M. Hong, and J. Kwo. Single-crystal epitaxial europium iron garnet films with strain-induced perpendicular magnetic anisotropy: Structural, strain, magnetic, and spin transport properties. Phys. Rev. Mater., 6 (2022) 054412.

[7] C. N. Wu, C. C. Tseng, K. Y. Lin, C. K. Cheng, S. L. Yeh, Y. T. Fanchiang, M. Hong, and J. Kwo. High-quality single-crystal thulium iron garnet films with perpendicular magnetic anisotropy by off-axis sputtering. AIP Adv., 8 (2018) 055904.

[8] E. Enriquez, A. Chen, Z. Harrell, P. Dowden, N. Koskelo, J. Roback, M. Janoschek, C. Chen., and Q. Jia. Oxygen Vacancy-Tuned Physical Properties in Perovskite Thin Films with Multiple B-site Valence States. Sci. Rep., 7 (2017) 46184.

[9] E. Enriquez, A. Chen, Z. Harrell, X. Lü, P. Dowden, N. Koskelo, M. Janoschek, C. Chen, and Q. Jia. Oxygen vacancy-driven evolution of structural and electrical properties in $SrFeO_{3-\delta}$ thin films and a method of stabilization. Appl. Phys. Lett., 109 (2016) 141906.

[10] J. Ding, T. Liu, H. Chang, and M. Wu. Sputtering Growth of Low-Damping Yttrium-Iron-Garnet Thin Films. IEEE Magn. Lett., 11 (2020) 5502305.

[11] S. Tan, W. Zhang, L. Yang, J. Chen, and Z. Wang. Intrinsic defects in yttrium iron garnet: A first-principles study. J. Appl. Phys., 128 (2020) 183904.

[12] R. D. Shannon. Revised Effective Ionic Radii and Systematic Studies of Interatomic Distances in Halides and Chalcogenides. Acta. Cryst. A, 32 (1976) 751-767.

[13] H. Heinke, M. O. Möller, D. Hommel, and G. Landwehr. Relaxation and mosaicity profiles in epitaxial layers studied by high resolution X-ray diffraction. J. Cryst. Growth, 135 (1994) 41-52.

[14] C. Hauser, T. Richter, N. Homonnay, C. Esienschmidt, M. Qaid, H. Deniz, D. Hesse, M. Sawicki, S. G. Ebbinghaus, and G. Schmidt. Yttrium Iron Garnet Thin Films with Very Low Damping by Recrystallization of Amorphous Material. Sci. Rep., 6 (2016) 20827.

[15] M. C. Onbasli, A. Kehlberger, D. H. Kim, G. Jakob, M. Kläui, A. V. Chumak, B. Hillebrands, and C. A. Ross. Pulsed laser deposition of epitaxial yttrium iron garnet films with low Gilbert damping and bulk-like magnetization. APL Mater., 2 (2014) 106102.

[16] M. Kubota, A. Tsukazaki, F. Kagawa, K. Shibuya, Y. Tokunaga, M. Kawasaki, and Y. Tokura. Stress-Induced Perpendicular Magnetization in Epitaxial Iron Garnet Thin Films. Appl. Phys. Express, 5 (2012) 103002.

[17] N. Kumar, N. G. Kim, Y. A. Park, N. Hur, J. H. Jung, K. J. Han, and K. J. Yee. Epitaxial growth of terbium iron garnet thin films with out-of-plane axis of magnetization. Thin Solid Films, 516 (2008) 7753-7757.

[18] E. R. Rosenberg, L. Beran, C. O. Avci, C. Zeledon, B. Song, C. Gonzales-Fuentes, J. Mendil, P. Gambardella, M. Veis, C. Garcia, G. S. D. Beach, and C. A. Ross. Magnetism and spin transport in rare-earth-rich epitaxial terbium and europium iron garnet films. Phys. Rev. Mater., 2 (2018) 094405.

[19] J. J. Bauer, E. R. Rosenberg, and C. A. Ross. Perpendicular magnetic anisotropy and spin mixing conductance in polycrystalline europium iron garnet thin films. Appl. Phys. Lett., 114 (2019) 052403.

[20] G. Winkler. *Magnetic Garnets* (Vieweg, Braunschweig, 1981).

[21] B. Samantaray, A. K. Singh, A. Perumal, R. Ranganathan, and P. Mandal. Spin dynamics and frequency dependence of magnetic damping study in soft ferromagnetic FeTaC film with a stripe domain structure. AIP Adv., 5 (2015) 067157.

[22] T. Miyadi. Ferrimagnetic Reasonance in Europium-Iron Garnet. J. Phys. Soc. Japan, 15 (1960) 12.

[23] V. H. Ortiz, B. Askook, J. Li, M. Aldosary, M. Biggerstaff, W. Yuan, C. Warren, Y. Kodera, J. E. Garay, I. Barsukov, and J. Shi. First- and second-order magnetic anisotropy and damping of europium iron garnet under high strain. Phys. Rev. Mater., 5 (2021) 124414.

[24] B. Buford, P. Dhagat, and A. Jander. A technique for error estimation of linewidth and damping parameters extracted from ferromagnetic resonance measurements. J. Appl. Phys., 117 (2015) 17E109.

[25] K. Uchida, J. Xiao, H. Adachi, J. Ohe, S. Takahashi, J. Ieda, T. Ota, Y. Kajiwara, H. Umezawa, H. Kawai, G. E. Bauer, S. Maekawa, and E. Saitoh. Spin Seebeck insulator, Nat. Mater., 9 (2010) 894-897.

[26] Y. Kajiwara, K. Harii, S. Takahashi, J. Ohe, K. Uchida, M. Mizuguchi, H. Umezawa, H. Kawai, K. Ando, K. Takanashi, S. Maekawa, and E. Saitoh. Transmission of electrical signals by spin-wave interconversion in a magnetic insulator. Nature, 464 (2010) 262-266.

[27] Z. L. Jiang, C. Z. Chang, M. R. Masir, C. Tang, Y. D. Xu, J. S. Moodera, A. H. MacDonald, and J. Shi. Enhanced spin Seebeck effect signal due to spin-momentum locked topological surface states. Nat. Commun., 7 (2016) 11458.

[28] M. Aldosary, J. Li, C. Tang, Y. Xu, J.-G. Zheng, K. N. Bozhilov, and J. Shi. Platinum/yttrium iron garnet inverted structures for spin current transport. Appl. Phys. Lett., 108 (2016) 242401.

[29] J. X. Li, Y. D. Xu, M. Aldosary, C. Tang, Z. S. Lin, S. F. Zhang, R. Lake, and J. Shi. Observation of magnon-mediated current drag in Pt/yttrium iron garnet/Pt(Ta) trilayers. Nat. Commun., 7 (2016) 10858.

[30] P. Wei, F. Katmis, B. A. Assaf, H. Steinberg, P. Jarillo-Herrero, D. Heiman, and J. S. Moodera. Exchange-Coupling-Induced Symmetry Breaking in Topological Insulators. Phys. Rev. Lett., 110 (2013) 186807.

[31] M. Lang, M. Montazeri, M. C. Onbasli, X. Kou, Y. Fan, P. Upadhyaya, K. Yao, F. Liu, Y. Jiang, W. Jiang, K. L. Wong, G. Yu, J. Tang, T. Nie, L. He, R. N. Schwartz, Y. Wang, C. A. Ross, and K. L. Wang. Proximity induced high-temperature magnetic order in topological insulator–ferrimagnetic insulator heterostructure. Nano Letters, 14 (2014) 3459–3465.

[32] Z. Wang, C. Tang, R. Sachs, Y. Barlas, and J. Shi. Proximity-induced ferromagnetism in graphene revealed by the anomalous Hall effect. Phys. Rev. Lett., 114 (2015) 016603.

[33] C. Tang, C.-Z. Chang, G. Zhao, Y. Liu, Z. Jiang, C.-X. Liu, M. R. McCartney, D. J. Smith, T. Chen, J. S. Moodera, and J. Shi. Above 400 K robust perpendicular ferromagnetic phase in a topological insulator. Sci. Adv., 3 (2017) e1700307.

[34] B. L. Giles, Z. H. Yang, J. S. Jamison, and R. S. Myers. Long-range pure magnon spin diffusion observed in a nonlocal spin-Seebeck geometry. Phys. Rev. B, 92 (2015) 224415.

[35] L. J. Cornelissen, J. Liu, R. A. Duine, J. B. Youssef, and B. J. van Wees. Long-distance transport of magnon spin information in a magnetic insulator at room temperature. Nat. Phys., 11 (2015) 1022–1026.

[36] C.-X. Liu, X.-L. Qi, X.I. Dai, Z. Fang, and S.-C. Zhang. Quantum Anomalous Hall Effect in $Hg_{1-Y}Mn_YTe$ Quantum Wells. Phys. Rev. Lett., 101 (2008) 146802.

[37] Z. Qiao, W. Ren, H. Chen, L. Bellaiche, Z. Zhang, A. H. MacDonald, and Q. Niu. Quantum Anomalous Hall Effect in Graphene Proximity Coupled to an Antiferromagnetic Insulator. Phys. Rev. Lett., 112 (2014) 116404.

[38] S. Emori, B. A. Gray, H.-M. Jeon, J. Peoples, M. Schmitt, K. Mahalingam, M. Hill, M. E. McConney, M. T. Gray, U. S. Alaan, A. C. Bornstein, P. Shafer, A. T. N'Diaye, E. Arenholz, G. Haugstad. K.-Y. Meng, F. Yang, D. Li, S. Mahat, D. G. Cahill, P. Dhagat, A. Jander, N. X. Sun, Y. Suzuki, and B. M. Howe. Coexistence of Low Damping and Strong Magnetoelastic Coupling in Epitaxial Spinel Ferrite Thin Films. Adv. Mater., 29 (2017) 1701130.

[39] C. Tang, P. Sellappan, Y. W. Liu, Y. D. Xu, J. E. Garay, and J. Shi. Anomalous Hall hysteresis in $Tm_3Fe_5O_{12}$/Pt with strain-induced perpendicular magnetic anisotropy. Phys. Rev. B, 94 (2016) 140403(R).

[40] P. Sellappan, C. Tang, J. Shi, and J. E. Garay. An integrated approach to doped thin films with strain-tunable magnetic anisotropy: powder synthesis, target preparation and pulsed laser deposition of Bi:YIG. Mater. Res. Lett., 5 (2017) 41–47.

[41] L. Soumah, N. Beaulieu, L. Qassym, C. Carrétéro, E. Jacquet, R. Lebourgeois, J. B. Youssef, P. Bortolotti, V. Cros, and A. Anane. Ultra-low damping insulating magnetic thin films get perpendicular. Nat. Commun., 9 (2018) 3355.

[42] C. N. Wu, C. C. Tseng, Y. T. Fianchiang, C. K. Cheng, K. Y. Lin, S. L. Yeh, S. R. Yang, C. T. Wu, T. Liu, M. Wu, M. Hong, and J. Kwo. High-quality thulium iron garnet films with perpendicular magnetic anisotropy by *off-axis* sputtering – correlation between magnetic properties and film strain. Sci. Rep., 8 (2018) 11087.